TECHNISCHE
UNIVERSITÄT
DARMSTADT

Ab initio calculations of neutron-rich nuclei with many-body operators

at the Department of Physics
of the Technische Universität Darmstadt

submitted in fulfillment of the requirements
for the degree of Doctor rerum naturalium (Dr. rer. nat.)

Doctoral thesis
by Matthias Heinz

First referee report: Prof. Achim Schwenk, Ph.D.
Second referee report: Prof. Dr. Thomas Papenbrock

Darmstadt 2024

Ab initio calculations of neutron-rich nuclei with many-body operators
Ab-Initio-Rechnungen von neutronenreichen Atomkernen mit Vielteilchenoperatoren

Doctoral thesis by Matthias Heinz
Darmstadt, Technische Universität Darmstadt

Submission: May 3, 2024, Defense: June 3, 2024, Publication in TUprints: 2024

Abstract

The structure of atomic nuclei has far reaching consequences, including implications for fundamental interactions, the astrophysical synthesis of heavy elements, and the properties of matter in neutron stars. First-principles, or ab initio, nuclear structure theory aims to describe the structure of atomic nuclei based on inter-nucleonic interactions, connecting our understanding of nuclear structure to our understanding of the strong interaction. This approach has two key ingredients: nuclear forces describing the interactions between the protons and neutrons, collectively nucleons, making up nuclei; and many-body calculations computing the properties of many-nucleon systems starting from these nuclear forces. In this thesis, we tackle key challenges in ab initio many-body calculations to reach higher accuracy and to describe heavier systems.

Ab initio many-body methods capable of describing more than just the lightest elements rely on controlled, systematically improvable approximations in their solution of the many-body problem. The in-medium similarity renormalization group (IMSRG) is one such method. Its standard truncation at the normal-ordered two-body level, the IMSRG(2), has been used very successfully over the past decade to develop a comprehensive ab initio description of medium-mass nuclei. In this thesis, we develop the IMSRG(3), the next truncation order including normal-ordered three-body operators in the many-body solution. The extension of the IMSRG to the IMSRG(3) level brings greater precision to theoretical predictions of energies and charge radii. Furthermore, it gives substantial corrections to other quantities of interest where IMSRG(2) predictions are insufficient, such as the prediction of shell structure at doubly-magic nuclei. With the IMSRG(2) and the IMSRG(3) together, many-body uncertainties due to the approximate solution of the many-body problem can be robustly quantified. In addition to developing the IMSRG(3), we improve the treatment of three-body forces in IMSRG calculations, extending the reach of ab initio calculations to heavy nuclei and providing converged predictions of ground-state properties of ^{208}Pb. We also introduce multiple ways to accelerate IMSRG calculations, through basis optimization via the perturbatively improved natural orbitals and through importance truncation techniques applied to many-body operators in the IMSRG.

Using the improvements of the IMSRG we developed, we investigate carbon, calcium, and ytterbium isotopes in close collaboration with current experimental efforts. The IMSRG(3) improves the description of the structure of ^{48}Ca, resolving a long-standing overprediction of the closed-shell structure by the IMSRG(2). We also investigate the unresolved discrepancies between theory and experiment in calcium charge radii. In ytterbium isotopes, we provide nuclear structure input for a search for a possible new boson in isotope shifts of atomic transitions. Based on our input, we identify the leading signal in ytterbium isotope shifts to be due to the structure of ytterbium isotopes, not the possible new boson. From this, we extract information on $\delta\langle r^4\rangle$, giving access to a new nuclear structure observable related to deformation. This highlights the importance of nuclear theory to understand nuclear structure effects in searches for new physics.

These developments break new ground for ab initio nuclear theory, paving the way to a more comprehensive and precise description of atomic nuclei with many promising and interesting applications.

Zusammenfassung

Ab-Initio-Rechnungen von neutronenreichen Atomkernen mit Vielteilchenoperatoren

Die Struktur von Atomkernen hat weitreichende Konsequenzen, u.a. für die beobachtete Stärke fundamentaler Wechselwirkungen, die astrophysikalische Synthese schwerer Elemente, und die Materialeigenschaften von Neutronensternen. Die Ab-Initio-Kernstrukturtheorie zielt darauf ab, die Struktur von *Atomkernen* auf der Grundlage von Kernkräften zwischen *Nukleonen* (d.h. Protonen und Neutronen) zu beschreiben. Diese Herangehensweise verbindet unser Verständnis der Kernstruktur mit dem der starken Wechselwirkung und hat zwei Schlüsselkomponenten: *Kernkräfte*, die die Wechselwirkungen zwischen den Nukleonen beschreiben, aus welchen sich die Kerne zusammensetzen; und *Vielteilchenrechnungen*, die aus diesen Kernkräften die Eigenschaften von Vielteilchensystemen errechnen. In dieser Arbeit behandeln wir wichtige Herausforderungen innerhalb solcher Ab-Initio-Vielteilchenrechnungen, die zur Beschreibung schwererer Systeme mit größerer Genauigkeit überwunden werden müssen.

Ab-Initio-Vielteilchenmethoden, die uns in die Lage versetzen mehr als nur die leichtesten Elemente verlässlich zu beschreiben, müssen auf kontrollierten, systematisch verbesserbaren Näherungen bei der Lösung des Vielteilchenproblems beruhen. Die In-Medium Similarity Renormalization Group (IMSRG) ist eine solche Methode. Ihre Standardtrunkierung auf dem normalgeordneten Zweiteilchenniveau, die IMSRG(2), wurde in dem letzten Jahrzehnt sehr erfolgreich eingesetzt, um eine umfassende Ab-Initio-Beschreibung von mittelschweren Kernen zu entwickeln. In dieser Arbeit entwickeln wir die IMSRG(3), die nächste Ordnung in diesem Trunkierungsschema, die in der Vielteilchenlösung zusätzliche normalgeordnete Dreiteilchenoperatoren beinhaltet. Die Erweiterung der IMSRG zur IMSRG(3) erhöht die Präzision theoretischer Vorhersagen von Energien und Ladungsradien. Darüber hinaus liefert sie wesentliche Korrekturen für andere interessante Größen, für die die Präzision der IMSRG(2) nicht ausreicht, wie zum Beispiel die Vorhersage der Schalenstruktur bei doppeltmagischen Kernen. Der Vergleich von Vorhersagen der IMSRG(2) und IMSRG(3) erlaubt eine robuste Quantifizierung von Unsicherheiten, die auf der näherungsweisen Lösung des Vielteilchenproblems beruhen.

Zusätzlich zur Entwicklung der IMSRG(3) verbessern wir auch die technische Handhabung der Dreiteilchenkräfte innerhalb der IMSRG, um den Anwendungsbereich von Ab-Initio-Berechnungen auf die schwersten natürlich vorkommenden Kerne auszudehnen und konvergierte Vorhersagen für die Grundzustandseigenschaften von ^{208}Pb bereitzustellen. Weiterhin führen wir mehrere Methoden zur Beschleunigung von IMSRG-Rechnungen ein: (i) eine Basisoptimierung durch Verwendung von perturbativ verbesserten natürlichen Orbitalen, und (ii) die Anwendung diverser vorteilshafter Trunkierungstechniken auf Vielteilchenoperatoren in der IMSRG.

Unter Verwendung der von uns hier entwickelten Verbesserungen der IMSRG, sowie in enger Zusammenarbeit mit aktuellen experimentellen Untersuchungen, betrachten wir als nächstes Kohlenstoff-, Calcium- und Ytterbiumisotope. Die IMSRG(3) verbessert die Beschreibung der Struktur von ^{48}Ca und löst ein langjähriges Problem der IMSRG(2) bei der Vorhersage der geschlossenen Schalen in diesem Massenbereich.

Bisher ungelöste Diskrepanzen zwischen Theorie und Experiment bei den Calcium-Ladungsradien sind ein weiterer Gegenstand unserer Untersuchungen. Für Ytterbium liefern wir Kernstrukturvorhersagen zur Suche nach einem möglichen neuen Boson in Isotopenverschiebungen von atomaren Übergängen. Basierend auf unseren Vorhersagen identifizieren wir als führenden Beitrag zur Isotopenverschiebung in Ytterbium einen Kernstruktureffekt anstelle der andernorts vorgeschlagenen Wechselwirkung mit einem postulierten neuen Boson. Aus unserer Analyse extrahieren wir Informationen über $\delta\langle r^4\rangle$, eine neue Kernstrukturobservable, die bestimmte radiale Verformungen der Kerndichteverteilung charakterisiert. Diese Einsicht unterstreicht die wichtige Rolle der Kerntheorie bei der Suche nach neuer Physik in Prozessen, bei denen die innere Struktur des Atomkerns eine Rolle spielt.

Die hier beschreibenen Entwicklungen eröffnen neue Möglichkeiten für die Ab-Initio-Kernstrukturtheorie; sie ebnen den Weg zu einer umfassenderen und präziseren Beschreibung von Atomkernen und versprechen damit zahlreiche interessante und neuartige Anwendungen.

Contents

Part II Method advances

Part III Applications

Figures

Tables

Chapter 1

Introduction

Atomic nuclei are exciting laboratories, both theoretically and experimentally, to test and refine our understanding of fundamental physics [1]. Improved knowledge of the structure of nuclei has far-reaching implications. We learn about nuclear forces and how they emerge from strong interactions in the standard model at low energies [2–4]. Based on the same nuclear forces, we can predict the properties of dense matter in neutron stars [5–9], also dominated by strong interactions and with densities comparable to those in heavy nuclei [10–12]. Moreoever, we learn how various complex phenomena in nuclei emerge from nuclear forces and quantum many-body physics [13–25]. Constraining the properties of neutron-rich nuclei improves our understanding of the rapid neutron-capture process [26–29], occuring in neutron-star mergers and some supernovae and responsible for most of the synthesis of elements heavier than iron [30–32]. At the same time, with high-precision measurements in atoms and nuclei and complementary theory predictions we can test our understanding of fundamental interactions and search for new physics beyond the standard model [33–36]. With this broad reach, developments towards high-precision theoretical predictions of nuclear structure with robustly quantified uncertainties are particularly relevant.

In this thesis, the focus is the improved theoretical description of the structure of atomic nuclei using first-principles, or ab initio, many-body methods. Nuclei are made up of protons and neutrons, collectively referred to as nucleons. A first-principles description of nuclei amounts to solving the many-body Schrödinger equation

$$H\,|\Psi\rangle = E\,|\Psi\rangle\,, \tag{1.1}$$

which has two key ingredients: nuclear Hamiltonians H describing the interactions between nucleons; and many-body calculations or simulations of A interacting nucleons to describe A-body nuclei, obtaining the ground state $|\Psi\rangle$. Nuclear forces and ab initio many-body methods are each challenging fields of active research, and in the past three decades paradigm shifts and developments in both have drastically extended the reach and the precision of such calculations [37–52], nicely visualized in Fig. 1.1. In both cases, the key shifts have been towards low-resolution descriptions appropriate for the description of low-energy physics coupled with controlled, systematically improvable expansions.

Low-resolution nuclear forces make use of effective field theory and renormalization group methods to provide an efficient low-energy description of nuclear interactions. Of crucial importance here is the insight that when considering low-energy phenomena we have limited resolution, and thus details at short distances corresponding to small wavelengths or high energies do not affect the big picture at long distances we are interested in. Effective field theories (EFTs) work within this picture by providing a general low-energy expansion for unresolved short-distance physics in terms of contact interactions while explicitly including long-distance physics resolved at low energies [53, 54]. Chiral EFT for nuclear forces [55–58] has been very successful at producing quantitative nuclear interactions, in particular also including three-body forces

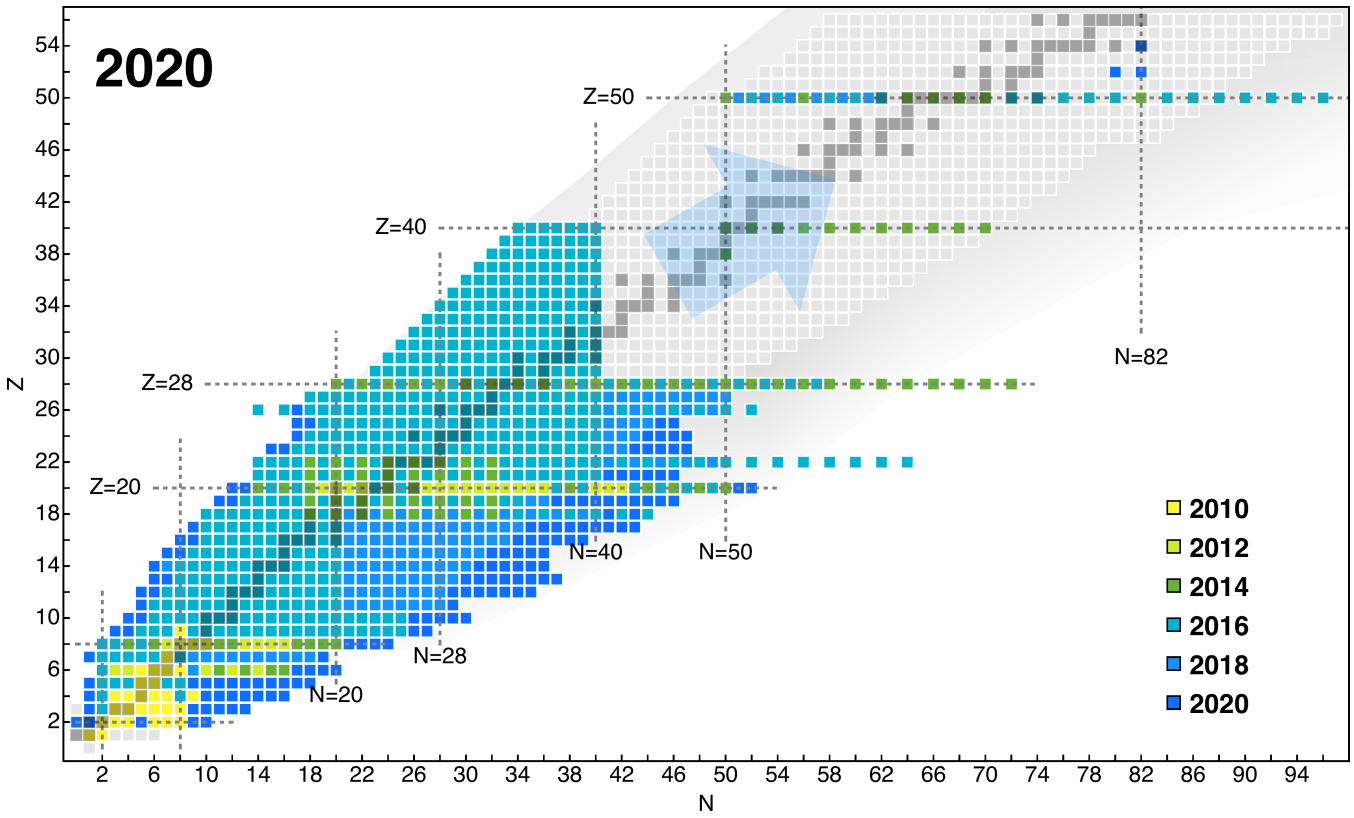

Figure 1.1: Progress in ab initio nuclear theory from 2010 to 2020. The chart of nuclides as a function of neutron number N and proton number Z, with stable isotopes indicated by dark gray squares. Isotopes for which converged ab initio calculations based on two- and three-body nuclear interactions have been published are indicated by the colored squares. The blue arrow indicates expected near-term progress towards heavier systems and a more comprehensive description of open-shell systems in particular. Figure from Ref. [86].

necessary for the quantitative description of nuclear many-body systems [59–61]. Renormalization group (RG) methods fit nicely into this picture, allowing one to systematically dial the resolution of nuclear forces via transformations that integrate out or decouple short-distance physics [62–69]. The combination of these two synergistic approaches has spurred the development of various low-resolution nuclear forces with many interesting perspectives for further improvements [70].

Nuclear structure theory, the prediction of the properties of atomic nuclei, was traditionally the domain of phenomenological methods like the shell model and density functional theory (DFT) [71–85]. While generally successful in the regions where they are fit, phenomenological many-body methods lack a systematic connection to nuclear forces limiting predictive power when extrapolating to exotic systems. On the other hand, ab initio many-body methods require no adjustment or fitting to specific parts of the nuclear landscape, giving them predictive power even in exotic systems [86]. The cost for this predictive power is the simulation of an A-body system with A interacting nucleons, a formidable formal and computational task.

The aforementioned efficient, low-resolution description of nuclear forces based on chiral EFT and RG transformations has allowed for ab initio nuclear many-body methods to thrive. Limited for a long time to quantum Monte Carlo (QMC) simulations using phenomenological two- and three-body forces [87, 88], low-resolution nuclear forces allowed for basis expansion methods to yield converged results, leading to first ab initio many-body calculations based on chiral EFT potentials using the no-core shell model (NCSM) [89].

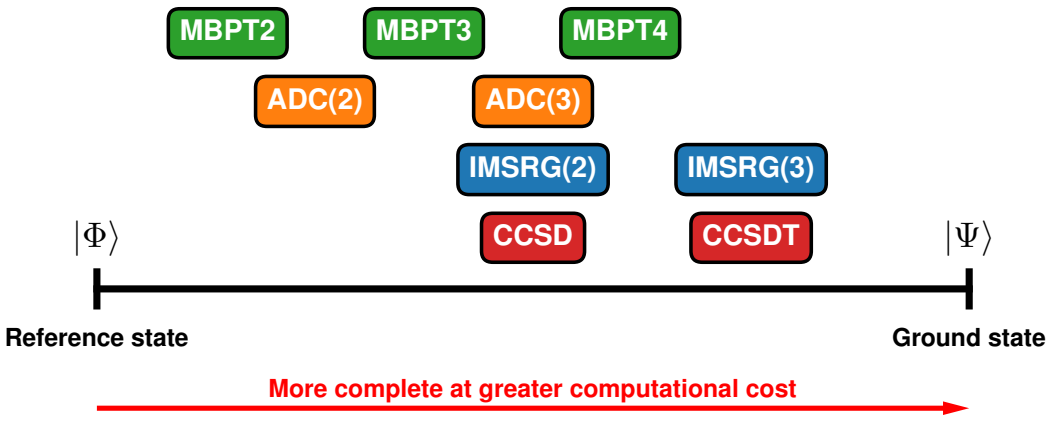

Figure 1.2: The many-body expansion. A schematic overview of many-body expansion methods, computing systematic corrections to the reference state $|\Phi\rangle$ to obtain more quantitative approximations to the ground state $|\Psi\rangle$. We show truncations various of methods at several orders organized from left to right in terms of computational cost and "completeness" (a more complete truncation provides a better approximation of the exact ground state): many-body perturbation theory at second, third, and fourth order (MBPT2, MBPT3, and MBPT4); self-consistent Green's function theory within the second- and third-order algebraic diagrammatic construction (ADC) [ADC(2) and ADC(3)]; the in-medium similarity renormalization group at the normal-ordered two- and three-body truncations [IMSRG(2) and IMSRG(3)]; and coupled-cluster theory truncated at the singles and doubles level (CCSD) and at the singles, doubles, and triples level (CCSDT).

Nuclear forces based on chiral EFT have since also been adapted for use in QMC calculations [90]. Still, both QMC and the NCSM solve the Schrödinger equation in a quasi-exact manner. This means they are limited in mass range to $A \lesssim 16$ due to the exponential scaling of the methods in mass number A. This can be seen in Fig. 1.1, where in 2010 (yellow) ab initio calculations were strongly limited in their reach.

The extension to heavier systems is possible by introducing controlled approximations to the solution of the many-body Schrödinger equation, with most methods employing what is called the many-body expansion. Here, the key idea is that the ground state of a system $|\Psi\rangle$ can be efficiently approximated by a leading-order reference state $|\Phi\rangle$. This approximation is unfortunately not quantitative, but one can efficiently compute corrections to the reference state to arrive at a quantitative description, and these corrections can be computed with computational costs that scale as a low polynomial of the basis size N [86].[1] This reduction of the computational scaling from exponential to polynomial is what allows such methods to be applied to systems as heavy as ^{208}Pb [47, 49] and has led to the rapid expansion of the reach of ab initio methods to heavy nuclei from 2010 to 2020 seen in Fig. 1.1.

This many-body expansion can be formulated in different ways, schematically represented in Fig. 1.2, leading to different many-body methods, such as many-body perturbation theory (MBPT) [91], coupled-cluster (CC) theory [92], self-consistent Green's function (SCGF) theory [93], and the in-medium similarity renormalization group (IMSRG) [94, 95]. All of these methods are formulated such that in some infinite limit one solves the Schrödinger equation exactly, but in practice one only needs low-order expansions to arrive at a quantitative description of many low-energy phenomena. Complementarily, recently developed approximate lattice methods [96–98] are scalable to heavier nuclei, where the approximations are in the specific definitions of leading order interactions required to tame the fermion sign problem and the (first-order) perturbative treatment of higher-order interactions.

[1] Typical basis sizes N are on the order of $\sim 10A$, making this effectively a polynomial scaling also in system size A.

Employing low-resolution nuclear forces and scalable many-body methods, ab initio nuclear theory has tremendous reach. Nuclear forces have free parameters that must be fit to data, but once such forces have been fit they can be used consistently to describe few-body scattering, homogeneous nuclear matter, and nuclei all over the nuclear chart. This consistency gives ab initio calculations predictive power in exotic systems where phenomenological methods rely on uncontrolled extrapolations [44]. At the same time, being able to compute different many-body systems from a single Hamiltonian allows us to test nuclear forces in a variety of contexts and rule out those forces that only reproduce some, but not all observables of interest [47].

A key ingredient here is the ability to quantify the uncertainties of ab initio predictions, resulting from the use of approximate theories for nuclear forces and approximate many-body methods. Both effective field theories and many-body expansion methods rely on systematically improvable expansions that can in practice be truncated at relatively low order. As a result, ab initio calculations are always approximate and predictions must be coupled with estimated uncertainties. Fortunately, systematically improvable methods with order-by-order convergence are perfect for assessing uncertainties due to missing higher orders [99]. In the past decade, Bayesian methods have been established to study this order-by-order convergence [100] and infer distributions of underlying theory parameters [101]. These methods, combined with emulators for few- and many-body calculations [102–105], allow ab initio nuclear theory to give complete posterior predictive distributions for observables, making statistically meaningful comparison with experiment and other theory predictions possible. In practice, such uncertainty quantification is still challenging, but assessing the uncertainty due to truncations in the EFT is steadily becoming more routine. A major milestone for ab initio nuclear theory is treating the uncertainties due to many-body expansion truncations in the same way.

1.1 Overview of this thesis

In this thesis, we improve the precision and efficiency of IMSRG calculations with the ultimate goal of making high-precision, uncertainty-quantified predictions of nuclear structure observables possible. Our developments improve the treatment of three-body forces in calculations of heavy nuclei, make many-body calculations more efficient through informed model-space truncations, and extend the many-body expansion in the IMSRG to the next order, the IMSRG(3), including normal-ordered three-body operators in the many-body solution. Developing the IMSRG(3) in particular is a milestone for nuclear structure theory, offering at the same time higher precision and the ability to robustly quantify many-body uncertainties in IMSRG calculations. We explore these developments in studies of carbon, calcium, and ytterbium isotopes, seeking to understand and quantify many-body uncertainties in our calculations.

Part of the results of this thesis have been published in Refs. [45, 49, 52, 106–108]. In the chapters outlined below, I discuss my contributions to each of the relevant publications.

This thesis is organized into the following chapters:

- Chapters 2, 3, and 4 introduce the fundamentals necessary to understand the developments in this thesis. Chapter 2 introduces nuclear forces, the basic input for our many-body calculations, emphasizing the role of effective field theory and renormalization group methods. Chapter 3 introduces the formal basics of many-body theory in general, and Chapter 4 introduces the IMSRG, the many-body method we use throughout this thesis.
- In Chapter 5, we present a framework to precisely include three-body forces in many-body calculations via normal ordering in a Jacobi basis [49]. This approach avoids truncations that have limited ab initio calculations of heavy nuclei, and we present converged ground-state energies and charge radii of ^{208}Pb predicted by the IMSRG.

- In Chapter 6, we present two complementary developments that allow us to efficiently truncate IMSRG calculations to reduce their computational cost. First, we construct perturbatively improved natural orbital bases to optimize the computational bases we use in IMSRG calculations [106]. Our results establish the benefits of basis optimization for many-body calculations, allowing for converged results in substantially smaller model spaces. Second, we explore importance truncation in the IMSRG [107], making informed truncations to compress our IMSRG calculations by as much as 99% while introducing negligible errors. The truncation strategies we establish for IMSRG calculations are generalizable to other many-body methods and will play an important role in making high-precision, high-cost many-body methods like the IMSRG(3) computationally tractable.

- In Chapter 7, we develop the IMSRG(3) [45], the next order in the IMSRG many-body method including normal-ordered three-body operators in the many-body solution. We test the IMSRG(3) and various approximations of it against exact theory results obtained from diagonalizations, establishing the precision of the method. We find that lower-cost approximations of the IMSRG(3) are able to give similarly precise results at substantially reduced computational cost. Such approximations, in particular an approximation we name the IMSRG(3)-N^7, pave the way to IMSRG(3) calculations in medium-mass nuclei, where the computational cost of the full IMSRG(3) would be prohibitive.

- In Chapter 8, we investigate the structure of ^{12}C and ^{13}C in IMSRG calculations [108], including also converged IMSRG(3)-N^7 calculations. The IMSRG(3) allows us to assess the many-body uncertainties in our calculations, and we find that the cluster structure of these systems, especially ^{12}C, leads to larger many-body uncertainties in our predictions.

- In Chapter 9, we perform preliminary studies of the structure of calcium isotopes using the IMSRG(3)-N^7 approximation. We are unable to provide fully converged results, but we still find that the IMSRG(3)-N^7 provides an improved description of the structure of ^{48}Ca, giving important corrections to the predicted 2^+ excitation energy. We explore correlated uncertainties, improved three-body basis truncations, and a new scalable numerical implementation as ways to reach fully converged IMSRG(3)-N^7 results.

- In Chapter 10, we compute the ground-state properties of ytterbium isotopes as input for a search for signals of a possible new boson in ytterbium isotope shifts [52]. Our fully uncertainty-quantified input explains the leading signal as an effect of the nuclear structure of ytterbium isotopes, which are heavily deformed. This complicated deformation makes the further analysis for new physics challenging, but we are able to extract information on $\delta\langle r^4\rangle$ from our measurements, giving access to a new nuclear structure observable related to deformation.

- We offer a final conclusion in Chapter 11.

This thesis opens up two new frontiers for IMSRG calculations, the frontier of heavy nuclei through the improved treatment of three-body forces and the frontier of precision predictions using the IMSRG(3), and explores them in subsequent applications. Establishing precise, fully uncertainty-quantified predictions with the IMSRG sets the foundation for many interesting studies exploring nuclear structure in exotic nuclei, in new physics searches, and in astrophysical environments.

Part I

Fundamentals

Chapter 2

Nuclear forces

The starting point for ab initio calculations of nuclei are nuclear forces describing interactions between nucleons. While conceptually simple, determining nuclear forces is a long-standing challenge for low-energy nuclear theory. This challenge ultimately lies in the fact that nucleons are not the fundamental degrees of freedom through which we understand the strong interaction. The theory of the strong interaction, quantum chromodynamics (QCD), is given in terms of quark and gluon degrees of freedom. At low energies these are confined in hadrons like nucleons, and so nuclear forces are residual effective strong interactions between bound quarks and gluons. Moreover, analytically deriving expressions for these effective strong interactions is currently not possible, as large values of the strong coupling constant $\alpha_{\rm s}(q^2)$ at low energies prevent a perturbative treatment.

Still, over many years our understanding of nuclear forces has been refined to a point where today it is both very quantitative and at the same time rooted in our understanding of QCD. Following the postulate of the one-pion exchange potential by Yukawa [109], initial efforts to obtain realistic nuclear interactions employed phenomenological parametrizations [110, 111] or tuned meson-exchange models [112–116] to fit nucleon-nucleon potentials that achieved a high quality reproduction of nucleon-nucleon scattering data. These efforts made great strides in setting the foundation for ab initio nuclear structure calculations, but it quickly became clear that a description of nuclei based on only two-body forces is incomplete: Three-nucleon forces are a necessary ingredient for a quantitative description of nuclear structure [59–61, 117–127]. Such phenomenological approaches lacked the predictive power to arrive at comprehensive, systematically improvable descriptions of three-body forces.

Based on these challenges, the paradigm of low-resolution nuclear theory appropriate for the description of low-energy phenomena was established for nuclear forces [55, 65, 66, 68, 128–134]. Essentially any description of nuclear forces is necessarily approximate, limited by either theory truncations or incomplete parametrizations, and nuclear forces are not unique, but scale- and scheme-dependent. As a result, low-energy nuclear theory has the freedom to choose to construct forces in such a way that emphasizes the reproduction of relevant low-energy physics. This paradigm is a crucial part of modern nuclear theory, where nowadays effective field theories and renormalization group methods are key ingredients to constructing the low-resolution nuclear forces that provide an efficient, predictive description of nuclear interactions in low-energy many-body systems.

In this chapter, we introduce chiral effective field theory and renormalization group methods for nuclear forces, both essential to understand the nuclear potentials used in this thesis, and explain how the uncertainty in our understanding of nuclear forces can be robustly quantified. This discussion is selective, focusing on details relevant for this thesis, and we refer the reader to the excellent reviews and articles in Refs. [54, 56, 57, 68, 100, 135] for a more comprehensive treatment.

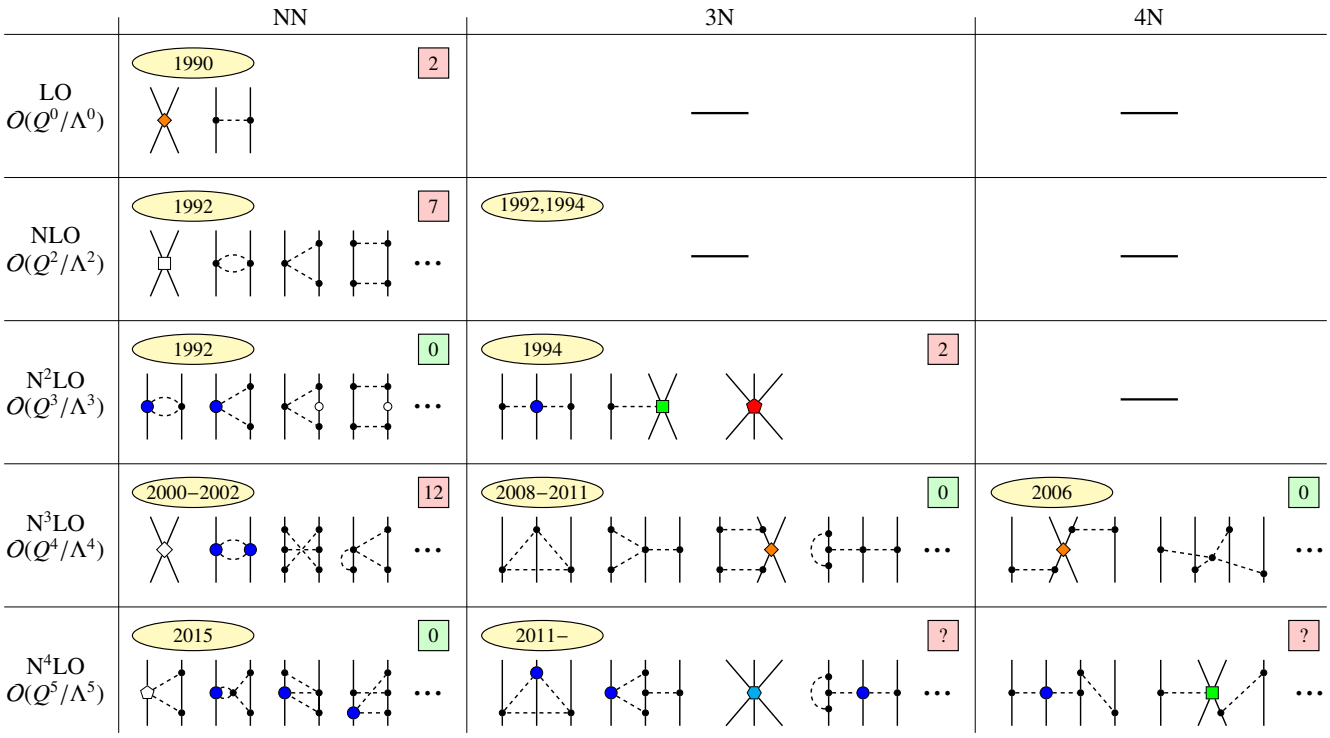

Figure 2.1: Contributions to NN, 3N, and 4N interactions in chiral EFT up to order N^{4}LO. Solid lines indicate nucleon propagators. Dashed lines indicate pion propagators. The number of new LECs for the new interaction contributions at each new order is shown in the top right corner. Figure from Ref. [61].

2.1 Effective field theories for nuclear forces

Effective field theories are a pillar of modern physics, broadly employed to capture relevant phenomena in systems characterized by multiple momentum scales and clear scale separations. They provide a way to define effective degrees of freedom and interactions between those in a systematically improvable expansion. The key ingredient is a clear separation of scales between relevant low-energy phenomena and irrelevant high-energy physics that the theory will not resolve. This allows for an efficient expansion of low-energy physics. Crucially, effective theories are constructed in a general way based on symmetries. Through this they can be connected to a more fundamental theory by respecting the known symmetries (exact and approximate) of the underlying theory.

Defining an EFT requires identifying three ingredients [54]: degrees of freedom of the theory; a high-momentum scale Λ_b characterizing unresolved physics; and a set of symmetries the theory must respect. The task is then to construct the most general Lagrangian with the chosen degrees of freedom consistent with the underlying symmetries [53]. The result is a theory that resolves low-energy interactions explicitly and expands high-energy interactions in terms of a general expansion in low momenta Q or light masses m over the breakdown scale Λ_b. This general expansion captures short-distance details of the underlying theory and comes with free parameters, known as low-energy constants (LECs) or also Wilson coefficients, which must be fit to data or matched to simulations of the underlying theory [136–142].

Chiral EFT is an effective theory for nuclear forces describing interactions between nucleons in terms of pion exchanges and short-range contact interactions [56, 57]. It is connected to chiral perturbation theory [143–147] (used to describe, for example, pion-nucleon scattering) via the common underlying chiral

symmetry of QCD, resulting in the same effective Lagrangian and common LECs. For the constuction of the EFT, QCD has various relevant symmetries, but the one that gives chiral EFT its character is the aforementioned approximate chiral symmetry. Chiral symmetry is an approximate global $\mathrm{SU}(2)_L \times \mathrm{SU}(2)_R$ symmetry of the QCD Lagrangian. This symmetry is spontaneously broken in nature, giving rise to the anomalously light pion as the Goldstone boson of the spontaneously broken $\mathrm{SU}(2)_A$ symmetry, and also explicitly broken by the nonzero quark masses and electroweak interactions [148–150]. Accounting for this symmetry and its breaking at low energies is what connects chiral perturbation theory and chiral effective field theory with our understanding of QCD.

With this, the symmetries and the degrees of freedom (nucleons and pions) of the effective theory are fixed. Looking at the next heaviest meson not explicitly included, we can identify the breakdown scale to be around the mass of the ρ meson, $\Lambda_\mathrm{b} \sim m_\rho \approx 770\,\mathrm{MeV}$.[1] The low-energy scales of the theory are the characteristic momenta Q that we consider and the pion mass $m_\pi \sim 140\,\mathrm{MeV}$. This clear separation of scales allows chiral EFT to provide an efficient, robust expansion for nuclear interactions in terms of pion exchanges and contact interactions, made systematic by a power counting scheme.

The final result of this approach in the Weinberg power counting [55] is shown in Fig. 2.1. The leading order (LO) description of nuclear forces is given by nucleon-nucleon (NN) interactions, with the one-pion exchange (indicated by the dashed line between the solid nucleon lines) and two contact interactions (indicated by the orange diamond). At higher orders, the nucleon-nucleon interactions become more complicated, with many more pion-exchange contributions coming in at each order and further contact interactions at next-to-leading order (NLO) and next-to-next-to-next-to-leading order ($\mathrm{N^3LO}$). We note also that the blue vertices in certain pion-exchange diagrams indicate pion-nucleon couplings that are fixed in chiral perturbation theory for pion-nucleon scattering [152, 153]. Fitting the LECs associated with the LO, NLO, and $\mathrm{N^3LO}$ contacts to scattering data and summing up all contributions allows modern chiral EFT NN potentials to provide a high-precision description of nucleon-nucleon scattering data up to laboratory energies of 290 MeV [154–160].

At the same time, chiral EFT naturally and consistently predicts the appearance of three-nucleon (3N) forces at next-to-next-to-leading order ($\mathrm{N^2LO}$). Here, one immediately has two short-range 3N interactions (indicated by the green square and the orange pentagon) with two LECs c_D, c_E to be fit to data but also a long-range pion-exchange term with the same pion-nucleon couplings as before. Furthermore, the 3N contributions at the next order, $\mathrm{N^3LO}$, are predicted without any new LECs, with the only couplings coming from lower orders in the power counting. This nicely shows the consistency of chiral EFT and the resulting predictive power. Four-nucleon (4N) forces appear at $\mathrm{N^3LO}$ without any LECs to fit [161–164] but are generally not included in ab initio calculations today. The 3N LECs c_D and c_E cannot be determined from NN scattering data and are often fit to uncorrelated observables in three- and four-body systems, such as the ^{3}H binding energy and the ^{3}H β-decay half life [61]. Recent approaches have also explored alternative fits to medium-mass nuclei and/or nuclear matter properties to better capture saturation properties [47, 165–167].

Given the low excitation energy of the Δ resonance of the nucleon at $m_\Delta - m_\mathrm{N} \approx 300\,\mathrm{MeV}$, a so-called Δ-full chiral EFT formulation has been developed to include the Δ as a low-energy degree of freedom in the effective theory [47, 167–170]. A notable change in this formulation is that 3N forces already appear at NLO, one order early than without explicit inclusion of the Δ resonance [169]. Such forces have been derived and optimized up to $\mathrm{N^2LO}$.

In general, nuclear potentials must be explicitly regularized to make divergent integrals over intermediate momenta convergent, introducing a dependence on the regularization scheme and the cutoff scale Λ used.

[1] Throughout this thesis, we employ units such that $\hbar = c = 1$. This means energies have units of fm^{-1} expressed in length dimensions, and we can quickly convert between MeV and fm using $\hbar c = 1 = 197.3269804\,\mathrm{MeV\,fm}$ [151].

Table 2.1: Summary of chiral EFT potentials used in this thesis. We name the potentials used in this thesis, providing the references in which they were constructed. For the NN potentials, we provide the chiral order, regularization cutoff Λ, and SRG resolution scale λ (if relevant). For NN+3N potentials, we provide the chiral order, regularization cutoff Λ, and SRG resolution scale λ (if relevant) for the 3N potential as well, which may differ from the NN potential.

Name	Refs.	NN			3N		
		Order	Λ (MeV)	λ (fm^{-1})	Order	Λ (MeV)	λ (fm^{-1})
N^{3}LO EM 500	[154]	N^{3}LO	500	-	-	-	-
N^{3}LO EM 500 $\lambda = 1.8\,\mathrm{fm}^{-1}$	[154]	N^{3}LO	500	1.8	-	-	-
N^{3}LO EMN 450	[157]	N^{3}LO	450	-	-	-	-
N^{3}LO EMN 500	[157]	N^{3}LO	500	-	-	-	-
1.8/2.0 (EM)	[171]	N^{3}LO	500	1.8	N^{2}LO	394	-
2.0/2.0 (EM)	[171]	N^{3}LO	500	2.0	N^{2}LO	394	-
2.2/2.0 (EM)	[171]	N^{3}LO	500	2.2	N^{2}LO	394	-
N^{3}LO 450	[157],[166]	N^{3}LO	450	-	N^{3}LO	450	-
N^{3}LO 500	[157],[166]	N^{3}LO	500	-	N^{3}LO	500	-
N^{3}LO 500 $\lambda = 2.0\,\mathrm{fm}^{-1}$	[157],[166]	N^{3}LO	500	2.0	N^{3}LO	500	2.0
N^{2}LO$_{\mathrm{sat}}$	[165]	N^{2}LO	450	-	N^{2}LO	450	-
ΔN^{2}LO$_{\mathrm{GO}}$	[167]	N^{2}LO	394	-	N^{2}LO	394	-

This dependence can be understood as an artifact related to the uncertainty due to working at a finite order in the EFT. Each additional order in the EFT cancels out the scale dependence of the previous order, and in the limit of infinite order all observables should not depend on the regularization scheme or scale (for reasonable choices of scheme and scale). Alternatively, we can consider the scheme and scale dependence as to some extent quantifying the intrinsic uncertainty in our forces due to operating at finite order in the EFT [68]. We return to this topic of uncertainty quantification for nuclear forces in Sec. 2.3.

Nowadays, there are many optimized chiral EFT NN+3N potentials, with various construction schemes for the NN potentials [154–159, 165, 167, 172–179] and different approaches to fitting the consistent 3N potentials [61, 166, 180, 181]. To quickly understand the essential characteristics of a given potential, one can consider the chiral order and the cutoff scale Λ used in the regularization. Most high-quality chiral EFT potentials used in nuclear structure today are either at N^{2}LO or N^{3}LO and employ a regulator cutoff between $\Lambda = 394\,\mathrm{MeV}$ and $500\,\mathrm{MeV}$. We summarize the potentials used in this thesis in Table 2.1.

Despite its success and ubiquity, there are still many open questions regarding the derivation of potentials via chiral EFT and their consistent application in many-body calculations. For example, there are multiple schools of thought regarding what the correct power counting for nuclear potentials is [182–184]. Additionally, the uncertainties from the regularization scheme and scale for nuclear potentials are still often dominant in many-body calculations [40, 47, 185]. In particular, potentials that are most successful in nuclear structure are the ones that deviate the strongest from the consistency philosophy of chiral EFT, employing inconsistent orders and regularizations for the NN and 3N potentials [51, 171, 186] and/or fitting to many-body data [165, 167, 187], motivating developing chiral EFT to even higher orders to reduce uncertainties [188]. However, the rapid expansion of the range of ab initio calculations over the past two decades has been in no small part due to the introduction of chiral potentials and the development of auxiliary tools to aid in their application to many-body calculations.

2.2 The similarity renormalization group

Renormalization group methods [62–68, 189–192] allow one to connect theories at different resolution scales via smooth transformations that integrate out or decouple high-energy states from the problem. Effectively, they allow one to dial the resolution of a theory systematically, allowing one to shift to a low-resolution description that makes subsequent calculations much more tractable.

The similarity renormalization group (SRG) [63, 64, 67, 189] is the most wide-spread renormalization group method for nuclear physics today. Instead of integrating out high-energy states from the problem, it aims to construct a unitary transformation of the Hamiltonian decoupling these states from relevant low-energy states:

$$H(s) = U(s)\, H\, U^\dagger(s)\,. \tag{2.1}$$

The transformation is chosen to be a function of a continuous flow parameter s, allowing one to rewrite Eq. (2.1) as the flow equation

$$\frac{dH(s)}{ds} = [\eta(s), H(s)]\,, \tag{2.2}$$

with the generator $\eta(s) = U(s)dU^\dagger(s)/ds$, the commutator $[A, B] = AB - BA$, and the initial condition $H(s = 0) = H$. The SRG unitary transformation is performed by solving the coupled differential equation, Eq. (2.2), from $s = 0$ towards $s \to \infty$.

A unitary transformation of the Hamiltonian and consistent transformation of all other operators leaves observables unchanged. While it is possible to do this for two- and three-body systems [190–192], it is infeasible for heavier systems, meaning an exact application of the SRG is generally not possible. Still, the SRG can very effectively be used to transform two- and three-body potentials and other operators to "softer" low-resolution forms, decoupling low- and high-momentum states. This transformation is exact in the two- and three-body systems, leaving all observables like differential cross sections, binding energies, charge radii, and half lives unchanged. NN phase shifts are also preserved by the transformation. Still, in four- and higher-body systems, the SRG induces many-body potentials that are not captured in the two- and three-body SRG evolution. These missing many-body forces are the price one pays for the transformation to lower resolution, a common feature of all renormalization group methods.

The standard generator definition for SRG calculations today is

$$\eta(s) = [T_{\rm rel}, H(s)]\,, \tag{2.3}$$

with the relative kinetic energy $T_{\rm rel}$. This generator choice $\eta = [X, H]$ builds off the intuition from Wegner [64] that such a generator will drive H to the form of the operator X. $T_{\rm rel}$ is diagonal in momentum space, with no coupling between low- and high-momentum states, so choosing $X = T_{\rm rel}$ generates the desired decoupling. In fact, things become very intuitive if one changes variables to

$$\lambda = \frac{1}{s^{1/4}}\,, \tag{2.4}$$

which has units of fm^{-1} and goes from $\lambda \to \infty$ towards $\lambda = 0$ during the SRG evolution. Doing this, one sees that off-diagonal NN potential matrix elements SRG transformed to a resolution scale λ are exponentially suppressed for $p^2 - p'^2 \geq \lambda^2$ for incoming and outgoing relative momenta p and p' [67].

Thus λ functions as a resolution or cutoff scale for the SRG-evolved potential with the intuition that physics at momentum scales above λ has been decoupled. This can be seen quite nicely in Fig. 2.2. The N^{4}LO EMN 500 NN potential [157] has a cutoff of $\Lambda = 500\,\mathrm{MeV} \approx 2.5\,\mathrm{fm}^{-1}$. In the left two panels for $\lambda = 5.0\,\mathrm{fm}^{-1}$ and $\lambda = 4.0\,\mathrm{fm}^{-1}$, the potential is hardly affected by the SRG transformation as λ is still

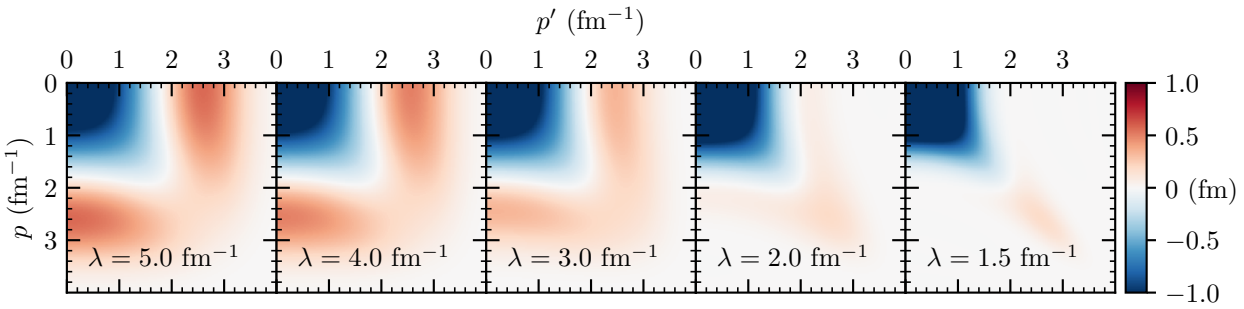

Figure 2.2: SRG evolution of a chiral EFT NN potential. Contour plots of $V(p, p')$ for the N^{4}LO EMN 500 NN potential from Ref. [157] in the ^{3}S$_1$ part of the ^{3}S$_1$-^{3}D$_1$ channel SRG evolved to resolution scales λ.

considerably larger than 2.5 fm^{-1}. Evolving to even lower resolution scales, we see that the potential begins to change with $V(p, 0)$ for $p \geq \lambda$ being driven to 0. At $\lambda = 1.5$ fm^{-1}, the low- to high-energy couplings present in the initial potential have all been transformed away, leaving a very soft NN potential.

These soft SRG-evolved potentials can be used as input for many-body calculations, which benefit immensely from the decoupling [68, 190, 191, 193–196]. In practice, using low-resolution potentials means substantially smaller model-space sizes can be used (see Chapters 3 and 4 for details), reducing computational costs and allowing converged results in larger systems. Still, the missing induced many-body forces from the SRG evolution mean that many-body observables will not be fully invariant under the SRG transformation. The trick is to operate in a middle ground, evolving far enough to get soft potentials that make many-body calculations substantially easier while not evolving too far such that induced many-body forces remain small and under control (ideally smaller than the EFT uncertainty for the forces). This can be probed by using multiple forces at different resolution scales λ and checking how observable predictions depend on λ. A strong dependence would indicate significant missing contributions from many-body forces while no dependence would indicate approximate renormalization group invariance, a desirable outcome [68].

Included in the summary of the potentials used in this thesis in Table 2.1 are several SRG-evolved potentials, most of which are either NN-only SRG-evolved potentials or NN+3N potentials that have been consistently evolved. A notable exception is the set of potentials introduced in Ref. [171], the 1.8/2.0 (EM), 2.0/2.0 (EM), and 2.2/2.0 (EM) potentials. For these potentials, the N^{3}LO EM 500 NN potential [154] is SRG evolved to a resolution scale λ. The 3N potential is regularized with a lower cutoff $\Lambda_{3N} = 2.0$ fm^{-1} and the 3N LECs are fit to the ^{3}H binding energy and the ^{4}He point-proton radius. This hybrid approach was adopted out of necessity, as consistent NN+3N SRG evolution in momentum space was not possible at the time, but the basic intuition is that refitting the 3N potential after the SRG evolution captures many of the induced 3N interactions that one would get from a consistent NN+3N SRG evolution. These potentials have been exceptionally successful in nuclear structure calculations, especially the 1.8/2.0 (EM) potential, which gives an excellent reproduction of ground-state energies, spectra, and differential charge radii up to heavy nuclei [3, 44, 51, 61].

2.3 Uncertainty quantification for nuclear forces

Nuclear forces are inherently uncertain. In chiral EFT, this uncertainty comes primarily from the truncation in chiral order, but also from the regularization scheme and scale, the strategy for fitting to data, and possibly the resolution scale coming from a further renormalization group transformation. Quantifying all of these sources of uncertainty is challenging, but in recent years substantial progress has been made on giving statistically meaningful, robust estimates of nuclear Hamiltonian uncertainties [100, 101, 135].

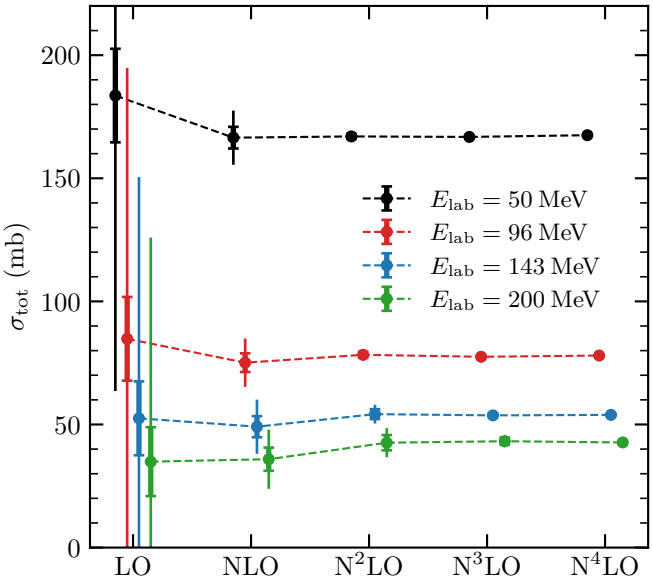

Figure 2.3: Bayesian estimates for the chiral EFT truncation uncertainty. Total proton-neutron scattering cross section $\sigma_{\rm tot}$ calculated order by order at different energies using potentials from Ref. [155]. The thick and thin error bars indicate 68% and 95% degree-of-belief intervals obtained via Bayesian uncertainty quantification [100]. Figure adapted from Ref. [100].

In principle, all EFT uncertainties arise due to the truncation of the EFT at a finite order. The leading approach to understanding this truncation uncertainty [100, 135, 155, 176] postulates an expansion of the observable X in chiral order n

$$X = X_{\rm ref} \sum_{n=0}^{\infty} c_n Q^n , \tag{2.5}$$

with dimensionful reference scale $X_{\rm ref}$, the dimensionless expansion coefficients c_n, and the expansion parameter[2]

$$Q = \frac{\max(p, m_\pi)}{\min(\Lambda, \Lambda_{\rm b})} . \tag{2.6}$$

The error due to a truncation at finite order k should roughly behave as

$$\Delta X^{(k)} \sim X_{\rm ref}\, c_{k+1} Q^{k+1} . \tag{2.7}$$

Intuitively, chiral EFT should provide a well-behaved convergent prediction for X, so given a proper definition of the expansion parameter Q the expansion coefficients c_n should be of natural size, meaning of order 1. This means c_{k+1} can be estimated based on the $c_0, \ldots, c_k$ from the available orders, either by taking the maximum magnitude from previous orders (called the EKM prescription in the literature) [155, 176] or by performing a Bayesian analysis to determine a distribution for the expansion coefficients c_n to arrive at a statistical distribution for the final error $\Delta X^{(k)}$ [100, 135, 197–199].

This approach is nicely demonstrated in Fig. 2.3, where the total proton-neutron scattering cross section at various energies is predicted at multiple orders in chiral EFT. The predictions from chiral EFT converge

[2]Note that the notation for the expansion parameter, Q, used in Refs. [100, 176] overlaps with the previous notation for external momenta in effective field theories. From the context, it should be clear which Q is meant, also by considering that an external momentum Q has dimensions of fm^{-1} and an expansion parameter Q is dimensionless.

very systematically when going to higher orders. Additionally, the truncation uncertainty, assessed using the approach discussed above, allows the error at lower orders to be robustly quantified, and at N^4LO one sees that the truncation uncertainty is very small. Specifically, one sees that the higher-order predictions generally lie within the uncertainty estimates of the lower-order predictions, demonstrating a very nice consistency.

There are a few key benefits of the Bayesian tools [99] used for uncertainty quantification [100, 135, 197–199], LEC inference [200–204], and experimental design [205]. One is the ability to encode prior knowledge into the analysis in the form of priors. This forces us to confront and quantify the assumptions going into an analysis, making it possible to also investigate the sensitivity to these assumptions and test them against the data. The second is that the final predicted or inferred values will in fact be distributions. Based on these distributions, we can make statistically robust degree-of-belief statements for values, investigate correlations, and even explore the reasons behind unexpected distribution forms, such as bimodal distributions. Finally, Bayesian statistics comes with a suite of model checking procedures, which assist tremendously in validating and refining our analyses.

In recent years, a complementary approach to Hamiltonian uncertainty quantification has been introduced in nuclear theory using the methods of history matching and importance resampling [47, 50, 101, 206–208]. The central goal is to capture the uncertainty in nuclear Hamiltonians in distributions for the LECs. The way this is achieved is by sampling the parameter space broadly and then confronting these samples with data.

In a first stage, called history matching, LEC combinations are compared against a collection of data [207, 208]. At this point, the only goal is to determine if these LEC combinations produce predictions that do not plausibly reproduce experimental data. This requires two things. First, it is essential that one accounts for the theory and experimental uncertainties in this comparison, which are typically dominated by the EFT truncation uncertainty. For this estimate, one generally uses the prescription discussed above. Second, the LEC combinations that one tests should be exhaustive, covering all edges of the parameter space, so one needs to try many millions or billions of parameter combinations. For this reason, it is very important to have efficient emulators for theory predictions, which give "good enough" estimates for the predicted values for a given parameter combination at a tiny fraction of the cost of a full theoretical prediction. Fortunately such emulators have proliferated in nuclear physics in recent years [102–105, 209–225], making such ambitious analyses possible.

At the end of history matching, one is typically left with some small set of valid LEC combinations that passed all implausibility checks. This set on its own, however, does not provide a proper statistical distribution; the samples that remain carry no information about how relatively likely or unlikely they are given the data. In a second stage, called importance resampling, theoretical predictions from the remaining samples are compared against data accounting for all uncertainties to assign relative likelihoods to each sample [101, 206]. The data one compares to here can be the same as in the history matching step, but importantly one can also perform this calibration against additional other observables that might not have been accessible in the history matching stage. The final result is a set of LEC combinations with relative likelihoods that can be understood as coming from an underlying distribution for the LECs. This set can be used to linearly propagate the distribution of LECs to a sampled posterior predictive distribution for an observable by simply evaluating the observable for each LEC combination and weighting that prediction by the LEC combination's relative likelihood.

Uncertainty quantification for nuclear forces is still challenging, but methods to do it robustly are becoming well established and the analyses are becoming more and more routine. This thesis focuses on developments in many-body methods that, in the long term, will make comparable uncertainty quantification

(including many-body uncertainties discussed in the next two chapters) possible in nuclear structure calculations.

Chapter 3

Many-body basics

Solving the quantum many-body problem given an input Hamiltonian is a standard challenge in many fields of physics, including condensed-matter physics, atomic physics, molecular physics, and, of course, nuclear physics. The tools to approach this problem efficiently, second quantization, normal ordering, mean-field approximations, and (non)perturbative expansions beyond the mean field, are well-established [226–230], and in this chapter we briefly review the most important formalisms and concepts from the perspective of nuclear physics. This sets the foundation for a focused discussion of the in-medium similarity renormalization group, the central many-body method of this thesis, and the method developments and nuclear structure applications presented.

3.1 Second quantization

Second quantization provides us with the tools to efficiently represent many-body states that respect the required antisymmetry under the exchange of indistinguishable fermions. The basic strategy is to define field operators that obey this antisymmetry and to then use those to construct states and many-body operators.

We start by considering a basis for a single fermion $\{|p\rangle\}$, a single-particle or one-body basis, where p is a collective index for all of the quantum numbers of the state. This basis can be chosen in different ways (for example, as $|\mathbf{k}m_s m_t\rangle$ for calculations in infinite matter), and for finite nuclei a convenient choice is

$$|p\rangle = |n(ls)jm_j m_t\rangle\,, \tag{3.1}$$

with the following quantum numbers: the radial excitation number n, the orbital angular momentum l, the spin $s = 1/2$, the total angular momentum j from coupling l and s, its projection m_j, and the isospin projection m_t distinguishing protons and neutrons.[1] The harmonic oscillator energy quantum number $e = 2n + l$ is often used to organize and truncate such single-particle bases. The field operators $a_p^\dagger$ and a_p create and annihilate a particle in the state $|p\rangle$, respectively:

$$a_p^\dagger\,|0\rangle = |p\rangle\,, \tag{3.2}$$
$$a_p\,|p\rangle = |0\rangle\,, \tag{3.3}$$
$$a_p^\dagger\,|p\rangle = 0\,, \tag{3.4}$$
$$a_p\,|0\rangle = 0\,. \tag{3.5}$$

[1] In this thesis, where it applies we use the convention that protons have $m_t = 1/2$ and neutrons have $m_t = -1/2$.

Here $|0\rangle$ is the physical vacuum, the state with no particles.

Once one considers constructing states of multiple fermions, second quantization differs from standard quantum mechanics ("first quantization"). Traditionally, one would set up the two-body basis as the product of two distinguishable single-particle bases, $\{|p\rangle_1\}$ and $\{|q\rangle_2\}$. The simple product states $|p\rangle_1 |q\rangle_2$, however, do not satisfy the required antisymmetry for fermions, and the basis must be reduced to those linear combinations of simple product states that are appropriately antisymmetric:

$$\left\{\frac{|p\rangle_1 |q\rangle_2 - |q\rangle_1 |p\rangle_2}{\sqrt{2}}\right\}, \text{ with } q > p\,. \tag{3.6}$$

In the case of two-body states, this is still relatively simple, but this approach rapidly becomes unwieldy for many-body states.

In second quantization, one simply demands that the field operators obey

$$\{a_p^\dagger, a_q^\dagger\} = 0\,, \tag{3.7}$$
$$\{a_p, a_q\} = 0\,, \tag{3.8}$$
$$\{a_p^\dagger, a_q\} = \delta_{pq}\,, \tag{3.9}$$

where the anticommutator $\{A, B\} = AB + BA$. This gives the two-body states $a_p^\dagger a_q^\dagger |0\rangle = |pq\rangle$, which have the properties

$$|pq\rangle = a_p^\dagger a_q^\dagger |0\rangle = -a_q^\dagger a_p^\dagger |0\rangle = -|qp\rangle\,, \tag{3.10}$$
$$|pp\rangle = -|pp\rangle = 0 \tag{3.11}$$

resulting from the antisymmetry of the field operators.

This also naturally extends to many-body states, allowing us to efficiently generate an antisymmetric A-body product state

$$a_{p_1}^\dagger \cdots a_{p_A}^\dagger |0\rangle = |p_1 \ldots p_A\rangle\,, \tag{3.12}$$

known as a Slater determinant.[2] Such a state is fully characterized by its occupation numbers n_p,

$$a_p^\dagger a_p |p_1 \ldots p_A\rangle = n_p |p_1 \ldots p_A\rangle\,. \tag{3.13}$$

$n_p = 1$ for states occupied in the Slater determinant (that is, $p \in \{p_1, \ldots, p_A\}$), and $n_p = 0$ for the remaining states not occupied in the Slater determinant. When one considers states that are not a single Slater determinant (as we do in Section 4.4), the occupation numbers can also generally take on values between 0 and 1.

Within the same formalism, it is easy to define many-body operators to represent interactions or transitions between many-body states. For one-body operators, the definition is simple:

$$O^{(1\mathrm{B})} = \sum_{pq} O_{pq} a_p^\dagger a_q\,. \tag{3.14}$$

If O has a well-defined Hermiticity $h_O = 1, -1$, then $O_{qp} = h_O O_{pq}$. One can quickly verify that $O^{(1\mathrm{B})}$ preserves particle number (meaning that matrix elements between states with different particle number vanish) and that $O^{(1\mathrm{B})}$ acting on $|0\rangle$ vanishes.

[2] The "determinant" part of "Slater determinant" comes from the fact that in first quantization the state can be understood as the determinant of a matrix of single-particle states where the A rows span the sets of state quantum numbers and the A columns span the coordinates of the different particles.

Two-body operators are defined as

$$O^{(2B)} = \frac{1}{(2!)^2} \sum_{pqrs} O_{pqrs} a_p^\dagger a_q^\dagger a_s a_r \,. \tag{3.15}$$

There are a few things worth noting in the definitions. First, the order of indices $pqrs$ in O_{pqrs} differs from the order in the field operator string that follows, simply as a result of considering what field operators are required to connect $\langle pq|$ and $|rs\rangle$ without an overall prefactor of -1. Second, the overall factor of $1/(2!)^2$ comes from the fact that the sums over p, q, r, and s are completely unrestricted. In the two-body basis $|pq\rangle$ and $|qp\rangle$ are the same state, differing by just an overall factor of -1. Thus, the minimal two-body space in second quantization is $|pq\rangle$, $q < p$. However, it is generally convenient to accept redundancy in the two-body basis and simply include an overall factor accounting for the overcounting in the basis, leading to a factor of 1/2! for each bra and ket bases.

The operator $O^{(2B)}$ gives 0 when acting on a state with less than two particles and conserves particle number. The matrix elements O_{pqrs} have a few useful properties: for definite Hermiticity h_O,

$$O_{rspq} = h_O O_{pqrs} \,; \tag{3.16}$$

and antisymmetry means that

$$O_{pqrs} = -O_{pqsr} = -O_{qprs} = O_{qpsr} \,. \tag{3.17}$$

This is very easily generalized to three-body operators,

$$O^{(3B)} = \frac{1}{(3!)^2} \sum_{pqrstu} O_{pqrstu} a_p^\dagger a_q^\dagger a_r^\dagger a_u a_t a_s \,, \tag{3.18}$$

with analogous Hermiticity and antisymmetry properties, and also higher-body operators, which are generally not used in nuclear theory currently and thus we do not treat in this work.

3.2 Normal ordering

Normal ordering is a technique that allows many-body operators and their contributions to be efficiently represented with respect to a given state, called the reference state. Simply stated, this is done by accounting for the reference-state expectation value of operators and pulling this out. However, normal ordering goes beyond this and allows the effects of, for example, three-body operators to be partially captured via normal-ordered one-body and two-body operators. This rearrangement of many-body interactions allows for many-body methods to be efficiently formulated and evaluated once a reference state has been determined, as we discuss in this chapter and the next.

For this discussion, we start by considering an A-particle Slater-determinant reference state

$$|\Phi\rangle = \Big[\prod_{i=1}^{A} a_i^\dagger \Big] |0\rangle \,. \tag{3.19}$$

It is useful to distinguish between states occupied in $|\Phi\rangle$ with $n_i = 1$, known as hole states, and unoccupied states with $n_a = 0$, known as particle states. We use the convention for state indices that hole states are labeled i, j, ..., particle states are labeled a, b, ..., and general states are labeled p, q, ... Normal ordering may also be extended to general reference states [231], but this is beyond the scope of this work.

A string of field operators is in normal order with respect to $|\Phi\rangle$ if all the field operators that would annihilate the reference state are to the right of the remaining field operators in the string. Field operators

that annihilate $|\Phi\rangle$ are hole state creation operators $a_i^\dagger$ and particle state annihilation operators a_a. We indicate this normal ordering by $:ABC\ldots:$, where

$$:ABC\ldots: = \mathrm{sign}(\sigma)\sigma(ABC\ldots)\,, \tag{3.20}$$

and σ is a permutation of $ABC\ldots$ that brings it into normal order.[3] So, for example, $:a_a^\dagger a_i^\dagger: = a_a^\dagger a_i^\dagger$ as the field operators are already in normal order, and

$$:a_a^\dagger a_i: = -a_i a_a^\dagger = a_a^\dagger a_i - \{a_a^\dagger, a_i\}\,. \tag{3.21}$$

In the latter example, we see the downfall of normal ordering "by hand," as one needs to identify a permutation of field operators that is in normal order (made complicated by the necessary distinction between particles and holes), identify an appropriate sequence of pairwise permutations to get everything into normal order, perform the permutations manually, and keep track of minus signs and Kronecker deltas for individual pairwise permutations.

The task of bringing an arbitrary string of field operators into normal order is made systematic and easy by Wick's theorem [232]. The core of Wick's theorem is the normal ordering of two field operators AB, where

$$:AB: = AB - \overbracket{AB}\,. \tag{3.22}$$

The Wick contraction $\overbracket{AB}$ is defined as the reference-state expectation value of AB, $\langle\Phi|\,AB\,|\Phi\rangle$. For the various combinations of field operators, these contractions are

$$\overbracket{a_p^\dagger a_q^\dagger} = 0\,, \tag{3.23}$$

$$\overbracket{a_p^\dagger a_q} = n_p\delta_{pq}\,, \tag{3.24}$$

$$\overbracket{a_p a_q^\dagger} = (1-n_p)\delta_{pq}\,, \tag{3.25}$$

$$\overbracket{a_p a_q} = 0\,. \tag{3.26}$$

Note that the contraction in Eq. (3.24) only contributes for hole states, and the contraction in Eq. (3.25) only contributes for particle states.

The power of this approach becomes clear when normal ordering an arbitrary string of operators $ABCDEF\ldots$. With Wick's theorem, one is able to rewrite a general string of operators as a sum of terms consisting of normal-ordered operators and Wick contractions:

$$\begin{aligned} ABCDEF\ldots = {} & :ABCDEF\ldots: \\ & + \overbracket{AB}:CDEF\ldots: \; - \overbracket{AC}:BDEF\ldots: \; + \text{singles} \\ & + (\overbracket{AB}\,\overbracket{CD} - \overbracket{AC}\,\overbracket{BD} + \overbracket{AD}\,\overbracket{BC}):EF\ldots: \; + \text{doubles} \\ & + \cdots + \text{ full contractions}\,. \end{aligned} \tag{3.27}$$

To simplify the contraction and pull it out of the normal-ordered product, we must anticommute the contracted operators such that they are adjacent, giving rise to the minus signs above. Even more powerful is Wick's theorem applied to the product of two normal-ordered products $:ABC\ldots::XYZ\ldots:$, where only contractions between the two terms must be considered. Considering additionally that only certain

[3] The sign of σ is 1 if σ decomposes into an even number of pairwise permutations and -1 if it decomposes into an odd number.

kinds of contractions contribute allows one with a bit of practice to perform normal ordering very efficiently. A diagrammatic approach to doing so is provided by Goldstone or Hugenholtz diagrams, which further simplify the task by providing diagrammatic rules to avoid identifying and collecting identical terms in the normal ordering [229].

In this thesis, we do not explicitly derive the normal ordering of expressions. Most expressions we give are well established and validated, and new expressions derived for our research were cross-checked against automatic normal ordering tools [233]. Still, for the interested and motivated reader, Wick's theorem, a little bit of patience, and a lot of care are all that are required to rederive the many-body formalisms we discuss.

Let us now consider normal ordering a Hamiltonian, which is the first step needed for the IMSRG and most reference-state-based many-body methods. In nuclear physics, Hamiltonians generally have the form

$$H = T_{\text{int}}^{(1+2\text{B})} + V_{\text{NN}}^{(2\text{B})} + V_{\text{3N}}^{(3\text{B})}, \tag{3.28}$$

which can be split into one- through three-body parts

$$H^{(1\text{B})} = T_{\text{int}}^{(1\text{B})}, \tag{3.29}$$
$$H^{(2\text{B})} = T_{\text{int}}^{(2\text{B})} + V_{\text{NN}}^{(2\text{B})}, \tag{3.30}$$
$$H^{(3\text{B})} = V_{\text{3N}}^{(3\text{B})}. \tag{3.31}$$

Here, V_{NN} and V_{3N} are the two- and three-body potentials, respectively, and T_{int} is the intrinsic kinetic energy (with the center-of-mass kinetic energy subtracted). This subtraction causes T_{int} to have one- and two-body parts, defined as

$$T_{\text{int}}^{(1\text{B})} = \Big(1 - \frac{1}{A}\Big) \sum_i \frac{\mathbf{k}_i^2}{2m}, \tag{3.32}$$
$$T_{\text{int}}^{(2\text{B})} = -\frac{1}{Am} \sum_{i<j} \mathbf{k}_i \cdot \mathbf{k}_j \tag{3.33}$$

with the single-particle momentum $\mathbf{k}_i$ of nucleon i.

Normal ordering a given Hamiltonian with respect to a reference state $|\Phi\rangle$ is formally simple:

$$E = \sum_i n_i H_{ii}^{(1\text{B})} + \frac{1}{2} \sum_{ij} n_i n_j H_{ijij}^{(2\text{B})} + \frac{1}{6} \sum_{ijk} n_i n_j n_k H_{ijkijk}^{(3\text{B})}, \tag{3.34}$$
$$f_{pq} = H_{pq}^{(1\text{B})} + \sum_i n_i H_{piqi}^{(2\text{B})} + \frac{1}{2} \sum_{ij} n_i n_j H_{pijqij}^{(3\text{B})}, \tag{3.35}$$
$$\Gamma_{pqrs} = H_{pqrs}^{(2\text{B})} + \sum_i n_i H_{pqirsi}^{(3\text{B})}, \tag{3.36}$$
$$W_{pqrstu} = H_{pqrstu}^{(3\text{B})}, \tag{3.37}$$

where we employ the conventional names for the normal-ordered zero- through three-body parts of the Hamiltonian, E, f, Γ, and W. Note that Eqs. (3.34)–(3.37) are not specific to the Hamiltonian and the normal-ordered matrix elements of other operators can be obtained analogously.

The normal ordering can also be reversed:

$$H^{(3B)}_{pqrstu} = W_{pqrstu}\,, \tag{3.38}$$

$$H^{(2B)}_{pqrs} = \Gamma_{pqrs} - \sum_i n_i H^{(3B)}_{pqirsi}\,, \tag{3.39}$$

$$H^{(1B)}_{pq} = f_{pq} - \sum_i n_i H^{(2B)}_{piqi} - \frac{1}{2}\sum_{ij} n_i n_j H^{(3B)}_{pijqij}\,, \tag{3.40}$$

$$E_{\text{res.}} = E - \sum_i n_i H^{(1B)}_{ii} - \frac{1}{2}\sum_{ij} n_i n_j H^{(2B)}_{ijij} - \frac{1}{6}\sum_{ijk} n_i n_j n_k H^{(3B)}_{ijkijk}\,, \tag{3.41}$$

where Eqs. (3.38)–(3.41) are to be evaluated in order. Here we allow for a residual energy $E_{\text{res.}}$ that is 0 if we just normal order H and then undo the normal ordering. Later we consider undoing the normal ordering after doing some approximate transformations of the normal-ordered H, where $E_{\text{res.}}$ is not 0 and in fact contains important information about many-body forces from these calculations. These "un-normal-ordered" interactions can be provided to other many-body methods to treat other parts of the problem, as we discuss for the valence-space IMSRG in Section 4.4.

3.3 Hartree-Fock

Hartree-Fock (HF) is a conceptually simple method, and here we focus on the basic concepts and outline steps to arrive at an HF solution. Solving for the ground state $|\Psi\rangle$ can be seen as minimizing the energy functional

$$E\big[\,|\Psi\rangle\,\big] = \frac{\langle\Psi|\,H\,|\Psi\rangle}{\langle\Psi|\Psi\rangle}\,. \tag{3.42}$$

For interacting systems, the exact ground state is generally not a single Slater determinant, but a linear combination of many Slater determinants. Hartree-Fock seeks to identify the Slater determinant $|\Phi\rangle$ that minimizes Eq. (3.42) within the space of Slater determinants,

$$E\big[\,|\Phi\rangle\,\big] = \frac{\langle\Phi|\,H\,|\Phi\rangle}{\langle\Phi|\Phi\rangle}\,. \tag{3.43}$$

This state serves as an energetically optimal starting point for a many-body expansion to compute the ground state of the system.

Our goal is to arrive at a Slater determinant $|\Phi\rangle_{\text{HF}}$, which can be written as a product state in the basis $\{|p\rangle_{\text{HF}}\}$. We start from a harmonic oscillator (HO) starting point $|\Phi\rangle_{\text{HO}}$ with single-particle basis $\{|p\rangle_{\text{HO}}\}$. An unknown unitary transformation $C_{pp'}$ connects these two bases,

$$|p\rangle_{\text{HF}} = \sum_{p'} C_{pp'}\,|p'\rangle_{\text{HO}}\,, \tag{3.44}$$

so once we have solved for this transformation, we can construct our HF state. This solution is obtained iteratively, where at iteration i we have a trial state $|\Phi\rangle_i$ and basis $\{|p\rangle_i\}$ connected to the HO basis via $C^{(i)}_{pp'}$.

We have split the following discussion into three parts: first, we carefully discuss single-particle bases and their properties; then, we discuss how Hartree-Fock is solved iteratively, using many of the properties of single-particle bases to arrive at a unitary transformation to the HF basis $C_{pp'}$. These two sections are rather technical, but explain in detail how one solves for the HF basis and provide useful expressions for

basis transformations and related quantities. Finally, we discuss the properties of the HF basis to provide a starting point for our discussion of many-body perturbation theory, a perturbative expansion around the reference state $|\Phi\rangle$.

3.3.1 Single-particle bases and one-body densities

In most contexts in many-body nuclear physics, the single-particle basis is fixed, and the goal is to solve for many-body operators with respect to this single-particle basis $\{|p\rangle\}$. However, when optimizing the single-particle basis itself, one clearly needs to consider how to transform between bases and how to represent operators and states in different bases. Fortunately, this is generally straightforward, especially with the definition of one-body density matrices for states introduced in Eq. (3.60).

We consider bases A and B, $\{|p\rangle_{\rm A}\}$ and $\{|p\rangle_{\rm B}\}$, connected by a unitary transformation $C_{pp'}$,[4] such that

$$|p\rangle_{\rm B} = \sum_{p'} C_{pp'} \, |p'\rangle_{\rm A} \,, \tag{3.45}$$

$$|p\rangle_{\rm A} = \sum_{p'} C_{p'p} \, |p'\rangle_{\rm B} \,. \tag{3.46}$$

The field operators for the two bases are not identical, related by

$$b_p^\dagger = \sum_{p'} C_{pp'} a_{p'}^\dagger \,, \tag{3.47}$$

$$b_p = \sum_{p'} C_{p'p} a_{p'} \,, \tag{3.48}$$

$$a_p^\dagger = \sum_{p'} C_{p'p} b_{p'}^\dagger \,, \tag{3.49}$$

$$a_p = \sum_{p'} C_{pp'} b_{p'} \,. \tag{3.50}$$

This leads to the general fermionic anticommutation relations

$$\{b_p^\dagger, a_q^\dagger\} = 0 \,, \tag{3.51}$$

$$\{b_p, a_q\} = 0 \,, \tag{3.52}$$

$$\{b_p, a_q^\dagger\} = C_{qp} \,, \tag{3.53}$$

$$\{b_p^\dagger, a_q\} = C_{pq} \,. \tag{3.54}$$

An operator O can be easily transformed from basis A to B. Given the zero- through three-body matrix elements of O in basis A, O_0, O_{pq}, O_{pqrs}, and O_{pqrstu}, the matrix elements in basis B are

$$\tilde{O}_0 = O_0 \,, \tag{3.55}$$

$$\tilde{O}_{pq} = \sum_{p'q'} C_{pp'} C_{q'q} O_{p'q'} \,, \tag{3.56}$$

$$\tilde{O}_{pqrs} = \sum_{p'q'r's'} C_{pp'} C_{qq'} C_{r'r} C_{s's} O_{p'q'r's'} \,, \tag{3.57}$$

$$\tilde{O}_{pqrstu} = \sum_{p'q'r's't'u'} C_{pp'} C_{qq'} C_{rr'} C_{s's} C_{t't} C_{u'u} O_{p'q'r's't'u'} \,. \tag{3.58}$$

[4] For our applications, $C_{pp'}$ is real, meaning that where complex conjugation would typically be required (for example for transformations of bra states) we may simply use $C^*_{pp'} = C_{pp'}$ to simplify things. Furthermore, for the inverse transformation $C^\dagger = C^T$, we typically evaluate the transposition explicitly ($C^*_{pp'} = C_{p'p}$).

For a Slater determinant constructed as a product state in basis A

$$|\Phi\rangle_{\rm A} = \Big[\prod_{i=1}^{A} a_i^\dagger\Big]\,|0\rangle\,, \tag{3.59}$$

it is fully characterized by its occupations in basis A, $n_p^{|\Phi\rangle_{\rm A}}$.[5] Once we try to represent $|\Phi\rangle_{\rm A}$ in basis B, it is no longer a simple product state and thus no longer has simple occupation numbers in basis B. Instead, the more general characterization of a Slater determinant in any orthonormal single-particle basis is via the one-body density matrix:

$$\rho_{pq}^{|\Phi\rangle_{\rm A}} = \langle\Phi|\, b_p^\dagger b_q\,|\Phi\rangle\,. \tag{3.60}$$

For the state $|\Phi\rangle_{\rm A}$, the basis $\{|p\rangle_{\rm A}\}$ is the eigenbasis of $\rho^{|\Phi\rangle_{\rm A}}$:

$$\rho_{pq}^{|\Phi\rangle_{\rm A}} = n_p^{|\Phi\rangle_{\rm A}}\delta_{pq}\,. \tag{3.61}$$

In basis B, the matrix elements of $\rho^{|\Phi\rangle_{\rm A}}$ are given by a simple unitary transformation

$$\rho_{pq}^{|\Phi\rangle_{\rm A}} = \sum_{p'q'} C_{pp'}C_{q'q}n_{p'}^{|\Phi\rangle_{\rm A}}\delta_{p'q'}\,. \tag{3.62}$$

Similarly, for a product state in basis B

$$|\Phi\rangle_{\rm B} = \Big[\prod_{i=1}^{A} b_i^\dagger\Big]\,|0\rangle \tag{3.63}$$

the one-body density matrix elements in basis A are

$$\rho_{pq}^{|\Phi\rangle_{\rm B}} = \sum_{p'q'} C_{p'p}C_{qq'}n_{p'}^{|\Phi\rangle_{\rm B}}\delta_{p'q'}\,. \tag{3.64}$$

3.3.2 Iterative solution

It can be shown that the state $|\Phi\rangle_{\rm HF}$ that minimizes Eq. (3.43) has a one-body density matrix $\rho^{\rm HF}$ such that

$$[\rho^{\rm HF}, f^{\rm HF}] = 0\,, \tag{3.65}$$

where $f^{\rm HF}$ is the normal-ordered one-body Hamiltonian (normal ordered with respect to $|\Phi\rangle_{\rm HF}$) as given by Eq. (3.35) [234–236]. This means that $\rho^{\rm HF}$ and $f^{\rm HF}$ share an eigenbasis, the HF single-particle basis, and so finding a basis in which $f^{\rm HF}$ is diagonal corresponds to finding the HF basis, allowing one to construct $|\Phi\rangle_{\rm HF}$.

As mentioned above, Hartree-Fock is solved iteratively. At iteration i one has a trial product state $|\Phi\rangle_i$ constructed from basis $\{|p\rangle_i\}$ with a one-body density matrix in the starting HO basis $\rho_{pq}^{(i)}$. We solve for a unitary transformation from basis $\{|p\rangle_{\rm HO}\}$ to basis $\{|p\rangle_{i+1}\}$. This is done by constructing $f^{(i)}$ in the HO basis and diagonalizing it. In the basis $\{|p\rangle_i\}$,

$$\tilde{f}_{12}^{(i)} = \tilde{H}_{12}^{(1{\rm B})} + \sum_{p'} n_{p'}^{(i)}\tilde{H}_{1p'2p'}^{(2{\rm B})} + \frac{1}{2}\sum_{p'r'} n_{p'}^{(i)}n_{r'}^{(i)}\tilde{H}_{1p'r'2p'r'}^{(3{\rm B})}\,, \tag{3.66}$$

[5] For this discussion, we are painfully verbose to be clear which state occupation numbers and density matrices characterize. Elsewhere, we leave this away as it is (hopefully) clear which reference state is at play.

where the tilde means the Hamiltonian matrix elements have been transformed from the HO basis to $\{|p\rangle_i\}$ as in Eqs. (3.56)–(3.58). Reexpressing everything in the HO basis gives

$$\begin{aligned} f_{12}^{(i)} &= H_{12}^{(1\mathrm{B})} + \sum_{p'} n_{p'}^{(i)} \sum_{pq} C_{p'p} C_{qp'} H_{1p2q}^{(2\mathrm{B})} \\ &\quad + \frac{1}{2} \sum_{p'r'} n_{p'}^{(i)} n_{r'}^{(i)} \sum_{pqrs} C_{p'p} C_{qp'} C_{r'r} C_{sr'} H_{1pr2qs}^{(3\mathrm{B})} \\ &= H_{12}^{(1\mathrm{B})} + \sum_{pq} H_{1p2q}^{(2\mathrm{B})} \sum_{p'q'} n_{p'}^{(i)} \delta_{p'q'} C_{p'p} C_{qq'} \\ &\quad + \frac{1}{2} \sum_{pqrs} H_{1pr2qs}^{(3\mathrm{B})} \sum_{p'q'} n_{p'}^{(i)} \delta_{p'q'} C_{p'p} C_{qq'} \sum_{r's'} n_{r'}^{(i)} \delta_{r's'} C_{r'r} C_{ss'} \\ &= H_{12}^{(1\mathrm{B})} + \sum_{pq} \rho_{pq}^{(i)} H_{1p2q}^{(2\mathrm{B})} + \frac{1}{2} \sum_{pqrs} \rho_{pq}^{(i)} \rho_{rs}^{(i)} H_{1pr2qs}^{(3\mathrm{B})} , \end{aligned} \tag{3.67}$$

employing the definition of the one-body density matrix in Eq. (3.64).

Diagonalizing $f^{(i)}$ gives us the unitary transformation $C^{(i+1)}$, which defines a new single-particle basis $\{|p\rangle_{i+1}\}$ with $|p\rangle_{i+1} = \sum_{p'} C_{pp'}^{(i+1)} |p'\rangle_{\mathrm{HO}}$. We construct a new trial state $|\Phi\rangle_{i+1}$ as a product state in this basis, we compute the density $\rho^{(i+1)}$, and we start another iteration. The iterative approach reaches convergence when the eigenvalues of the diagonalization of $f^{(i)}$,

$$e_p^{(i)} C_{pq}^{(i+1)} = \sum_r f_{pr}^{(i)} C_{rq}^{(i+1)} , \tag{3.68}$$

are stable between iterations such that $e_p^{(i+1)} \approx e_p^{(i)}$ within tolerances.

3.3.3 General properties

An important feature of the HF basis, in addition to the energetic optimization of the reference state $|\Phi\rangle = |\Phi\rangle_{\mathrm{HF}}$, is that the normal-ordered one-body matrix elements f_{pq} are diagonal, with $f_{pq} = \varepsilon_p \delta_{pq}$. ε_p are the single-particle energies of the system, which define the mean-field spectrum. Here, "mean field" refers to the fact that Hartree-Fock solves for an average one-body potential that binds all the particles in the system. This mean field differs in general for protons and neutrons, both due to isospin asymmetry in systems where $Z \neq N$ and due to isospin charge independence breaking effects (like the Coulomb potential between protons).

Figure 3.1 shows the mean-field spectrum of a schematic harmonic oscillator with spin-orbit interactions and of Hartree-Fock calculations (specifically HF+NAT, described in Sec. 6.1.2.2) of ^{16}O and ^{12}C.[6] We caution at this point that single-particle energies and the mean-field spectrum are not observable quantities. Still, they provide an intuitive guide to understand phenomena in nuclear structure. For example, we very nicely see the different energies for proton and neutron orbitals due to repulsive contributions to proton-proton interactions like the Coulomb interaction. In heavier systems, this difference becomes very pronounced as exemplified by ^{100}Sn ($N = Z = 50$), which is symmetric and essentially at the proton drip line, and ^{208}Pb ($Z = 82$, $N = 126$), which marks the end of the valley of stability.

Hartree-Fock does an excellent job of optimizing occupied single-particle states, making them independent of the initial HO basis used to store interaction matrix elements. This is not the case for particle states,

[6] In this thesis, we use the orbital labeling $^{n+1}l_j$, such that the lowest lying orbital is $1s_{1/2}$.

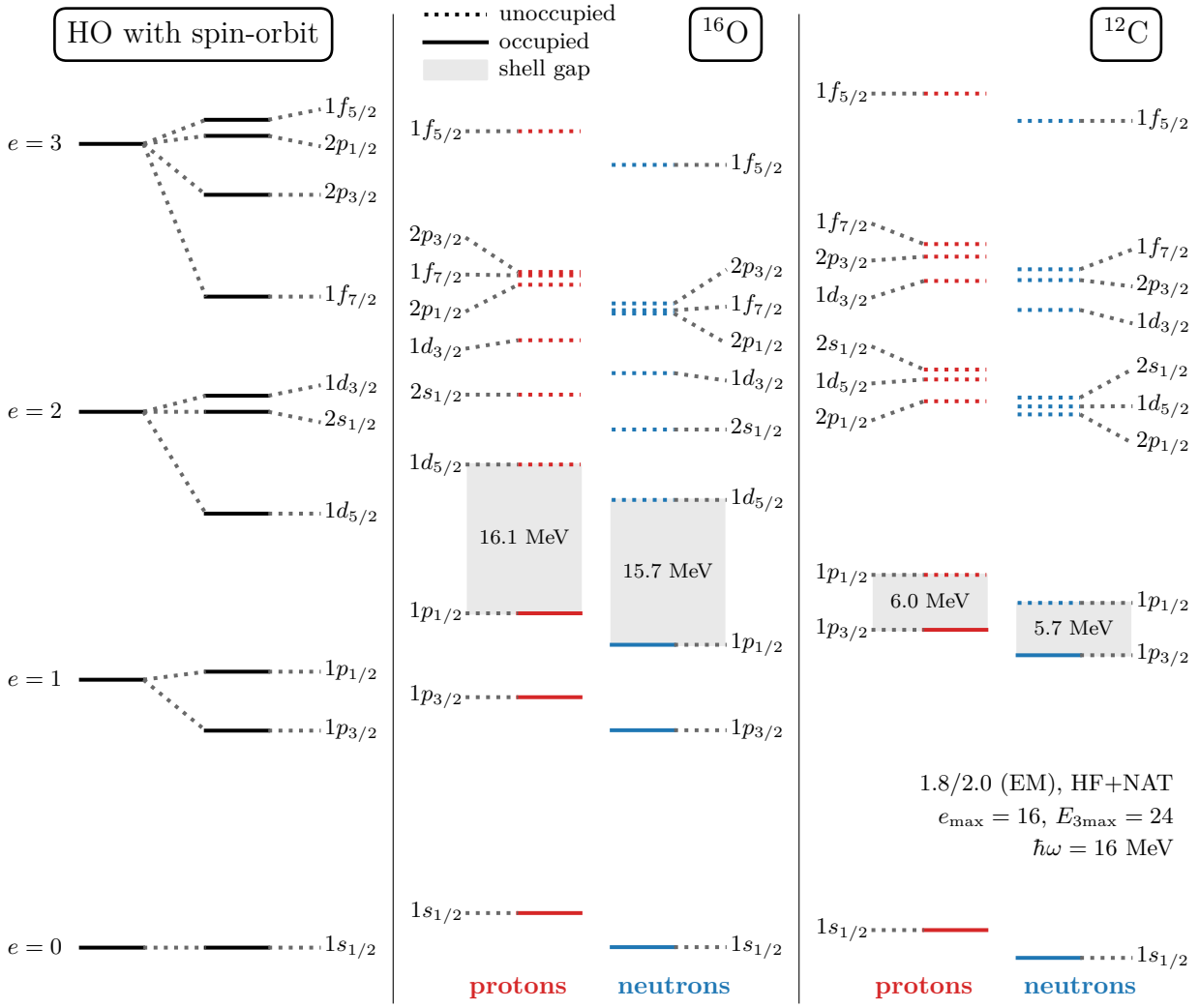

Figure 3.1: Mean-field single-particle levels. *Left:* Single-particle levels from a schematic harmonic oscillator with spin-orbit interactions. *Center, right:* Single-particle levels for ^{16}O (*center*) and ^{12}C (*right*) obtained from ab initio Hartree-Fock calculations. We show the HF+NAT single-particle levels (see Chapter 6 for details) for occupied (*solid*) and unoccupied (*dotted*) orbitals for ^{16}O and ^{12}C computed using the 1.8/2.0 (EM) Hamiltonian in an $e_{\max} = 16$, $E_{3\max} = 24$, $\hbar\omega = 16$ MeV model space. We highlight the large shell gap of the doubly-magic ^{16}O and the considerably smaller shell gap of ^{12}C with a light gray band.

which are generally very sensitive to details of the initial basis. The optimization of hole states allows Hartree-Fock to generally capture bulk properties of the system quite well, with the HF energy $E_{\rm HF} = E$ from Eq. (3.34) capturing a lot of the binding energy of the system. Additionally, densities and radii are also qualitatively correct at the Hartree-Fock level.

However, for many interesting observables and also for a quantitative description of bulk properties, the HF state and the mean-field picture are insufficient. It is the task of many-body methods to construct a systematic expansion around $|\Phi\rangle$ to capture what are called "many-body correlations," driven by the residual interactions of the nucleons with respect to the reference state. These residual interactions are given by the normal-ordered many-body parts of the Hamiltonian, Γ and W.

One obvious solution is to take the HF state and the mean-field picture and to construct a basis of

Slater determinants to span the A-body Hilbert space. To be concrete, given an A-particle reference state $|\Phi\rangle$, the Hilbert space is spanned by states where holes have been excited into particles:

$$|\Phi_i^a\rangle = a_a^\dagger a_i \,|\Phi\rangle\,, \tag{3.69}$$
$$|\Phi_{ij}^{ab}\rangle = a_a^\dagger a_b^\dagger a_i a_j \,|\Phi\rangle\,, \tag{3.70}$$
$$|\Phi_{ijk}^{abc}\rangle = a_a^\dagger a_b^\dagger a_c^\dagger a_i a_j a_k \,|\Phi\rangle\,, \tag{3.71}$$
$$\ldots,$$

known as 1-particle 1-hole ($1p1h$), 2-particle 2-hole ($2p2h$), and 3-particle 3-hole ($3p3h$) states, with up to A-particle A-hole states. Given such a basis, one simply needs to construct the Hamiltonian matrix elements in this basis and diagonalize it to get the ground-state energy and wave function.

The challenge with this approach is that the basis grows much too quickly for large numbers of particles. This can be understood relatively simply: the number of B-particle B-hole combinations possible for A particles in a single-particle basis of size N is given by the product of binomial coefficients

$$\binom{A}{B}\binom{N-A}{B} \sim A!(N-A)!\,. \tag{3.72}$$

This factorial scaling of the basis size is completely prohibitive for medium-mass nuclei, preventing so-called full "configuration space" diagonalizations of Hamiltonians. Still the configuration space picture is quite intuitive and handy, and we make use of it to motivate the developments in the chapters to come.

More efficient many-body methods stray from the path of exact diagonalization and seek to instead build an approximate expansion that converges towards the exact result [86, 91–95]. The key here is the reference-state starting point and the ability to define residual interactions with respect to it via Γ and W. Accounting for these interactions in a perturbative way gives many-body perturbation theory, discussed in the following section. More sophisticated nonperturbative approaches can also be constructed based on the same ideas, like coupled-cluster theory [92] and the IMSRG [94, 95], discussed in the next chapter.

3.4 Many-body perturbation theory

Many-body perturbation theory is a powerful, formally and conceptually tractable method to include so-called "dynamic correlations" beyond the reference state into the many-body solution. It has been used very successfully in calculations of nuclear matter also at finite temperature [8, 61, 166, 171, 237–242] and has also seen success in nuclear structure calculations when using soft SRG-evolved Hamiltonians [91, 243, 244]. Even without using it to solve the many-body problem, MBPT is useful in constructing improved bases and performing informed truncations, discussed in Chapter 6, and as an intuitive guide to understand and improve complex nonperturbative many-body methods, discussed in Chapter 7.

Given its success and ubiquity, MBPT is well-covered in textbooks and review articles (we refer the interested reader to Refs. [91, 229, 230]). For this reason, we do not cover the formalism here, but focus instead on the setup, the underlying principles, and the key results.

Any perturbative scheme relies on a partitioning of the Hamiltonian $H = H_0 + gH_1$ into an exactly solved Hamiltonian H_0 and a perturbation gH_1, where g is set to 1 once the perturbative expansion has been set up. For MBPT, there are a few choices for partitionings, but a convenient conventional choice is the Møller-Plesset partitioning, with

$$H_0 = E + \mathrm{diag}(f)\,, \tag{3.73}$$
$$H_1 = f - \mathrm{diag}(f) + \Gamma + W\,. \tag{3.74}$$

Since f is diagonal in the HF basis, this just simplifies to $H_0 = E + f$, $H_1 = \Gamma + W$ when starting from an HF reference state. In the following discussion, we assume that we are using an HF reference state and basis for simplicity.

The relevant ingredients for the MBPT expansion are the diagonal matrix elements of f, $\varepsilon_p = f_{pp}$, known as the single-particle energies, and the residual interactions Γ and W. We focus on the case where we employ the so-called normal-ordered two-body approximation for the Hamiltonian, truncating the residual three-body interactions W. While including W in MBPT is not conceptually challenging, it leads to considerable additional formal complexity and computational cost [166, 241, 242, 245].

In this case, MBPT up to second order only produces one contribution for corrections to the reference-state energy,

$$E^{(2)} = \frac{1}{4} \sum_{ijab} \frac{\Gamma_{ijab}\Gamma_{abij}}{\varepsilon_{ij}^{ab}} \,, \tag{3.75}$$

where

$$\varepsilon_{ij\ldots}^{ab\ldots} = \varepsilon_i + \varepsilon_j + \ldots - (\varepsilon_a + \varepsilon_b + \ldots) \,. \tag{3.76}$$

Note that this difference of single-particle energies is always negative, so the second-order MBPT correction is always negative ($\Gamma_{ijab} = \Gamma_{abij}$ due to Hermiticity).

At third order, there are three contributions,

$$E^{(3)} = E^{(3)}_{\text{ph}} + E^{(3)}_{\text{pp}} + E^{(3)}_{\text{hh}} \,, \tag{3.77}$$

with

$$E^{(3)}_{\text{ph}} = -\sum_{abcijk} \frac{\Gamma_{ijab}\Gamma_{kbic}\Gamma_{ackj}}{\varepsilon_{ij}^{ab}\varepsilon_{kj}^{ac}} \,, \tag{3.78}$$

$$E^{(3)}_{\text{pp}} = \frac{1}{8} \sum_{abcdij} \frac{\Gamma_{ijab}\Gamma_{abcd}\Gamma_{cdij}}{\varepsilon_{ij}^{ab}\varepsilon_{ij}^{cd}} \,, \tag{3.79}$$

$$E^{(3)}_{\text{hh}} = \frac{1}{8} \sum_{abijkl} \frac{\Gamma_{ijab}\Gamma_{klij}\Gamma_{abkl}}{\varepsilon_{ij}^{ab}\varepsilon_{kl}^{ab}} \,. \tag{3.80}$$

The "ph" refers to the fact that the middle interaction Γ_{kbic} is between a particle ($c \to b$) and a hole ($i \to k$), and similar reasons apply to $E^{(3)}_{\text{pp}}$ and $E^{(3)}_{\text{hh}}$.

We are now equipped to discuss general features of MBPT energy contributions. A common matrix element in all energy contributions is $\Gamma_{p'ph'h}$ (in our expressions always the rightmost term), which excites two holes out of the reference state into particle states. From the reference state, this is the only allowed interaction, as the reference state has no fermions occupying the particle states. Once particles have been excited out of the reference state, more general interactions can contribute, like particle-hole interactions $\Gamma_{p'h'ph}$ as in Eq. (3.78), particle-particle interactions $\Gamma_{p'''p''p'p}$ as in Eq. (3.79), or hole-hole interactions $\Gamma_{h'''h''h'h}$ as in Eq. (3.80). Finally, to connect back to the reference state, all excited particles must return to the missing holes in the reference state, accomplished by the $\Gamma_{h'hp'p}$ matrix elements.

The three contributions at third order are somewhat special. They each have analogous higher-order terms where the pp, hh, or ph interaction is iterated. As an example, at fourth order there is one contribution,

$$E^{(4)}_{\text{hh-ladder}} = \frac{1}{16} \sum_{abijklmn} \frac{\Gamma_{ijab}\Gamma_{mnij}\Gamma_{klmn}\Gamma_{abkl}}{\varepsilon_{ij}^{ab}\varepsilon_{mn}^{ab}\varepsilon_{kl}^{ab}} \,, \tag{3.81}$$

with two subsequent hole-hole interactions. Such contributions, known as particle-particle and hole-hole ladders and particle-hole rings, can be summed to all orders to capture some many-body physics nonperturbatively [227, 246–248].

As also known from perturbation theory, for intermediate states (for example following a $2p2h$ excitation) there is always an associated energy denominator. In MBPT, this energy denominator is very simple (because the reference-state energy cancels out), consisting of simple differences of single-particle energies $\varepsilon_{ijkl\ldots}^{abcd\ldots}$. These single-particle energies always have the form of Eq. (3.76), subtracting particle state energies from hole state energies, where the particle states by definition have larger single-particle energies. If the energy gap between the highest hole state and the lowest particle state is large, MBPT contributions at higher orders are rapidly suppressed by the appearance of multiple large energy denominators. In Fig. 3.1, we see such a large shell gap for ^{16}O, making MBPT rapidly convergent when using soft Hamiltonians [243].

On the other hand if the energy gap is very small, as is the case for ^{12}C in Fig. 3.1, the perturbative expansion is challenging, typically not actually convergent at all. This can be seen as a sign that the Hartree-Fock mean-field picture is insufficient to provide a good starting point for a perturbative expansion, requiring the many-body expansion to work hard to capture dynamic correlations. This can be the case for very nonperturbative Hamiltonians, but it can also be caused by exotic structures that cannot be well described by a Slater determinant.

It is also the case when considering open-shell systems, where the reference state is essentially degenerate with respect to its excitations. In such cases, one can consider a more general mean-field picture allowing for a reference state with a more general structure [249, 250] and typically breaking certain symmetries of the many-body problem [251–256]. Such approaches are state-of-the-art in ab initio nuclear structure today, and in the case of symmetry breaking it is still being actively researched how to effectively break and restore symmetries.

The derivation of MBPT energy contributions is most practically done via a diagrammatic approach [229]. This involves two steps: the generation of all possible diagrams; and the evaluation of the diagram using diagram rules, giving the interactions and energy denominators along with the overall symmetry factor [for example, the factor of 1/8 in Eq. (3.79)]. Derivation via diagrams makes this process easier, but it is still cumbersome and error-prone when done by hand, and so automated tools have been developed to handle the systematic generation of all terms up to high orders [8, 166, 257, 258].

At the same time, going to high orders in MBPT is technically quite challenging. This is for two reasons. First, the number of diagrams at higher orders grows rapidly, with 39 diagrams at fourth order, in contrast to one at second order and three at third order, and quickly growing intractable beyond that. This is even worse if one allows residual three-body interactions W, where at third order there are already 17 diagrams [245]. Numerically implementing and optimizing such a large amount of terms is infeasible for humans, but can be approached again using automated tools for code generation [166, 233, 257].

Second, the computational cost of high-order MBPT diagrams is quite high. If we consider a single-particle basis of size N with A holes and $N - A \approx N$ particles, fourth-order MBPT diagrams cost between $\mathcal{O}(N^2A^6)$ and $\mathcal{O}(N^6A^2)$ to evaluate. By contrast, nonperturbative many-body methods such as CC or the IMSRG have powerful approximations that scale like $\mathcal{O}(N^6)$ per iteration (requiring only between ten and a few hundred iterations). Given that these methods are generally more powerful, less complex, and can flexibly target observables beyond the ground-state energy, this makes high-order MBPT less attractive. Moreover, MBPT is only rarely convergent at high orders [91, 243], meaning that nonperturbative methods are generally necessary for a quantitative solution to the many-body problem. For this thesis, the IMSRG, discussed in the next chapter, is the method of choice for all of the reasons mentioned here: it is flexible, nonperturbative, formally simple, and quite precise at low-order approximations.

3.5 Uncertainty quantification for many-body calculations

Before discussing the IMSRG, a few comments are in order about general sources of uncertainty in many-body calculations. In Section 4.7, we revisit this topic from the specific perspective of the IMSRG.

At the heart of the many-body methods we discuss are many-body operators, where the matrix elements are represented in a single-particle basis. Recall that for finite nuclei we use a basis with states

$$|p\rangle = |nljm_j m_t\rangle \,, \tag{3.82}$$

which are generally taken initially to be eigenstates of the isotropic three-dimensional harmonic oscillator. Hartree-Fock (in a spherically symmetric framework) preserves this structure, and so do other basis optimizations considered in nuclear theory [106, 259].

For many-body calculations, the single-particle basis must be truncated, and it is important to demonstrate convergence with respect to the single-particle basis size and its parameters. The basis truncation for the initial HO basis is typically taken as $e_{\max} \geq e_p = 2n + l$ for any state $|p\rangle$ in the basis. The underlying HO basis also has an intrinsic frequency $\hbar\omega$. In the infinite basis size limit, all results would be independent of $\hbar\omega$, but working in a finite truncated basis, results must be invariant to small changes in $e_{\max}$ and $\hbar\omega$ to be considered converged. In nuclei, $e_{\max} = 12$, 14, 16 is typically sufficient for medium-mass ($A \leq 60$), medium-heavy ($60 \leq A \leq 140$), and heavy systems ($A \geq 140$) when using an HF basis. Such truncations are generally easily accessible for many-body calculations, and so the model-space uncertainty due to finite basis size is well under control and can be quantified by performing two calculations at $e_{\max}$ and $e_{\max} \pm 2$.

An additional model-space uncertainty enters in the handling of matrix elements of three-body forces V_{pqrstu}. For typical $e_{\max}$, the basis size is of the order $N \sim 2000$, meaning the three-body matrix elements require 10^9 GB to store. Even fully exploiting symmetries of three-body forces, storing V_{pqrstu} without truncations is completely out of reach. For this reason, three-body matrix elements for many-body calculations must be truncated, and one typically truncates in the three-body basis, only including states $|pqr\rangle$ where $e_p + e_q + e_r \leq E_{3\max}$. For calculations, one must also demonstrate convergence with respect to $E_{3\max}$, quantifiable by varying $E_{3\max}$ by ± 2. For most of the past decade, this truncation was limited to $E_{3\max} = 16$, 18, which is sufficient to converge calculations for nuclei up to $A \sim 70$ with relatively soft Hamiltonians. In heavy nuclei, for example ^{132}Sn, such values of $E_{3\max}$ are completely insufficient, and recent developments discussed in Chapter 5 have extended and bypassed this truncation completely, allowing converged calculations of ^{208}Pb [46, 47, 49].

The model-space uncertainties discussed above are relatively easy to explore and quantify. The same is not true for the many-body approximation used in MBPT discussed above and also the IMSRG and other methods. All of these methods are necessarily approximate, allowing them to describe medium-mass nuclei at relatively low computational cost. For example, in MBPT we only compute energy contributions up to some finite order, typically third order. To quantify the uncertainty due to missing orders, one needs to understand how they behave. This is made complicated by the limited orders one has access to (typically only one or two approximations, like second and third order MBPT) and by the fact that the higher orders are not guaranteed to converge nicely (for example, MBPT is known to generally diverge at high orders). With such limited knowledge, one can compare results from different many-body methods to get insight into missing higher-order contributions, or one can push a single method to higher orders to (hopefully) see signals of rapid convergence. In this thesis, we develop the IMSRG to the next order and explore the many-body convergence of the method. As we discuss in Section 4.7, this makes it possible to quantify the IMSRG many-body uncertainty, a key milestone for nuclear structure theory.

Chapter 4

The in-medium similarity renormalization group

Within the diverse set of many-body methods available for nuclear structure theory [76, 86, 88, 89, 91–96], the in-medium similarity renormalization group [94, 95, 260, 261] has emerged as a particularly scalable, powerful, and versatile method. Originally developed to compute ground-state properties of closed-shell systems, it has since been extended to also access open-shell systems [95, 249, 250, 261–263] and to compute a much broader set of nuclear structure properties, including spectra [249, 250, 261, 264], electromagnetic observables [265–267], nuclear responses [268], weak decays [35, 269, 270], continuum efects [271], and nuclear matrix elements for beyond-standard-model transitions [36, 249, 272, 273]. This has established the IMSRG as an integral part of the nuclear theory landscape today and makes improvements on the method and novel applications highly relevant not just to nuclear structure but also to adjacent fields like nuclear astrophysics and fundamental interactions as well as to many-body method developments in quantum chemistry and condensed-matter physics.

In this chapter, we introduce the IMSRG. We focus on the intuition and concepts behind the method necessary to understand the developments on the IMSRG in Chapters 6 and 7 and the applications of the method in Chapters 5 and 8–10. For the reader interested in exploring more details, we refer them to the comprehensive reviews in Refs. [94, 95].

4.1 Formalism

The IMSRG builds on the SRG approach, solving for a targeted continuous unitary transformation of a Hamiltonian

$$H(s) = U(s)\, H\, U^\dagger(s) \tag{4.1}$$

via the solution of the SRG flow equation

$$\frac{dH(s)}{ds} = [\eta(s), H(s)]\,. \tag{4.2}$$

The desired unitary transformation is achieved via an appropriate definition of the generator η. For the IMSRG this is generally a unitary transformation that partially diagonalizes the Hamiltonian, as shown in Fig. 4.1, giving the ground-state energy E and wave function $|\Psi\rangle = U(s)\,|\Phi\rangle$. A key aspect of the IMSRG is that Eq. (4.2) is formulated in terms of operators that are normal ordered with respect to a reference state $|\Phi\rangle$ for the system of interest. This makes the IMSRG unitary transformation system-specific, rather than general like the free-space SRG for nuclear potentials, allowing it to very effectively capture induced

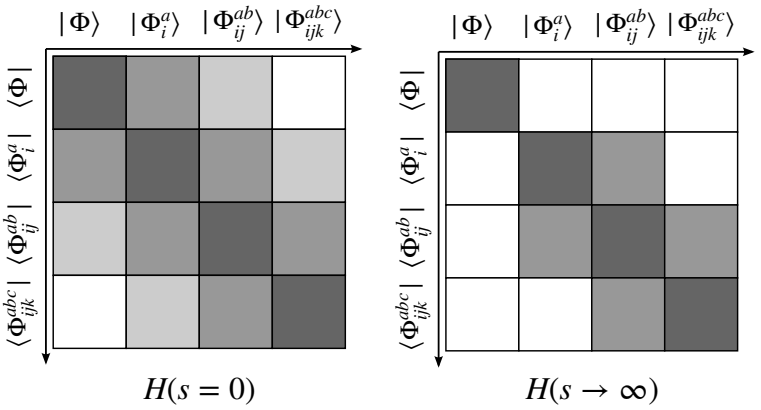

Figure 4.1: The IMSRG unitary transformation. A schematic representation of the IMSRG unitary transformation in the normal-ordered two-body approximation. The initial Hamiltonian $H(s=0)$ has nonzero matrix elements coupling the reference state $|\Phi\rangle$ to its 1-particle 1-hole and 2-particle 2-hole excitations $|\Phi_i^a\rangle$ and $|\Phi_{ij}^{ab}\rangle$, respectively. The initial Hamiltonian is unitarily transformed to give the final Hamiltonian $H(s\to\infty)$ in such a way that these matrix elements are 0, meaning the ground-state energy is simply the reference-state expectation value $\langle\Phi|H(s\to\infty)|\Phi\rangle$. Figure adapted from Ref. [94].

many-body interactions via the continuous normal ordering. This is the feature that makes the IMSRG able to describe many-body systems while the free-space SRG is currently limited to the two- and three-body level [61, 94].

The IMSRG also makes it easy to consider other observables, such as charge radii or nuclear matrix elements for transitions. For general observables, the corresponding operator O is normal ordered with respect to $|\Phi\rangle$ and transformed consistently

$$O(s) = U(s)\,O\,U^\dagger(s)\,. \tag{4.3}$$

The transformed operator can then be used to compute ground-state expectation values or to evaluate matrix elements between two states in a transition.

In this thesis, we only consider ground-state energies, spectra, and ground-state charge radii. Ground-state energies and spectra can be obtained from the Hamiltonian, so the only operators we need to consider transforming consistently are those associated with the charge radius. We compute the charge radius as

$$R_{\rm ch}^2 = \langle R_{\rm p}^2\rangle + \langle r_{\rm so}^2\rangle + r_{\rm p}^2 + \frac{N}{Z}r_{\rm n}^2 + \frac{3}{4M^2}\,, \tag{4.4}$$

with the nucleon mass M, neutron number N, and proton number Z. Here, $\langle R_{\rm p}^2\rangle$ and $\langle r_{\rm so}^2\rangle$ are the nuclear point-proton radius and nuclear spin-orbit radius expectation values, with the operator expressions

$$R_{\rm p}^2 = \sum_i \Big[(1+\tau_i)\frac{1}{2Z}\Big(1-\frac{2}{A}\Big) + \frac{1}{A^2}\Big]\mathbf{r}_i^2 + \sum_{i<j}\Big[\frac{2}{A^2} - \frac{2}{AZ}\Big(1+\frac{\tau_i+\tau_j}{2}\Big)\Big]\mathbf{r}_i\cdot\mathbf{r}_j\,, \tag{4.5}$$

$$r_{\rm so}^2 = -\sum_i \frac{\mu_i - Q_i/2}{ZM^2}(\kappa_i+1)\,. \tag{4.6}$$

μ_i gives the magnetic moment of the particle species in state i (relative to the nuclear magneton $\mu_{\rm N}$)

$$\mu_i = \begin{cases} 2.793 & \text{if } i \text{ is a proton,} \\ -1.913 & \text{if } i \text{ is a neutron,} \end{cases} \tag{4.7}$$

Q_i gives the charge of the particle species in state i

$$Q_i = \begin{cases} 1 & \text{if } i \text{ is a proton,} \\ 0 & \text{if } i \text{ is a neutron,} \end{cases} \tag{4.8}$$

and κ_i gives the spin-orbit correction

$$\kappa_i = \begin{cases} l_i & \text{if } j_i = l_i - \frac{1}{2}, \\ -(l_i+1) & \text{if } j_i = l_i + \frac{1}{2}. \end{cases} \tag{4.9}$$

$\langle R_{\rm p}^2 \rangle$ is the dominant contribution to the charge radius, and $\langle r_{\rm so}^2 \rangle$ accounts for spin-orbit corrections [274].[1] The remaining three corrections in Eq. (4.4) are due to finite proton and neutron charge radii, where we use the values $r_{\rm p}^2 = 0.771\,\text{fm}^2$ and $r_{\rm n}^2 = -0.115\,\text{fm}^2$, and the relativistic Darwin-Foldy correction [276]. In Chapter 10, we also introduce $R_{\rm p}^4$ as an additional operator we evaluate to gain access to higher-order moments of the charge distribution.

The IMSRG is particularly flexible in what kinds of unitary transformations can be generated and what approaches one can take to describe the many-body system and compute expectation values and transition matrix elements. We describe two of these approaches in Sections 4.3 and 4.4.

4.2 Truncation schemes

The starting point for the IMSRG is the normal-ordered Hamiltonian

$$H = E + f + \Gamma + W\,. \tag{4.10}$$

The integration of Eq. (4.2) will cause the evolving Hamiltonian to also have induced many-body interactions

$$H(s) = E(s) + f(s) + \Gamma(s) + W(s) + \ldots\,. \tag{4.11}$$

For an A-body system, up to A-body interactions need to be included for an exact solution for the ground-state energy. This is impossible for many-body systems, so the IMSRG employs truncations in many-body operators. Practically such truncations yield approximate many-body methods that are able to compute the structure of medium-mass and heavy nuclei efficiently.

The IMSRG(2) truncates the IMSRG equations at the normal-ordered two-body level. This means that the Hamiltonian

$$H(s) = E(s) + f(s) + \Gamma(s) + W(s) + \ldots \tag{4.12}$$

is truncated such that

$$H(s) = E(s) + f(s) + \Gamma(s) \tag{4.13}$$

for all s. An identical truncation is employed for all operators, including the generator

$$\eta(s) = \eta^{(1\text{B})}(s) + \eta^{(2\text{B})}(s)\,, \tag{4.14}$$

[1] Our expression for $r_{\rm so}^2$ in Eq. (4.6) corrects an error in the expression of Ref. [274] pointed out by Martin Hoferichter. The correction is simple:

$$\mu_i - Q_i \to \mu_i - Q_i/2\,.$$

The error in the previous implementation and validity of the correction were ensured by calculations of the $\Phi''(q)$ nuclear responses, which are related to the spin-orbit radius at $q = 0$ [275].

which does not have a zero-body part due to its anti-Hermiticity. This approximation is systematically improvable by allowing also three- and higher-body operators in the IMSRG solution.

To derive the IMSRG(2), one considers the IMSRG commutator

$$[\eta(s), H(s)] = [\eta^{(1\mathrm{B})}(s) + \eta^{(2\mathrm{B})}(s), E(s) + f(s) + \Gamma(s)] \tag{4.15}$$

with the normal-ordered two-body truncation applied. This expression, specifically the products of operators arising due to the commutator, needs to be brought into normal order, which can be accomplished via Wick's theorem. This is generally done by considering the individual terms

$$[\eta(s), H(s)] = [\eta^{(1\mathrm{B})}(s), f(s)] + [\eta^{(1\mathrm{B})}(s), \Gamma(s)] - [f(s), \eta^{(2\mathrm{B})}(s)] + [\eta^{(2\mathrm{B})}(s), \Gamma(s)] \tag{4.16}$$

and normal ordering them individually.

These individual terms can be expressed in terms of fundamental commutators between a K-body operator A and an L-body operator B. Such a commutator produces an operator C such that

$$[A^{(K\mathrm{B})}, B^{(L\mathrm{B})}] = \sum_{M=|K-L|}^{K+L-1} C^{(M\mathrm{B})}. \tag{4.17}$$

This relation makes it clear how the IMSRG commutator induces many-body interactions even when the initial operators only have up to two- or three-body interactions. It is useful to distinguish between the different M-body parts of C, and we use the convenient notation $[K, L] \to M$ to indicate the commutator contribution such that

$$C^{(M\mathrm{B})} = [A^{(K\mathrm{B})}, B^{(L\mathrm{B})}]^{(M\mathrm{B})}\,. \tag{4.18}$$

For the IMSRG(2), due to the normal-ordered two-body truncation, there are only 7 relevant fundamental commutators, $[1,1] \to 0$, $[1,1] \to 1$, $[1,2] \to 1$, $[1,2] \to 2$, $[2,2] \to 0$, $[2,2] \to 1$, and $[2,2] \to 2$. We provide a detailed discussion of IMSRG fundamental commutators, including complete general expressions up to the normal-ordered three-body level, in Appendix B.

Plugging the IMSRG(2) commutators back into the IMSRG flow equation one gets the IMSRG(2) flow equations:

$$\frac{dE}{ds} = \sum_{pq} (n_p \bar{n}_q - \bar{n}_p n_q)\, \eta_{pq} f_{qp} + \frac{1}{4} \sum_{pqrs} (n_p n_q \bar{n}_r \bar{n}_s - \bar{n}_p \bar{n}_q n_r n_s)\, \eta_{pqrs} \Gamma_{rspq}\,, \tag{4.19}$$

$$\begin{aligned} \frac{df_{12}}{ds} &= \sum_{p} (\eta_{1p} f_{p2} - f_{1p} \eta_{p2}) + \sum_{pq} (n_p \bar{n}_q - \bar{n}_p n_q)\, (\eta_{pq} \Gamma_{1q2p} - f_{pq} \eta_{1q2p}) \\ &\quad + \frac{1}{2} \sum_{pqr} (\bar{n}_p \bar{n}_q n_r + n_p n_q \bar{n}_r)\, (\eta_{1rpq} \Gamma_{pq2r} - \Gamma_{1rpq} \eta_{pq2r})\,, \end{aligned} \tag{4.20}$$

$$\begin{aligned} \frac{d\,\Gamma_{1234}}{ds} &= (1 - P_{12}) \sum_{p} (\eta_{1p} \Gamma_{p234} - f_{1p} \eta_{p234}) - (1 - P_{34}) \sum_{p} (\eta_{p3} \Gamma_{12p4} - f_{p3} \eta_{12p4}) \\ &\quad + \frac{1}{2} \sum_{pq} (\bar{n}_p \bar{n}_q - n_p n_q)\, (\eta_{12pq} \Gamma_{pq34} - \Gamma_{12pq} \eta_{pq34}) \\ &\quad - (1 - P_{12})(1 - P_{34}) \sum_{pq} (n_p \bar{n}_q - \bar{n}_p n_q)\, \eta_{p23q} \Gamma_{1qp4}\,, \end{aligned} \tag{4.21}$$

where the permutation operator P_{pq} exchanges the indices p and q in the following expression (ensuring antisymmetry of two-body matrix elements), and $\bar{n}_p = 1 - n_p$. For clarity, we have suppressed the s dependence of $E(s)$, $f(s)$, $\Gamma(s)$, and $\eta(s)$.

Equations (4.19)–(4.21) are a large set of coupled differential equations with the initial condition $E(s=0)=E$, $f(s=0)=f$, and $\Gamma(s=0)=\Gamma$, and these must be integrated from $s=0$ towards $s\to\infty$ until a fixed point where $[\eta(s),H(s)]\approx 0$ is reached. We discuss this condition in the next two sections.

The most expensive parts of the IMSRG(2) equations are the final two terms of Eq. (4.21). These scale like $\mathcal{O}(N^6)$ in the size of the single-particle basis N. Depending on the definition of the generator, one can show that it is in fact only $\mathcal{O}(A^2N^4)$, but generally this naive computational cost scaling gives a good assessment of the cost of the IMSRG(2) relative to other many-body methods.[2]

The IMSRG(2) truncation in Eq. (4.13) truncates also the initial Hamiltonian at $s=0$, discarding the residual three-body force W (as is also the case in our discussion of MBPT in Sec. 3.4). This truncation is known as the normal-ordered two-body (NO2B) approximation for the Hamiltonian, and this approximation is essential for the IMSRG(2), which only includes up to NO2B operators. The effect of this approximation has been studied in CC and NCSM calculations [277–279], and W has been observed to contribute at the subpercent level to binding energies in light and medium-mass nuclei. For this reason (and the formal complexity of including a three-body Hamiltonian in CC calculations), the NO2B approximation is widely used for IMSRG and CC calculations of medium-mass and heavy nuclei.

The structure of Eqs. (4.19)–(4.21) is not particularly transparent, but one can make a connection with MBPT to understand the many-body physics captured by the IMSRG(2). We refer the interested reader to Refs. [94, 280] and only discuss a few key points here. Upon inspection, the second term in Eq. (4.19) looks a lot like the second-order MBPT correction to the energy in Eq. (3.75). This is not coincidental, and although it is not directly obvious how this works out with the integration this term does in fact account for all second-order MBPT corrections in the IMSRG(2).

The IMSRG(2) is complete up to third order in MBPT, but also includes plenty of higher-order contributions and does so nonperturbatively. Excellent examples of this are the particle-particle and hole-hole ladder diagrams. In the second-to-last term of Eq. (4.21), one sees that there are two contributions accounting for the interaction between two holes (n_pn_q) and the interaction between two particles ($\bar{n}_p\bar{n}_q$). These terms account for pp and hh interactions in a way that gives the right contributions at third order, but also at all higher orders. This means the IMSRG(2) resums the full set of pp and hh ladder diagrams, accounting for this physics nonperturbatively. While it is less obvious from the form of the expression, the final term in Eq. (4.21) similarly generates the full set of ph ring diagrams. This is a clear demonstration of the power of nonperturbative many-body methods: a general formulation allows one to automatically capture a lot of physics in a way that would require considerable formal work and selection by hand in the case of MBPT.

A final feature of the IMSRG is that the method is size extensive, meaning that the error between the theoretical exact result and the IMSRG(2) result scales like the system size (and not worse). Specifically, this applies to the correlation expansion after Hartree-Fock, so

$$|(E_{\text{exact}}-E_{\text{HF}})-(E_{\text{IMSRG(2)}}-E_{\text{HF}})|\sim A\,. \tag{4.22}$$

This is also a feature of CC and MBPT, and in the case of the IMSRG and CC this arises because both methods are formulated as a commutator expansion of the many-body problem. This guarantees that so-called "disconnected" diagrams are not included in the calculations (as they vanish in the commutator), and the final result only includes connected diagram contributions that would also be included in (high-order) MBPT.

[2] In fact, solving the IMSRG via the Magnus expansion (see Sec. 4.5) requires the evaluation of general fundamental commutators (making no assumptions on the form of A or B in $[A,B]$), which then causes the IMSRG(2) to explicitly scale as $\mathcal{O}(N^6)$.

Our discussion here is focused on the IMSRG(2), which is the well-established standard for IMSRG calculations. A key development of this thesis is the extension of the IMSRG to the three-body level, the IMSRG(3) discussed formally in Chapter 7, and its application to high-precision calculations in nuclei. The IMSRG(3) is a systematic improvement of the IMSRG method, bringing the method closer to an exact treatment of the many-body problem. It brings greater precision, but comes at a higher computational cost as the treatment of three-body operators presents a considerable formal and computational challenge.

4.3 Single-reference decoupling

In the standard IMSRG, where a Slater-determinant reference state is employed, the target of the IMSRG transformation is a unitary transformation of the Hamiltonian that achieves a partial diagonalization, extracting the ground-state energy and (indirectly) the ground-state wave function. This is shown schematically in Fig. 4.1. For the initial (unevolved) Hamiltonian, the Hamiltonian can couple the ground-state $|\Phi\rangle$ to its excitations $|\Phi_i^a\rangle$, $|\Phi_{ij}^{ab}\rangle$.[3] A full diagonalization of the Hamiltonian would decouple $|\Phi\rangle$ from all excitations, but also all excitations from each other. The minimal decoupling we actually want to achieve is a block diagonalization such that $|\Phi\rangle$ is decoupled from excitations, but we enforce no decoupling on any other states. This is what is shown in Fig. 4.1 for the transformed Hamiltonian.

The task is to tailor the IMSRG unitary transformation to achieve this decoupling. This can be achieved through a proper definition of the generator η. For the IMSRG equation in Eq. (4.2) to integrate to a stable result as $s \to \infty$, $[\eta(s), H(s)]$ must vanish. This can trivially occur for two definitions of η, $\eta(s) = 0$ and $\eta(s) = H(s)$, both of which lead to no change of the Hamiltonian. In the original studies of the SRG [64], a useful nontrivial definition of η was found to be

$$\eta(s) = [H_{\rm od}(s), H_{\rm d}(s)]\,, \tag{4.23}$$

where the Hamiltonian is split into two parts $H(s) = H_{\rm d}(s) + H_{\rm od}(s)$. $H_{\rm od}$ is the "off-diagonal" part of the Hamiltonian, coupling parts of the Hamiltonian that one wants to decouple. If decoupling is achieved, $H_{\rm od}(s \to \infty) \approx 0$ following the SRG transformation. The remaining "diagonal" part of the Hamiltonian $H_{\rm d} = H - H_{\rm od}$ changes minimally with no explicit decoupling enforced. The form of η in Eq. (4.23), known as the Wegner generator, has been used in a broad range of contexts generally achieving the desired decoupling in practice.

A clear question is: what is the appropriate definition of $H_{\rm od}(s)$ for IMSRG calculations? Fortunately, our discussion has made it clear that we want to suppress matrix elements of $H(s)$ that couple $|\Phi\rangle$ with its excitations. These are:

$$\langle \Phi_i^a | H | \Phi \rangle = f_{ai}\,, \tag{4.24}$$
$$\langle \Phi | H | \Phi_i^a \rangle = f_{ia}\,, \tag{4.25}$$
$$\langle \Phi_{ij}^{ab} | H | \Phi \rangle = \Gamma_{abij}\,, \tag{4.26}$$
$$\langle \Phi | H | \Phi_{ij}^{ab} \rangle = \Gamma_{ijab}\,, \tag{4.27}$$
$$\ldots.$$

These matrix elements coupling the reference state and its excitations must be driven to 0 by the IMSRG transformation, and we can use this to define η.

[3] At the NO2B level, these are the only excitations that couple directly to the reference state, while higher excitations are coupled via successive particle-hole excitations. If we include W in our initial Hamiltonian, couplings to $|\Phi_{ijk}^{abc}\rangle$ would also be allowed.

The Wegner generator discussed above is generally successful in SRG studies, but for the IMSRG different generators have proliferated where matrix elements of η are (quasi)linearly proportional to matrix elements of $H_{\rm od}$. These generators, introduced below, have the benefits that they are easier to construct and that they make the analysis of the IMSRG via perturbation theory easier.

For completeness, we introduce the three generators most commonly used in IMSRG calculations, the White, imaginary-time, and arctan generators. The White generator has the nonzero matrix elements

$$\eta_{ia} = \frac{f_{ia}}{\Delta_{ia}^{(1\mathrm{B})}}\,, \tag{4.28}$$

$$\eta_{ai} = -\frac{f_{ai}}{\Delta_{ia}^{(1\mathrm{B})}}\,, \tag{4.29}$$

$$\eta_{ijab} = \frac{\Gamma_{ijab}}{\Delta_{ijab}^{(2\mathrm{B})}}\,, \tag{4.30}$$

$$\eta_{abij} = -\frac{\Gamma_{abij}}{\Delta_{ijab}^{(2\mathrm{B})}}\,, \tag{4.31}$$

$$\ldots\,.$$

Here and in the following definitions, the energy denominators $\Delta_{ia}^{(1\mathrm{B})}$ and $\Delta_{ijab}^{(2\mathrm{B})}$ can simply be taken to be the Møller-Plesset definitions,

$$\Delta_{ia}^{(1\mathrm{B})} = \varepsilon_i - \varepsilon_a\,, \tag{4.32}$$

$$\Delta_{ijab}^{(2\mathrm{B})} = \varepsilon_i + \varepsilon_j - (\varepsilon_a + \varepsilon_b)\,, \tag{4.33}$$

$$\ldots\,,$$

as is done in this work. Another alternative is to use the Epstein-Nesbet energy denominators as is discussed in Ref. [94]. In practice, Møller-Plesset and Epstein-Nesbet energy denominators behave very similarly, leading to the same IMSRG decoupling behavior.

The imaginary-time generator has the nonzero matrix elements

$$\eta_{ia} = \mathrm{sign}(\Delta_{ia}^{(1\mathrm{B})}) f_{ia}\,, \tag{4.34}$$

$$\eta_{ai} = -\mathrm{sign}(\Delta_{ia}^{(1\mathrm{B})}) f_{ai}\,, \tag{4.35}$$

$$\eta_{ijab} = \mathrm{sign}(\Delta_{ijab}^{(2\mathrm{B})}) \Gamma_{ijab}\,, \tag{4.36}$$

$$\eta_{abij} = -\mathrm{sign}(\Delta_{ijab}^{(2\mathrm{B})}) \Gamma_{abij}\,, \tag{4.37}$$

$$\ldots\,.$$

The arctan generator, a regularized version of the White generator that prevents large generator matrix

elements for vanishing energy denominators, has the nonzero matrix elements

$$\eta_{ia} = \frac{1}{2} \arctan \frac{2f_{ia}}{\Delta_{ia}^{(1B)}} , \tag{4.38}$$

$$\eta_{ai} = -\frac{1}{2} \arctan \frac{2f_{ai}}{\Delta_{ia}^{(1B)}} , \tag{4.39}$$

$$\eta_{ijab} = \frac{1}{2} \arctan \frac{2\Gamma_{ijab}}{\Delta_{ijab}^{(2B)}} , \tag{4.40}$$

$$\eta_{abij} = -\frac{1}{2} \arctan \frac{2\Gamma_{abij}}{\Delta_{ijab}^{(2B)}} , \tag{4.41}$$

$$\ldots .$$

The choice of generator may have a qualitative impact on how easy the IMSRG equations are to solve, but all generators that produce the correct decoupling give equivalent results up to many-body truncation effects. In this thesis, we use the arctan generator for nearly all calculations except for the results of Ref. [45] in Chapter 7, where we use the imaginary-time generator. In this case, we tested generator dependence and found changes in ground-state energies of less than 1 keV [45]. A practical thing to note is that the units of s depend on the generator employed: for the White and arctan generators s has units of 1; for the imaginary-time generator s has units of MeV^{-1}; and for the Wegner generator s has units of MeV^{-2}.

4.4 Valence-space decoupling

When one considers open-shell systems, the single-reference approach discussed previously stops making sense. A single Slater-determinant reference state would consist of a few fermions occupying a partially filled orbital, which would be degenerate with respect to "excitations" within the same orbital. This means the clear separation between particles and holes is blurred, and a different perspective is needed. This problem can be approached using techniques to break symmetries in order to lift the degeneracy. These symmetries must later be restored, which is formally and computationally challenging.

The valence-space picture, which is the basis for the shell model [71, 72], takes a different approach. The mean-field picture is split into three parts. Particles in the static core are not excited and do not interact with particles outside the core. The remaining few particles above the core are active in a valence space, where all possible excitations and interactions are allowed. Crucially, the valence space is relatively small, decoupled from the remaining outside space of higher energy orbitals, making a complete diagonalization possible. The blurring line between particles and holes in the single-reference picture is replaced by a complete active space around the Fermi surface. A simple diagonalization in this active space completely solves the many-body problem for interactions that would be difficult to account for otherwise.

The challenge from a microscopic perspective lies in obtaining an effective Hamiltonian in the valence space and accounting for the structure of the static core appropriately. Essentially since the introduction of the shell model, the long history of developments on nuclear forces has been paralleled by efforts to arrive at effective shell-model interactions based on these forces, with generally lackluster success for atomic nuclei [73, 281–285]. In the mean time, phenomenologically tuned shell-model interactions proliferated and were quite successful (albeit only close to where the interactions were originally fit) [74, 77, 286–292].

With a bit of rethinking, the IMSRG can be used to obtain microscopic, effective shell-model Hamiltonians in a systematic nonperturbative way [95, 261–263]. This general, nonperturbative treatment is the difference

maker, allowing the IMSRG to succeed where older approaches to computing effective Hamiltonians failed. Additionally, this perspective connects nicely with the SRG philosophy of transforming the Hamiltonian such that it is easier diagonalize [61, 67–69, 190–195, 249, 250, 293, 294], in this case possible to diagonalize in the shell model.

The great benefit of the IMSRG in this approach is how easily the generator can be tweaked to suppress additional couplings in the Hamiltonian. To arrive at a valence-space Hamiltonian, we must decouple the core (c), valence (v), and outside (o) spaces fully. The only allowed one-body matrix elements are $f_{cc'}$, $f_{vv'}$, and $f_{oo'}$, and similarly the only allowed two-body matrix elements are $\Gamma_{cc'c''c'''}$, $\Gamma_{vv'v''v'''}$, and $\Gamma_{oo'o''o'''}$.[4] The remaining matrix elements are H_{od} in the valence-space decoupling, and the generator definitions in Sec. 4.3 are easily applied to this more general off-diagonal Hamiltonian. This is generally safe as the core states have lower energies than the valence states, which have lower energies than the outside states, preventing vanishing energy denominators.

Following such a decoupling procedure $H(s \to \infty)$ can be fed into a shell-model code to be diagonalized. This gives access to not only the ground state, but also excited states, and one can use this solution to evaluate expectation values or transition matrix elements of other effective operators $O(s \to \infty)$. This makes the valence-space IMSRG (VS-IMSRG) immediately able to access observables like spectra and transition strengths that would otherwise require an equation-of-motion extension to the single-reference IMSRG.

It is useful to discuss a few technical details on normal ordering here for completeness. The initial treatment in the VS-IMSRG is identical to the single-reference IMSRG; we solve for a single-particle basis (for example, via Hartree-Fock), construct our reference state from the lowest A states in that basis, and normal order our Hamiltonian and all operators with respect to this state. The only difference is that the occupation numbers n_p may take on fractional values for orbitals that are only partially filled [95, 261]. Still we perform the normal ordering using the exact same expressions, Eqs. (3.34)–(3.37), summing over all core and valence states. The IMSRG equations are then solved in a two-step procedure, first decoupling the core states c from valence v and outside states o, and then decoupling the valence space fully as described above.

To use these matrix elements in shell-model calculations, we must undo the normal ordering using Eqs. (3.38)–(3.41). We then normal order with respect to our core using Eqs. (3.34)–(3.37) with all sums restricted to only core states c. This gives us our remaining "free" effective operators in the valence space. For the Hamiltonian we find the zero- through two-body parts E_{core}, $f_{vv'}$, and $\Gamma_{vv'v''v'''}$. All remaining matrix elements are decoupled and irrelevant for the further shell-model calculations.

4.5 Magnus-expansion formulation

The standard formulation of the IMSRG integrating Eq. (4.2) makes consistently evolving other operators challenging. To obtain the transformation of an operator O,

$$O(s) = U(s)\, O\, U^\dagger(s)\,, \tag{4.42}$$

the operator must be consistently evolved using the same flow equation

$$\frac{dO(s)}{ds} = [\eta(s), O(s)]\,, \tag{4.43}$$

with the initial condition $O(s=0) = O$. This is conceptually simple, but in practice $\eta(s)$ is only available as we are transforming $H(s)$, so $O(s)$ must be transformed at the same time as $H(s)$, extending the set of

[4] A technical detail is that many shell-model solvers expect a diagonal one-body Hamiltonian, so we typically also suppress $f_{vv'}$ where $v \neq v'$.

coupled differential equations. For a single operator, this is still manageable, but if one is interested in transforming many operators [for example, densities $\rho(r)$ at many r or form factors $F(q)$ at many q] the consistent evolution of all the operators becomes prohibitive.

The key problem here is that by integrating the flow equation we do not have direct access to the unitary transformation generated by the IMSRG, $U(s)$. An approach that resolves this challenge is the Magnus expansion [295–297]. The Magnus expansion postulates the form $U(s) = \exp(\Omega(s))$ for the unitary transformation generated by the IMSRG in terms of the anti-Hermitian Magnus operator $\Omega(s)$. The normal flow equation for the Hamiltonian can be converted into a flow equation for $\Omega(s)$,

$$\frac{d\Omega(s)}{ds} = \sum_{k=0}^{\infty} \frac{B_k}{k!} \mathrm{ad}^k_{\Omega(s)}(\eta(s)) \,. \tag{4.44}$$

Here, B_k are the Bernoulli numbers, and $\mathrm{ad}^k_X(Y)$ are the recursively defined commutators

$$\mathrm{ad}^0_X(Y) = Y \,, \tag{4.45}$$
$$\mathrm{ad}^k_X(Y) = [X, \mathrm{ad}^{k-1}_X(Y)] \,. \tag{4.46}$$

The solution for $\Omega(s)$ requires $\eta(s)$ [which depends on $H(s)$], so $\Omega(s)$ and $H(s)$ are solved for together. $\Omega(s \to \infty)$ then gives the full IMSRG unitary transformation in terms of a single operator. This can be saved once and then reused many times independently to transform other operators of interest using the Baker-Campbell-Hausdorff (BCH) formula,

$$O(s) = e^{\Omega(s)} O e^{-\Omega(s)} = \sum_{k=0}^{\infty} \frac{1}{k!} \mathrm{ad}^k_{\Omega(s)}(O) \,. \tag{4.47}$$

In general, the Magnus operator is truncated at the same many-body level as all other operators, so at the two-body level for the IMSRG(2).

The Magnus expansion is numerically very robust, allowing for considerable simplifications. The sum in Eq. (4.44) can be truncated at relatively low $k_{\max}$, and the integration in s for $\Omega(s)$ can be performed using a crude Euler method. These features, in addition to the clear benefit of having direct access to the IMSRG transformation, make the Magnus expansion the approach of choice for IMSRG calculations today. In this thesis, we use the Magnus-expansion formulation for nearly all calculations except for the results of Ref. [45] in Chapter 7, where we directly integrate the IMSRG flow equation.

4.6 IMSRG successes and challenges

The IMSRG(2), introduced in nuclear physics in 2011 [260], has emerged as a remarkably powerful and flexible method to describe nuclear structure. In a single-reference context, it has many of the same strengths as other nonperturbative reference-state-based many-body methods like CC or SCGF. Important work has been done to allow a diverse set of operators to be consistently transformed by the IMSRG, allowing many observables including complex electromagnetic observables to be computed [264–267].

The valence-space extension of the IMSRG has been particularly powerful. This extension was suggested very early in the IMSRG's development [262] and was made conceptually and formally simple by the fact that the unitary IMSRG transformation gives a Hermitian transformed Hamiltonian, easily interfacing with existing shell-model machinery [95, 261, 263]. This is to be contrasted with the derivation of effective shell-model interactions within coupled-cluster theory, where a generalized non-Hermitian solver must be used to perform the shell-model diagonalization [298–300]. The VS-IMSRG allows the IMSRG to access all

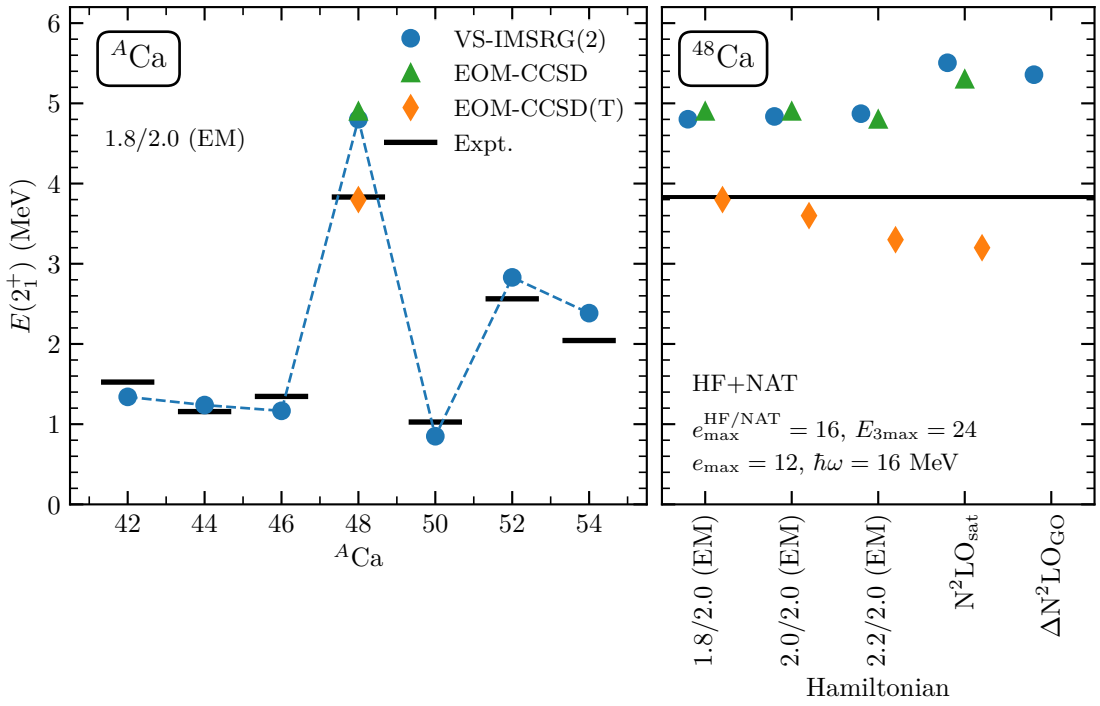

Figure 4.2: First 2^+ excitation energies of neutron-rich calcium isotopes. *Left:* 2^+ excitation energies $E(2_1^+)$ of neutron-rich calcium isotopes predicted by VS-IMSRG(2) calculations and coupled-cluster calculations from Ref. [39], with all calculations using the 1.8/2.0 (EM) Hamiltonian [171]. *Right:* 2^+ excitation energies $E(2_1^+)$ of ^{48}Ca computed using several Hamiltonians [165, 167, 171]. Our VS-IMSRG(2) calculations (*blue circles*) use HF+NAT bases computed in an $e_{\max}^{\mathrm{HF/NAT}} = 16$, $E_{3\max} = 24$, $\hbar\omega = 16$ MeV model space before being truncated to $e_{\max} = 12$ for the IMSRG calculation (see Chapter 6 for details) and are consistent with the VS-IMSRG(2) predictions in Ref. [3] using the 1.8/2.0 (EM) Hamiltonian. The EOM-CCSD calculations (*green triangles*) are truncated at the two-body level, analogous to the VS-IMSRG(2), while the EOM-CCSD(T) calculations (*orange diamonds*) include three-body contributions. Experimental values from Ref. [303].

systems that are accessible to the shell model, extending its reach tremendously. A few highlight studies enabled by this are the prediction of the closed-shell structure of ^{78}Ni [42] and the global prediction of separation energies up of ~ 700 isotopes up to iron to explore the locations of drip lines [44].

The derivation of a valence-space Hamiltonian in the VS-IMSRG has not been the only successful extension of the IMSRG approach. Powered by the development of a complete multireference treatment of the IMSRG equations [301, 302] (performing normal ordering with respect to a general, non-Slater-determinant reference state), various approaches have been explored to access open-shell systems. The details of these methods [249, 250] are beyond the scope of this thesis, but intuitively there are two important steps. First, a suitable multireference approximation to the ground-state is obtained, using a restricted diagonalization or a method more tailored to capture deformation in the system of interest, typically done via generator coordinate method calculations. Then the IMSRG(2) is solved with the general multireference normal ordering. This approach is not able to decouple the ground-state completely and so a final diagonalization is performed to get the ground state and other observable expectation values. The ideas here are very similar to the VS-IMSRG, with ability to support more general reference states at the cost of greater formal and computational complexity.

The IMSRG(2) truncation in its various forms has been very successful for certain observables. In

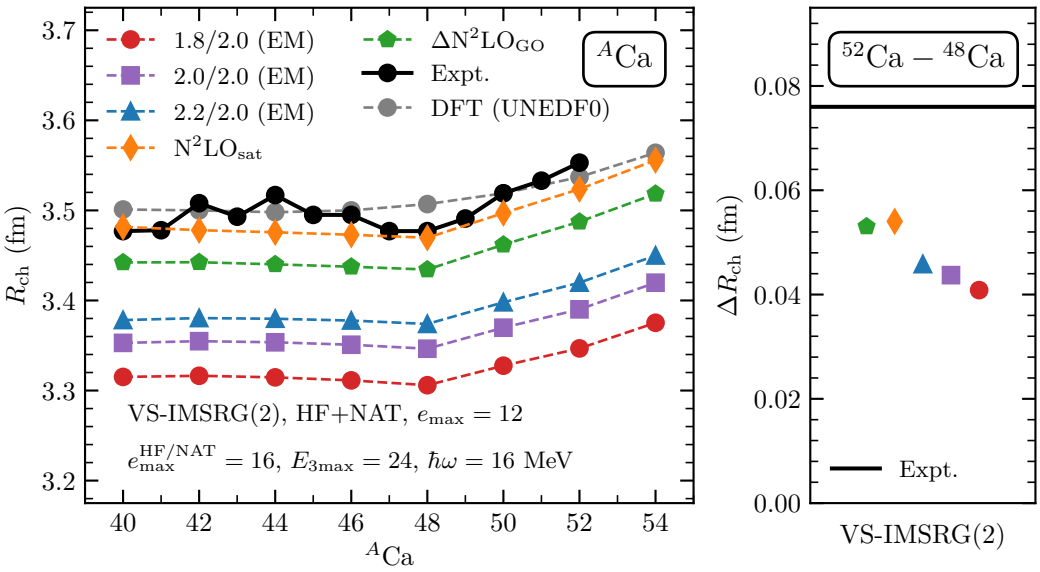

Figure 4.3: Discrepancies between nuclear theory predictions and measured charge radii for neutron-rich calcium isotopes. *Left:* Charge radii $R_{\rm ch}$ of calcium isotopes from ^{40}Ca to ^{54}Ca. *Right:* Charge radius differences $\Delta R_{\rm ch}$ between ^{52}Ca and ^{48}Ca. We compare our VS-IMSRG(2) predictions for several Hamiltonians (*colored markers*) [165, 167, 171] with experimental results (*black solid line*) and DFT predictions using the UNEDF0 functional (*gray dashed line*) from Ref. [307]. Our VS-IMSRG(2) calculations use HF+NAT bases computed in an $e_{\rm max}^{\rm HF/NAT} = 16$, $E_{3\rm max} = 24$, $\hbar\omega = 16$ MeV model space before being truncated to $e_{\rm max} = 12$ for the IMSRG calculation (see Chapter 6 for details).

particular, ground-state energies are captured extremely well by the IMSRG(2), not requiring a perturbative three-body correction like CC to get high accuracy [3, 44, 86, 94]. However, the normal-ordered two-body truncation has also reached its limits for some observables in the past decade. Three notable examples are the overprediction of dipole polarizabilities α_D when considering excitation of a nucleus by an electromagnetic probe [304, 305]; the general underprediction of $B(E2, 2^+ \to 0^+)$ transition strengths (where two-body currents may also play an important role) [267, 306]; and the overprediction of excitation energies of the first 2^+ state in closed-shell nuclei [3, 39, 42]. For a quantitative prediction of such observables, more complex many-body effects must be captured, which means using more complete, but more expensive many-body truncations like the IMSRG(3) or CC approximations with three-body operators.

One case that we revisit in this thesis is the first 2^+ energy of ^{48}Ca, presented in Fig. 4.2. In the left panel, we see VS-IMSRG(2) predictions for $E(2_1^+)$ for ^{42}Ca to ^{54}Ca using the 1.8/2.0 (EM) Hamiltonian, which gives a good reproduction of the energies of most calcium isotopes. A notable exception here is ^{48}Ca, a doubly-magic nucleus, where the VS-IMSRG(2) substantially overpredicts the 2^+ energy. This overprediction is not unique to the 1.8/2.0 (EM) Hamiltonian, as seen in the right panel for five different chiral EFT Hamiltonians [165, 167, 171], indicating that it is due to the IMSRG(2) truncation. In Ref. [39], Hagen *et al.* investigated the ^{48}Ca 2^+ energy with coupled-cluster calculations, using CC approximations at the normal-ordered two-body level, EOM-CCSD, and also including three-body effects, EOM-CCSD(T). There, they found a similar overprediction for many Hamiltonians at the two-body level, giving results very consistent with the VS-IMSRG(2) results. Including three-body effects in the coupled-cluster calculations provides significant corrections, bringing the 2^+ energy down considerably. In Chapter 9, we revisit this deficiency of the VS-IMSRG(2) with the IMSRG(3), expecting three-body operators in the IMSRG produce a similar correction.

There are also some puzzles in ab initio nuclear structure theory. In these cases, it is not clear whether the existing discrepancy to experiment is due to deficiencies or uncertainties of the Hamiltonian or due to the many-body approximation. A key example is the trend of charge radii in neutron-rich calcium isotopes [307], shown in Fig. 4.3. Ab initio calculations fail to capture the key features, the "crown" or "parabola" in charge radii between ^{40}Ca and ^{48}Ca [308] (which have nearly the same charge radius) and the steep increase in charge radii after ^{48}Ca [307]. In the left panel of Fig. 4.3, we see that the VS-IMSRG(2) predictions of absolute radii are strongly Hamiltonian-dependent. In particular, the low-resolution Hamiltonians from Ref. [171] give smaller radii than experiment. This behavior was originally related to nuclear matter saturation properties of the interactions [3, 166], but recent results have suggested that the picture connecting nuclear matter saturation density and nuclear charge radii is not completely clear [185]. However, the relative trends for all Hamiltonians are very similar. Charge radii are predicted to be flat from ^{40}Ca to ^{48}Ca and then increase considerably after ^{48}Ca. This misses the larger charge radius of ^{44}Ca relative to ^{40}Ca and ^{48}Ca. In the right panel, we see that the increase in the charge radius of ^{52}Ca relative to ^{48}Ca is also consistently underpredicted by all Hamiltonians. These trends are generally challenging to reproduce, also in coupled-cluster calculations [307, 309] and in phenomenological shell model and density functional theory calculations [307, 310], but recent work exploring and optimizing the Fayans functional for radii have allowed for a better description of calcium radii [82, 309, 311, 312]. An important step to understand what is missing in ab initio calculations is going to the next order in the many-body approximation to quantify and reduce many-body uncertainties.

4.7 Uncertainty quantification for the IMSRG

Uncertainty quantification for many-body calculations is challenging, and the IMSRG is no exception. There are multiple sources of uncertainties, and assessing the magnitude of those uncertainties typically requires performing larger, more expensive calculations.

For an IMSRG calculation, the errors we make are due to the many-body approximation [typically the IMSRG(2)], the finite model space ($e_{\max}$ and $E_{3\max}$, as discussed in Sec. 3.5), and the IMSRG numerical solution. The IMSRG solver errors are due to many different choices that are made to set up an IMSRG calculations. These choices include: the generator; the decoupling threshold that determines when a calculation terminates; the numerical integration approach; and the handling of the Magnus operator.[5] Generally, one can control for these solver errors, and their effects are well understood and small. Model-space errors are also well understood and can be controlled for in most systems.

Errors due to the many-body approximation are considerably less well understood, but are particularly important for the predictive power of ab initio methods in exotic systems. A common strategy has been to compare IMSRG(2) predictions based on a given Hamiltonian to predictions from other many-body methods for the same Hamiltonian. Other methods, like CC and SCGF, employ other many-body approximations, so the extent to which multiple complementary approximate many-body methods agree gives some insight into the general uncertainties of the methods. In particular, IMSRG, CC, and SCGF calculations can be compared to results from exact diagonalizations in light systems, where the effect of the many-body approximation is unambiguous. This was done, for example, for ground-state energies in oxygen isotopes [86],

[5] The unitary transformation in the Magnus expansion is typically split up into a series of smaller unitary transformations solved for and performed sequentially,

$$U(s \to \infty) = U_N U_{N-1} \dots U_2 U_1 \,, \tag{4.48}$$

each parameterized by their own Magnus operator. This approach has the benefit that small unitary transformations are easy to solve for and the Magnus and BCH expansions converge quickly. How this splitting is performed is one choice that must be made in IMSRG calculations, and the sensitivity to this choice is due to the many-body approximation at play in IMSRG calculations.

and one found that the approximate many-body methods reproduce exact binding energies to within about 1%.

Such comparisons between complementary many-body methods inspire confidence in the robustness of the many-body approximations at play, but there are open questions and also limits to this approach. First, these different methods are complementary, but not fully independent. The many-body approximations employed are often similar, motivated by arguments from perturbation theory, and as a result all methods may miss the same physics essential to reproduce a given observable and thus agree on a wrong result. For bulk properties of nuclei this is unlikely, but for more exotic observables this has been observed [306].

At the same time, comparisons between two many-body methods are only possible for systems accessible by multiple approaches. The IMSRG, CC, and SCGF have different strengths, and in general different systems and observables are accessible to each method. In such cases where a given approach is uniquely able to provide predictions, one would still like to be able to robustly assess the many-body uncertainty, and this involves going to high orders in the many-body expansion. This has been done in CC theory, comparing CCSD [coupled-cluster with singles and doubles, a comparable truncation to the IMSRG(2)] with various approximations that also include three-body operators [313–319]. Within the IMSRG, this requires going beyond the IMSRG(2) and investigating the effects of three-body operators in the IMSRG(3). Such calculations are tremendously expensive, but available due to the developments in this thesis, and robust many-body uncertainty quantification for IMSRG calculations is now becoming possible.

Part II

Method advances

Chapter 5

Normal-ordered three-body forces for heavy nuclei

When computing heavy nuclei beyond $A \sim 100$, the treatment of three-body forces in many-body calculations becomes a challenge. Storing complete three-body matrix elements in a single-particle basis $\langle pqr|V_{3\mathrm{N}}|stu\rangle$ would require 10s or 100s of TB of memory, so a truncation on three-body states $E_{3\mathrm{max}} \geq e_p + e_q + e_r$ is typically used when transforming $V_{3\mathrm{N}}$ to a single-particle basis. Standard values of $E_{3\mathrm{max}} = 16$, 18 are sufficiently converged in systems with $A \leq 100$ for soft Hamiltonians, but for heavier systems a strong dependence on $E_{3\mathrm{max}}$ is observed in ground-state energy predictions, indicating that the three-body truncation is insufficient to fully capture the three-body potential in larger systems.

Recent efforts have refined the treatment of three-body forces within the normal-ordered two-body approximation, where the three-body force is normal ordered with respect to a reference state $|\Phi\rangle$ and treated at the effective two-body level in the following many-body calculation. In this approximation, what is actually used in the many-body calculation is

$$\Gamma^{3\mathrm{N}}_{pqrs} = \sum_t \tilde{n}_t \langle pqt|V_{3\mathrm{N}}|rst\rangle = \sum_{tt'} \rho_{tt'} \langle pqt|V_{3\mathrm{N}}|rst'\rangle \tag{5.1}$$

from Eq. (3.36).[1] In practice, allowed values of t, t' are strongly constrained by symmetries, so only a subset of the complete set of matrix elements of $V_{3\mathrm{N}}$ must be stored to compute $\Gamma^{3\mathrm{N}}$. This approach is exploited by Miyagi *et al.* in Ref. [46], allowing NO2B many-body calculations up to $E_{3\mathrm{max}} = 28$. We present a complementary approach where Eq. (5.1) is evaluated in a relative basis without ever needing to store $V_{3\mathrm{N}}$ in a single-particle basis, circumventing the need for an $E_{3\mathrm{max}}$ truncation at all [49]. The improved treatment of $V_{3\mathrm{N}}$ is sufficient to deliver converged ground-state energies and radii for ^{208}Pb, opening the frontier of heavy nuclei to ab initio calculations. This work is published in Ref. [49].

5.1 Normal ordering in a Jacobi basis

Nuclear forces are efficiently represented in a plane-wave partial-wave basis (see Chapter 3 and Appendix A of Ref. [61] for details). Such bases exploit the Galilean and rotational invariance of nuclear interactions, making them the basis of choice for the construction of NN and 3N potential matrix elements. The 3N single-particle basis $|\tilde{\mathbf{k}}_1\tilde{\mathbf{k}}_2\tilde{\mathbf{k}}_3\rangle$ with $|\tilde{\mathbf{k}}_i\rangle = |\mathbf{k}_i m_{s_i} m_{t_i}\rangle$ is highly redundant in comparison. This redundancy

[1] In this chapter, we denote the occupation number for the state t by $\tilde{n}_t$, distinguishing it from the radial excitation number n_t, for notational consistency with Ref. [49].

is the cause of the computational challenges in normal ordering 3N potentials in a single-particle basis. To get around this, we reformulate the normal ordering procedure in Eq. (5.1) in a relative basis.

We start from a single-particle plane-wave basis,

$$\langle \tilde{\mathbf{k}}_1' \tilde{\mathbf{k}}_2' | \Gamma^{3\mathrm{N}} | \tilde{\mathbf{k}}_1 \tilde{\mathbf{k}}_2 \rangle = \int \frac{d\mathbf{k}_3 d\mathbf{k}_3'}{(2\pi)^6} \sum_{m_{s_3} m_{s_3}'} \sum_{m_{t_3} m_{t_3}'} \rho(\tilde{\mathbf{k}}_3, \tilde{\mathbf{k}}_3') \, \langle \tilde{\mathbf{k}}_1' \tilde{\mathbf{k}}_2' \tilde{\mathbf{k}}_3' | V_{3\mathrm{N}} | \tilde{\mathbf{k}}_1 \tilde{\mathbf{k}}_2 \tilde{\mathbf{k}}_3 \rangle \,, \tag{5.2}$$

with the density matrix

$$\rho(\tilde{\mathbf{k}}_3, \tilde{\mathbf{k}}_3') = \delta_{m_{t_3} m_{t_3}'} \sum_{n_3 l_3 j_3 m_{j_3}} \tilde{n}_3 \, \langle \tilde{\mathbf{k}}_3' | \varphi_{n_3 l_3 j_3 m_{j_3} m_{t_3}} \rangle \, \langle \varphi_{n_3 l_3 j_3 m_{j_3} m_{t_3}} | \tilde{\mathbf{k}}_3 \rangle \,. \tag{5.3}$$

This density matrix is constructed from the orbitals occupied in the reference state,

$$\langle \mathbf{k}_i m_{s_i} m_{t_i} | \varphi_{n_i l_i j_i m_{j_i} m_{t_i}} \rangle = \sum_{m_{l_i}} \mathcal{C}^{j_i m_{j_i}}_{l_i m_{l_i} \frac{1}{2} m_{s_i}} \, Y_{l_i m_{l_i}}(\hat{\mathbf{k}}_i) \, \varphi_{n_i l_i j_i m_{j_i} m_{t_i}}(k_i) \,, \tag{5.4}$$

with the Clebsch-Gordan coefficients $\mathcal{C}^{jm_j}_{lm_l 1/2\ m_s}$ coupling the single-particle orbital angular momentum and spin to the total angular momentum, the spherical harmonics Y_{lm_l}, and the angular orientation $\hat{\mathbf{k}}$ and modulus $k = |\mathbf{k}|$ of the vector $\mathbf{k}$.

Equation (5.2) may be reexpressed in terms of the relative momenta $\mathbf{p}$ and $\mathbf{q}$ and the two-body and three-body center-of-mass momenta $\mathbf{P}$ and $\mathbf{P}_{3\mathrm{N}}$,

$$\mathbf{p} = \frac{1}{2}(\mathbf{k}_1 - \mathbf{k}_2) \,, \tag{5.5}$$

$$\mathbf{P} = \mathbf{k}_1 + \mathbf{k}_2 \,, \tag{5.6}$$

$$\mathbf{q} = \frac{1}{3}(2\mathbf{k}_3 - \mathbf{P}) \,, \tag{5.7}$$

$$\mathbf{P}_{3\mathrm{N}} = \mathbf{k}_3 + \mathbf{P} \,, \tag{5.8}$$

yielding

$$\langle \tilde{\mathbf{p}}' \mathbf{P}' | \Gamma^{3\mathrm{N}} | \tilde{\mathbf{p}} \mathbf{P} \rangle = \int \frac{d\mathbf{k}_3 d\mathbf{k}_3'}{(2\pi)^6} \sum_{m_{s_3} m_{s_3}'} \sum_{m_{t_3} m_{t_3}'} \rho(\tilde{\mathbf{k}}_3, \tilde{\mathbf{k}}_3') \, \langle \tilde{\mathbf{p}}' \tilde{\mathbf{q}}' | V_{3\mathrm{N}} | \tilde{\mathbf{p}} \tilde{\mathbf{q}} \rangle \, (2\pi)^3 \delta(\mathbf{P}_{3\mathrm{N}} - \mathbf{P}_{3\mathrm{N}}') \,. \tag{5.9}$$

The three-body center-of-mass dependence is trivial due to Galilean invariance, but the two-body center-of-mass dependence in the normal-ordered 3N interaction is not as one integrates over $\mathbf{k}_3 \neq \mathbf{k}_3'$.

To arrive at plane-wave partial-wave matrix elements, we perform a partial-wave decomposition of the three-body states $|\tilde{\mathbf{p}}\tilde{\mathbf{q}}\rangle$ and the generalized two-body states $|\tilde{\mathbf{p}}\mathbf{P}\rangle$. For the three-body states,

$$\begin{aligned} |\tilde{\mathbf{p}}\tilde{\mathbf{q}}\rangle = |\mathbf{p} S M_S T M_T \, \mathbf{q} m_s m_t\rangle = \sum_{L M_L} \sum_{l m_l} Y^*_{L M_L}(\hat{\mathbf{p}}) Y^*_{l m_l}(\hat{\mathbf{q}}) \sum_{J M_J} \sum_{j m_j} \mathcal{C}^{J M_J}_{L M_L S M_S} \mathcal{C}^{j m_j}_{l m_l \frac{1}{2} m_s} \\ \times \sum_{\mathcal{J} M_{\mathcal{J}}} \sum_{\mathcal{T} M_{\mathcal{T}}} \mathcal{C}^{\mathcal{J} M_{\mathcal{J}}}_{J M_J j m_j} \mathcal{C}^{\mathcal{T} M_{\mathcal{T}}}_{T M_T \frac{1}{2} m_t} \, |pq[(LS)J(ls)j]\mathcal{J}(Tt)\mathcal{T}\rangle \,, \end{aligned} \tag{5.10}$$

with the magnitudes of the Jacobi momenta $p = |\mathbf{p}|$ and $q = |\mathbf{q}|$; the orbital angular momentum L, spin S, total angular momentum J, and the isospin T of the two-body subsystem of particles 1 and 2 with Jacobi momentum p; orbital angular momentum l, spin $s = 1/2$, total angular momentum j, and the isospin

$t = 1/2$ of particle 3 relative to the two-body subsystem; and the total three-body angular momentum $\mathcal{J}$ and total three-body isospin $\mathcal{T}$. It is convenient to use the compact notation

$$|pq\alpha\rangle = |pq[(LS)J(ls)j]\mathcal{J}(Tt)\mathcal{T}\rangle\,, \tag{5.11}$$

where the index α collects all the partial-wave quantum numbers.

The two-body state decomposition works analogously, and we arrive at states

$$|pP[(\bar{L}\bar{S})\bar{J}\bar{L}_{\mathrm{CM}}]\bar{J}_{\mathrm{tot}}M_{\bar{J}_{\mathrm{tot}}}\bar{T}M_{\bar{T}}\rangle = |pP\gamma\rangle\,, \tag{5.12}$$

with the relative partial-wave quantum numbers associated with p, $\bar{L}$, $\bar{S}$, $\bar{J}$, $\bar{T}$, and $M_{\bar{T}}$ (distinguished from the analogous quantum numbers in $|pq\alpha\rangle$ by an overline), and the center-of-mass orbital angular momentum $\bar{L}_{\mathrm{CM}}$ coupled to the total two-body angular momentum $\bar{J}_{\mathrm{tot}}$. Again, all partial-wave quantum numbers are collected in γ for convenience.

Applying the decomposition to Eq. (5.9) and simplifying yields

$$\begin{aligned}\langle p'P'\gamma'|\Gamma^{3\mathrm{N}}|pP\gamma\rangle = \sum_{\substack{\mathcal{J}\mathcal{T}\\ ll'jj'}}\int d\hat{\mathbf{P}}d\hat{\mathbf{P}}'\frac{d\mathbf{k}_3}{(2\pi)^3}\,\langle p'q'\alpha'|V_{3\mathrm{N}}|pq\alpha\rangle \\ \times\sum_{\substack{j_xj_yj_z\\ m_ym_z}}\sum_{M_{\bar{L}_{\mathrm{CM}}}}\sum_{M'_{\bar{L}_{\mathrm{CM}}}}\sum_{m_lm'_l} A^{\alpha\alpha'\gamma\gamma'}_{j_xj_yj_z}B^{\bar{T}\bar{T}'M_{\bar{T}}\mathcal{T}}_{j_xj_yj_zm_ym_z}(\mathbf{k}_3,\mathbf{k}'_3) \\ \times\mathcal{C}^{j_ym_y}_{lm_l\bar{L}'_{\mathrm{CM}}M'_{\bar{L}_{\mathrm{CM}}}}\mathcal{C}^{j_zm_z}_{l'm'_l\bar{L}_{\mathrm{CM}}M_{\bar{L}_{\mathrm{CM}}}} \\ \times Y^*_{\bar{L}_{\mathrm{CM}}M_{\bar{L}_{\mathrm{CM}}}}(\hat{\mathbf{P}})\,Y_{\bar{L}'_{\mathrm{CM}}M'_{\bar{L}_{\mathrm{CM}}}}(\hat{\mathbf{P}}')\,Y^*_{lm_l}(\hat{\mathbf{q}})\,Y_{l'm'_l}(\hat{\mathbf{q}}')\,,\end{aligned} \tag{5.13}$$

with the superscripts α and γ indicating the dependence on all of the quantum numbers defined in Eqs. (5.11) and (5.12), respectively. We introduced the quantities

$$\begin{aligned}A^{\alpha\alpha'\gamma\gamma'}_{j_xj_yj_z} &= \delta_{\bar{J}J}\delta_{\bar{J}'J'}(-1)^{-\bar{J}+\bar{J}'+j+j'+2j_x+j_y-j_z}\hat{\mathcal{J}}^2\hat{j}\hat{j}'\hat{j}_y\hat{j}_z\hat{j}_x^2 \\ &\times\begin{Bmatrix}\bar{L}'_{\mathrm{CM}} & l & j_y\\ \frac{1}{2} & j_x & j\end{Bmatrix}\begin{Bmatrix}\bar{L}_{\mathrm{CM}} & l' & j_z\\ \frac{1}{2} & j_x & j'\end{Bmatrix}\begin{Bmatrix}j_x & \bar{L}'_{\mathrm{CM}} & j\\ \bar{L}_{\mathrm{CM}} & \bar{J}_{\mathrm{tot}} & \bar{J}\\ j' & \bar{J}' & \mathcal{J}\end{Bmatrix},\end{aligned} \tag{5.14}$$

and

$$\begin{aligned}B^{\bar{T}\bar{T}'M_{\bar{T}}\mathcal{T}}_{j_xj_yj_zm_ym_z}(\mathbf{k}_3,\mathbf{k}'_3) = \sum_{M_{\mathcal{T}}}\sum_{j_um_u}\sum_{\substack{n_3l_3j_3m_{j_3}\\ m_{l_3}m'_{l_3}m_{t_3}}}\hat{j}_3^2\,\mathcal{C}^{j_um_u}_{l_3m_{l_3}j_zm_z}\mathcal{C}^{j_um_u}_{l_3m'_{l_3}j_ym_y}\,\mathcal{C}^{\mathcal{T}M_{\mathcal{T}}}_{\bar{T}M_{\bar{T}}\frac{1}{2}m_{t_3}}\mathcal{C}^{\mathcal{T}M_{\mathcal{T}}}_{\bar{T}M_{\bar{T}}\frac{1}{2}m_{t_3}} \\ \times\begin{Bmatrix}j_x & \frac{1}{2} & j_y\\ \frac{1}{2} & j_3 & l_3\\ j_z & l_3 & j_u\end{Bmatrix}Y_{l_3m'_{l_3}}(\hat{\mathbf{k}}'_3)\,Y^*_{l_3m_{l_3}}(\hat{\mathbf{k}}_3)\varphi_{n_3l_3j_3m_{j_3}m_{t_3}}(k_3)\,\varphi_{n_3l_3j_3m_{j_3}m_{t_3}}(k'_3)\,,\end{aligned} \tag{5.15}$$

with $\hat{j} = \sqrt{2j+1}$ for all angular momentum quantum numbers and the Wigner $9j$ and $6j$ symbols [320]. In addition we introduced the auxiliary quantum numbers j_x, j_y, j_z, and j_u as well as their projections m_y, m_z, and m_u. These intermediate quantities are obtained by coupling l with $\bar{L}'_{\mathrm{CM}}$ to j_y, l' with $\bar{L}_{\mathrm{CM}}$ to j_z, l_3 with j_y and j_z to j_u, and $s = 1/2$ with j_y and j_z to j_x.

5.2 Practical considerations

At this point, the discussion of a few practical considerations is in order. First, Eq. (5.13) requires the density of the reference state $|\Phi\rangle$ as input. This reference state is ideally computed via Hartree-Fock or a perturbative natural orbitals calculation. Implicit in this is the dependence on the 3N potential, which enters the construction of the mean-field potential. It would in principle be possible to do the Jacobi normal ordering in Eq. (5.13) iteratively to also solve the HF and NAT equations, but the normal ordering is too expensive for this to be practical. Instead, the reference state is constructed once from a truncated single-particle 3N potential that is still restricted by some $E_{3\mathrm{max}}$ cut. This is a pragmatic solution that takes advantage of the fact that mean-field approaches converge more quickly in $E_{3\mathrm{max}}$ than the following IMSRG calculations. This means that even for ^{132}Sn an HF reference state constructed at $E_{3\mathrm{max}} = 18$ provides a density ρ that is converged in $E_{3\mathrm{max}}$ (as we see later in this chapter) and can be used for the normal ordering in a relative basis.

A second important consideration is the necessary truncations in the Jacobi normal ordering and how they compare with the single-particle normal ordering. From Eq. (5.13), we see that there are two kinds of truncations one could impose: truncations on the external two-body partial-wave numbers in γ; and/or truncations on the summed-over three-body partial-wave numbers $\mathcal{J}$, l, l'. Note that these truncations serve to limit the computational cost of the normal ordering, but do not arise due to any practical limits on memory; in principle, the truncations on γ can be taken quite large without producing prohibitively large normal-ordered 3N matrix element files. We find that it is conceptually and computationally practical to impose a truncation on $\bar{J}_{\mathrm{tot}}$ and $\bar{L}_{\mathrm{CM}}$ and to allow all other quantum numbers to extend to their limits. This choice gives nice convergence patterns for ground-state energies and radii, and we are able to test it systematically in the following.

The truncations in $\bar{J}_{\mathrm{tot}}$ and $\bar{L}_{\mathrm{CM}}$ in the Jacobi normal ordering are quite different from the $E_{3\mathrm{max}}$ truncation in the single-particle normal ordering. $E_{3\mathrm{max}}$ primarily truncates in the radial oscillator numbers n, given the higher "cost" of n in $e = 2n + l$, imposing strong infrared and ultraviolet cuts on the three-body force [321–325]. By contrast, the Jacobi normal ordering is free of such cuts due to the representation of $\Gamma^{3\mathrm{N}}$ in momentum space. The truncation in $\bar{J}_{\mathrm{tot}}$, the total two-body angular momentum for the effective potential, intuitively lines up with the expectation that important many-body physics is restricted to relatively low $\bar{J}_{\mathrm{tot}}$. The reference state of ^{132}Sn only allows coupling up to $\bar{J}_{\mathrm{tot}} = 9$, and for ^{208}Pb this only extends to $\bar{J}_{\mathrm{tot}} = 11$. This is to be contrasted with the maximum value allowed by the model space, which is $\bar{J}_{\mathrm{tot}} = 29$ for $e_{\mathrm{max}} = 14$ and $\bar{J}_{\mathrm{tot}} = 33$ for $e_{\mathrm{max}} = 16$. The truncation in $\bar{L}_{\mathrm{CM}}$ is a bit less intuitively clear, as it relates to the ability to resolve the center-of-mass dependence of the effective potential, but we find that $\bar{L}_{\mathrm{CM}} \sim \bar{J}_{\mathrm{tot}}$ is sufficient to yield convergence with respect to $\bar{L}_{\mathrm{CM}}$.

For IMSRG calculations, we must transform $\Gamma^{3\mathrm{N}}$ to a two-body single-particle basis. This transformation proceeds in two steps. First, we transform to a relative HO basis

$$|NN_{\mathrm{CM}}\gamma\rangle = \int dp\, dP\, p^2 P^2 R_{N\bar{L}}(p, b_{\mathrm{rel}}) R_{N_{\mathrm{CM}}\bar{L}_{\mathrm{CM}}}(P, b_{\mathrm{CM}})\, |pP\gamma\rangle\,, \tag{5.16}$$

with the oscillator lengths $b_i = 1/\sqrt{M\omega_i}$ and the radial part $R_{N\bar{L}}$ of the harmonic oscillator wave function in momentum space is given by $R_{N\bar{L}}(p, b) = \langle p\bar{L}|N\bar{L}\rangle$. The oscillator parameters are related by [61]

$$b_{\mathrm{rel}} = \sqrt{2}\, b\,, \quad b_{\mathrm{CM}} = \frac{1}{\sqrt{2}}\, b\,, \tag{5.17}$$

where b is the single-particle oscillator length of the HO basis. Then we transform from relative HO states

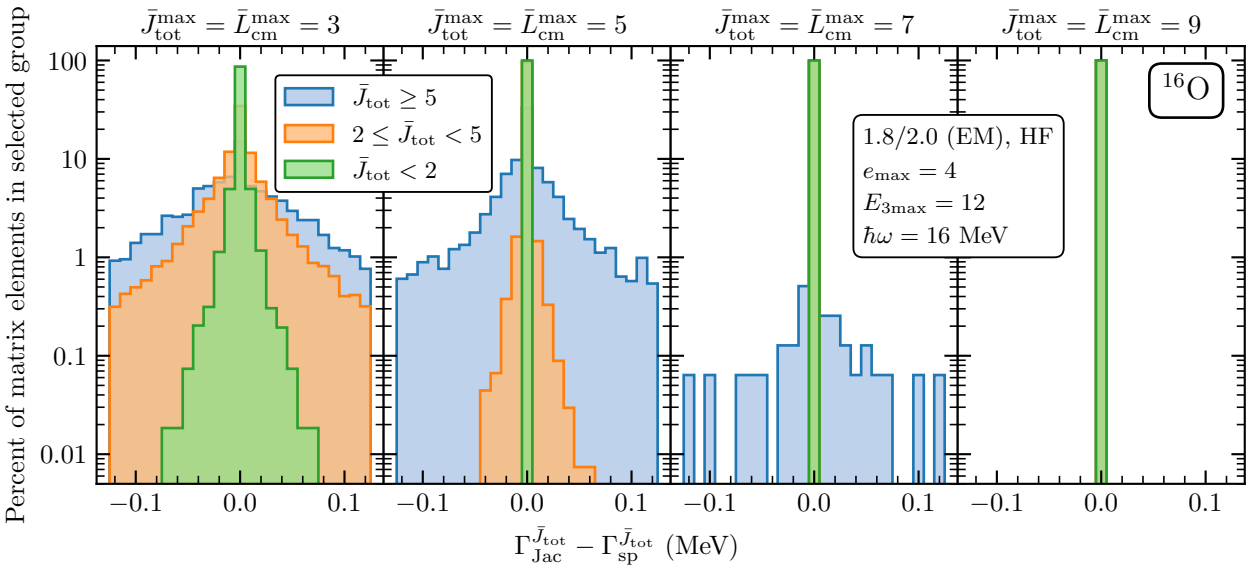

Figure 5.1: Matrix element differences in the Jacobi and single-particle normal ordering. Distributions of differences $\Gamma^{\text{3N}}_{\text{Jac}} - \Gamma^{\text{3N}}_{\text{sp}}$ for different $\bar{J}_{\text{tot}}$ blocks of $\bar{J}_{\text{tot}} < 2$ (*green*), $2 \leq \bar{J}_{\text{tot}} \leq 5$ (*orange*), and $\bar{J}_{\text{tot}} \geq 5$ (*blue*) in the effective two-body interaction. We show results for different truncations in the Jacobi normal ordering, using $\bar{J}^{\max}_{\text{tot}} = \bar{L}^{\max}_{\text{CM}} = 3$, 5, 7, and 9 in the first through fourth panel, respectively. The y axis shows the percentage of matrix elements with the difference specified on the x axis in the selected $\bar{J}_{\text{tot}}$ block. Results are shown for the 1.8/2.0 (EM) 3N interaction with $e_{\max} = 4$, $E_{3\max} = 12$, and $\hbar\omega = 16$ MeV using an ^{16}O HF reference state. Figure from Ref. [49].

to single-particle HO states

$$|(ab)\bar{J}_{\text{tot}}\bar{T}M_{\bar{T}}\rangle = \sum_{\lambda\bar{S}} \hat{j}_a\hat{j}_b\hat{\lambda}^2\hat{\bar{S}}\hat{\bar{J}} \begin{Bmatrix} l_a & s_a & j_a \\ l_b & s_b & j_b \\ \lambda & \bar{S} & \bar{J}_{\text{tot}} \end{Bmatrix} \sum_{\substack{N_{\text{CM}}\bar{L}_{\text{CM}} \\ N\bar{L}}} \langle (N_{\text{CM}}\bar{L}_{\text{CM}}N\bar{L})\lambda | (n_a l_a n_b l_b)\lambda\rangle$$
$$\times \sum_{\bar{J}} (-1)^{\bar{L}+\bar{S}+\bar{J}} \begin{Bmatrix} \bar{S} & \bar{L} & \bar{J} \\ \bar{L}_{\text{CM}} & \bar{J}_{\text{tot}} & \lambda \end{Bmatrix} |N_{\text{CM}}N\left[(\bar{L}\bar{S})\bar{J}\bar{L}_{\text{CM}}\right]\bar{J}_{\text{tot}}\bar{T}M_{\bar{T}}\rangle\,. \tag{5.18}$$

Here, we employ the Wigner $9j$ and $6j$ symbols [320] and the relative to single-particle HO brackets [326–329] to transform relative HO states to single-particle HO states:

$$|(n_a l_a n_b l_b)\,\lambda\rangle = \sum_{N_{\text{CM}}\bar{L}_{\text{CM}}N\bar{L}} \langle (N_{\text{CM}}\bar{L}_{\text{CM}}N\bar{L})\lambda | (n_a l_a n_b l_b)\lambda\rangle\, |(N_{\text{CM}}\bar{L}_{\text{CM}}N\bar{L})\lambda\rangle\,. \tag{5.19}$$

Performing these transformations and decoupling from coupled isospin $\bar{T}$, $M_{\bar{T}}$, we arrive at our desired coupled two-body single-particle basis states $|(pq)\bar{J}_{\text{tot}}\rangle$.

In this basis, we can perform benchmarks with the single-particle normal ordering both at the matrix element level and the level of predicted ground-state energies. We start with the former, where we compare the matrix elements $\Gamma^{\bar{J}_{\text{tot}}}_{pqrs} = \langle (pq)\bar{J}_{\text{tot}}|\Gamma^{\text{3N}}|(rs)\bar{J}_{\text{tot}}\rangle$ obtained in the single-particle normal ordering as in Eq. (5.1) and in the Jacobi normal ordering as in Eq. (5.13). For a clean comparison, we use the single-particle truncations $e_{\max} = 4$, $E_{3\max} = 12$ such that no $E_{3\max}$ cut is active and test the robustness of our truncations in the Jacobi normal ordering. We normal order the 3N part of the 1.8/2.0 (EM) Hamiltonian [171] with respect to an HF reference state for ^{16}O computed at $\hbar\omega = 16$ MeV.

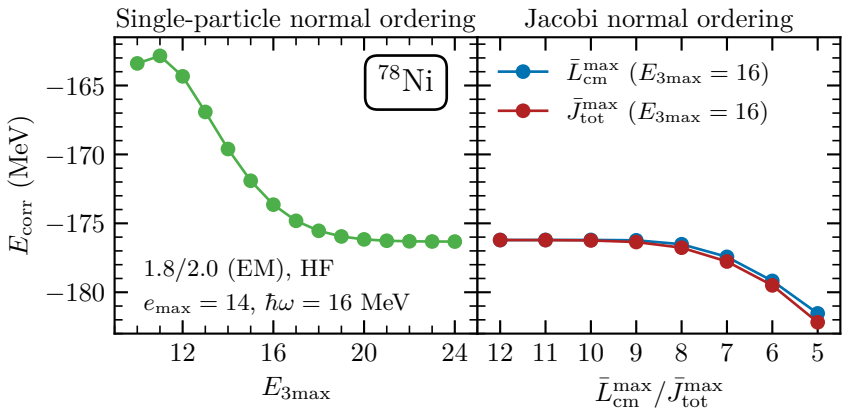

Figure 5.2: IMSRG(2) correlation energies for ^{78}Ni. *Left:* Correlation energies $E_{\rm corr}$ as a function of $E_{3\max}$ in the single-particle normal ordering. *Right:* Correlation energies $E_{\rm corr}$ as a function of $\bar{L}^{\max}_{\rm CM}$ and $\bar{J}^{\max}_{\rm tot}$ in the Jacobi normal ordering. The blue line shows $E_{\rm corr}$ as a function of $\bar{L}^{\max}_{\rm CM}$ while keeping $\bar{J}^{\max}_{\rm tot}$ at its maximal value of 12, and the red line shows $E_{\rm corr}$ as a function of $\bar{J}^{\max}_{\rm tot}$ while keeping $\bar{L}^{\max}_{\rm CM}$ at its maximal value of 12. Results are obtained using the 1.8/2.0 (EM) interaction, an $e_{\max} = 14$ model space, and an oscillator frequency of $\hbar\omega = 16$ MeV in the HF basis. The Jacobi normal ordering uses an $E_{3\max} = 16$ HF reference state. Figure from Ref. [49].

The distibution of matrix element differences for the Jaocbi normal-ordered matrix elements $\Gamma^{\rm 3N}_{\rm Jac}$ and the single-particle normal-ordered matrix elements $\Gamma^{\rm 3N}_{\rm sp}$ is shown in Fig. 5.1. We divide the matrix elements into different blocks based on $\bar{J}_{\rm tot}$, considering a low-$\bar{J}_{\rm tot}$ block with $\bar{J}_{\rm tot} \leq 2$, an intermediate block with $2 \leq \bar{J}_{\rm tot} \leq 5$, and a high-$\bar{J}_{\rm tot}$ block with $\bar{J}_{\rm tot} \geq 5$ (the maximum allowed $\bar{J}_{\rm tot}$ is 9 for $e_{\max} = 4$). Performing the Jacobi normal ordering with the truncations $\bar{J}^{\max}_{\rm tot} = \bar{L}^{\max}_{\rm CM} = 3$ yields considerable matrix element differences in all blocks. Increasing the truncation to 5 allows the Jacobi normal ordering to perfectly reproduce the single-particle normal ordering result in the low-$\bar{J}_{\rm tot}$ block, with decreasing discrepancies for higher $\bar{J}_{\rm tot}$ as well. Further increasing the truncation to 7 brings the intermediate block into excellent agreement, and by increasing it to 9 we find that the Jacobi normal ordering and single-particle normal ordering give numerically the exact same matrix elements. This both affirms that our derivation and implementation is correct and gives a sense for what truncations are required to accurately reproduce matrix elements of $\Gamma^{\rm 3N}$ for different $\bar{J}_{\rm tot}$. From our results, it generally seems to be the case that $\bar{L}^{\max}_{\rm CM} = \bar{J}_{\rm tot} + 2$ gives good reproduction of matrix elements up to $\bar{J}_{\rm tot}$.

Accurately reproducing matrix elements is a good check, but in practice not all matrix elements are equally important in many-body calculations [107, 330–332]. In the following we test $\Gamma^{\rm 3N}$ obtained from Jacobi and single-particle normal ordering in IMSRG(2) calculations. $\Gamma^{\rm 3N}$ can be included in IMSRG(2) calculations at the same cost as $V_{\rm NN}$, with only slightly modified normal ordering expressions [compare with Eqs. (3.34)–(3.36)]

$$E = \sum_i n_i H^{\rm (1B)}_{ii} + \frac{1}{2}\sum_{ij} n_i n_j (H^{\rm (2B)}_{ijij} + \frac{1}{3}\Gamma^{\rm 3N}_{ijij}) \,, \tag{5.20}$$

$$f_{pq} = H^{\rm (1B)}_{pq} + \sum_i n_i (H^{\rm (2B)}_{piqi} + \frac{1}{2}\Gamma^{\rm 3N}_{piqi}) \,, \tag{5.21}$$

$$\Gamma_{pqrs} = H^{\rm (2B)}_{pqrs} + \Gamma^{\rm 3N}_{pqrs} \,. \tag{5.22}$$

To understand the effects of the $\bar{J}^{\max}_{\rm tot}$, $\bar{L}^{\max}_{\rm CM}$ truncations in many-body calculations, we consider $e_{\max} = 14$ IMSRG(2) calculations for ^{78}Ni using Jacobi and single-particle normal-ordered 3N potentials as input.

We use the 1.8/2.0 (EM) Hamiltonian [171] for all the applications discussed in this chapter, and use the NuHamil code to access large $E_{3\mathrm{max}}$ in the single-particle normal ordering [333]. Note that for $e_{\mathrm{max}} = 14$, we cannot reach either $E_{3\mathrm{max}}$-completeness in the single-particle normal ordering or $\bar{J}^{\mathrm{max}}_{\mathrm{tot}}$-completeness in the Jacobi normal ordering, so such a comparison represents a test of both truncation efficiency and consistency in realistic many-body calculations.

In Fig. 5.2, we show the IMSRG(2) correlation energy $E_{\mathrm{corr}} = E_{\mathrm{IMSRG(2)}} - E_{\mathrm{HF}}$ as a function of $E_{3\mathrm{max}}$ for the single-particle normal ordering in the left panel and as a function of $\bar{J}^{\mathrm{max}}_{\mathrm{tot}}$ and $\bar{L}^{\mathrm{max}}_{\mathrm{CM}}$ for the Jacobi normal ordering in the right panel. In the single-particle normal ordering, we observe that E_{corr} converges quickly in $E_{3\mathrm{max}}$, with the energy converged to within 1 MeV at $E_{3\mathrm{max}} = 18$. For our Jacobi normal ordering, we show convergence with respect to $\bar{J}^{\mathrm{max}}_{\mathrm{tot}}$ and $\bar{L}^{\mathrm{max}}_{\mathrm{CM}}$ separately, with the red line showing convergence in $\bar{J}^{\mathrm{max}}_{\mathrm{tot}}$ with $\bar{L}^{\mathrm{max}}_{\mathrm{CM}} = 12$ and the blue line showing convergence in $\bar{L}^{\mathrm{max}}_{\mathrm{CM}}$ with $\bar{J}^{\mathrm{max}}_{\mathrm{tot}} = 12$. The Jacobi normal ordering converges systematically to the same E_{corr} value, and even moderate truncations of $\bar{J}^{\mathrm{max}}_{\mathrm{tot}} = \bar{L}^{\mathrm{max}}_{\mathrm{CM}} = 9$ are sufficient to be converged well within 1 MeV. Recall that the ^{78}Ni reference state typically has the neutron $1g_{9/2}$ orbital occupied, meaning the reference state can couple to up to $\bar{J}_{\mathrm{tot}} = 9$.

5.3 Applications to heavy nuclei

Up until the developments in Refs. [46, 49], ^{78}Ni was at the limit of comfortable convergence in $E_{3\mathrm{max}}$. Applications to heavier systems at $A \sim 100$ and beyond [41, 43] had to contend with nonnegligible model-space uncertainties or exploit features of e_{max} and $E_{3\mathrm{max}}$ convergence for specific observables to safely extrapolate. We now explore applications in the heavy nuclei ^{132}Sn and ^{208}Pb to establish the improved normal ordering approaches as robust and powerful ways to tackle nuclear structure in heavy systems.

In Fig. 5.3, we consider IMSRG(2) calculations of ^{132}Sn using the 1.8/2.0 (EM) Hamiltonian. All calculations are performed at $e_{\mathrm{max}} = 14$, $\hbar\omega = 12$ MeV, using an HF reference state. In the single-particle normal ordering (left panels), one observes that E_{HF} is converged within 1 MeV around $E_{3\mathrm{max}} = 18$ while E_{corr}, and as a result $E_{\mathrm{IMSRG(2)}}$, converge more slowly. Convergence within 1 MeV is reached around $E_{3\mathrm{max}} = 24$, highlighting the importance of improved normal ordering in fully capturing the NO2B 3N interaction.

We study the convergence in the Jacobi normal ordering with respect to $\bar{J}^{\mathrm{max}}_{\mathrm{tot}}$ with $\bar{L}^{\mathrm{max}}_{\mathrm{CM}} = 12$ and with respect to $\bar{L}^{\mathrm{max}}_{\mathrm{CM}}$ with $\bar{J}^{\mathrm{max}}_{\mathrm{tot}} = 12$. We test the dependence on the reference state by employing $E_{3\mathrm{max}} = 18$ and $E_{3\mathrm{max}} = 28$ reference states. The results for E_{HF}, E_{corr}, and $E_{\mathrm{IMSRG(2)}}$ are the same for both reference states. This indicates that the HF solution converges more quickly with respect to $E_{3\mathrm{max}}$ and one can rely on a reference state computed at relatively small $E_{3\mathrm{max}}$ as input for the Jacobi normal ordering.

We observe systematic convergence in both $\bar{J}^{\mathrm{max}}_{\mathrm{tot}}$ and $\bar{L}^{\mathrm{max}}_{\mathrm{CM}}$, with E_{corr} converged within 1 MeV around $\bar{J}^{\mathrm{max}}_{\mathrm{tot}} = \bar{L}^{\mathrm{max}}_{\mathrm{CM}} = 11$. Again, this aligns well with the fact that the ^{132}Sn reference state can couple up to $\bar{J}_{\mathrm{tot}} = 11$. The converged correlation energies in the single-particle and Jacobi normal ordering agree to within 1 MeV.

Considering $E_{\mathrm{IMSRG(2)}}$, one observes a slightly larger difference between the two approaches, which can be traced back to different converged values for E_{HF}. We understand this difference to be due to differences in how three-body forces are handled in the two approaches. These differences are:

1. whether $V_{3\mathrm{N}}$ is antisymmetrized in the HO basis or in the Jacobi momentum-space basis;

2. what truncations are employed for J and l in α [see Eq. (5.11)];

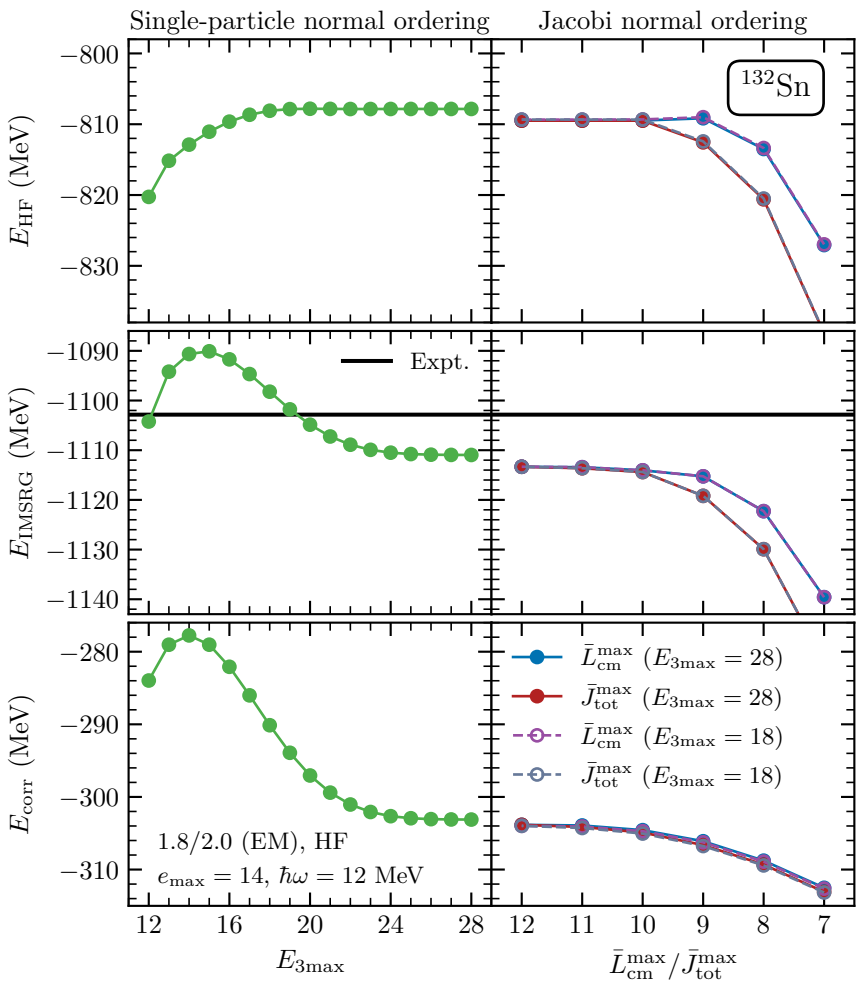

Figure 5.3: Hartree-Fock and IMSRG(2) energies for ^{132}Sn. Same as Fig. 5.2 but for ^{132}Sn and $\hbar\omega = 12$ MeV. We also show the HF energy E_{HF} and IMSRG energy E_{IMSRG} in the top and middle panel, respectively, and increased the $E_{3\mathrm{max}}$ range in the single-particle normal ordering (*left*) to $E_{3\mathrm{max}} = 28$. The Jacobi normal ordering (*right*) uses an $E_{3\mathrm{max}} = 28$ HF reference state (*filled circles*) and an $E_{3\mathrm{max}} = 18$ HF reference state (*open circles*). Figure from Ref. [49].

3. and what floating-point precision is used to store $V_{3\mathrm{N}}$ matrix elements and transformation coefficients during the various stages of the calculations.

The single-particle normal ordering typically antisymmetrizes $V_{3\mathrm{N}}$ in the Jacobi HO basis, uses $J^{\mathrm{max}} = 8$, $J^{\mathrm{max}} = 7$, and $J^{\mathrm{max}} = 6$ for three-body channels α with $\mathcal{J} \leq 5/2$, $\mathcal{J} = 7/2$, and $\mathcal{J} \geq 9/2$, respectively, and no restriction on l, and employs half precision for the storage $V_{3\mathrm{N}}$ in a single-particle basis (which is required to reach $E_{3\mathrm{max}} = 28$). By contrast, the Jacobi normal ordering antisymmetrizes $V_{3\mathrm{N}}$ in the Jacobi momentum-space basis, uses $J^{\mathrm{max}} = 5$, $l^{\mathrm{max}} = 5$ everywhere, and employs single precision or higher at all stages in the calculation. The $J^{\mathrm{max}} = 5$, $l^{\mathrm{max}} = 5$ truncation is closely tied to the necessary antisymmetrization in momentum space for the Jacobi normal ordering, as the antisymmetrization in momentum space is approximate, and keeping J^{max} and l^{max} relatively low ensures proper antisymmetry [61].[2]

[2] In practice, it has been seen that channels with $J \geq 5$ typically only provide very small contributions in calculations of nuclei and nuclear matter [61].

	E_{HF} (MeV)	E_{IMSRG} (MeV)
Antisymmetrization in Jacobi HO basis		
single precision	−806.11	−1109.02
$J^{\max} = l^{\max} = 5$ truncation	−808.79	−1111.83
half precision	−807.84	−1110.49
Antisymmetrization in Jacobi momentum-space basis		
single precision	−807.19	−1110.27
$J^{\max} = l^{\max} = 5$ truncation	−809.05	−1112.29
Jacobi normal ordering		
$\bar{L}^{\max}_{\mathrm{CM}} = \bar{J}^{\max}_{\mathrm{tot}} = 13$	−809.49	−1113.33

Table 5.1: Impact of 3N potential treatment in normal ordering for ^{132}Sn. Hartree-Fock energies E_{HF} and IMSRG(2) ground-state energies E_{IMSRG} for ^{132}Sn for an $e_{\max} = 14$ and $E_{3\max} = 24$ model space. Results are given for different 3N interaction files in the single-particle normal ordering. The first three rows apply the antisymmetrization in the Jacobi HO basis, whereas the next two rows perform the antisymmetrization in the Jacobi momentum-space basis in comparison to the Jacobi normal ordering results in the bottom row. If not stated otherwise, the single-particle normal ordering uses the truncation of $J^{\max} = 8$, 7, and 6 (as described in the main text) and no l truncation. The truncation $J^{\max} = l^{\max} = 5$ is used in the Jacobi normal ordering. Table from Ref. [49].

We tested the effects of these differences by varying the treatment in the single-particle normal ordering at $e_{\max} = 14$, $E_{3\max} = 24$, where one can also use single precision to store the matrix elements. The results for HF and IMSRG(2) energies are listed in Table 5.1. One sees that varying the treatment of $V_{3\mathrm{N}}$ in the single-particle normal ordering to that used in the Jacobi normal ordering brings the results systematically into agreement. In general, the differences affect the correlation energy less, indicating that this is mostly about small differences in matrix elements that are particularly important at the HF level. Overall, the agreement is still very good ($\sim 3\,$MeV on a binding energy of $\sim 1100\,$MeV), but calculations in heavy nuclei reveal small uncertainties in how we treat three-body forces in preparation for many-body calculations. These uncertainties are still smaller than IMSRG(2) uncertainties on binding energies in these systems and much smaller than uncertainties in the Hamiltonians employed.

Turning our attention to the ground-state energy of ^{208}Pb in Fig. 5.4, we find a similar picture as for ^{132}Sn, but with slower convergence due to the heavy mass. In particular, we find that $e_{\max} = 14$ is insufficient for model-space convergence, and we provide IMSRG(2) calculations of the ground-state energy at $e_{\max} = 16$. In the single-particle normal ordering, the HF solution continues to converge quickly with respect to $e_{\max}$ and $E_{3\max}$, with $e_{\max} = 14$, $E_{3\max} = 20$ being sufficient to converge E_{HF}. For E_{corr}, the convergence is more challenging. Going from $e_{\max} = 14$ to $e_{\max} = 16$ gives about a 2% correction, and sub-MeV convergence in $E_{3\max}$ is not quite reached. Still, the convergence patterns up to $e_{\max} = 16$ and $E_{3\max} = 28$ are likely sufficient for an exponential extrapolation if precision greater than $\pm 5\,$MeV is desired [46, 47]. This is not relevant at the IMSRG(2) level, but at the IMSRG(3) level, where the many-body solution would be accurate to within 2–3 MeV, model-space uncertainties due to $e_{\max}$ and $E_{3\max}$ would need to be reduced.

In the right panels of Fig. 5.4, we show results for the Jacobi normal ordering with respect to $\bar{J}^{\max}_{\mathrm{tot}}$ with $\bar{L}^{\max}_{\mathrm{CM}} = 13$ and with respect to $\bar{L}^{\max}_{\mathrm{CM}}$ with $\bar{J}^{\max}_{\mathrm{tot}} = 13$. We employ an $E_{3\max} = 28$ HF reference state, but note that an $E_{3\max} = 20$ HF reference state would likely yield indistinguishable results. We observe systematic convergence in $\bar{J}^{\max}_{\mathrm{tot}}$ and $\bar{L}^{\max}_{\mathrm{CM}}$, with convergence to within 1–2 MeV reached at $\bar{J}^{\max}_{\mathrm{tot}} = \bar{L}^{\max}_{\mathrm{CM}} = 13$. This

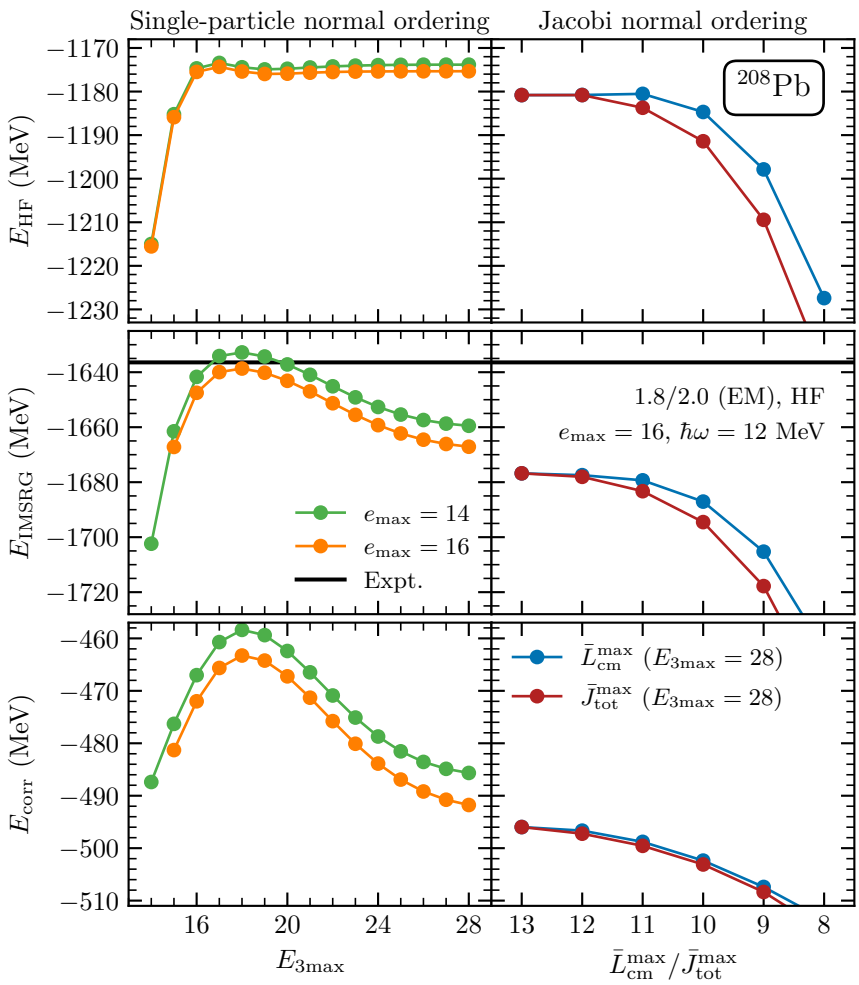

Figure 5.4: Hartree-Fock and IMSRG(2) energies for ^{208}Pb. Same as Fig. 5.3 but for ^{208}Pb. The single-particle normal ordering results (*left*) are shown for $e_{\mathrm{max}} = 14$ and $e_{\mathrm{max}} = 16$ model spaces. The Jacobi normal ordering (*right*) uses an $e_{\mathrm{max}} = 16$ and $E_{3\mathrm{max}} = 28$ HF reference state. Figure from Ref. [49].

once again aligns with the fact that the ^{208}Pb reference state can couple up to $\bar{J}_{\mathrm{tot}} = 13$ due to the neutron $1i_{13/2}$ orbital being occupied. For E_{corr}, the agreement with the single-particle normal ordering is good within the remaining $E_{3\mathrm{max}}$ uncertainty. For E_{HF}, we see a similar discrepancy between the two normal ordering approaches as in ^{132}Sn, with slightly larger absolute differences due to the larger system and larger HF energy. At the IMSRG(2) level, these differences are acceptable, and the consistency of the two normal ordering approaches is important to establish their correctness in heavy systems.

Finally, in Fig. 5.5, we show charge radii as computed by the IMSRG(2) using the single-particle and Jacobi normal ordering approaches. Charge radii are known to be efficiently captured at the HF level, with only small corrections from the IMSRG(2) or other many-body methods. As an example, at the HF level, $R_{\mathrm{ch}} = 5.14$ fm, which is to be contrasted with the IMSRG(2) prediction of 5.19 fm. It is, therefore, unsurprising to see that R_{ch} converges similarly to E_{HF}, with convergence in the single-particle normal ordering reached around $e_{\mathrm{max}} = 14$, $E_{3\mathrm{max}} = 20$. The Jacobi normal ordering converges nicely to the same result, further demonstrating the consistency of the two approaches.[3]

[3]The HF value of R_{ch} is the same for both normal ordering approaches, so it is only possible for a difference to arise due to

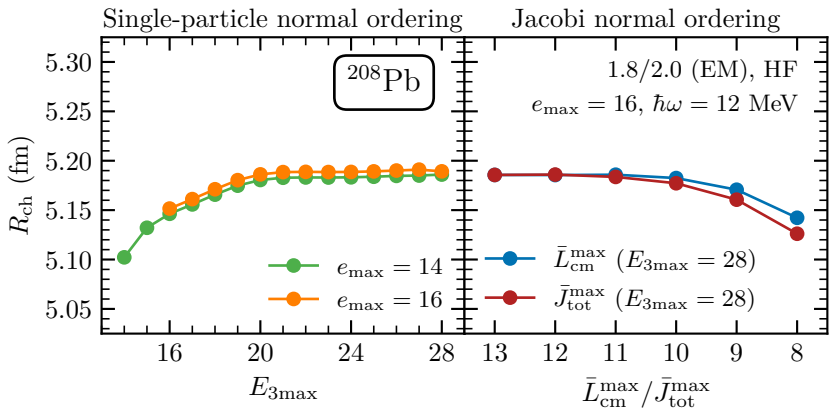

Figure 5.5: IMSRG(2) charge radii for ^{208}Pb. Same as the middle panel of Fig. 5.4 but for the charge radius $R_{\rm ch}$. Figure from Ref. [49].

Overview and perspectives

This discussion of the developments of Ref. [49] establishes normal ordering in a relative basis as a way to converge the contributions of three-body forces in heavy nuclei. We derived the equations to obtain normal-ordered three-body interactions $\Gamma^{\rm 3N}$ in a relative basis and introduced $\bar{J}^{\max}_{\rm tot}$ and $\bar{L}^{\max}_{\rm CM}$ as the relevant key truncations at play in the normal ordering, replacing $E_{3\max}$ in single-particle normal ordering. We demonstrated consistency with traditional single-particle normal ordering, both on the matrix-element level and in many-body calculations in ^{16}O, ^{48}Ca, and ^{78}Ni (where only the latter was discussed in this chapter). In calculations of ^{132}Sn and ^{208}Pb we showed systematic convergence and consistency with the large-$E_{3\max}$ developments by Miyagi *et al.* [46]. These developments together offer a long-term perspective for ab initio studies of heavy nuclei, where further developments on many-body methods and their implementations will be necessary to provide a global ab initio description.

My contributions in Ref. [49] touched the relative normal ordering, the handling of the matrix elements of $\Gamma^{\rm 3N}$, and the inclusion of $\Gamma^{\rm 3N}$ in IMSRG calculations. I worked on the numerical optimization of the normal ordering implementation, which is generally very computationally expensive due to the multidimensional integrals and sums that need to be evaluated. I formally extended the treatment of the density in the normal ordering to allow it to describe systems where only one of two spin-orbit partner orbitals is occupied (for example, ^{24}O where the neutron $1d_{5/2}$ orbital is occupied, but the $1d_{3/2}$ orbital is unoccupied). Additionally, I worked on the approaches used to include $\Gamma^{\rm 3N}$ in IMSRG calculations. I implemented the general two-body transformation to a single-particle basis, accounting for the center-of-mass dependence appropriately. I performed the systematic matrix element benchmarks in ^{16}O and implemented the file formats used to read the matrix elements into IMSRG calculations.

Given the cost of Jacobi normal ordering calculations, it is an important outstanding task to further accelerate the numerical implementation. Still, we expect the Jacobi normal ordering to play the role of an expensive high-fidelity method in cases where the large-$E_{3\max}$ developments of Miyagi *et al.* are insufficient. In such cases, the better infrared and ultraviolet convergence of the Jacobi normal ordering may be important to give converged results. Extensions to more complicated references states [244, 249, 250, 256, 334, 335] or in deformed many-body calculations [251, 252] are also conceivable on the longer term, and it remains to be understood how the $E_{3\max}$ and $\bar{J}^{\max}_{\rm tot}/\bar{L}^{\max}_{\rm CM}$ truncations differ in such applications.

many-body correlations (because of differences in $\Gamma^{\rm 3N}$) on the small corrections computed by the IMSRG(2). With this in mind, the agreement is unremarkable, but of course important to confirm.

Chapter 6

Truncations for the IMSRG from perturbation theory

Despite its efficient computational scaling for medium-mass and heavy nuclei, the IMSRG is still a computationally challenging many-body method, requiring large-scale calculations on supercomputers to solve realistic problems in nuclei. This computational challenge is especially pronounced when considering higher-order many-body truncations like the IMSRG(3) (see Chapter 7) [45], deformed single-particle bases where angular momentum coupling cannot be applied [251, 336], or tensor operators as required to describe electromagnetic transitions [265–267] and complex nuclear responses [268, 275, 337, 338]. To address this, one can make informed truncations to restrict the model-space size required for converged calculations and thus reduce the computational cost of IMSRG calculations.

In this chapter, we discuss two complementary approaches to making informed, controllable truncations in IMSRG calculations leveraging cheap perturbation theory calculations. First, we present the application of the perturbatively improved natural orbital basis in IMSRG calculations, allowing converged calculations in smaller model spaces [106]. Second, we discuss a different approach to performing importance truncation (IT) in IMSRG calculations, demonstrating that for soft Hamiltonians significant truncations are possible without introducing considerable errors in IMSRG predictions [107]. The results discussed in this chapter are published in Refs. [106, 107].

6.1 Natural orbitals

The starting point for many-body calculations of finite nuclei are nuclear Hamiltonian matrix elements in an HO basis. While this generic, system-independent representation is practical as a starting point, the explicit dependence on $\hbar\omega$ means that setting up an efficient reference state $|\Phi\rangle$ requires the optimizing the basis to obtain a better ground-state estimate. This is conventionally done via Hartree-Fock calculations (discussed in Section 3.3), which optimize the hole orbitals for a system of interest to obtain an energetically optimal, frequency independent Slater-determinant reference state. However, the HF basis, despite producing the energetically optimal reference state, is not necessarily the ultimate basis choice, owing primarily to the fact that it does not effectively optimize particle states not occupied in the reference state to efficiently capture interactions relevant to describe the wave function of the system of interest.

In this section, we explore the construction and application of the natural orbital basis in IMSRG calculations. The natural orbitals have a long history of success in quantum chemistry [339–353] and were recently explored in nuclear physics contexts [251, 259, 354–356]. In particular, the success of perturbative natural orbitals and the proliferation of highly optimized localized basis sets in quantum chemistry has

spurred interest in ab initio nuclear theory in developing and employing improved bases in many-body calculations [357–359].

We establish one strategy to establish faster model-space convergence using the natural orbitals. Model-space convergence in many-body calculations is tested by checking the dependence of predicted observables on $\hbar\omega$ and $e_{\max}$. For this reason, in the following sections we focus heavily on discussing the frequency (in)dependence of our results and investigating convergence in $e_{\max}$, ultimately establishing a way to provide $\hbar\omega$- and $e_{\max}$-independent predictions at small model-space truncations, significantly reducing the costs of the IMSRG calculations of the systems considered. This strategy is generically applicable to many-body methods that use an $e_{\max}$-like single-particle truncation to set up their bases for many-body calculations.

6.1.1 Construction

The natural orbital basis is defined as the eigenbasis of the one-body density matrix, with matrix elements given by

$$\rho_{pq} \equiv \frac{\langle\Psi| : a_p^\dagger a_q : |\Psi\rangle}{\langle\Psi|\Psi\rangle}\,, \tag{6.1}$$

where $|\Psi\rangle$ denotes the exact ground state. Instead of employing the exact ground state, which is exponentially expensive to construct, one may construct the density matrix for an approximation of the ground state. The simplest approximation is a single Slater determinant, for example the HF state, giving the density matrix (in its eigenbasis)

$$\rho^{\mathrm{HF}} = \begin{pmatrix} \mathbf{1}_{\mathrm{hh}} & 0 \\ 0 & 0 \end{pmatrix}, \tag{6.2}$$

where $\mathbf{1}_{\mathrm{hh}}$ denotes the identity in the sub-block of hole states.

The full density matrix can be better approximated using perturbation theory, where keeping terms up to second order in the interaction the approximate density matrix becomes

$$\rho^{\mathrm{MP2}} \equiv \rho^{\mathrm{HF}} + \rho^{(02)} + \rho^{(20)} + \rho^{(11)}\,, \tag{6.3}$$

where

$$\rho_{pq}^{(mn)} \equiv \langle\Phi^{(m)}| : a_p^\dagger a_q : |\Phi^{(n)}\rangle \tag{6.4}$$

is the MBPT contribution to the density matrix arising from the bra and ket wave-function corrections at orders m and n, respectively. See Refs. [106, 259] for the full expressions for the contributions to $\rho^{(02)}$, $\rho^{(20)}$, and $\rho^{(11)}$.

Diagonalizing ρ^{MP2} gives the perturbatively improved natural orbital (abbreviated NAT) basis

$$\rho^{\mathrm{MP2}}\,|p\rangle_{\mathrm{NAT}} = n_p^{\mathrm{NAT}}\,|p\rangle_{\mathrm{NAT}}\,, \tag{6.5}$$

with the NAT occupation number n_p^{NAT}. The states $|p\rangle_{\mathrm{NAT}}$ are related to the HF states $|p\rangle_{\mathrm{HF}}$ via a unitary transformation, so it is easy to transform all operators to the NAT basis via the familiar expressions in Sec. 3.3.1. However, since the perturbatively improved state used to construct ρ^{MP2} is not a single Slater determinant, n_p^{NAT} are no longer simply 0 or 1. The NAT construction has included many-body correlations in the density matrix, "smearing out" the Fermi surface of the HF state. Low-lying hole states still have NAT occupations close to 1, and high-lying particle states still have NAT occupations close to 0, but hole and particle states near the Fermi surface have occupation numbers considerably different from 1 and 0,

respectively. This means n_p^{NAT} can tell us something about how strong the many-body correlation effects are for a given state $|p\rangle_{\mathrm{NAT}}$. This metric is used as an organizational principle in IT procedures and in many-body basis constructions, as we discuss later in this chapter.

Once we have obtained the NAT basis by diagonalizing ρ^{MP2}, we want to use it as a starting point for many-body calculations. At this point, a few subtleties come into play. The NAT density is not the density of a Slater determinant, which is the reason why the NAT occupations are smeared out around the Fermi surface. Many many-body methods like the IMSRG expect, however, that the computational basis is the eigenbasis of the density and that the density corresponds to a single Slater determinant, meaning that we have $\rho\,|p\rangle = n_p\,|p\rangle$. This means it is not immediately obvious how to use our NAT basis appropriately when setting up our IMSRG calculations. Here we employ a pragmatic approach, constructing our reference state for IMSRG calculations from the A lowest states in the NAT basis:

$$|\Phi\rangle_{\mathrm{NAT}} = \Big[\prod_{i=1}^{A} a^\dagger_{i,\mathrm{NAT}}\Big]\,|0\rangle\,. \tag{6.6}$$

In Sec. 6.1.2.2, we consider an alternative approach where we construct a mixed basis from the HF and NAT bases and use our HF reference state in that basis, avoiding the need to redefine our reference state.

In the following, we consider two chiral Hamiltonians: the NN+3N N^{3}LO 450 Hamiltonian with the NN potential constructed in Ref. [157] and the consistent 3N potential constructed in Ref. [166]; and the NN+3N 1.8/2.0 (EM) Hamiltonian constructed in Ref. [171]. The unevolved N^{3}LO 450 Hamiltonian is substantially less perturbative than the 1.8/2.0 (EM) Hamiltonian, and this difference allows us to see the sensitivity of our results on the perturbativeness of the employed Hamiltonian.

Constructing the NAT basis for ^{16}O using the N^{3}LO 450 Hamiltonian at $e_{\mathrm{max}} = 10$, we find the desired frequency independence in particle radial wave functions, shown in Fig. 6.1. Of the shown orbitals, only the proton $1p_{3/2}$ is occupied in ^{16}O, and the remaining orbitals are particle states. We see that for the HO basis (left column), all orbitals are manifestly dependent on $\hbar\omega$, as observed by the changing radial wave functions going from $\hbar\omega = 16\,\mathrm{MeV}$ to $\hbar\omega = 36\,\mathrm{MeV}$. In the HF basis (middle column), we see that the $1p_{3/2}$ orbital is optimized such that it is independent of $\hbar\omega$. The weak change for $\hbar\omega = 36\,\mathrm{MeV}$ is an artifact of the $e_{\mathrm{max}} = 10$ truncation together with the suboptimal, large HO frequency leading to significant infrared truncations in the HF calculation. The particle states, however, all show strong $\hbar\omega$ dependence in the radial wave functions, demonstrating that they are not properly optimized by HF. In the NAT basis (right column), one observes substantially reduced frequency dependence in all radial wave functions, demonstrating the successful basis optimization by the NAT construction.

Looking closely, we see that for some frequencies the NAT $2p_{1/2}$ squared radial wavefunctions have three peaks, rather than two as expected from the radial quantum number. This is the NAT basis optimization doing its job: the many-body correlations from the NAT construction tend towards smaller, more compact orbitals, and for smaller HO frequencies (with larger radial extent in coordinate space) the NAT basis is assembled from a linear combination of high n HO orbitals to have larger amplitudes at small r. In this case, the $e_{\mathrm{max}} = 10$ truncation serves to limit the ability of the NAT basis to also optimize the tail of the wave function at large r, causing the visible third maximum.

In Fig. 6.2, we show a similar picture as in Fig. 6.1 for ^{16}O using the 1.8/2.0 (EM) Hamiltonian. The HF basis (left) is really only frequency independent for the proton $1p_{3/2}$ state. The NAT basis constructed in $e_{\mathrm{max}} = 10$ (middle) shows essentially perfect frequency independence for all shown orbitals, with the slight $\hbar\omega$ dependence for the $2p_{1/2}$ orbital being ironed out by employing a larger $e_{\mathrm{max}} = 14$ model space (right). This demonstrates two main features of the NAT construction: first, it is better able to optimize away frequency dependence for softer Hamiltonians (as is reasonable for a perturbative construction); second, it

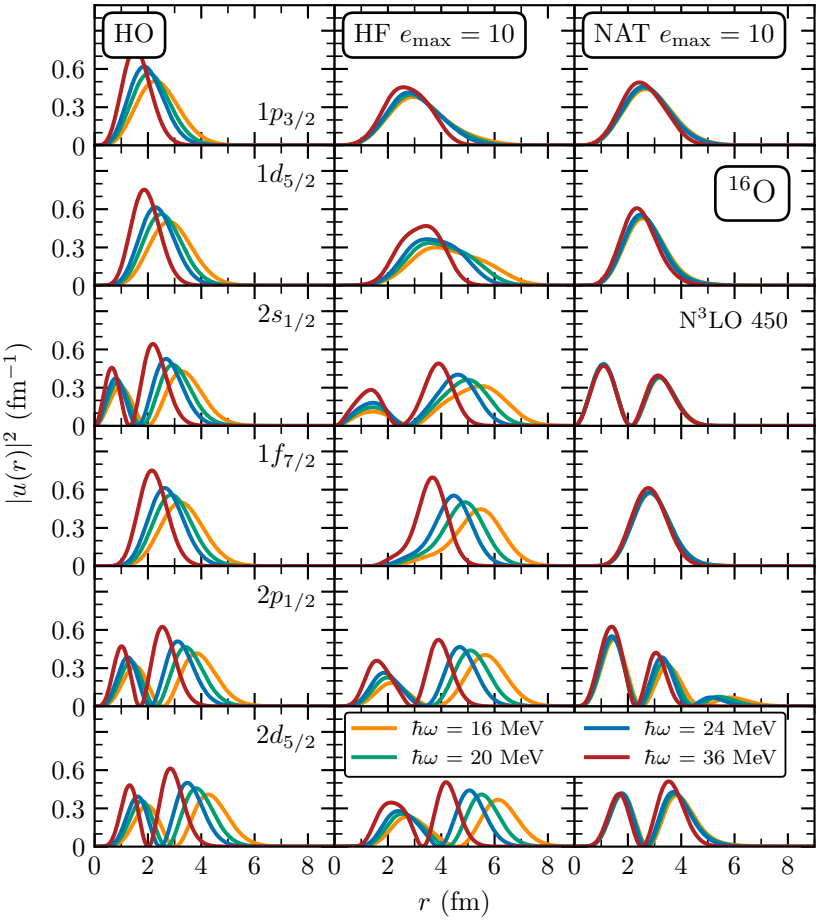

Figure 6.1: HO frequency optimization of the HF and NAT bases. Squared absolute value of the radial wave function $u(r)$ of ^{16}O for different proton orbitals in the HO, HF, and NAT bases in the first, second, and third columns, respectively. We show results for the occupied $1p_{3/2}$ (*first row*) and some of the first unoccupied orbitals (*second through sixth rows*) for the N^{3}LO 450 Hamiltonian at various oscillator frequencies $\hbar\omega$. The HF and NAT orbitals include single-particle HO states up to $e_{\max} = 10$, and three-body forces are truncated at $E_{3\max} = 14$ for the HF and NAT basis constructions. Figure from Ref. [106].

benefits from large model-space truncations to minimize the effects of infrared and ultraviolet cuts in the starting HO matrix elements of the Hamiltonian.

6.1.2 Efficient use in many-body calculations

Applying the HF and NAT bases to IMSRG(2) calculations of ^{40}Ca in Fig. 6.3, we find a somewhat puzzling picture. Despite the optimization of the orbitals, the predictions of ground-state energies and charge radii in the NAT basis do not show reduced frequency dependence or faster $e_{\max}$ convergence compared the predictions in the HF basis. This is particularly surprising as the NAT basis clearly led to substantially faster convergence and reduced frequency dependence in NCSM calculations in Ref. [259].

Understanding this behavior requiries considering how the two main changes induced by using the NAT basis (the new reference state and the unitary transformation of the basis) affect the many-body calculation. From Figs. 6.1 and 6.2, one can see that the occupied orbitals are not significantly changed in the NAT basis, so the NAT reference state is very similar to the HF reference state. This means that the NAT basis

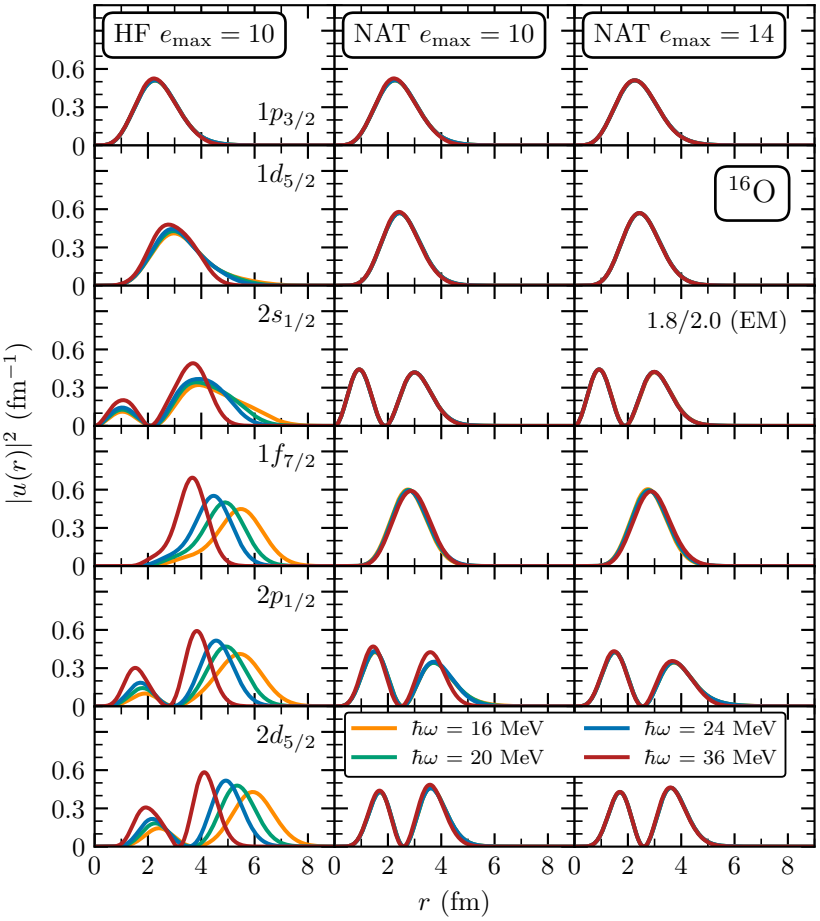

Figure 6.2: HO frequency optimization of the NAT basis in large model spaces. Same as Fig. 6.1 but for the 1.8/2.0 (EM) Hamiltonian showing results for the HF and NAT bases using $e_{\max} = 10$ in the left and middle columns, respectively, as well as $e_{\max} = 14$ for the NAT basis in the right column. Figure from Ref. [106].

construction primarily generates a unitary transformation of the particle states such that the low-lying particle states become frequency independent. The frequency dependence in the basis must go somewhere, and as a result clearly lands in the high-energy highly virtual single-particle states.

Another important realization is that the commutators that are evaluated in the IMSRG (and also CC theory) are invariant under single-particle unitary transformations (assuming that the one-body density is consistently transformed). This means the methods are approximately invariant under unitary transformations of the particle states.[1] As a result, it is unsurprising that IMSRG(2) calculations using HF and NAT bases constructed in the same model space give very similar ground-state energy and charge radius predictions. They both start from a nearly identical reference state, and the unitary transformation of the particle space leaves the working equations of the theory essentially invariant.

Properly benefitting from the NAT basis optimization requires a more clever approach, and we discuss a few strategies developed in this direction in the following sections.

[1] This invariance is only approximate because the definition of the generator η in the IMSRG is *not* fully invariant under unitary transformations.

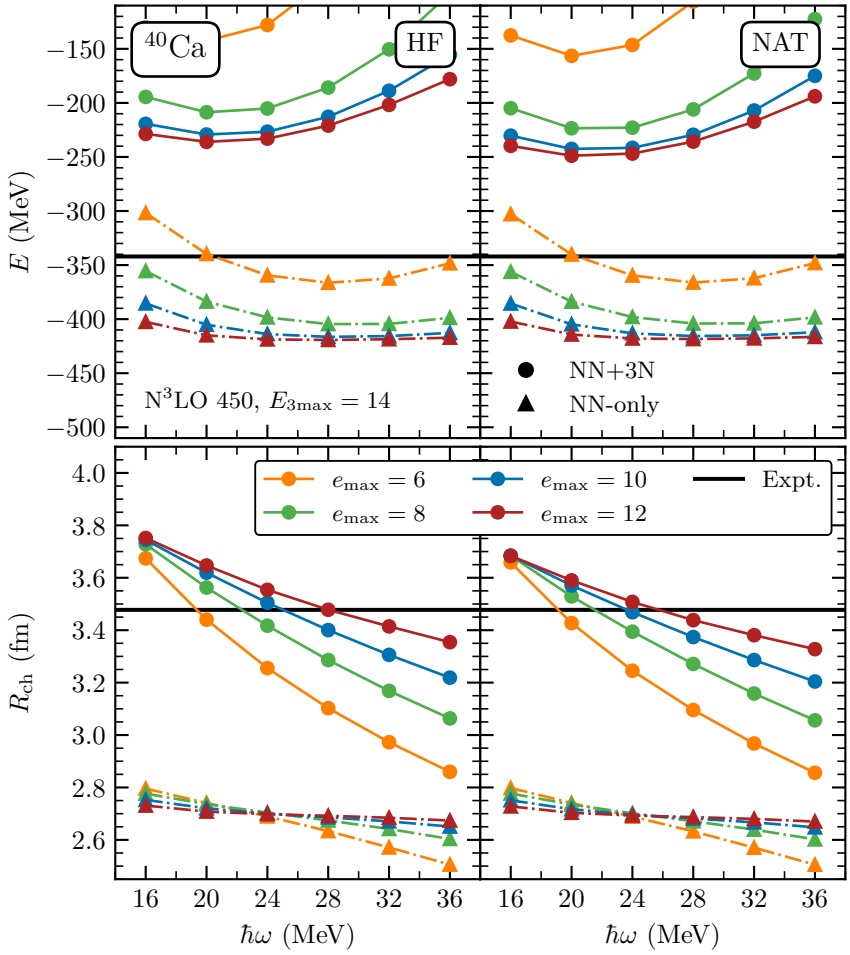

Figure 6.3: Naive application of NAT basis in IMSRG(2) calculations. IMSRG(2) ground-state energies E (*upper row*) and charge radii $R_{\rm ch}$ (*lower row*) of ^{40}Ca as a function of the oscillator frequency $\hbar\omega$ for the NN-only N^{3}LO EMN 450 (*triangles*) and NN+3N N^{3}LO 450 (*circles*) Hamiltonians. We show results for the HF and NAT bases in the left and right panels, respectively, using several single-particle truncations $e_{\rm max}$ with $E_{3\rm max} = 14$. Experimental values from Refs. [360, 361]. Figure from Ref. [106].

6.1.2.1 Basis truncation

The strategy we employ to exploit the NAT basis optimization is hinted at in Fig. 6.2, where going from $e_{\rm max} = 10$ to $e_{\rm max} = 14$ allows the NAT construction to better optimize the low-lying particle space. In very broad terms, the strategy constructs the NAT basis in a large model space $\mathcal{M}_{\rm full}$ before truncating to a small model space $\mathcal{M}_{\rm reduced}$ for the following IMSRG(2) calculation.

Constructing the NAT basis amounts to setting up a basis

$$\{|p\rangle_{\rm NAT} = \sum_{p'} C_{pp'} \, |p'\rangle_{\rm HF} \, , \; p, p' \in \mathcal{M}_{\rm full}\} \tag{6.7}$$

in a given model space $\mathcal{M}_{\rm full}$, for our purposes parametrized by $e_{\rm max}^{\rm HF/NAT}$. For large $e_{\rm max}^{\rm HF/NAT}$, the low-lying $|p\rangle_{\rm NAT}$ are well optimized, in particular including very high radial quantum numbers n in the construction of the radial part of the NAT state wave function. Truncating in the NAT basis after this means keeping a

basis

$$\{|p\rangle_{\mathrm{NAT}} = \sum_{p'} C_{pp'} |p'\rangle_{\mathrm{HF}}\,,\; p \in \mathcal{M}_{\mathrm{reduced}}, p' \in \mathcal{M}_{\mathrm{full}}\} \tag{6.8}$$

in a smaller model space $\mathcal{M}_{\mathrm{reduced}}$ parametrized by e_{max}. In this basis construction, we keep the optimized low-lying NAT states while truncating out highly virtual states that are not optimized by the NAT basis at all.

Intuitively, by constructing the NAT basis in $\mathcal{M}_{\mathrm{full}}$ we are informing the basis construction about very high-energy interactions in the HF basis. However, the low-resolution picture of nuclear many-body physics suggests that interaction effects are dominated by excitations near the Fermi surface, exciting nucleons a few (but certainly not 10) oscillator shells outside the reference state. In the NAT basis, this picture is effectively realized because the particle space is appropriately optimized by the NAT construction. This means that one no longer needs a large model space $\mathcal{M}_{\mathrm{full}}$ to capture high-energy virtual excitations, but a smaller model space $\mathcal{M}_{\mathrm{reduced}}$ will suffice. How small $\mathcal{M}_{\mathrm{reduced}}$ can be depends on the system size, the perturbativeness of the Hamiltonian, and the quality of the basis optimization.

In Figs. 6.4 and 6.5, we explore this strategy in IMSRG(2) calculations using the 1.8/2.0 (EM) Hamiltonian. For the NAT calculations (right panels), we construct the HF and NAT basis in $\mathcal{M}_{\mathrm{full}}$ with $e_{\mathrm{max}}^{\mathrm{HF/NAT}} = 14$ and truncate to $\mathcal{M}_{\mathrm{reduced}}$ with $e_{\mathrm{max}} = 6$, 8, 10, 14 for the IMSRG(2) calculation. The HF-based IMSRG(2) calculations construct the HF basis and perform the IMSRG(2) calculation in the same model space $\mathcal{M}_{\mathrm{reduced}}$.[2]

Ground-state energy and charge radius predictions for ^{40}Ca are shown in Fig. 6.4. Comparing results using the HF and NAT bases, we find reduced frequency dependence at smaller e_{max} truncations. Additionally, the convergence with respect to e_{max} is drastically improved, with the charge radius converged at $e_{\mathrm{max}} = 8$ and the ground-state energy converged at $e_{\mathrm{max}} = 10$. The remaining $\hbar\omega$ dependence is due to the remaining $e_{\mathrm{max}}^{\mathrm{HF/NAT}} = 14$ truncation, also visible in the $e_{\mathrm{max}} = 14$ HF results.

In Fig. 6.5, we see a similar picture for ^{78}Ni. The NAT results are substantially less dependent on $\hbar\omega$, and convergence with respect to e_{max} is also improved. As ^{78}Ni is slightly heavier, $e_{\mathrm{max}} = 10$ is not fully sufficient to converge the ground-state energy to within 1 MeV, but $e_{\mathrm{max}} = 12$ (not shown) is certainly fully converged.

In ^{78}Ni, one also sees that the improved frequency independence and convergence is limited by the $e_{\mathrm{max}}^{\mathrm{HF/NAT}}$ of the HF/NAT basis construction. $e_{\mathrm{max}}^{\mathrm{HF/NAT}} = 14$ is not sufficient to completely avoid infrared and ultraviolet convergence problems for suboptimal $\hbar\omega$, so there is still clear benefit for operating at the "optimal" $\hbar\omega$. Up to $A \sim 100$, this is $\hbar\omega = 16$ MeV for the 1.8/2.0 (EM) Hamiltonian, while for heavier systems this shifts to 14, 12, and 10 MeV.

The strategy outlined here is remarkably successful at accelerating convergence for IMSRG calculations. It is also very straightforward in its application. One simply needs to construct the NAT basis in as large a model space as possible, making the basis and reference state insensitive to the infrared and ultraviolet truncations of the $e_{\mathrm{max}}^{\mathrm{HF/NAT}}$ employed. One can then truncate aggressively in e_{max} and investigate convergence in relatively cheap IMSRG(2) calculations. The reduced e_{max} required is especially valuable for IMSRG(3) calculations, where model-space size causes substantial challenges.

The success of the NAT basis makes it the basis of choice for most applications discussed in this thesis. We routinely construct NAT bases in $e_{\mathrm{max}}^{\mathrm{HF/NAT}} = 16$, where the basis construction is still cheaper than an

[2] Truncating the HF basis using two model spaces $\mathcal{M}_{\mathrm{full}}$ and $\mathcal{M}_{\mathrm{reduced}}$ does not work because the HF basis does not effectively optimize the particle states. This means that the IMSRG(2) must include all states in $\mathcal{M}_{\mathrm{full}}$ to account for highly virtual, but nonnegligible high-energy excitations of nucleons.

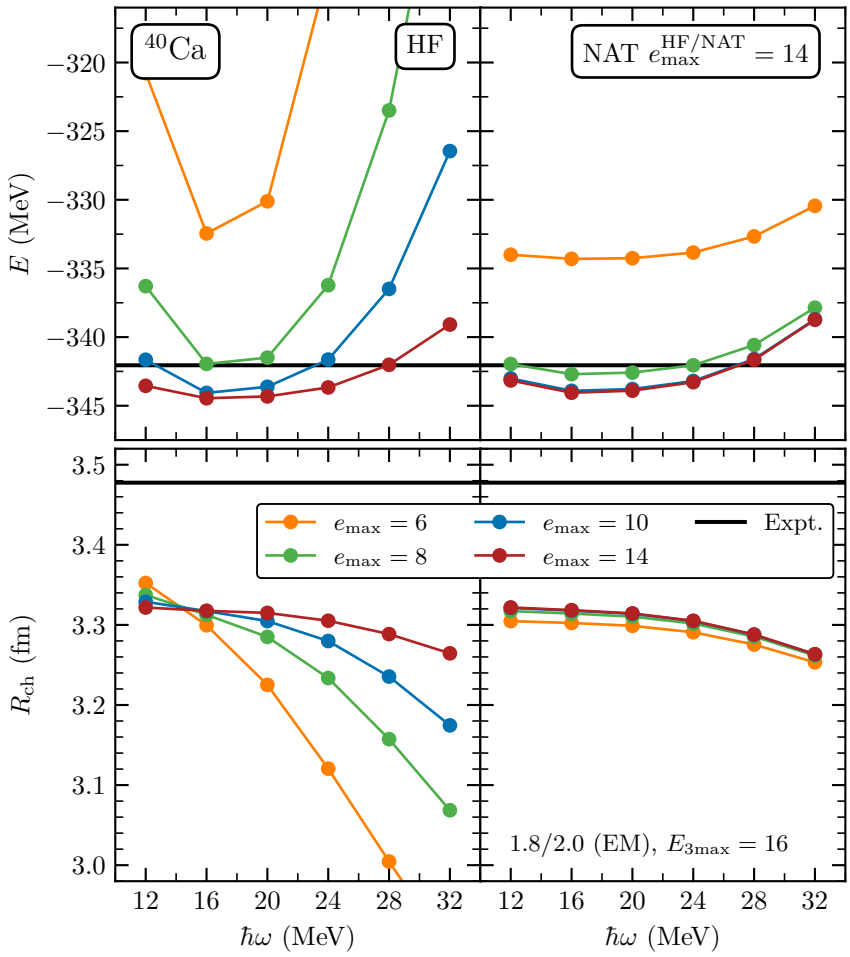

Figure 6.4: Improved convergence of ^{40}Ca using truncated NAT basis. IMSRG(2) ground-state energies E (*upper row*) and charge radii R_{ch} (*lower row*) of ^{40}Ca as a function of the oscillator frequency $\hbar\omega$ in the HF and NAT bases for the 1.8/2.0 (EM) Hamiltonian. We use a model space $\mathcal{M}_{\mathrm{full}}$ with $e_{\max}^{\mathrm{HF/NAT}} = 14$ to construct the NAT basis, whereas the IMSRG calculations are performed for $e_{\max} = 6$, 8, 10, and 14, with $E_{3\max} = 16$ in both cases. Experimental values from Refs. [360, 361]. Figure from Ref. [106].

$e_{\max} = 12$ IMSRG(2) solution. The success of the NAT basis opens up the door to further improved bases that further accelerate $e_{\max}$ convergence for many-body calculations. Until the basis construction becomes more expensive than the untruncated many-body calculation, one profits from this approach in terms of total computational cost.

6.1.2.2 Mixing HF and NAT bases

Despite its clear success, the perturbatively constructed natural orbital basis also has a few challenges. These challenges are related to the fact that the improved density matrix is constructed perturbatively, which makes it cheap to compute, but at the same time fragile when dealing with reference states where perturbation theory breaks down. One case investigated in Ref. [106] is ^{12}C, where the very weak shell closure makes perturbation theory a poor choice to describe the ground state. This leads to among other things unphysical negative NAT occupation numbers n_p^{NAT}, which indicate strong correlations in the relevant orbitals caused by a poor reference state for perturbation theory [106, 347].

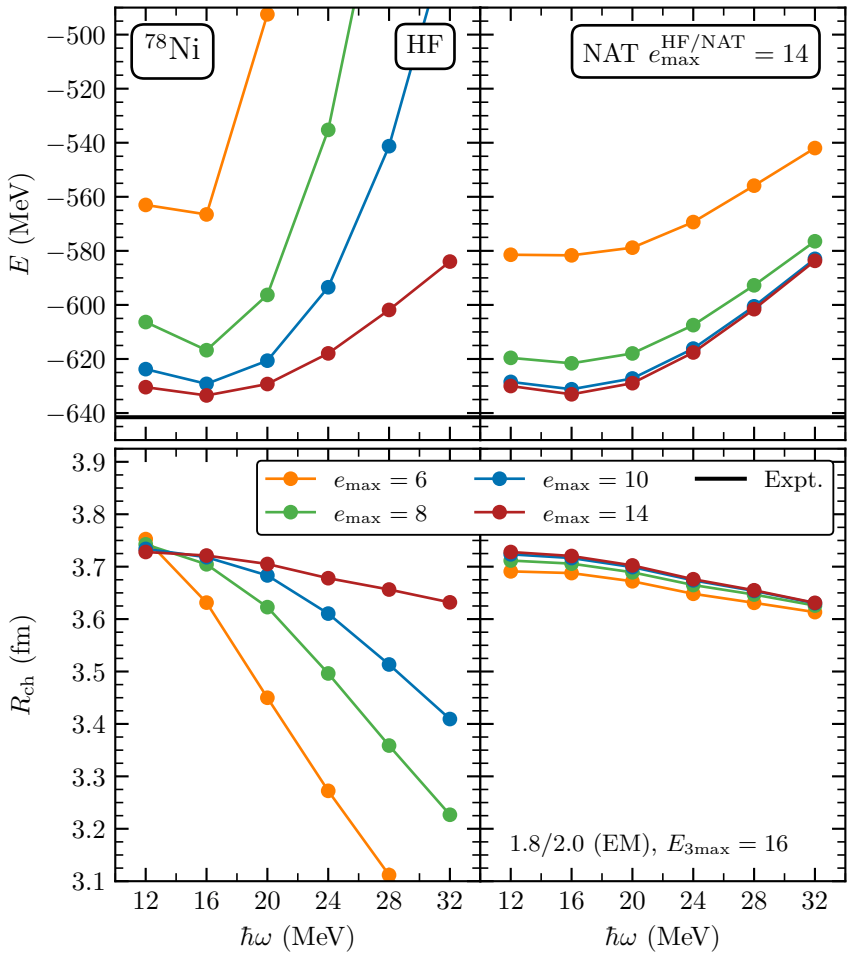

Figure 6.5: Improved convergence of ^{78}Ni using truncated NAT basis. Same as Fig. 6.4 but for ^{78}Ni. Note that the experimental ground-state energy from Ref. [361] is extrapolated. Figure from Ref. [106].

In Chapter 8, we discuss IMSRG(3) calculations of ^{12}C and ^{13}C. As the NAT basis is especially important for model-space convergence in the IMSRG(3), we investigated how to make it usable in ^{12}C. There are two key findings regarding the NAT basis that allow us to improve how we use it in many-body calculations.

The first finding is that the most effective organizational metric for NAT states is $|n_p^{\mathrm{NAT}}|$. When constructing the NAT states $|p\rangle_{\mathrm{NAT}} = |n(ls)jm_t\rangle_{\mathrm{NAT}}$ one must make a choice about quantum number assignments. Specifically, the radial quantum number n is arbitrary, so one must assign an increasing n to each state in the new basis. How to do so is not immediately clear,[3] and past investigations have considered sorting NAT states by n_p^{NAT} and by $\varepsilon_p = f_{pp}$. It was established that sorting by n_p^{NAT} yields more systematic convergence behavior, making it the preferable metric. In complex nonperturbative systems, this is complicated by the appearance of negative NAT occupation numbers for states, which we find are "important" according to their magnitude, not their value. This gives an effective way of organizing the NAT basis even in more challenging cases.

The second finding in ^{12}C is that in nonperturbative cases it is not the basis that breaks down, but

[3] It is clear that the hole states must be sorted below the particle states, which every reasonable scheme accomplishes.

the new reference state constructed in the NAT basis. As a reminder, in NAT calculations we typically construct the reference state $|\Phi\rangle_{\mathrm{NAT}}$ as a Slater determinant of the lowest A states in the NAT basis. In standard cases, this is nearly identical to the HF reference state, so the NAT reference state is comparable. In ^{12}C, this construction breaks down, and the NAT reference state $|\Phi\rangle_{\mathrm{NAT}}$ (even with no model-space truncation) performs substantially worse than the HF reference state. This shows that a considerable part of the problem is the poor reference state from the NAT basis.

This makes it clear that the NAT basis for ^{12}C is optimized in a useful way, but at the same time produces a suboptimal reference state. A hybridization of HF and NAT offers a way forward. We use $|p\rangle_{\mathrm{HF}}$ for all states occupied in the reference state, orthogonalize $|p\rangle_{\mathrm{NAT}}$ for the unoccupied NAT basis with respect to the occupied HF states, and use this orthogonalized NAT basis for the particle states. Specifically, we go through the unoccupied states in order of decreasing $|n_p^{\mathrm{NAT}}|$, and orthogonalize these with respect to the orthogonalized basis $|q\rangle_{\mathrm{HF+NAT}}$, $q < p$, where for the lowest A states we take $|p\rangle_{\mathrm{HF+NAT}} = |p\rangle_{\mathrm{HF}}$.

This solution makes sense because the HF hole states are already optimized (truly optimized to produce the lowest HF energy) and thus frequency independent. The NAT basis is optimized to include many-body correlations in low-lying particle states. Combining the two yields both an energetically optimal reference state and a well optimized low-lying particle state basis, allowing for rapidly converging calculations. This is beneficial for ensuring model-space convergence in challenging systems like ^{12}C. At the same time, as we show in Chapter 8, it does not solve the challenging many-body characteristics of these systems, which might require high-order many-body truncations like the IMSRG(3) to properly address. Still, the hybrid HF+NAT basis addresses a clear weakness of the perturbatively improved NAT basis, making it a valuable improvement in constructing an efficient starting point for many-body calculations.

6.1.2.3 Three-body basis truncations

We have emphasized a few times that the NAT occupation numbers n_p^{NAT}, or more specifically their magnitude $|n_p^{\mathrm{NAT}}|$, give valuable insight into the importance of the associated single-particle state $|p\rangle_{\mathrm{NAT}}$. This allows one to efficiently truncate the single-particle basis, but can also be used to truncate the substantially larger two- and three-body bases employed in many-body calculations.

We focus heavily on two-body truncations in IMSRG(2) calculations in the next section, so here we briefly highlight the optimization of the three-body basis in the context of coupled-cluster calculations. Performing coupled-cluster calculations with three-body operators at the CCSDT-1 level [92, 251, 313, 362] is challenging, and any reduction in the amount of three-body matrix elements that must be computed and stored reduces the cost of these calculations considerably. The three-body cluster amplitudes T_3 are represented in a basis of three-hole ket states and a basis of three-particle bra states: $\langle abc|T_3|ijk\rangle$. Storing all possible amplitudes for a given $e_{\max}$ without truncations is impossible for most nuclei, so the three-body bases are typically truncated. A conventional truncation is the $E_{3\max}$ truncation, giving the three-body basis

$$\{|pqr\rangle\,,\ e_p + e_q + e_r \leq E_{3\max}\}\,. \tag{6.9}$$

When using NAT orbitals, one can also consider guiding the basis construction using the NAT occupation numbers. This was done in Ref. [251], where the three-hole basis

$$\{|ijk\rangle\,,\ \bar{n}_i^{\mathrm{NAT}}\bar{n}_j^{\mathrm{NAT}}\bar{n}_k^{\mathrm{NAT}} \geq \varepsilon_{\mathrm{NAT}}\} \tag{6.10}$$

and the three-particle basis

$$\{\langle abc|\,,\ n_a^{\mathrm{NAT}}n_b^{\mathrm{NAT}}n_c^{\mathrm{NAT}} \geq \varepsilon_{\mathrm{NAT}}\} \tag{6.11}$$

are truncated based on the NAT occupation numbers with $\bar{n}_i^{\mathrm{NAT}} = 1 - n_i^{\mathrm{NAT}}$ and a chosen threshold $\varepsilon_{\mathrm{NAT}}$. This truncation gives greater importance to states with strongly "smeared out" occupation numbers

indicating strong many-body correlations, which tend to be near the Fermi surface. This synergizes nicely with the fact that T_3 is an operator to generate triple excitations around the Fermi surface. This truncation was shown to be substantially more efficient than $E_{3\max}$ and allowed for converged CCSDT-1 calculations in neon and magnesium [251], and it will be an important step for IMSRG(3) developments to exploit a similarly efficient three-body truncation.

6.2 Importance truncation for the IMSRG

The core idea of importance truncation is that making informed selections in setting up theoretical calculations allows one to achieve the same precision as general expansions at substantially reduced cost. This formulation is intentionally vague as importance truncation has been realized in many different ways in many-body calculations.

A classic well-established example is IT in the no-core shell model, yielding the so-called IT-NCSM [330, 363]. In the NCSM, a diagonalization of the many-body Hamiltonian is set up in a basis of Slater-determinant configurations, as discussed in Sec. 3.3.3. Generically, this configuration basis is truncated using an uninformed $N\hbar\omega$ truncation.[4] However, such a configuration basis grows too quickly for converged calculations in medium-light nuclei like ^{16}O, so in IT one subselects only the configurations that are estimated to be most important for the description of the ground-state wave function. Such an estimate is made using perturbation theory and can also be used to assess the uncertainty due to the induced IT error. This approach has been very successful in the NCSM and is routinely used in calculations today.

In this section, we establish the importance-truncated IMSRG (IT-IMSRG), a strategy for importance truncation in the IMSRG [107] focusing on truncating two-body matrix elements, which drive the storage and computational cost of IMSRG(2) calculations. The goals for the IT-IMSRG (or IT in any method) are clear: substantially reduced cost of the problem through informed truncations; systematic convergence towards the untruncated result together with a way to assess the magnitude of the IT error; effectiveness and robustness in a variety of contexts; and clear computational benefits relative to untruncated calculations.

6.2.1 Matrix element truncation

Our approach to IT in the IMSRG is to truncate the matrix elements of two-body operators O_{pqrs}. This can be generalized to three-body matrix elements, which dominate the cost of IMSRG(3) calculations, but in the following we focus on a robust comparison with the untruncated IMSRG(2). We decide for each index combination $pqrs$ whether the matrix element O_{pqrs} is important based on an IT measure, which we discuss later. Generically, this amounts to evaluating an importance $\kappa_{pqrs}(O)$ for each $pqrs$, where larger κ_{pqrs} means "more important." This IT measure produces a "mask" dependent on the IT measure and importance truncation threshold $\kappa_{\min}$:

$$\kappa^{\text{mask}}_{pqrs} = \begin{cases} 1 & \text{if } pqrs \text{ is important (i.e., } \kappa_{pqrs} \geq \kappa_{\min}), \\ 0 & \text{otherwise.} \end{cases} \tag{6.12}$$

Given such a mask, the matrix elements of a two-body operator O_{pqrs} can be split into an important part,

$$O^{\text{imp.}}_{pqrs} = \kappa^{\text{mask}}_{pqrs} O_{pqrs} \,, \tag{6.13}$$

[4] $N_{\max}\hbar\omega$ allows all excited configurations of the reference state $|\Phi\rangle$ that are excited by $N_{\max}$ oscillator shells or less in the harmonic oscillator picture.

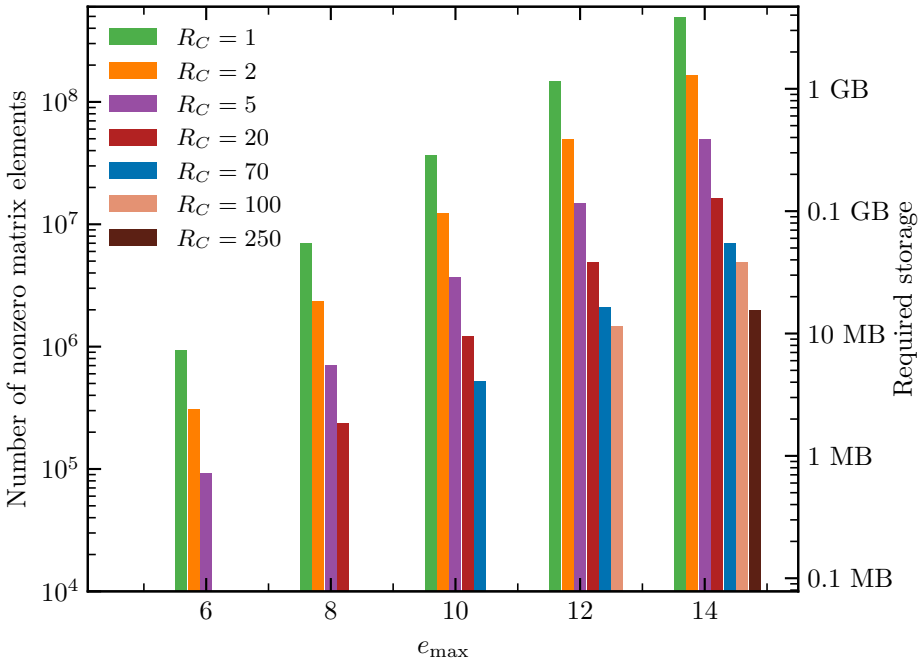

Figure 6.6: Demonstration of possible compression of two-body matrix elements. Total number (*left y axis*) and corresponding storage requirements (*right y axis*) of nonzero two-body matrix elements for different compression ratios R_C for model-space sizes $e_{\max}$. For $R_C = 1$ the number of matrix elements corresponds to the initial Hamiltonian without any IT. Figure from Ref. [107].

and a residual part,

$$O^{\text{res.}}_{pqrs} = (1 - \kappa^{\text{mask}}_{pqrs}) O_{pqrs} \,. \tag{6.14}$$

Keeping only the important part of all two-body matrix elements in the IMSRG amounts to solving the flow equation for only a subset of single-particle index combinations. The residual part may be treated approximately independent of the IT-IMSRG solution. The treatment of the residual part may either be used to correct for the truncation or to quantify the uncertainty due to the IT.

One subtlety here is that the IMSRG commutator may induce non-zero contributions in "unimportant" index combinations. We disregard these contributions and solve the IT-IMSRG flow equations solely for the important part:

$$\frac{dH^{\text{imp.}}}{ds} = [\eta^{\text{imp.}}(s), H^{\text{imp.}}(s)] \,, \tag{6.15}$$

$$\frac{dH^{\text{res.}}}{ds} = 0 \,. \tag{6.16}$$

The benefit of this IT approach is that the IT-IMSRG needs to solve a substantially reduced amount of coupled differential equations based on the IT mask that is determined once at the start of a calculation. This benefit is characterized by a compression ratio,

$$R_C = \frac{\#\text{ of nonzero matrix elements}}{\#\text{ of nonzero matrix elements} - \#\text{ of IT-neglected matrix elements}} \,, \tag{6.17}$$

given by the ratio of the number of initial nonzero two-body matrix elements over the number of remaining nonzero two-body matrix elements after the IT. Truncating no matrix elements yields $R_C = 1$, increasing

with increasing number of matrix elements truncated. This effect is demonstrated in Fig. 6.6 for different model-space sizes. For $e_{\max} = 14$, the standard cost of storing the nearly 500 million two-body matrix elements is approximately 4 GB. Truncating 99% of matrix elements to achieve a compression ratio $R_C = 100$ reduces this cost to around 40 MB. This is less than the storage cost of untruncated $e_{\max} = 8$ two-body matrix elements, and in the following we show that such compression is possible at high accuracy in the IT-IMSRG for soft Hamiltonians.

For our comparisons in the IT-IMSRG(2), we always compare to untruncated IMSRG(2) results, aiming to reproduce these as accurately as possible. Ideally, the IT induces an error that is negligible when compared to Hamiltonian and many-body uncertainties. For the IMSRG(2), the many-body uncertainty on ground-state energies is about 1–2% of the correlation energy E_{corr}. For this reason, acceptable fidelity for the IT-IMSRG(2) would be up to about 0.5% of E_{corr}.

In our work, we found that the IT is especially sensitive to truncating in specific particle-hole blocks of the two-body Hamiltonian. Based on a detailed study of truncations in individual blocks [107, 364], we identified two blocks as being prime candidates for importance truncation: the pppp block with 4-particle interactions, and the hppp (and its Hermitian conjugate pphp) with hole-particle to particle-particle interactions. Truncating in these blocks allows for substantial compression (as the number of particles far exceeds the number of holes) while producing small, controllable IT truncation errors in calculations.

Based on this truncation selection, we introduce a perturbative estimate for the error induced by the IT in the hppp and pppp blocks. The IMSRG(2) is complete up to third order in perturbation theory [94], so we assess the IT error as the MBPT contributions up to third order truncated through the IT. Second order MBPT corrections only depend on the hhpp block and are unaffected by our truncations. The terms that are impacted by our truncation appear at third order. Thus we define our IT error estimate based on the third-order MBPT contributions involving the residual Hamiltonian:

$$E_{\text{IT}}^{(3)} = E_{\text{pp}}^{(3)} + E_{\text{hppp}}^{(3)}\,, \tag{6.18}$$

with the two parts given by

$$E_{\text{pp}}^{(3)} = \frac{1}{8}\sum_{abcdij} \frac{\Gamma_{ijab}\,\Gamma^{\text{res.}}_{abcd}\,\Gamma_{cdij}}{\varepsilon^{ab}_{ij}\varepsilon^{cd}_{ij}}\,, \tag{6.19}$$

$$E_{\text{hppp}}^{(3)} = \frac{1}{2}\sum_{abcij} \frac{\Gamma_{ijab}\,\Gamma^{\text{res.}}_{abcj}\,f_{ci}}{\varepsilon^{ab}_{ij}\varepsilon^{c}_{i}} + \frac{1}{2}\sum_{abcij} \frac{f_{ai}\,\Gamma^{\text{res.}}_{ajcb}\,\Gamma_{cbij}}{\varepsilon^{a}_{i}\varepsilon^{bc}_{ij}}\,, \tag{6.20}$$

where the IT-neglected matrix elements are given by $\Gamma^{\text{res.}}$ as defined in Eq. (6.14) and the matrix elements Γ and f without superscript correspond to the initial two- and one-body contributions of the normal-ordered Hamiltonian.

6.2.1.1 Importance measures

We introduce and explore several importance measures for the IT-IMSRG(2). Our goal is to develop measures that are cheap to construct and allow for robust, systematic compression in both perturbative and nonperturbative contexts.

The simplest measure we consider uses matrix element magnitude as an importance measure:

$$\kappa^{\Gamma}_{pqrs}(\Gamma) = |\Gamma_{pqrs}|\,. \tag{6.21}$$

The intuition for this measure is that large matrix elements produce larger contributions in the IMSRG(2) flow equations and are thus more important to include. It is linear in Γ, with an $\mathcal{O}(N^4)$ cost of construction.

An obvious deficiency of this measure is that it doesn't account for system details (beyond the normal ordering of the 3N interactions).

A more refined version of the κ^{Γ} measure includes information about the single-particle spectrum of the system via the inclusion of MBPT-like energy denominators:

$$\kappa^{\Gamma/\varepsilon}_{pqrs}(\Gamma) = |\Gamma_{pqrs}/\varepsilon_{\text{sum}}| \,. \tag{6.22}$$

The standard MBPT energy denominators involve equal numbers of holes and particles, which is not the case for the pppp and hppp blocks. For this reason, we compute more general MBPT denominators for these blocks, defined as

$$\varepsilon_{\text{sum}} = \begin{cases} 4\varepsilon_{\text{F}} - \varepsilon_{p_1} - \varepsilon_{p_2} - \varepsilon_{p_3} - \varepsilon_{p_4} & \text{for pppp,} \\ 2\varepsilon_{\text{F}} + \varepsilon_{h} - \varepsilon_{p_1} - \varepsilon_{p_2} - \varepsilon_{p_3} & \text{for hppp.} \end{cases} \tag{6.23}$$

Here ε_{F} is the Fermi energy, the energy of the energetically highest-lying hole orbital.[5] The intuition behind the $\kappa^{\Gamma/\varepsilon}$ measure is that matrix elements are enhanced or suppressed in importance depending on where the involved single-particle states lie relative to the Fermi surface. This stems from MBPT, where all interactions come with energy denominators that suppress the contributions of high-energy states far from the Fermi surface. This measure is similar in spirit to MBPT-inspired IT measures in the NCSM [330], Bogoliubov MBPT [331], and Gorkov SCGF [332]. $\kappa^{\Gamma/\varepsilon}$ is linear in Γ, with an $\mathcal{O}(N^4)$ cost of construction.

When using a natural orbital basis, one has access to even more correlation information via the NAT occupation numbers n_p^{NAT}, and it is possible to construct an importance measure based on this information. As a reminder, the NAT occupation numbers indicate strong many-body correlations when n_i^{NAT} is significantly different from 1 for hole states or when n_a^{NAT} is significantly different from 0 for particle states.

The simplest measure we consider using the NAT occupation numbers is based on a product of occupation numbers, also used to truncate the three-body basis in CC calculations [251]:

$$\kappa^{n}_{pqrs} = \prod_{i\in\{p,q,r,s\}} \begin{cases} |n_i^{\text{NAT}}| & \text{if } i \text{ is a particle state,} \\ |1 - n_i^{\text{NAT}}| & \text{if } i \text{ is a hole state.} \end{cases} \tag{6.24}$$

The product is given by the natural orbital occupation numbers for the p, q, r, and s orbitals, with n_a^{NAT} for particle states and $\overline{n}_i^{\text{NAT}} = (1 - n_i^{\text{NAT}})$ for hole states. The intuition behind the κ^n measure is that by considering the product of the relevant hole/particle NAT occupation numbers we give the greatest importance to matrix elements with interactions between strongly correlated states near the Fermi surface and the smallest importance to matrix elements with interactions between weakly correlated states far from the Fermi surface. κ^n is independent of Γ, with an $\mathcal{O}(N^4)$ cost of construction, but implicitly relies on Γ in the construction of the NAT basis. It also cannot be effectively used in HF-based calculations.

Combining κ^n and κ^{Γ} gives a slightly more sophisticated measure that also accounts for "interaction strength" via matrix element magnitude:

$$\kappa^{\Gamma n}_{pqrs}(\Gamma) = |\Gamma_{pqrs}| \times \prod_{i\in\{p,q,r,s\}} \begin{cases} |n_i^{\text{NAT}}| & \text{if } i \text{ is a particle state,} \\ |1 - n_i^{\text{NAT}}| & \text{if } i \text{ is a hole state.} \end{cases} \tag{6.25}$$

This seeks to combine the intuition behind κ^{Γ} and κ^n, sampling important states via the product of NAT occupation numbers while giving especially large importance to large matrix elements that contribute

[5] In general, the Fermi energies for protons and neutrons are different. We tested accounting for this explicitly and simply averaging proton and neutron Fermi energies, and the difference in IT-IMSRG(2) calculations is negligible.

strongly in the IMSRG equations. $\kappa^{\Gamma n}$ is linear in Γ, with an $\mathcal{O}(N^4)$ cost of construction. It also cannot be effectively used in HF-based calculations.

The final measure we consider differs in its construction and motivation from those discusssed above. This measure considers the IMSRG flow equation at $s = 0$ and analyzes the derivative to make an importance assessment:

$$\kappa^{\partial\Gamma}_{pqrs}(\Gamma) = \left|\frac{d\Gamma_{pqrs}}{ds}\right| = \left|\,[\eta, H]^{(2)}_{pqrs}\,\right| . \tag{6.26}$$

The intuition here is that matrix elements with initially large derivatives will change a lot due to the IMSRG solution, making them important to include in the IMSRG calculation. $\kappa^{\partial\Gamma}$ is quadratic in Γ, with an implicit dependence on Γ in η. It also has an $\mathcal{O}(N^6)$ cost of construction, making it considerably more expensive to construct than the other importance measures considered.

6.2.2 Application to nuclei

In the following, we employ the NAT basis (as discussed in the previous section) for all our calculations. We consider two NN+3N chiral Hamiltonians, the 1.8/2.0 (EM) Hamiltonian from Ref. [171] and the N^{3}LO 500 Hamiltonian with NN interactions constructed in Ref. [157] and consistent 3N interactions constructed in Ref. [166]. Furthermore, we consider the SRG evolution of the N^{3}LO 500 Hamiltonian to lower resolution scales λ to investigate the impact of Hamiltonian perturbativeness on our importance truncation. Note that the 1.8/2.0 (EM) Hamiltonian is rather soft while the unevolved N^{3}LO 500 Hamiltonian is fairly hard. In particular, in the model spaces we consider the N^{3}LO 500 Hamiltonian is not fully converged for medium-mass nuclei. However, for our purposes a clean comparison between IT-IMSRG(2) and IMSRG(2) results is still possible.

To understand the various importance measures introduced and select especially promising candidates for further study, we consider IT-IMSRG(2) calculations of ^{40}Ca in Fig. 6.7. For each importance measure, we show the effect of the IT going from no truncation ($R_C = 1$ on the left) to complete truncation of the pppp and hppp blocks ($R_C \sim 60$ on the right for the $e_{\max} = 10$ model space employed).

For the 1.8/2.0 (EM) Hamiltonian (top panel), we observe that fully truncating the pppp and hppp blocks only leads to a relatively small error on E_{corr}. At moderate to low compressions $R_C \sim 10$ all importance measures show systematic convergence towards the untruncated result. Additionally, the error on E_{corr} in this regime is small, less than 0.5% for all measures except for κ^{Γ}. The occupation-number-based measures κ^{n} and $\kappa^{\Gamma n}$ perform remarkably well, with very systematic convergence and small errors out to $R_C \sim 30$. This demonstrates the power of the NAT occupation numbers and the benefit of doing importance truncation when using such perturbative Hamiltonians.

For the N^{3}LO 500 Hamiltonian (bottom panel), we see that the IT produces considerably larger errors. Fully truncating the pppp and hppp blocks induces a nearly 8% error in E_{corr}, corresponding to an over 20 MeV error on the ground-state energy. Again, all measures converge towards the untruncated result systematically. The performance of the NAT-based measures κ^{n} and $\kappa^{\Gamma n}$ at low compressions $R_C \sim 3$–5 leaves much to be desired, with larger than acceptable errors at nearly no compression. At the same time, κ^{Γ} and $\kappa^{\Gamma/\varepsilon}$ perform remarkably well up to moderate compressions, with $\kappa^{\Gamma/\varepsilon}$ inducing only small errors within 0.5% up to $R_C \sim 30$. Such a nonperturbative Hamiltonian is a clear challenge for the IT, especially with its perturbative motivation. Still, some measures are able to perform quite robustly in this context.

For the next investigations, we choose to focus further on $\kappa^{\Gamma n}$ and $\kappa^{\Gamma/\varepsilon}$. $\kappa^{\Gamma n}$ shows remarkable performance for perturbative Hamiltonians, and $\kappa^{\Gamma/\varepsilon}$ performs well in perturbative contexts while also being very robust when using nonperturbative Hamiltonians. We note that while $\kappa^{\partial\Gamma}$ shows similar performance to other measures considered, it is more expensive to construct.

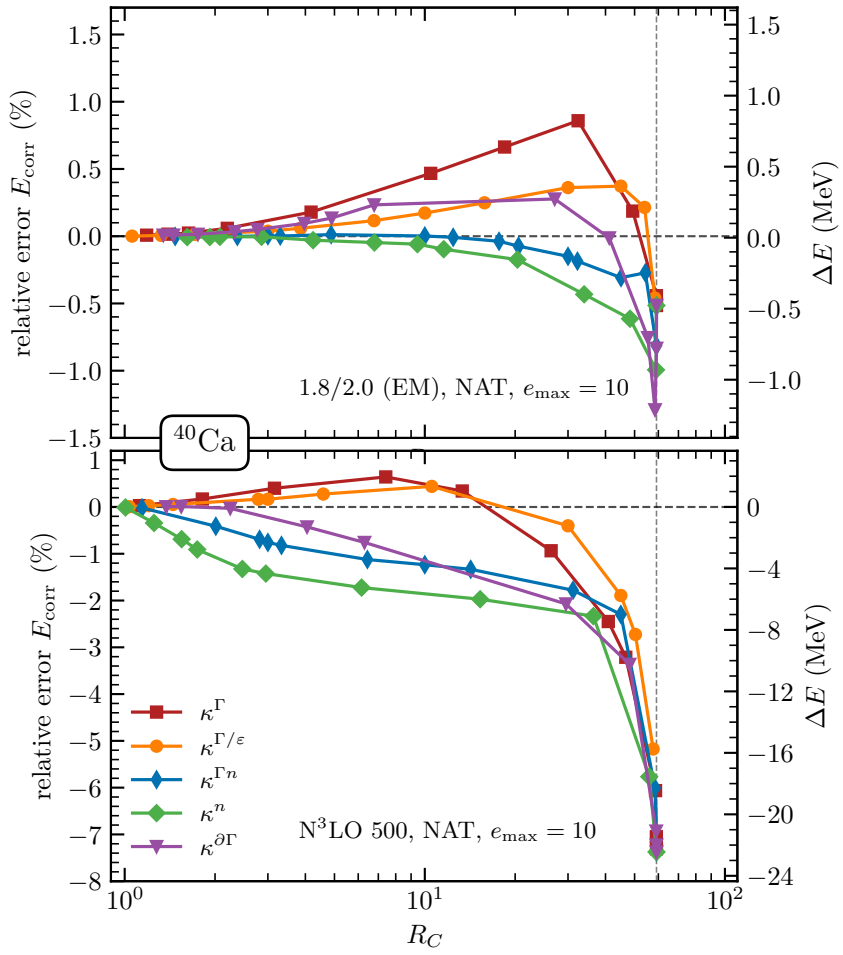

Figure 6.7: Performance of IT measures in IMSRG(2) calculations. Error on the ground-state energy of ^{40}Ca in the NAT basis as a function of compression ratio R_C for IT-IMSRG(2) calculations using five IT measures defined in Eqs. (6.21)–(6.26). In the top panel the 1.8/2.0 (EM) Hamiltonian is used, and in the bottom panel the N^{3}LO 500 Hamiltonian is used. The left y axis indicates the relative error on the correlation energy $E_{\rm corr}$, and the right y axis shows the absolute error on the ground-state energy. All calculations are performed in an $e_{\rm max} = 10$ model space. The dashed vertical line indicates the maximum compression ratio. Figure from Ref. [107].

In Fig. 6.8, we consider IT-IMSRG(2) calculations of ^{40}Ca using the 1.8/2.0 (EM) Hamiltonian and the $\kappa^{\Gamma n}$ and $\kappa^{\Gamma/\varepsilon}$ importance measures. We consider three model-space sizes, $e_{\rm max} = 6$, 10, and 14, and find that the greatest benefit in terms of possible compression comes in larger model spaces. For $e_{\rm max} = 6$, one finds that only mild compression is possible at all, making it unattractive for importance truncation. On the other hand, for $e_{\rm max} = 14$ one finds that both measures can reach $R_C = 100$ without inducing substantial errors. Given the fact that ^{40}Ca can be converged at $e_{\rm max} = 10$ in the NAT basis (see previous section), this makes sense. By going to larger model spaces, we are including many new matrix elements that are all unimportant for convergence, so an effective importance truncation approach should truncate essentially all of these matrix elements between $e_{\rm max} = 10$ and 14, giving much larger compression.

In Fig. 6.8, we also show the perturbative estimate of the IT error introduced in Eq. (6.18) as a band. While the IT error is only shown in one direction (based on the sign of the MBPT correction), it can be interpreted as the size of our IT uncertainty. With this in mind, we observe that the perturbative estimate gives an appropriate magnitude for the IT error when compared to the actual error to the untruncated

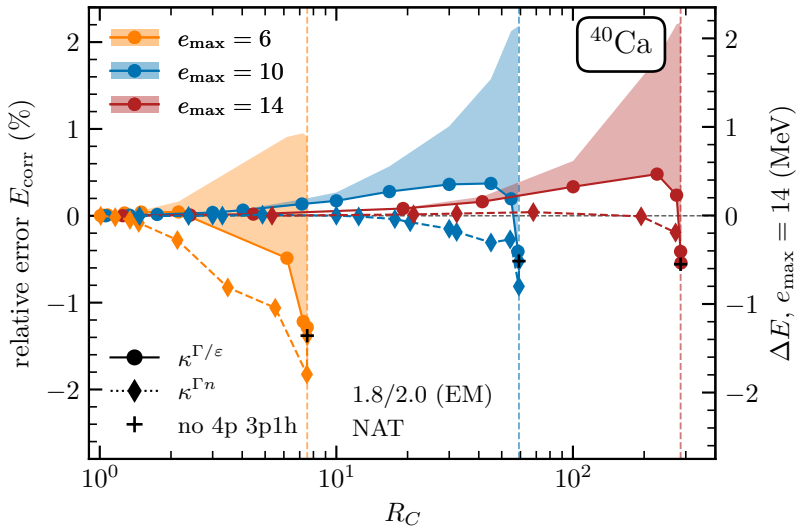

Figure 6.8: Compression in large model spaces using the 1.8/2.0 (EM) Hamiltonian. Relative IT-IMSRG(2) error on the correlation energy $E_{\rm corr}$ of ^{40}Ca in the NAT basis using the 1.8/2.0 (EM) Hamiltonian as a function of the compression ratio R_C for the model-space sizes $e_{\max} = 6$, 10, and 14. We show results for the IT measures $\kappa^{\Gamma/\varepsilon}$ (*circles*) and $\kappa^{\Gamma n}$ (*diamonds*). The right y axis indicates the absolute difference between the $e_{\max} = 14$ IT-IMSRG(2) results and the exact IMSRG(2) result. The MP3 energy correction for the $\kappa^{\Gamma/\varepsilon}$ IT-neglected contributions is indicated by the corresponding band for each model-space truncation and the vertical dashed lines correspond to the maximum R_C for the given model space. Figure from Ref. [107].

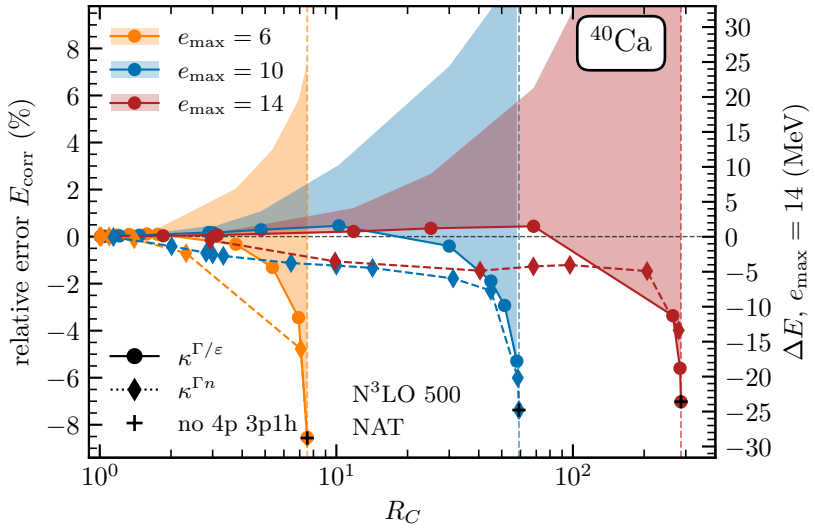

Figure 6.9: Compression in large model spaces using the N^{3}LO 500 Hamiltonian. Same as Fig. 6.8 but for the N^{3}LO 500 Hamiltonian. Figure from Ref. [107].

IMSRG(2) results. Only for the very largest compressions does the uncertainty estimate substantially overestimate the observed error.

In Fig. 6.9, we see a similar picture for IT-IMSRG(2) calculations of ^{40}Ca for the harder N^{3}LO 500 Hamiltonian. Substantial compressions are achievable in an $e_{\max} = 14$ model space, especially when using the $\kappa^{\Gamma/\varepsilon}$ measure. We find that this measure can also achieve sub-0.5% errors on $E_{\rm corr}$ at $R_C \sim 100$ in

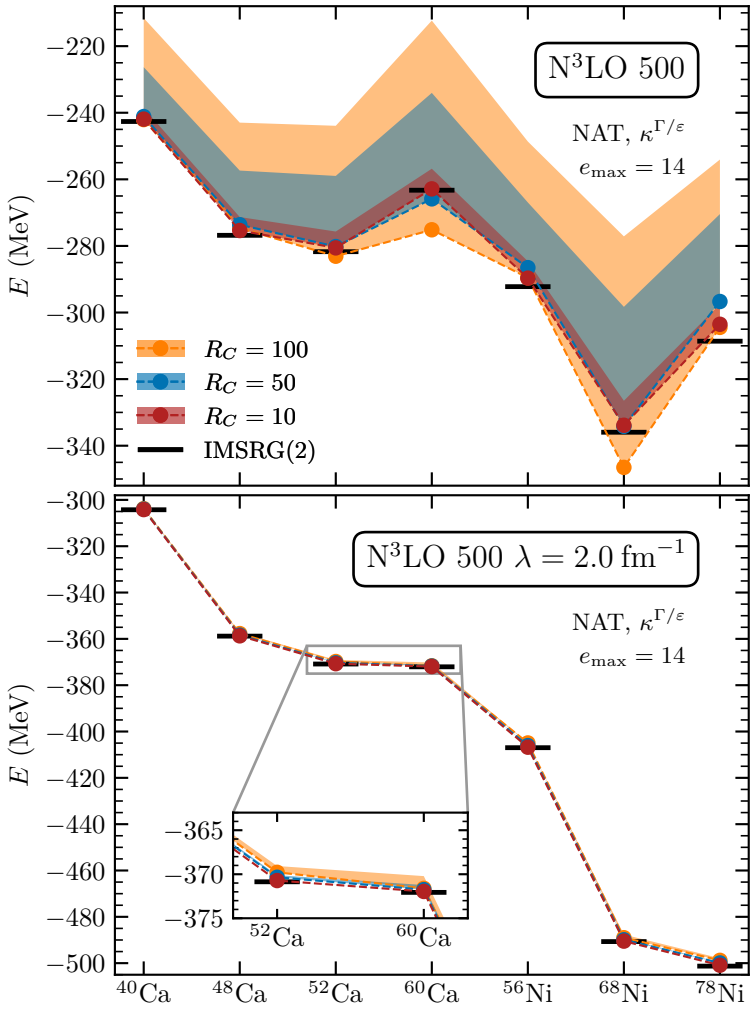

Figure 6.10: IT-IMSRG(2) for calcium and nickel isotopes. Ground-state energies E for selected calcium and nickel nuclei in the IT-IMSRG with compression ratios $R_C = 10$, 50, and 100 for the measure $\kappa^{\Gamma/\varepsilon}$. Results are shown for the NAT basis and the unevolved N^{3}LO 500 Hamiltonian (*top*) and SRG-evolved N^{3}LO 500 $\lambda = 2.0$ fm^{-1} Hamiltonian (*bottom*) in $e_{\max} = 14$ model spaces. Figure from Ref. [107].

$e_{\max} = 14$. On the other hand, the perturbative IT error estimate clearly overestimates the actual error for moderate compression ratios. We understand this to be an artifact of the perturbative construction combined with the use of a relatively hard Hamiltonian in this case. We emphasize also that even though the $\kappa^{\Gamma n}$ measure does not introduce merely negligible IT errors in this case, it still performs very robustly remaining within 2% of the IMSRG(2) E_{corr}. In general, our perturbatively inspired IT measures perform very well for soft Hamiltonians and moderately well at intermediate compressions for hard Hamiltonians.

In Fig. 6.10, we turn our attention to binding energies of heavier systems from ^{40}Ca to ^{78}Ni using the unevolved N^{3}LO 500 Hamiltonian (top panel) and the N^{3}LO 500 Hamiltonian SRG evolved to $\lambda = 2.0\,\text{fm}^{-1}$ (bottom panel). We use an $e_{\max} = 14$ model space and the $\kappa^{\Gamma/\varepsilon}$ IT measure, which shows balanced performance for harder and softer Hamiltonians. For the unevolved N^{3}LO 500 Hamiltonian, we find that $R_C = 10$ and 50 give reasonably small IT errors in calcium isotopes (albeit with substantially overestimated IT uncertainties indicated by the bands). For the nickel isotopes, $R_C = 100$ induces large, but still relatively reasonable IT errors. These results would not be acceptable for a quantitative description of the nuclei

involved, but still demonstrate the robustness of our approach when performing extreme truncations.

Using the SRG-evolved N^{3}LO 500 $\lambda = 2.0\,\mathrm{fm}^{-1}$ Hamiltonian, we find that the IT-IMSRG(2) performs remarkably well across all systems. Even strong truncations yielding $R_C = 100$ produce negligible IT errors for the IT-IMSRG(2) binding energies, and the uncertainties assessed by our perturbative IT error estimate are small and consistent with the observed differences to exact IMSRG(2) results. This establishes the IT-IMSRG(2) as a robust way to deliver quantitative descriptions of nuclei for soft Hamiltonians at high compressions.

6.2.3 Computational considerations

The possible compression demonstrated in the IT-IMSRG(2) is very promising, but ultimately one must also demonstrate computational benefits. In Ref. [107], we implemented the importance truncation within a dense IMSRG(2) solver [365], not exploiting the resulting sparsity but using the implementation to test the importance truncation. This means that the IT mask was constructed and applied as in Eq. (6.13) to maintain the importance truncation in the IMSRG(2) solver.

An ideal IT-IMSRG(2) implementation would fully leverage the sparsity of the importance-truncated two-body matrix elements to reduce the storage cost of the two-body operators and at the same time more efficiently solve the IT-IMSRG(2) flow equations using these matrix elements. While likely possible, we have not achieved such an implementation so far. In the following, we discuss a few strategies explored in Ref. [107] and unpublished explorations afterwards, highlighting the challenges we encountered with the sparse implementation.

In Ref. [107], we investigated replacing the dense matrix storage in our IT-IMSRG(2) solver with sparse matrices in the compressed sparse column (CSC) format [366, 367]. In the IMSRG(2), there are two terms that dominate the cost, the two-body particle-particle term, which looks like

$$C^{\mathrm{pp}}_{1234} = \frac{1}{2}\sum_{pq} \bar{n}_p \bar{n}_q \left(A_{12pq}B_{pq34} - B_{12pq}A_{pq34}\right), \tag{6.27}$$

and the two-body particle-hole term, which looks like

$$C^{\mathrm{ph}}_{1234} = 4\sum_{pq} (n_p \bar{n}_q - \bar{n}_p n_q) A_{p23q}B_{1qp4}\,. \tag{6.28}$$

Equation (6.27) scales like $\mathcal{O}(N^6)$, but is generally very efficiently computed as a matrix product. Equation (6.28) scales like $\mathcal{O}(N^5 A)$, but is much more challenging to optimally implement due to the splitting of the p and q indices onto the bra and ket sides of the two-body matrix elements.

We found that switching to a CSC sparse-matrix storage yielded immediate substantial speedups for the particle-particle term. However, the particle-hole term was slowed down considerably from its dense implementation. This performance change (and the general challenge of a sparse IT-IMSRG implementation) can be understood in terms of sparse-matrix formats and their computational features. The CSC format is optimized for efficient sparse matrix multiplication, naturally giving speedups in the particle-particle term. The tradeoff here is that the CSC format is not optimized for single matrix element access, or "random access," making such random accesses very slow in comparison. The problem is that the natural implementation of the particle-hole term is exclusively random accesses, meaning that using the CSC format leads to a computational slowdown despite needing to work with substantially fewer matrix elements.

There are of course sparse formats optimized for random access [for example, the dictionary of keys (DOK) format]. These are in turn not very efficient for matrix multiplication, which benefits very strongly

from "in-order" access in the CSC format. This "in-order" access is not possible for the DOK format because of how the dictionary behind the efficient random access works.

In the time since the publication of Ref. [107], we explored the development of sparse formats tailored to the problems in the IT-IMSRG(2). While the format is beyond the scope of this thesis, it is essentially a redundant hybrid between the CSC and DOK formats. The organizational scheme of the CSC format is used to store matrix elements in order and to provide fast matrix optimization, but an additional dictionary is provided to allow $\mathcal{O}(1)$ random matrix element access to facilitate the implementation of the particle-hole term. Implementing the IT-IMSRG(2) in this framework, we found at $e_{\max} = 14$ that our implementation begins to outperform the dense IMSRG(2) at a compression ratio $R_C \sim 40$ and a factor of 4 speed-up is achieved by $R_C \sim 200$.

While a nice demonstration of the possible computational gains, such speed-up numbers are still not sufficient to motivate a universal switch to the IT-IMSRG(2). The challenge here is that optimal algorithms for sparse tensor contractions (which would be the backbone of the IT-IMSRG) are much less well studied than dense tensor contraction algorithms. Tackling this problem will require targeted collaboration with supercomputing experts and computer scientists. Ultimately, there is a tradeoff to be made between truncations and optimizations that fit into the dense tensor contraction paradigm of many-body calculations (like the NAT truncation strategy introduced in the previous section) and the development of new specialized implementations and truncations requiring considerable redevelopment.

Overview and perspectives

This discussion of the developments of Refs. [106, 107] establishes complementary strategies to reduce the costs of IMSRG(2) calculations via informed truncations. The NAT basis provides an optimized single-particle basis informed about the structure of many-body correlations via perturbation theory. Importantly, this optimization brings most relevant many-body physics into low-lying states near the Fermi surface. This allows for the optimized basis to deliver fast convergence in $e_{\max}$, allowing IMSRG(2) calculations in smaller $e_{\max}$ to deliver converged results. This improved convergence combined with strategies to combine the NAT and HF bases make the natural orbitals a very powerful tool to accelerate many-body calculations.

The NAT basis and perturbative tools may also be used for importance truncation in two-body matrix elements in the IMSRG(2). We have established the IT-IMSRG(2) using various importance measures as a way to significantly compress IMSRG(2) calculations to use much less memory. This is the most powerful for soft Hamiltonians in large model spaces, but we saw compression potential even for harder Hamiltonians in heavy systems. There is still outstanding work to be done on this end to effectively leverage this compression in many-body calculations, but a systematic understanding of how to set up the importance truncation has now been formed.

My contributions to Refs. [106, 107] touched the basis truncation in the NAT basis, the computational development of the importance truncation, and the formal development and interpretation of the importance measures. I worked on the computational setup using a reduced model space for the IMSRG(2) solution, implementing the two model-space strategy established in Ref. [106]. In later applications using the NAT basis, I developed and tested the improved ordering of the NAT basis and the combination of the HF reference state with the NAT particle orbitals required for IMSRG(2) and IMSRG(3) calculations of ^{12}C. The IT-IMSRG(2) was first developed in my IMSRG(2) implementation before being transfered to the established IMSRG++ code [365]. I worked on the development and refinement of the importance measures in the IT-IMSRG(2), in particular $\kappa^{\Gamma/\varepsilon}$. I also performed substantial explorations of the truncations presented in this chapter working towards IMSRG(3) developments, where such truncations are essential to reducing the computational cost, including the development of a completely new sparse IT-IMSRG(2) solver that

successfully offered (modest) performance benefits relative to the untruncated IMSRG(2) in the IMSRG++ solver.

The success of the NAT basis is very promising for nuclear many-body theory. The perspective that with an optimized basis one is able to quickly converge many-body calculations opens up medium-mass nuclei to more comprehensive studies and enables well-converged calculations in heavy nuclei. There is still certainly room for further basis optimization, making the NAT basis less sensitive to perturbation theory challenges or just employing even further optimized bases as is done in quantum chemistry, and the strategies developed for combining hole orbitals from the HF basis with optimized single-particle bases offer a clear strategy to optimize the basis for many-body calculations without obvious compromises. The perspectives for importance truncation in the IMSRG are more open. It is an important task to establish a computational approach able to benefit from moderate compression such that the IT-IMSRG(2) offers considerable benefits over the untruncated IMSRG(2). This will require collaboration between physicists and computer scientists to develop strategies to efficiently evaluate sparse tensor contractions. At the same time, there is still room to improve the importance measures presented, making them more robust in nonperturbative contexts and making better estimates of the IT error with hard Hamiltonians.

Chapter 7

IMSRG(3)

The extension of the IMSRG to the next order, the IMSRG(3), is a milestone for the method and for nuclear structure theory as a whole. IMSRG(3) calculations provide a more precise many-body description of nuclei, important for the quantitative reproduction of certain observables. Moreover, the comparison of IMSRG(2) and IMSRG(3) results allows for the robust assessment of many-body uncertainties in calculations, which so far has mostly been accomplished via comparisons between predictions by complementary methods as discussed in Sections 3.5 and 4.7.

In this chapter, we develop the IMSRG(3). We explore the precision and the many-body uncertainty of the method in restricted model spaces where comparisons with exact results are available, and we outline a path to realistic IMSRG(3) calculations of medium-mass nuclei.

For the developments in this chapter, the initial computational developments and angular momentum coupling were completed in my Master's thesis [368], while the corrected derviation of the IMSRG(3) (see Appendix B), the approximations of the IMSRG(3) based on perturbative and computational arguments (discussed in Sections 7.2 and 7.3), and the exploration of these developments in nuclei also based on further computational developments (discussed in Sections 7.4 and 7.5) were completed in my doctoral studies. The work presented in Sections 7.2–7.4 is published in Ref. [45].

7.1 Formalism

The IMSRG(3) includes up to normal-ordered three-body parts in the Hamiltonian

$$H(s) = E(s) + f(s) + \Gamma(s) + W(s)\,, \tag{7.1}$$

the generator

$$\eta(s) = \eta^{(1\mathrm{B})}(s) + \eta^{(2\mathrm{B})}(s) + \eta^{(3\mathrm{B})}(s)\,, \tag{7.2}$$

the Magnus operator

$$\Omega(s) = \Omega^{(1\mathrm{B})}(s) + \Omega^{(2\mathrm{B})}(s) + \Omega^{(3\mathrm{B})}(s)\,, \tag{7.3}$$

and any other operators O

$$O(s) = O^{(0\mathrm{B})}(s) + O^{(1\mathrm{B})}(s) + O^{(2\mathrm{B})}(s) + O^{(3\mathrm{B})}(s) \tag{7.4}$$

in the IMSRG flow equations

$$\frac{dH(s)}{ds} = [\eta(s), H(s)]\,, \tag{7.5}$$

$$\frac{dO(s)}{ds} = [\eta(s), O(s)] \tag{7.6}$$

or in the Magnus approach

$$H(s) = e^{\Omega(s)} H e^{\Omega^\dagger(s)}\,, \tag{7.7}$$
$$O(s) = e^{\Omega(s)} O e^{\Omega^\dagger(s)}\,. \tag{7.8}$$

This complete nonperturbative treatment of three-body operators in the IMSRG(3) distinguish it from perturbative three-body treatments as for example in Λ-CCSD(T) [92, 317–319].

Conceptually and formally, this step is simple. All commutator evaluations now involve up to three-body operators, so the general commutator one must evaluate is

$$C = [A, B]\,, \tag{7.9}$$
$$C^{(0\mathrm{B})} + C^{(1\mathrm{B})} + C^{(2\mathrm{B})} + C^{(3\mathrm{B})} = [A^{(1\mathrm{B})} + A^{(2\mathrm{B})} + A^{(3\mathrm{B})}, B^{(1\mathrm{B})} + B^{(2\mathrm{B})} + B^{(3\mathrm{B})}]\,. \tag{7.10}$$

This product must be normal ordered, which we have done both by hand and using automated normal ordering tools [233]. Once this is done, one has derived all that is necessary for IMSRG(3) calculations. Note that the commutator in Eq. (7.10) is truncated, as $[A^{(3\mathrm{B})}, B^{(3\mathrm{B})}]$ has in general up to five-body parts.

It is convenient to break Eq. (7.10) into fundamental commutators $[K, L] \to M$, isolating individual commutator contributions

$$C^{(M\mathrm{B})} = [A^{(K\mathrm{B})}, B^{(L\mathrm{B})}]^{(M\mathrm{B})}\,, \tag{7.11}$$

as introduced in Section 4.2 and Appendix B. The IMSRG(3) includes 10 new fundamental commutators in addition to those included in the IMSRG(2), given in Table 7.2.[1] These fundamental commutators scale computationally as $\mathcal{O}(N^{K+L+M})$, from $\mathcal{O}(N^6)$ to $\mathcal{O}(N^9)$. This makes the IMSRG(3), despite its formal simplicity, an immense computational challenge, one that we address in various ways in this thesis.

7.2 Perturbative analysis

A great benefit of the generic nonperturbative expansion of the IMSRG and similar methods in many-body operators is the model independence of the approach combined with its rapid convergence for many observables. At the same time, this has the drawback that the relevant many-body physics (connecting to, for example, more traditional phenomenological intuition) is often not clear, and understanding this requires considerable formal analysis work.

A framework that has proven successful for the IMSRG is the perturbative analysis of the IMSRG flow equations [94, 280]. This connects the IMSRG with MBPT, making the perturbative content of the method clear. At the same time, it is possible to consider also nonperturbative many-body effects and identify them in the method. We focus on using the perturbative analysis to understand the importance of individual fundamental commutators in the IMSRG, which informs additional approximations of the IMSRG(3) that we explore in Section 7.3.

The intuitive understanding of the perturbative analysis is very clear when using the White generator

[1] Recall that $[L, K] \to M$ is simply $-1\times[K, L] \to M$, so one only needs to consider $K \leq L$ for a complete set of fundamental commutators.

in the IMSRG,

$$\eta_{ia} = \frac{f_{ia}}{\Delta_{ia}^{(1B)}}\,, \tag{7.12}$$

$$\eta_{ijab} = \frac{\Gamma_{ijab}}{\Delta_{ijab}^{(2B)}}\,, \tag{7.13}$$

$$\eta_{ijkabc} = \frac{W_{ijkabc}}{\Delta_{ijkabc}^{(3B)}}\,, \tag{7.14}$$

with Møller-Plesset energy denominators as defined in Eq. (4.32) and the following.

We focus on the case where we use an HF reference state and work in the NO2B approximation, where the initial off-diagonal matrix elements of f and all the initial matrix elements of W are 0. Working with a Møller-Plesset MBPT partitioning of the initial Hamiltonian,

$$H = f + g\,\Gamma\,, \tag{7.15}$$

we have the following power-counting scheme:

$$f_{pp} = \mathcal{O}(g^0)\,, \tag{7.16}$$

$$\Gamma_{pqrs} = \mathcal{O}(g^1)\,, \tag{7.17}$$

that is, the diagonal one-body matrix elements are $\mathcal{O}(g^0)$ and the two-body matrix elements are $\mathcal{O}(g^1)$.

Looking at the IMSRG flow equations, the zero-body part (up to the three-body level) has three contributions from the $[1,1] \to 0$, $[2,2] \to 0$, and $[3,3] \to 0$ commutators,

$$\begin{aligned}\left(\frac{dE}{ds}\right)_{110} &= \sum_{ia} \left(\eta_{ia}(s) f_{ai}(s) - \eta_{ai}(s) f_{ia}(s)\right) \\ &= 2\sum_{ia} \eta_{ia}(s) f_{ai}(s) = 2\sum_{ia} \frac{f_{ia}(s) f_{ai}(s)}{\Delta_{ia}^{(1B)}(s)}\,,\end{aligned} \tag{7.18}$$

$$\begin{aligned}\left(\frac{dE}{ds}\right)_{220} &= \frac{1}{2}\sum_{ijab} \eta_{ijab}(s)\Gamma_{abij}(s) \\ &= \frac{1}{2}\sum_{ijab} \frac{\Gamma_{ijab}(s)\Gamma_{abij}(s)}{\Delta_{ijab}^{(2B)}(s)}\,,\end{aligned} \tag{7.19}$$

$$\begin{aligned}\left(\frac{dE}{ds}\right)_{330} &= \frac{1}{18}\sum_{ijkabc} \eta_{ijkabc}(s) W_{abcijk}(s) \\ &= \frac{1}{18}\sum_{ijkabc} \frac{W_{ijkabc}(s) W_{abcijk}(s)}{\Delta_{ijkabc}^{(3B)}(s)}\,,\end{aligned} \tag{7.20}$$

which look remarkably similar to the second-order MBPT corrections to the energy. Indeed, if one approximates the hole-particle block matrix elements $f_{ia}(s)$, $\Gamma_{ijab}(s)$, and $W_{ijkabc}(s)$ by their basic suppression behavior due to the White generator [94],

$$f_{ia}(s) \approx f_{ia}(s=0)\exp(-s)\,, \tag{7.21}$$

$$\Gamma_{ijab}(s) \approx \Gamma_{ijab}(s=0)\exp(-s)\,, \tag{7.22}$$

$$W_{ijkabc}(s) \approx W_{ijkabc}(s=0)\exp(-s)\,, \tag{7.23}$$

and one approximates the energy denominators by their initial values, then Eqs. (7.18)–(7.20) can be analytically integrated to get the results

$$E(s\to\infty)_{110} \approx \sum_{ia} \frac{f_{ia}(s=0)f_{ai}(s=0)}{\Delta_{ia}^{(1\mathrm{B})}(s=0)}\,, \tag{7.24}$$

$$E(s\to\infty)_{220} \approx \frac{1}{4}\sum_{ijab} \frac{\Gamma_{ijab}(s=0)\Gamma_{abij}(s=0)}{\Delta_{ijab}^{(2\mathrm{B})}(s=0)}\,, \tag{7.25}$$

$$E(s\to\infty)_{330} \approx \frac{1}{36}\sum_{ijkabc} \frac{W_{ijkabc}(s=0)W_{abcijk}(s=0)}{\Delta_{ijkabc}^{(3\mathrm{B})}(s=0)}\,. \tag{7.26}$$

These are exactly the second-order MBPT corrections to the energy, and this shows that these corrections are absorbed into the IMSRG correlation energy, making the IMSRG at any many-body truncation second-order complete in MBPT. Recall that in our analysis (using an HF reference state and the NO2B approximation), f_{ia} and W_{ijkabc} are 0, so Eqs. (7.24) and (7.26) vanish. Nevertheless, the $[1,1]\to 0$ and $[3,3]\to 0$ commutators are important at higher orders, and the intuition above for how they generate contributions to the ground-state energy is key to understanding the perturbative analysis fully.

Extending this analysis to higher orders in MBPT requires considering how the hole-particle matrix elements of f, Γ, and W change over the course of the IMSRG evolution beyond the basic suppression of their initial values. On a high level, this corresponds to the IMSRG evolution "dressing" the one-, two-, and three-body vertices with effective interaction contributions that generate higher-order MBPT diagrams. A detailed analysis of this is given in Refs. [94, 280], but to make this concept a bit more concrete we discuss one contribution at a high level. Considering the particle-particle part of the $[2,2]\to 2$ commutator,

$$C_{1234} = \frac{1}{2}\sum_{pq} \bar{n}_p\bar{n}_q(A_{12pq}B_{pq34} - B_{12pq}A_{pq34})\,, \tag{7.27}$$

and plugging in $\mathcal{O}(g)$ matrix elements for $A=\eta$ and $B=H$, one sees that this generates $\mathcal{O}(g^2)$ matrix elements in Γ_{ijab} when integrated in s. Plugging this $\mathcal{O}(g^2)$ contribution together with an $\mathcal{O}(g)$ contribution into Eq. (7.19) gives a third-order contribution to the energy. Keeping track of all prefactors and energy denominators, one finds that the integration in s works out such that this is exactly the particle-particle third-order MBPT contribution given in Eq. (3.79). Similar results are obtained for the other third-order MBPT contributions, so one finds that the IMSRG(2) is complete up to third order in MBPT. This sets the intuitive foundation for the perturbative analysis.

Returning to our original power-counting scheme

$$H = f + g\,\Gamma\,, \tag{7.28}$$

with

$$f_{pp} = \mathcal{O}(g^0)\,, \tag{7.29}$$

$$\Gamma_{pqrs} = \mathcal{O}(g^1)\,, \tag{7.30}$$

we see that the hole-particle block of f is induced by the $[2,2]\to 1$ commutator (the $[1,2]\to 1$ commutator initially does not induce hole-particle contributions because f_{ia} and thus $\eta^{(1\mathrm{B})}$ are 0), and the matrix elements of W are induced by the $[2,2]\to 3$ commutator. This means

$$f_{ia} = \mathcal{O}(g^2)\,, \tag{7.31}$$

$$W_{pqrstu} = \mathcal{O}(g^2)\,, \tag{7.32}$$

Commutator	Cost	Perturbative order
$[1,1] \to 0$	$\mathcal{O}(N^2)$	g^4
$[1,1] \to 1$	$\mathcal{O}(N^3)$	g^4
$[1,2] \to 1$	$\mathcal{O}(N^4)$	g^5
$[1,2] \to 2$	$\mathcal{O}(N^5)$	g^2
$[2,2] \to 0$	$\mathcal{O}(N^4)$	g^2
$[2,2] \to 1$	$\mathcal{O}(N^5)$	g^4
$[2,2] \to 2$	$\mathcal{O}(N^6)$	g^3
$[2,2] \to 3$	$\mathcal{O}(N^7)$	g^4
$[1,3] \to 2$	$\mathcal{O}(N^6)$	g^5
$[1,3] \to 3$	$\mathcal{O}(N^7)$	g^4
$[2,3] \to 1$	$\mathcal{O}(N^6)$	g^5
$[2,3] \to 2$	$\mathcal{O}(N^7)$	g^4
$[2,3] \to 3$	$\mathcal{O}(N^8)$	g^5
$[3,3] \to 0$	$\mathcal{O}(N^6)$	g^4
$[3,3] \to 1$	$\mathcal{O}(N^7)$	g^6
$[3,3] \to 2$	$\mathcal{O}(N^8)$	g^5
$[3,3] \to 3$	$\mathcal{O}(N^9)$	g^6

Table 7.1: Summary of IMSRG(3) fundamental commutators. The lowest-order perturbative contributions to the energy provided by each of the IMSRG(3) fundamental commutators along with their computational costs. Table from Ref. [45].

and, as a result, their contributions to the energy are both $\mathcal{O}(g^4)$.

Thus, the contribution of any induced two-body parts to E is suppressed by $\mathcal{O}(g^1)$, and the contributions of induced one- and three-body parts to E are suppressed by $\mathcal{O}(g^2)$. This allows one to quickly perturbatively estimate the importance of different fundamental commutators, provided in Table 7.1.

It is worth noting that the $[1,1] \to 1$, $[1,2] \to 2$, and $[1,3] \to 3$ commutators have higher perturbative importance than their $[1,2] \to 1$, $[2,2] \to 2$, and $[2,3] \to 3$ counterparts, a consequence of the fact that they are sensitive to the diagonal part of f, which is $\mathcal{O}(g^0)$. The former $[1,B] \to B$ commutators are responsible for the suppression of the B-body hole-particle blocks of the Hamiltonian and play a central role in the behavior of the IMSRG evolution.

A key result of the analyses in Refs. [94, 280] is that the IMSRG(2) is complete up to third order in MBPT and contains many fourth-order diagrams as well. At the NO2B level, the IMSRG(3) accounts for the induced three-body effects, which are what is missing for the complete inclusion of fourth-order diagrams in the IMSRG(2), making the IMSRG(3) fourth-order complete at the NO2B level [94, 280].

7.3 Approximating the IMSRG(3)

In this chapter, we are able to perform full IMSRG(3) calculations because we work in restricted model spaces where the IMSRG(3) and also exact diagonalizations are computationally feasible. The IMSRG(3)

Commutator	Cost	Included in IMSRG(3)-...				
		MP4	N^7	N^8	g^5	full IMSRG(3)
$[2,2] \to 3$	$\mathcal{O}(N^7)$	✓	✓	✓	✓	✓
$[2,3] \to 2$	$\mathcal{O}(N^7)$	✓	✓	✓	✓	✓
$[1,3] \to 3$	$\mathcal{O}(N^7)$	✓	✓	✓	✓	✓
$[3,3] \to 0$	$\mathcal{O}(N^6)$	✓	✓	✓	✓	✓
$[2,3] \to 1$	$\mathcal{O}(N^6)$		✓	✓	✓	✓
$[1,3] \to 2$	$\mathcal{O}(N^6)$		✓	✓	✓	✓
$[3,3] \to 1$	$\mathcal{O}(N^7)$		✓	✓		✓
$[2,3] \to 3$	$\mathcal{O}(N^8)$			✓	✓	✓
$[3,3] \to 2$	$\mathcal{O}(N^8)$			✓	✓	✓
$[3,3] \to 3$	$\mathcal{O}(N^9)$					✓

Table 7.2: Summary of approximate IMSRG(3) truncations. The computational cost of the IMSRG(3) fundamental commutators and whether they are included in various approximate and full IMSRG(3) truncation schemes. Table from Ref. [45].

without truncations, however, is far too expensive for calculations of medium-mass nuclei in realistic model spaces ("realistic" meaning that the model-space truncations are sufficient to converge observables at the three-body level). This is also the case for CC theory with triples, which without any truncations yields the $\mathcal{O}(A^3N^6)$ CCSDT theory [314, 315]. In CC theory, a variety of approximations of CCSDT have proliferated accounting for the effects of triples in different ways [92, 313, 316–319, 362]. These approximations, while more expensive than CCSD, are well established and computationally feasible in nuclear structure calculations and play an important role where precision and uncertainty quantification are concerned. We aim to do the same for the IMSRG(3), establishing approximations of the IMSRG(3) that include the most essential features of the IMSRG(3) needed for high precision while remaining computationally tractable in large-scale calculations.

The strategy we employ is relatively simple. We include full three-body operators in our calculations (rather than treating three-body effects perturbatively). Of the 10 IMSRG(3) fundamental commutators that would be necessary for a full IMSRG(3) calculation, we select only a subset to keep in our equations. Ideally, we are able to neglect the most expensive fundamental commutators while introducing only small errors in the IMSRG(3) solution and substantially improving over the IMSRG(2). Our approach and the approximations we introduce in the following are summarized in Table 7.2.

The minimal IMSRG(3) scheme we consider includes four fundamental commutators, motivated by our typical NO2B starting point[2] and the perturbative analysis of the IMSRG(3). Starting from an NO2B initial Hamiltonian, a three-body part must be induced by the $[2,2] \to 3$ commutator. Once a three-body part is generated, its off-diagonal contributions must be suppressed, which is achieved by the $[1,3] \to 3$ commutator. Similarly, for the three-body part to affect observables, it must couple back to the zero- through two-body parts of the IMSRG(3). There are two $\mathcal{O}(g^4)$ commutators allowing the three-body part to "feed back" into lower-body parts, the $[2,3] \to 2$ and $[3,3] \to 0$ commutators. Including these four commutators yields the

[2]With the IMSRG(3), it is in principle no extra cost to also include the initial residual three-body Hamiltonian W. This is currently not done, but should be investigated in the future as it is a key advantage of the IMSRG over CC theory, where the theory needs to be generalized considerably to include a three-body Hamiltonian [277, 278].

IMSRG(3)-MP4 truncation. We note that in this truncation all $\mathcal{O}(g^4)$ commutators are included, making this truncation complete to fourth order in MBPT, motivating its name. The IMSRG(3)-MP4 is most similar to iterated coupled-cluster methods like CCSDT-1 [92, 313, 362], as both methods are fourth-order complete. However, CCSDT-1 scales like $\mathcal{O}(A^3N^4)$ while the IMSRG(3)-MP4 scales like $\mathcal{O}(N^7)$.

Beyond the IMSRG(3)-MP4 truncation, we consider two approaches to including further commutators. The first is inclusion based on computational cost, including first the cheapest of the remaining commutators before including the more expensive commutators. The rationale here is that by using this approach one can include as much "physics" as possible while increasing the computational cost incrementally, hopefully leading to a fairly faithful reproduction of the full IMSRG(3) results. The second approach is based on the perturbative analysis discussed in Section 7.2, where remaining commutators are included in the order of their perturbative importance. This physically motivated approach attempts to capture as best as possible the available physics in a consistent manner before including "higher-order" effects. One would hope to see that these higher-order effects generate only small changes in energies and in practical calculations some "complete" lower-order approximation could be used.

Following the first approach, including the $[2,3] \to 1$, $[1,3] \to 2$, and $[3,3] \to 1$ commutators on top of the IMSRG(3)-MP4 approximation yields a truncation that includes all IMSRG(3) commutators that cost $\mathcal{O}(N^7)$ or less. We refer to this truncation as the IMSRG(3)-N^7 truncation. The inclusion of the $[2,3] \to 3$ and $[3,3] \to 2$ commutators on top of this truncation yields the IMSRG(3)-N^8 truncation, which includes all commutators that cost $\mathcal{O}(N^8)$ or less. This truncation differs from the full IMSRG(3) only by the missing $[3,3] \to 3$ commutator.

Following the second approach, the next truncation we present includes the remaining $\mathcal{O}(g^5)$ commutators, the $[2,3] \to 1$, $[1,3] \to 2$, $[2,3] \to 3$, and $[3,3] \to 2$ commutators, on top of the IMSRG(3)-MP4 truncation. We refer to this truncation as the IMSRG(3)-g^5 truncation. This truncation includes two commutators that cost $\mathcal{O}(N^8)$, making that the cost of the truncation. The two remaining commutators are $\mathcal{O}(g^6)$, so this is the only complete perturbatively guided truncation between the IMSRG(3)-MP4 and full IMSRG(3) truncations.

7.4 Comparison against exact results

To test the precision of the IMSRG(3) and its approximations relative to the IMSRG(2), we consider IMSRG calculations of ground-state energies in an $e_{\max} = 2$ model space. In this model space, we are able to compare against exact results. For ^{4}He, we perform a full configuration interaction (FCI) diagonalization using the BIGSTICK code [369]. For ^{16}O, we perform NCSM diagonalizations based on the $e_{\max} = 2$ model space using the KSHELL code [370].

We focus on two soft chiral Hamiltonians, the N^{3}LO chiral NN potential from Ref. [154] SRG evolved to $\lambda = 1.8\,\mathrm{fm}^{-1}$ (referred to as "N^{3}LO EM 500 $\lambda = 1.8\,\mathrm{fm}^{-1}$") and the chiral NN+3N "1.8/2.0 (EM)" potential constructed in Ref. [171]. We also consider three harder chiral NN-only Hamiltonians, the N^{3}LO potential from Ref. [154] with a cutoff of 500 MeV (referred to as "N^{3}LO EM 500"), the N^{3}LO potential from Ref. [157] with a cutoff of 450 MeV (referred to as "N^{3}LO EMN 450"), and the N^{3}LO potential from Ref. [157] with a cutoff of 500 MeV (referred to as "N^{3}LO EMN 500").

We employ two basis sets, the HF and NAT bases. For the HF bases, the HF solution and subsequent IMSRG calculation are both performed in an $e_{\max} = 2$ model space. For the NAT bases, we follow the strategy discussed in Chapter 6 [106], using a model space of $e_{\max}^{\mathrm{HF/NAT}} = 14$ (with $E_{3\max} = 16$ for 3N forces where relevant) before truncating to $e_{\max} = 2$ for the IMSRG calculation.

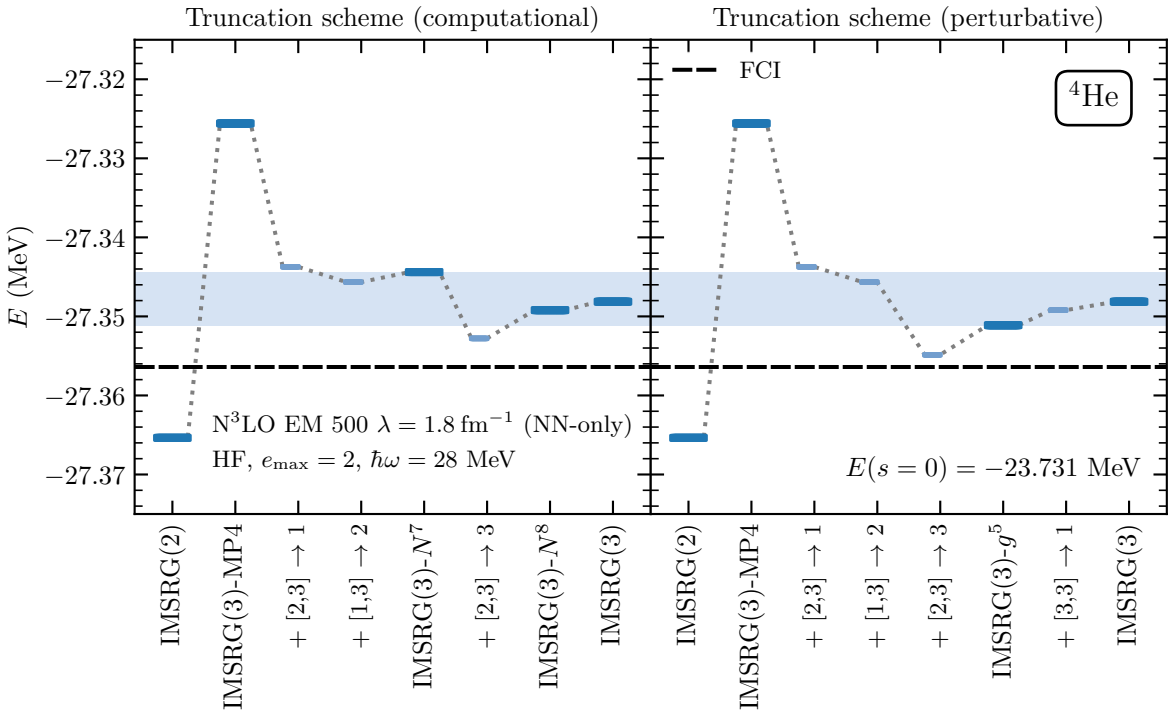

Figure 7.1: IMSRG(3) corrections for ^{4}He in the HF basis. Ground-state energies E of ^{4}He obtained in various truncation schemes using the N^{3}LO EM 500 $\lambda = 1.8\,\mathrm{fm}^{-1}$ NN-only Hamiltonian and an HF reference state following the computational and perturbative truncation orderings for the fundamental commutators (*left and right panels, respectively*). Thicker, darker bars correspond to the major truncations summarized in Table 7.2. Thinner, lighter bars correspond to intermediate truncations where a single fundamental commutator has been added relative to the truncation scheme to the left. The dashed line indicates the $e_{\max} = 2$ exact result obtained for this Hamiltonian. The blue band indicates the range spanned by the results obtained from the IMSRG(3)-N^7 and IMSRG(3)-g^5 truncations. The starting mean-field energy expectation value is provided in the bottom right corner. Figure from Ref. [45].

We solve the IMSRG equations via direct integration of the flow equations (rather than employing the Magnus expansion [297]), and we employ the imaginary-time generator throughout.

7.4.1 Helium-4

In the following, we discuss figures like Fig. 7.1, where ground-state energy predictions obtained via the IMSRG(2) and various IMSRG(3) approximations are compared against exact results indicated by the black dashed line. We investigate the convergence from the IMSRG(2) to the full IMSRG(3) truncations following the computational and perturbative approaches to approximating the IMSRG(3) discussed in Sec. 7.3 and summarized in Table 7.2. The "major truncations" given there are shown as thicker, wider, darker lines, while minor truncations including one fundamental commutator in addition to the truncation on the left are shown as thinner, narrower, lighter lines.

In the left panel, we follow the approach to approximating the IMSRG(3) based on computational cost: we start with the IMSRG(2) on the left; we add the $[2,2] \to 3$, $[2,3] \to 2$, $[1,3] \to 3$, and $[3,3] \to 0$ commutators to arrive at the IMSRG(3)-MP4; we further add the $[2,3] \to 1$, $[1,3] \to 2$, and $[3,3] \to 1$ commutators to arrive at the IMSRG(3)-N^7; we further add the $[2,3] \to 3$ and $[3,3] \to 2$ commutators to arrive at the IMSRG(3)-N^8; and we add the $[3,3] \to 3$ commutator to arrive at the IMSRG(3). In the

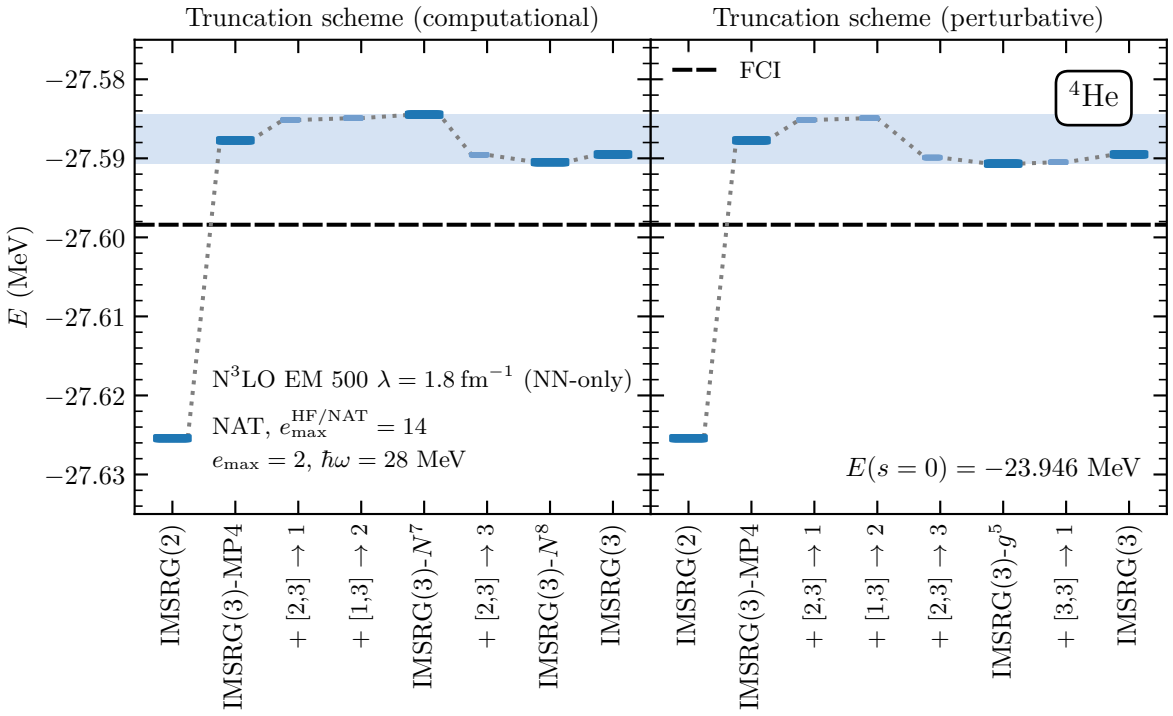

Figure 7.2: IMSRG(3) corrections for ^{4}He in the NAT basis. Same as Fig. 7.1 but using a NAT reference state constructed in an $e_{\max}^{\mathrm{HF/NAT}} = 14$ model space. Figure from Ref. [45].

right panel, we follow the approach to approximating the IMSRG(3) based on perturbative importance: we start with the IMSRG(2) on the left; we extend this to the IMSRG(3)-MP4; we further add the $[2,3] \to 1$, $[1,3] \to 2$, $[2,3] \to 3$, and $[3,3] \to 2$ commutators to arrive at the IMSRG(3)-g^5; and we add the $[3,3] \to 1$ and $[3,3] \to 3$ commutators to arrive at the IMSRG(3).

In Fig. 7.1, we consider IMSRG calculations of ^{4}He starting from an HF reference state using the N^{3}LO EM 500 $\lambda = 1.8\,\mathrm{fm}^{-1}$ Hamiltonian. The exact result for this Hamiltonian is shown by the black dashed line. We see that for this Hamiltonian and reference state, the IMSRG(2) error to the exact result is surprisingly small, less than 10 keV on a correlation energy of $E_{\mathrm{corr}} \sim 3.6$ MeV. The error of the full IMSRG(3) is similarly small. We see that the IMSRG(3)-MP4 contains significant repulsive contributions relative to the IMSRG(2), which can be understood by the fact that the quadruples in fourth-order MBPT are generally repulsive for these soft Hamiltonians and are included in the IMSRG(3)-MP4, but not in the IMSRG(2). Including more terms beyond the IMSRG(3)-MP4 yields the IMSRG(3)-N^7 and IMSRG(3)-N^8 truncations, which differ only weakly from the full IMSRG(3). We also see that most individual commutators only give small corrections to the energy, with the exception of the $[2,3] \to 1$ commutator. This establishes the systematic convergence of the IMSRG(3) and its approximations towards the exact result, and also suggests that low-cost IMSRG(3) commutators are sufficient to quantitatively approximate the full IMSRG(3) result.

In the right panel, we find that the IMSRG(3)-g^5 approximates the full IMSRG(3) quite well. A similar systematic convergence is observed for the individual commutators added beyond the IMSRG(3)-MP4, suggesting that the perturbative power counting is effective for this system and Hamiltonian. We note that the band spanned by the IMSRG(3)-N^7 and IMSRG(3)-g^5 approximations contains the IMSRG(3) result.

In Fig. 7.2, we consider starting from a NAT reference state instead. Here we find that the IMSRG(2)

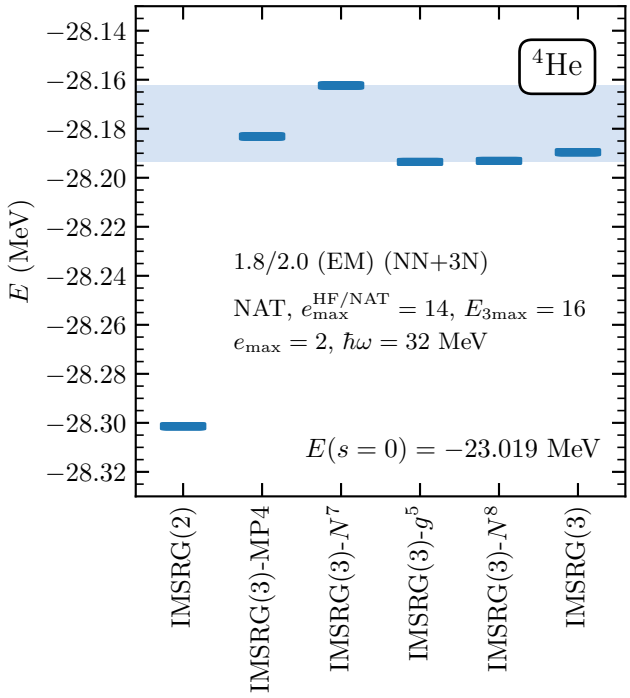

Figure 7.3: IMSRG(3) corrections for ^{4}He with the 1.8/2.0 (EM) Hamiltonian. Ground-state energies E of ^{4}He obtained in various truncation schemes using the 1.8/2.0 (EM) Hamiltonian and a NAT reference state. The blue band indicates the range spanned by the results obtained from the IMSRG(3)-N^7 and IMSRG(3)-g^5 truncations. The NAT basis is constructed in an $e_{\max}^{\mathrm{HF/NAT}} = 14$, $E_{3\max} = 16$, $\hbar\omega = 32$ MeV model space before being truncated to $e_{\max} = 2$ for the IMSRG calculations. The starting mean-field energy expectation value is provided in the bottom right corner. Figure from Ref. [45].

error to the exact result is larger, around 25 keV, which is more in line with the expected IMSRG(2) error of 1–2% of $E_{\mathrm{corr}} \sim 3.6$ MeV. This suggests the small IMSRG(2) error in the HF case above is coincidental. The IMSRG(3)-MP4, IMSRG(3)-N^7, IMSRG(3)-N^8, and IMSRG(3)-g^5 approximations show systematic convergence towards the IMSRG(3) result, which has only a small error less than 10 keV to the exact energy. Individual commutators generally give small corrections [beyond the large correction going from the IMSRG(2) to the IMSRG(3)-MP4], and the IMSRG(3) result lies in the band between the IMSRG(3)-N^7 and IMSRG(3)-g^5 approximations.

Comparing the computational and perturbative IMSRG(3) approximation approaches, we find that the IMSRG(3) is best approximated by the IMSRG(3)-N^8 and IMSRG(3)-g^5. This is somewhat unsurprising as these approximations only omit two and one commutators from the IMSRG(3), respectively. However, looking at the perturbative truncation scheme, one sees that the sizes of corrections generally follow the perturbative importances, with a large correction due to the $\mathcal{O}(g^4)$ contributions in IMSRG(3)-MP4, smaller corrections at $\mathcal{O}(g^5)$, and only very small $\mathcal{O}(g^6)$ corrections bringing the IMSRG(3)-g^5 to the full IMSRG(3). This suggests the perturbative importance estimate is a useful guide when using soft Hamiltonians. At the same time, the computational truncation scheme establishes the IMSRG(3)-N^7 in particular as being able to quantitatively approximate the full IMSRG(3) result at substantially lower computational cost, making it an excellent candidate for realistic calculations.

In Fig. 7.3, we find a similar picture when using the NN+3N 1.8/2.0 (EM) Hamiltonian with a NAT reference state. A considerable correction arises at the IMSRG(3)-MP4 truncation, but further adding

commutators only delivers small corrections. The IMSRG(3)-N^8 and IMSRG(3)-g^5 both approximate the full IMSRG(3) very well, but the IMSRG(3)-N^7 and IMSRG(3)-MP4 also provide good quantitative approximations of the IMSRG(3) result.

7.4.2 Oxygen-16

We extend our systematic study to ^{16}O to explore how our findings depend on the system considered. In ^{16}O, we perform NCSM diagonalizations using the KSHELL code [370], using $N_{\max} = 2$, 4, 6, and 8 truncations. We extrapolate these results to $N_{\max} \to \infty$ by fitting a decaying exponential in $N_{\max}$. We assess the uncertainty in the extrapolation by leaving one of $N_{\max} = 2$, 4, 6 out of the fit.

In Fig. 7.4, we consider IMSRG calculations of ^{16}O using the N^{3}LO EM 500 $\lambda = 1.8\,\mathrm{fm}^{-1}$ Hamiltonian and an HF reference state. We find that the IMSRG(2) error is about 180 keV, which is around 1.8% of the correlation energy. The IMSRG(3)-MP4 gives a sizeable repulsive correction, underbinding compared to exact results, and the IMSRG(3)-N^7, IMSRG(3)-N^8, and IMSRG(3)-g^5 give attractive corrections that converge systematically towards the full IMSRG(3). The IMSRG(3) differs from exact results by less than 40 keV, a substantial improvement in precision.

In Fig. 7.5, we consider the same calculations but using a NAT reference state. We find that the IMSRG(2) error is very small, less than 20 keV. This surprisingly small error is once again coincidental. The IMSRG(3)-MP4 gives a small repulsive correction, and the IMSRG(3)-N^7, IMSRG(3)-N^8, and IMSRG(3)-g^5 again give attractive corrections that converge systematically towards the full IMSRG(3). The IMSRG(3) differs from exact results by less than 30 keV.

We find quantitatively consistent results in ^{4}He and ^{16}O when one considers correlation energies for the different many-body calculations. This is summarized in Fig. 7.6, where we consider IMSRG calculations of ^{4}He and ^{16}O using HF and NAT reference states and the NN-only N^{3}LO EM 500 $\lambda = 1.8\,\mathrm{fm}^{-1}$ and the NN+3N 1.8/2.0 (EM) Hamiltonians. We compare the correlation energies of IMSRG(2) and various approximate IMSRG(3) calculations relative to the full IMSRG(3) correlation energy, $E_{\mathrm{corr,IMSRG(3)}}$. We find that the IMSRG(2) overbinds all systems considered, with up to 2% differences in the correlation energy. This gives us the rule of thumb that IMSRG(2) ground-state energy predictions have a many-body uncertainty of around 1–2% of E_{corr}. For all systems considered, the IMSRG(3)-MP4 truncation underbinds relative to the IMSRG(3), with up to 1% differences in E_{corr}. The IMSRG(3)-N^7 improves on this in most cases, bringing the the difference in E_{corr} down to 0.5% or less. The IMSRG(3)-g^5 very accurately reproduces the IMSRG(3) with differences in E_{corr} of less than 0.2%. We find that gray band between the IMSRG(3)-N^7 and IMSRG(3)-g^5 results includes the IMSRG(3) result for all systems shown.

7.4.3 IMSRG(3) with harder Hamiltonians

The previous sections focused on the soft N^{3}LO EM 500 $\lambda = 1.8\,\mathrm{fm}^{-1}$ and 1.8/2.0 (EM) Hamiltonians. In this section, we explore the many-body convergence when using hard Hamiltonians, focusing on the NN-only N^{3}LO EM 500, N^{3}LO EMN 450, and N^{3}LO EMN 500 Hamiltonians.

In Fig. 7.7, we explore various IMSRG calculations for the given Hamiltonians, showing their errors to exact results for various truncations. In the top plot, we consider ^{4}He, where the errors due to the IMSRG(2) approximation are considerable. These errors of 350–500 keV correspond to errors of 3.5–5% on the correlation energy, much larger than observed for soft Hamiltonians. Going to the IMSRG(3)-MP4 truncation reduces this error somewhat, but going to any higher-fidelity truncation reduces the error considerably. The full IMSRG(3) results are all within 100 keV of the exact results, but the same is also true for the IMSRG(3)-N^7 and IMSRG(3)-g^5 results.

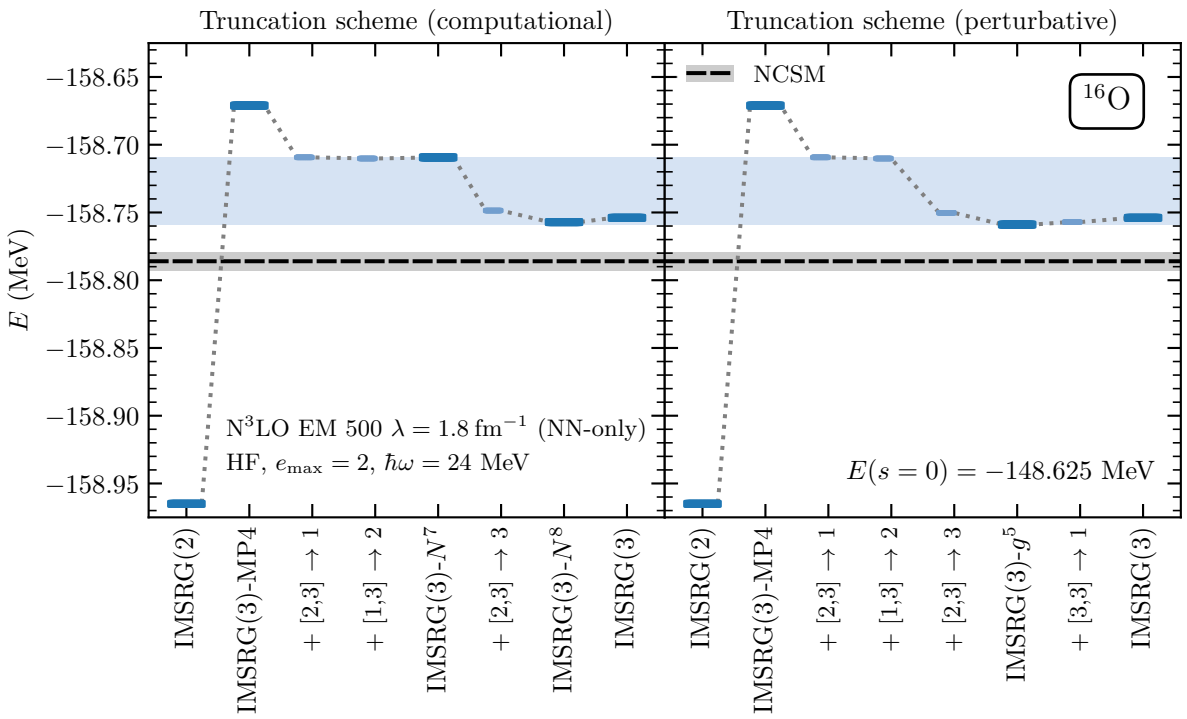

Figure 7.4: IMSRG(3) corrections for ^{16}O in the HF basis. Same as Fig. 7.1 but for ^{16}O with $\hbar\omega = 24$ MeV. Figure from Ref. [45].

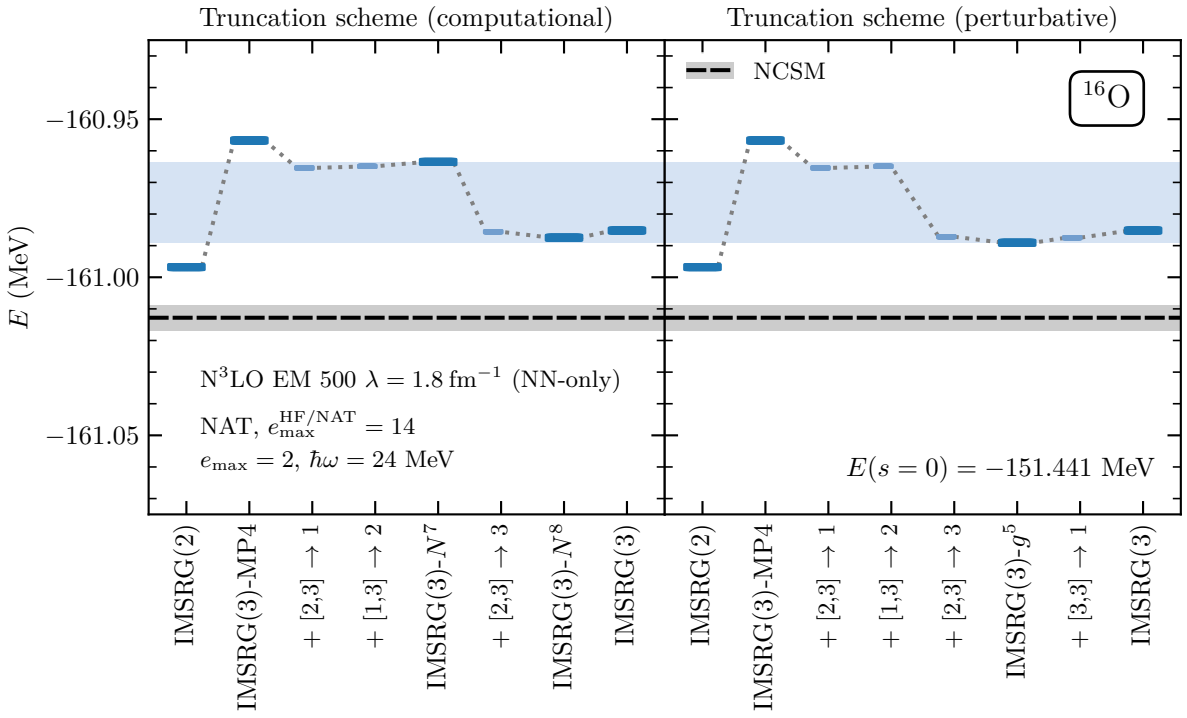

Figure 7.5: IMSRG(3) corrections for ^{16}O in the NAT basis. Same as Fig. 7.4 but using a NAT reference state constructed in an $e_{\max}^{\mathrm{HF/NAT}} = 14$ model space. Figure from Ref. [45].

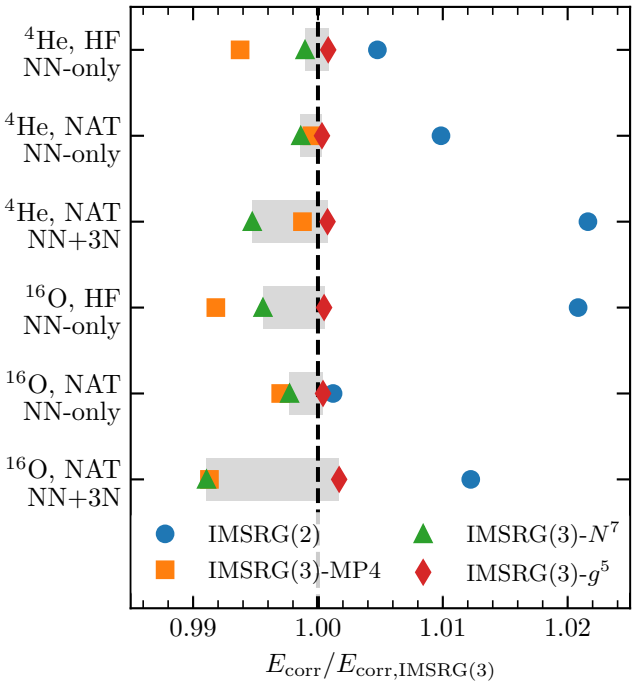

Figure 7.6: Performance of approximate IMSRG(3) truncations. Ratios of correlation energies E_{corr} obtained in IMSRG(2) and approximate IMSRG(3) calculations relative to the IMSRG(3) correlation energies $E_{\mathrm{corr,IMSRG(3)}}$ for different systems discussed in Ref. [45]. The gray band indicates the range spanned by the IMSRG(3)-N^7 and IMSRG(3)-g^5 results. Figure from Ref. [45].

In the bottom plot, we consider ^{16}O. The approximate IMSRG(3) truncations systematically improve over the IMSRG(2), and the final IMSRG(3) results differ from the exact results by just over 100 keV, which is an error of about 0.5% in the correlation energy for both Hamiltonians. For the N^{3}LO EM 500 Hamiltonian in the $e_{\mathrm{max}} = 2$ model space, the IMSRG(2) calculation of ^{16}O does not converge. The IMSRG(3) improves on this by delivering converged results that differ from exact results by about 3%, stabilizing the solution of IMSRG flow equations.

We see that the IMSRG(3) offers substantial, systematic improvements over the IMSRG(2). These improvements are largely already present in approximate IMSRG(3) truncations with lower computational cost, such as the IMSRG(3)-N^7. We note that the IMSRG(3) is not able to achieve as small of errors for these harder Hamiltonians as it is able to achieve for the N^{3}LO EM 500 $\lambda = 1.8\,\mathrm{fm}^{-1}$ Hamiltonian with errors of up to 0.6% in the correlation energy. This suggests that the many-body expansion in the IMSRG converges more slowly when using harder Hamiltonians (as one would also expect from perturbative arguments). Still, the convergence behavior of the IMSRG many-body expansion is systematic in the cases discussed here, and the general trends discussed the previous sections continue to hold.

7.5 Realistic IMSRG(3) calculations of nuclei

The work discussed in the previous sections and in Ref. [45] establishes two points: the many-body expansion in the IMSRG converges systematically in the systems considered, allowing the IMSRG(3) to deliver high-precision results for ground-state energies; the benefits of the IMSRG(3) can generally be reaped at considerably lower computational cost by leaving out selected unimportant, but computationally expensive terms. Specifically, the IMSRG(3)-N^7 and IMSRG(3)-MP4 approximations with their $\mathcal{O}(N^7)$

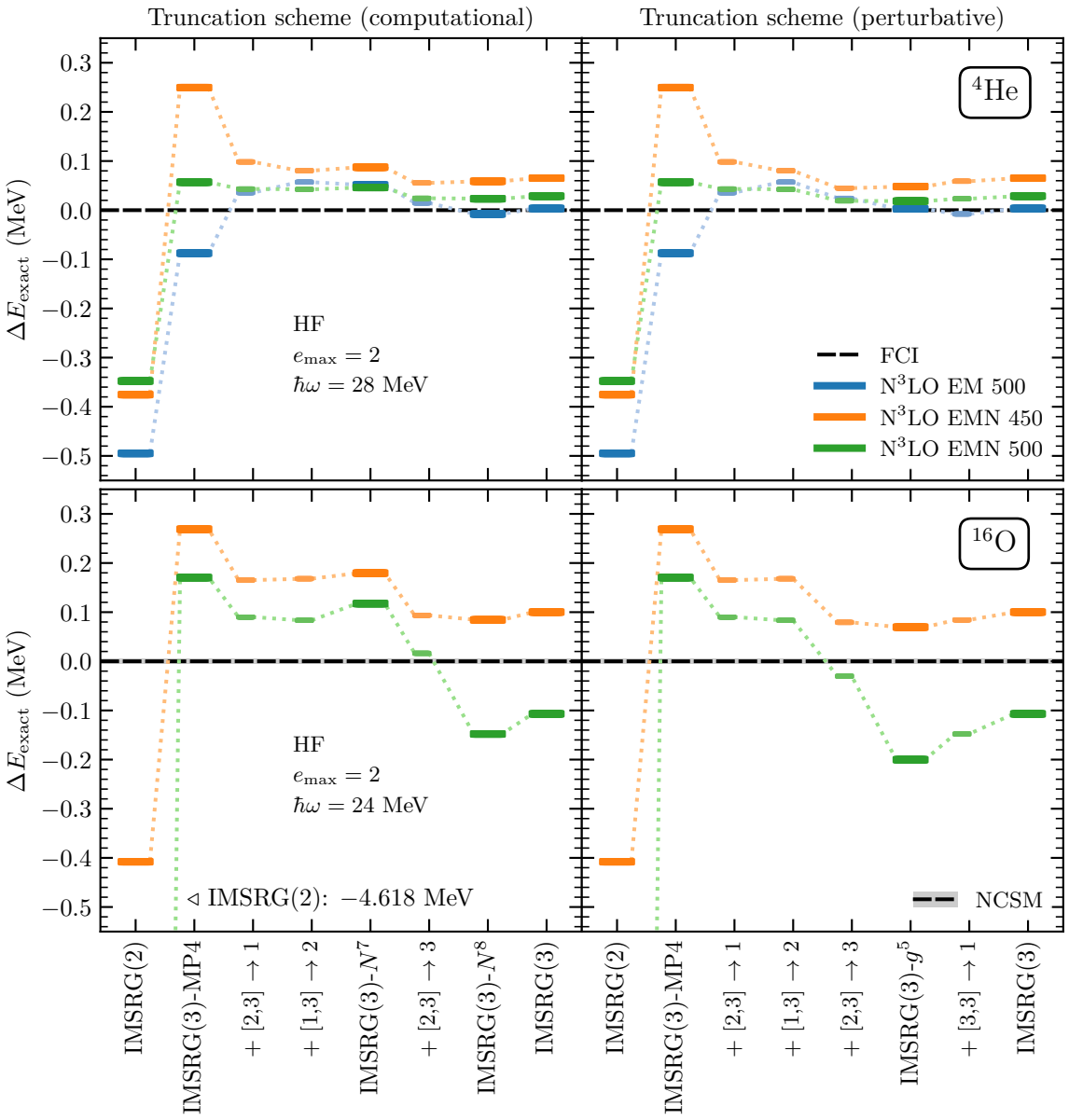

Figure 7.7: IMSRG(3) corrections for harder Hamiltonians. Differences of ground-state energies ΔE_{exact} of ^{4}He (*top*) and ^{16}O (*bottom*) obtained in various truncation schemes to exact results using several unevolved chiral Hamiltonians (*see text for details*) and an HF reference state following the computational (*left panels*) and perturbative (*right panels*) truncation ordering for the fundamental commutators. Thicker, darker bars correspond to the major truncations summarized in Table 7.2. Thinner, lighter bars correspond to intermediate truncations where a single fundamental commutator has been added relative to the truncation scheme to the left. Figure from Ref. [45].

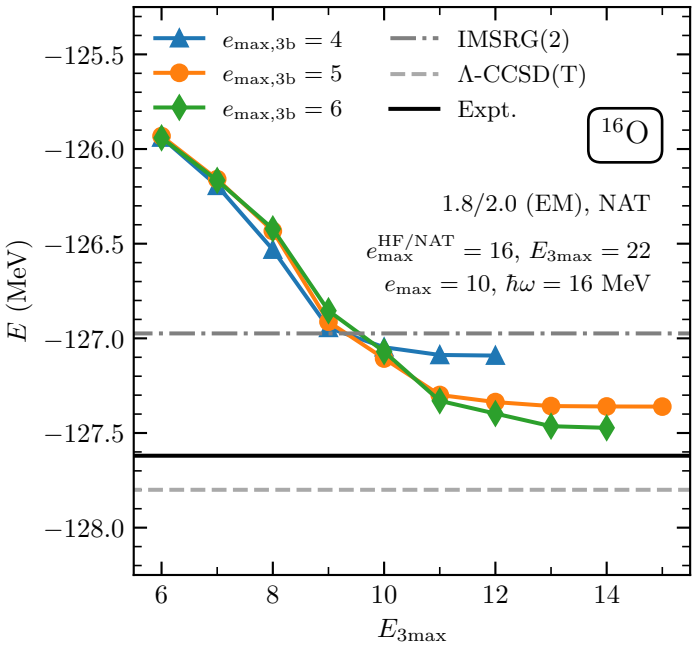

Figure 7.8: IMSRG(3) predictions for the ground-state energy of ^{16}O. The ground-state energy E of ^{16}O as predicted by the IMSRG(2) (*dash-dotted*), Λ-CCSD(T) (*dashed*), and the IMSRG(3)-N^7 as a function of $e_{\max,3b}$ and $E_{3\max}$ (*blue triangles, orange circles, green diamonds*) using the 1.8/2.0 (EM) Hamiltonian from Ref. [171]. For the IMSRG(3)-N^7 calculations, the NAT basis was constructed using $e_{\max}^{\mathrm{HF/NAT}} = 16$, $E_{3\max} = 22$ before being truncated to $e_{\max} = 10$. Λ-CCSD(T) value from Ref. [371]. Experimental value from Ref. [361].

computational scaling provide a tractable option to do "IMSRG(3)" calculations in realistic model spaces. The differences between the two truncations are subtle. In general, the IMSRG(3)-N^7 performed better than the IMSRG(3)-MP4 relative to the IMSRG(3), making it the preferred method, but the IMSRG(3)-MP4 may be useful to assess how sensitive certain results are to the IMSRG(3) approximation we employ.

In later chapters of this thesis, we explore IMSRG(3) calculations of nuclei in realistic model spaces (albeit not always fully converged). In these cases, these are always IMSRG(3)-N^7 calculations. Further, we currently use the IMSRG(3) calculations starting from an NO2B Hamiltonian, meaning the initial residual three-body interactions $W(s = 0)$ are discarded. We use the IMSRG(3) to capture induced many-body interactions as best as possible to probe the many-body truncation uncertainty without considering the NO2B approximation. This represents the cleanest initial exploration of the IMSRG(3), where one is able to test the effect of the inclusion of three-body operators independent of any other improvements. It also allows for clean comparison with CC calculations including triples, which always employ the NO2B approximation for the Hamiltonian. In the future, it will be interesting to explore the additional effect of including $W(s = 0)$ in IMSRG(3) calculations.

Given the immense cost of representing three-body operators in a single-particle basis, we employ additional truncations for the three-body basis in our IMSRG(3) calculations. We represent our three-body operators in a basis

$$\{|pqr\rangle\,,\ e_p \leq e_{\max,3b},\ e_q \leq e_{\max,3b},\ e_r \leq e_{\max,3b},\ e_p + e_q + e_r \leq E_{3\max}\}, \tag{7.33}$$

with the single-particle truncation $e_{\max,3b} \leq e_{\max}$ and the three-body truncation $E_{3\max}$. Fully relaxing these truncations means taking $e_{\max,3b} = e_{\max}$ and $E_{3\max} = 3e_{\max}$. This truncation approach, in particular

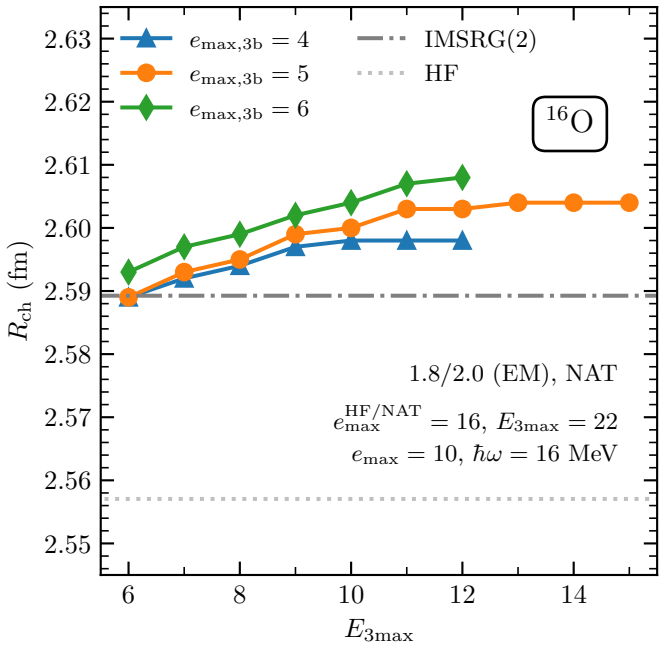

Figure 7.9: IMSRG(3) predictions for the charge radius of ^{16}O. The charge radius R_{ch} of ^{16}O as predicted by Hartree-Fock (*dotted*), the IMSRG(2) (*dash-dotted*), and the IMSRG(3)-N^7 as a function of $e_{\mathrm{max,3b}}$ and $E_{3\mathrm{max}}$ (*blue triangles, orange circles, green diamonds*) using the 1.8/2.0 (EM) Hamiltonian from Ref. [171]. For the IMSRG(3)-N^7 calculations, the NAT basis was constructed using $e_{\mathrm{max}}^{\mathrm{HF/NAT}} = 16$, $E_{3\mathrm{max}} = 22$ before being truncated to $e_{\mathrm{max}} = 10$.

the $e_{\mathrm{max,3b}}$ truncation, relies very heavily on the optimization of the particle states provided by the natural orbitals, which makes the additional $e_{\mathrm{max,3b}}$ cut well behaved. Alternative truncations based on NAT occupation numbers have been explored in CC calculations [251] and are being considered for improved IMSRG(3) calculations. For all the IMSRG calculations in the rest of this chapter and the following chapters, we employ the IMSRG++ code [365] for which we developed these computational strategies.

As a demonstration, we consider IMSRG(3)-N^7 calculations of the ground-state energy of ^{16}O using the 1.8/2.0 (EM) Hamiltonian [171] in Fig. 7.8. We find that for this Hamiltonian the IMSRG(2) reproduces the experimental binding energy quite well. Coupled-cluster results with perturbative triples (gray dashed line) lie even closer to the experimental value. Including three-body operators in the IMSRG by doing IMSRG(3)-N^7 calculations gives us insight into what the IMSRG(2) uncertainty is and what the exact result for this Hamiltonian is.

For our IMSRG(3)-N^7 calculations, we employ a NAT reference state and basis constructed in an $e_{\mathrm{max}}^{\mathrm{HF/NAT}} = 16$, $E_{3\mathrm{max}} = 22$ model space that we truncate to $e_{\mathrm{max}} = 10$ for the IMSRG calculation. We have access to $e_{\mathrm{max,3b}} = 4$ and 5 up to $E_{3\mathrm{max}} = 12$ and 15, respectively, and $e_{\mathrm{max,3b}} = 6$ up to $E_{3\mathrm{max}} = 14$. We observe systematic convergence of small corrections to the binding energy. We are able to converge within $E_{3\mathrm{max}}$, but have a small remaining model-space uncertainty of around 150 keV due to the $e_{\mathrm{max,3b}}$ truncation. The remaining many-body uncertainty of the IMSRG(3)-N^7 is likely also around 100 keV. Considering these uncertainties, we see that the IMSRG(3)-N^7 prediction is very compatible with the Λ-CCSD(T) prediction and for this Hamiltonian also in excellent agreement with the experimental value.

In Fig. 7.9, we study the same trends for the charge radius. We see a similar systematic convergence, with the caveat that the convergence in $e_{\mathrm{max,3b}}$ seems to be considerably slower. If one compares HF to IMSRG(2) to IMSRG(3)-N^7, one sees that IMSRG(3) corrections to the IMSRG(2) are not much smaller

than the IMSRG(2) corrections to HF. This seems to indicate the radii may have relatively larger IMSRG(3) corrections than ground-state energies, but this must be established more systematically across various nuclei and for various Hamiltonians.

The two examples above are based on single-reference IMSRG(3)-N^7 calculations, employing the standard decoupling described in Sec. 4.3. The applications discussed in the following chapters will mostly make use of the VS-IMSRG, both to easily describe open-shell systems and to access spectra. In the VS-IMSRG, we decouple an appropriate valence-space Hamiltonian as outlined in Sec. 4.4 to be subsequently diagonalized by the KSHELL code [370]. KSHELL is tremendously powerful and very flexible, but it has the notable limitation that it cannot include three-body Hamiltonian contributions in the diagonalization and cannot evaluate expectation values of three-body operators. At the VS-IMSRG(2) level, this is perfectly suitable as the normal-ordered two-body truncation restricts the shell-model Hamiltonian and the effective operators to the two-body level. At the VS-IMSRG(3) level, after completing the VS-IMSRG(3) solution we have a residual three-body Hamiltonian $W(s \to \infty)$ and also residual three-body terms in our operators $O^{(3B)}(s \to \infty)$. To work with KSHELL, we make the pragmatic choice to truncate all three-body terms before redoing the normal ordering to arrive at shell-model matrix elements. This corresponds to leaving out Eq. (3.38) and setting $H^{(3B)} = 0$ in Eqs. (3.39)–(3.41). This second normal-ordered two-body approximation relies on the hierarchy of many-body operators being maintained during the many-body solution, such that the truncated three-body terms are substantially less important than the kept two- and one-body terms. This maintained hierarchy is a reasonable assumption as if this is not the case then there are likely also more fundamental problems for the IMSRG many-body truncation. Still, it is an approximation that we would like to test in future work, working with no-core shell-model codes [89, 330, 369] able to handle three-body forces and operators.

Overview and perspectives

Our work in this chapter and in Ref. [45] breaks ground on high-precision nuclear structure calculations with the IMSRG(3). In particular, we show systematic many-body convergence from the IMSRG(2) to the IMSRG(3) for ground-state energies by providing detailed comparisons against exact results. This work establishes robust ways to approximate the IMSRG(3) at lower computational cost based on computational and perturbative schemes, and we show that these low-cost approximations provide nearly all of the precision of the IMSRG(3), which is especially beneficial in nonperturbative contexts. This opens the path to IMSRG(3) calculations in realistic model spaces for the precision description of nuclei, and we introduce the standard truncations $e_{\mathrm{max,3b}}$, $E_{3\mathrm{max}}$ that we use to truncate three-body operators to make IMSRG(3) calculations in medium-mass nuclei possible. These calculations are explored in the following chapters in various applications in close connection to nuclear structure experiment.

The IMSRG(3) developments here are a milestone for nuclear structure theory, but much still remains to be done. A key outstanding task is the efficient, scalable computational implementation of the IMSRG(3) to give fully converged results in heavy systems. Moreover, it is still very important to understand the many-body content of the IMSRG(2) and IMSRG(3) better to efficiently approximate the IMSRG(3) in a physics-guided manner. This understanding will certainly be observable-dependent, and building up an understanding of how different observables converge differently (as seen in Figs. 7.8 and 7.9) requires a better understanding of static versus dynamical correlations for short-range and long-range operators. Nevertheless, the IMSRG(3) is a key component in quantifying many-body uncertainties, which will make further understanding the method and many-body physics for different nuclear structure observables while accounting for input and method uncertainties possible.

Part III

Applications

Chapter 8

Ab initio studies of stable carbon isotopes

Light nuclei exhibit several interesting phenomena that make them attractive to study. Two notable examples are the relevance of α clusters in the structure of many light nuclei [22] and the appearance of neutron and proton halo nuclei near the drip lines [13, 14, 16]. Capturing these emergent many-body phenomena is theoretically challenging and represents an excellent test case for nuclear theory.

Recent measurements at the COALA (Collinear Apparatus for Laser Spectroscopy and Applied Science) setup at the Technische Universität Darmstadt [372, 373] investigated the charge radii of ^{12}C and ^{13}C using laser spectroscopy [108, 374–377]. We seek to provide complementary nuclear theory predictions using the VS-IMSRG. Carbon isotopes, especially ^{12}C, are not the ideal systems for the IMSRG: first, they are in a mass range that can be reached by exact methods, making the use of a scalable, but approximate many-body method less attractive; second, the relevance of clustering especially in ^{12}C is known to be challenging for many-body expansion methods, where the truncation at the two-body level may be insufficient [250, 261]. Still, for the VS-IMSRG(3) it represents a case where, due to the light masses, we are able to give well-converged IMSRG(3) results. We can use this to test the IMSRG(3) in systems with challenging nuclear structure and understand how it performs relative to other approaches.

In this chapter, we present VS-IMSRG(3)-N^7 results for ground-state energies and charge radii of ^{12}C and ^{13}C, focusing on the convergence of the many-body expansion and the behavior of the IMSRG results beyond the IMSRG(2) level. This work is in preparation for publication together with the results of the all-optical charge radius measurements at COALA by Patrick Müller *et al.* [108].

8.1 Calculational details

In this chapter, we solve for the ground-state properties of carbon isotopes using the VS-IMSRG, decoupling a p-shell valence-space Hamiltonian using the IMSRG++ code [365] for a subsequent diagonalization with KSHELL [370]. Our VS-IMSRG(3)-N^7 calculations use the strategy described in Sec. 7.5, employing a normal-ordered two-body approximation for the initial Hamiltonian and for the final decoupled operators.

For all calculations, we construct a hybrid HF+NAT basis (see Sec. 6.1.2.2) using an $e_{\max}^{\mathrm{HF/NAT}} = 14$, $E_{3\max} = 22$ model space with a frequency of $\hbar\omega = 16$ MeV. To assess model-space uncertainties we vary $e_{\max}^{\mathrm{HF/NAT}}$ and $E_{3\max}$ by ± 2. Following the basis construction, we truncate our model space to $e_{\max} = 10$ for the VS-IMSRG solution. Again, we vary this truncation by ± 2 to assess model-space uncertainties. We find ground-state energies and charge radii of ^{12}C and ^{13}C to be nicely converged for this choice of model space. For our VS-IMSRG(3)-N^7 calculations, we truncate our three-body operators using the model-space

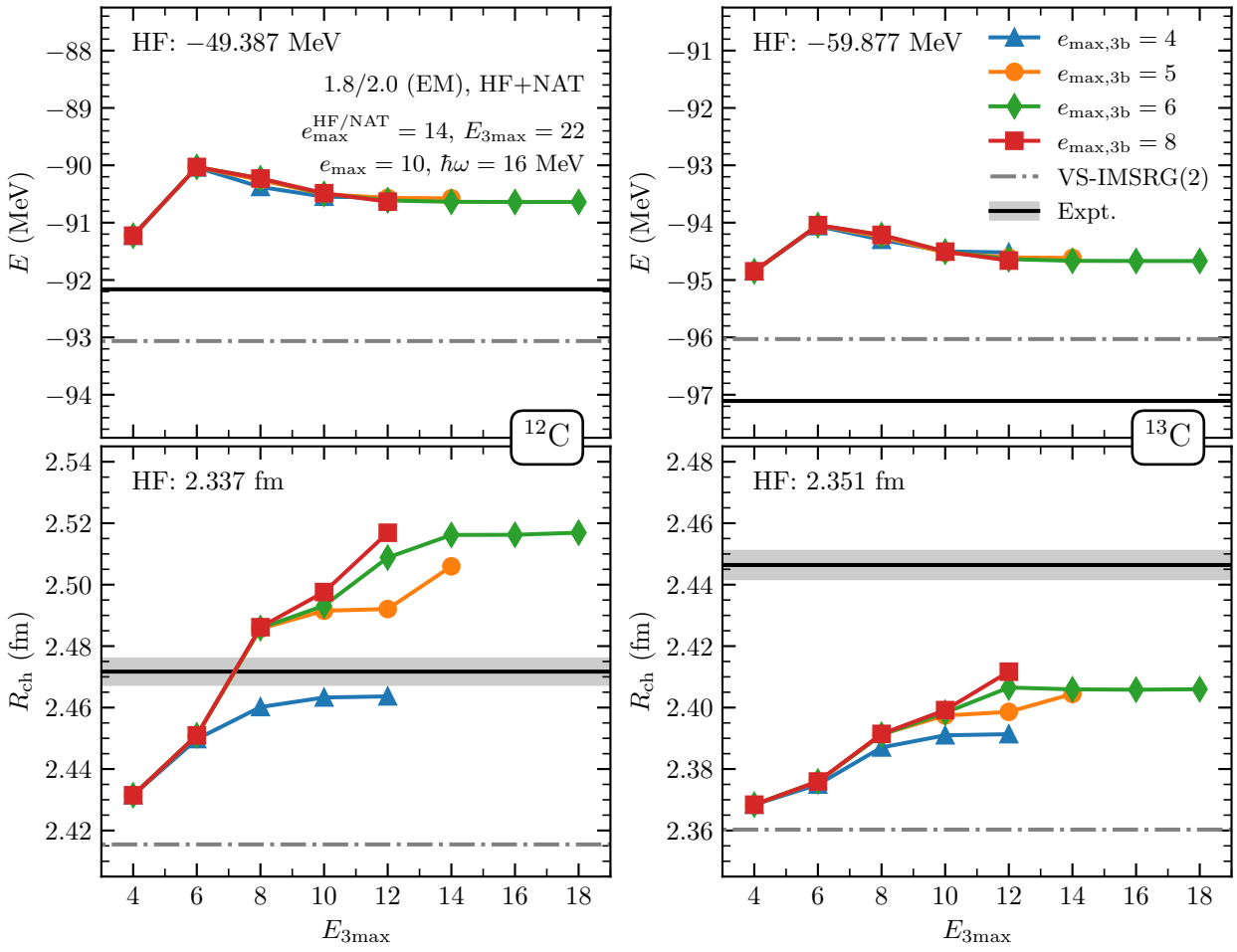

Figure 8.1: VS-IMSRG(3) predictions for ground-state energies and charge radii of ^{12}C and ^{13}C. Ground-state energies E (*top*) and charge radii R_{ch} (*bottom*) for ^{12}C (*left*) and ^{13}C (*right*) predicted by VS-IMSRG calculations using the 1.8/2.0 (EM) Hamiltonian [171]. Results from VS-IMSRG(3)-N^7 calculations are presented as a function of the three-body truncations $e_{\max,3b}$ and $E_{3\max}$. For each observable, the Hartree-Fock ground-state expectation value is shown in the top left corner of the appropriate panel. Our VS-IMSRG calculations use HF+NAT bases computed in an $e_{\max}^{\mathrm{HF/NAT}} = 14$, $E_{3\max} = 22$, $\hbar\omega = 16$ MeV model space before being truncated to $e_{\max} = 10$ for the IMSRG calculation. Experimental values from Refs. [108, 377, 379].

parameters $e_{\max,3b}$ and $E_{3\max}$ as described in Sec. 7.5 and investigate convergence with respect to these parameters.

We compute radii using Eq. (4.4). In this chapter, we use updated values for the proton and neutron squared charge radii from Ref. [378], with $r_{\mathrm{p}}^2 = 0.7071\,\mathrm{fm}^2$ and $r_{\mathrm{n}}^2 = -0.1155\,\mathrm{fm}^2$.

8.2 Ground-state properties

We start by considering IMSRG calculations of ^{13}C using the 1.8/2.0 (EM) Hamiltonian [171] in the right panels of Fig. 8.1. Hartree-Fock values for the ground-state energy and charge radius are given in the top left corner, and the IMSRG(2) values are shown as a dash-dotted gray line. We note that the IMSRG(2) correlation energy is 36 MeV, and the IMSRG(2) correction to the radius is very small at just over 0.01 fm.

Relative to the experimental values shown as solid black lines, the IMSRG(2) predictions underbind ^{13}C by 1 MeV and give a charge radius that is substantially too small. This is consistent with the general behavior of the 1.8/2.0 (EM) Hamiltonian giving good reproduction of ground-state energies while underpredicting charge radii systematically [3]. However, as we see in Sec. 8.4, this underprediction of the carbon charge radii is shared by all Hamiltonians we investigated.

Considering the IMSRG(3)-N^7 corrections to the energy, we observe very stable convergence in $e_{\mathrm{max,3b}}$ and $E_{3\mathrm{max}}$. Relatively small model-space truncations (for example, $e_{\mathrm{max,3b}} = 4$, $E_{3\mathrm{max}} = 12$) are sufficient to deliver converged results within 200 keV. The total IMSRG(3) corrections to the ground-state energy are about 1.4 MeV. This is a somewhat large correction, nearly 4% of the IMSRG(2) correlation energy, but within reason.

Turning our attention to the charge radius, we see slower convergence in $e_{\mathrm{max,3b}}$ and $E_{3\mathrm{max}}$, as also observed in Sec. 7.5 in ^{16}O for charge radii. It is also worth noting that the IMSRG(3) corrections of around 0.04 fm are large compared to the IMSRG(2) corrections to the HF radius. In this case, it is likely that the HF to IMSRG(2) correction is anomalously small.

Overall, the IMSRG(3) corrections to the ground-state energy and the charge radius converge nicely for ^{13}C, and their magnitudes suggest relatively systematic behavior of the many-body expansion. For the larger radius corrections, one must always keep in mind that charge radii are captured very efficiently at the Hartree-Fock level, and the IMSRG(2) and IMSRG(3) corrections are relatively minor adjustments. The IMSRG(3) corrections to the charge radius serve to improve the theory prediction relative to experiment. For the ground-state energy, however, the agreement with experiment gets worse.

In the left panels of Fig. 8.1, we consider IMSRG calculations of ^{12}C using the 1.8/2.0 (EM) Hamiltonian [171]. At the IMSRG(2) level, we see that ^{12}C is slightly overbound with respect to experiment and the charge radius is slightly underpredicted. For the ground-state energy, we once again observe systematic model-space convergence for our IMSRG(3)-N^7 calculations. The converged IMSRG(3) correction to the IMSRG(2) energy is about 2.4 MeV, about 5.5% of the IMSRG(2) correlation energy. Again, this is somewhat large compared to typical closed-shell systems, but within reason given the more complex structure of ^{12}C. The resulting IMSRG(3) ground-state energy prediction slightly underbinds ^{12}C with respect to experiment.

The picture for the charge radius of ^{12}C is quite different. The IMSRG(2) correction to the radius is 0.08 fm, very large when compared with ^{16}O in Fig. 7.9. The IMSRG(3) corrections on top of this converge much more slowly than in ^{13}C, with a notable large contribution coming in at $e_{\mathrm{max,3b}} = 5$. Overall, in large model spaces it still appears to reach convergence, especially considering the small corrections going from $e_{\mathrm{max,3b}} = 6$ to $e_{\mathrm{max,3b}} = 8$, but the absolute size of the IMSRG(3) charge radius corrections of 0.1 fm is concerning. These large corrections also serve to make the IMSRG(3) charge radius substantially larger than the measured value.

This slower convergence in the charge radius is likely a result of clustering being relevant in ^{12}C, but this hypothesis is difficult to test in the IMSRG. It is not immediately obvious what operator or observable would clearly show signs of clustering, but given such an operator it would be informative to consider it in correlation with charge radii at the IMSRG(2) and IMSRG(3) levels. Regardless, it is clear that it is challenging to fully capture the structure of ^{12}C in the IMSRG, leading to slow convergence of the many-body expansion as evidenced by the larger IMSRG(3) corrections. This is especially pronounced for the charge radius and less pronounced for the ground-state energy, suggesting that while the wave function changes a lot going from the IMSRG(2) to the IMSRG(3) the many-body interactions work out such that the energy is not very sensitive to these changes.

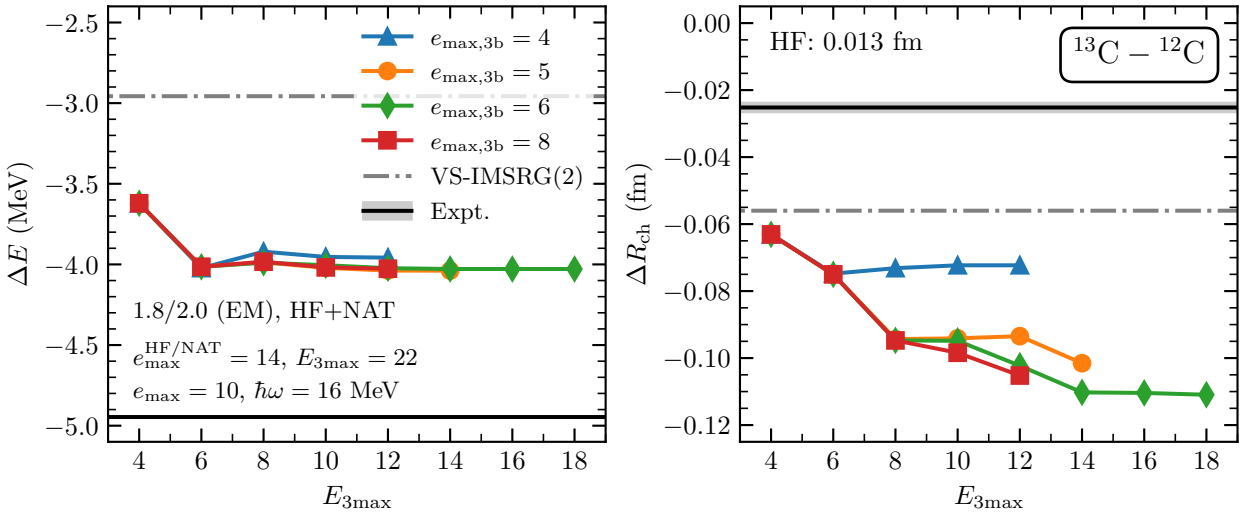

Figure 8.2: VS-IMSRG(3) predictions for differences of ground-state energies and charge radii between ^{13}C and ^{12}C. Differences in ground-state energies E (*left*) and charge radii R_{ch} (*right*) between ^{13}C and ^{12}C predicted by VS-IMSRG calculations using the 1.8/2.0 (EM) Hamiltonian [171]. Results from VS-IMSRG(3)-N^7 calculations are presented as a function of the three-body truncations $e_{\max,3b}$ and $E_{3\max}$. For the charge radius difference, the Hartree-Fock ground-state expectation value is shown in the top left corner of the panel. Our VS-IMSRG calculations use HF+NAT bases computed in an $e_{\max}^{\mathrm{HF/NAT}} = 14$, $E_{3\max} = 22$, $\hbar\omega = 16$ MeV model space before being truncated to $e_{\max} = 10$ for the IMSRG calculation. Experimental values from Refs. [108, 377, 379].

8.3 Differential quantities

In ab initio calculations, considering differential quantities such as radius differences or separation energies is generally advantageous because systematic errors leading to correlated uncertainties cancel out in the difference [3, 44, 47]. In Fig. 8.2, we consider differences of the ground-state energies E and the charge radii R_{ch} between ^{13}C and ^{12}C. In the case of correlated uncertainties, in particular correlated IMSRG(3) model-space uncertainties, these quantities should converge more quickly than their absolute values in Fig. 8.1.

In the left panel of Fig. 8.2, we consider the ground-state energy difference $E_{^{13}\mathrm{C}} - E_{^{12}\mathrm{C}}$, which is simply the negative neutron separation energy $-S_n$. We see considerable IMSRG(3) corrections on the IMSRG(2) prediction, which is not unexpected as we are looking at a difference of two large numbers. Still, the IMSRG(3) values converge very quickly in $e_{\max,3b}$ and $E_{3\max}$, plateauing at -4.0 MeV. This systematic behavior allows for converged results at very modest model-space sizes, making the ab initio prediction in principle substantially cheaper. The resulting energy difference is closer to the experimental value, but still 0.9 MeV too small.

In the right panel of Fig. 8.2, we consider the charge radius difference $R_{\mathrm{ch},^{13}\mathrm{C}} - R_{\mathrm{ch},^{12}\mathrm{C}}$. At the HF level, this quantity is positive, and substantial IMSRG(2) corrections serve to bring it down to a negative value of -0.056 fm. Compared with the experimental value of $-0.0253\,(14)$ fm [108, 377], the IMSRG(2) predicts a much larger decrease in the charge radius from ^{12}C to ^{13}C. The IMSRG(3) corrections on top of this converge very slowly and serve to bring the radius difference even more negative, with an estimated converged value at $-0.11\,(2)$ fm. From the slow convergence, we see that the model-space convergence behaviors in ^{12}C and ^{13}C are not correlated for charge radii. Moreover, the challenges in the description of ^{12}C produce exaggerated IMSRG(3) corrections in the difference, making the IMSRG(3) uncertainty naively estimated based on the difference between the IMSRG(2) and IMSRG(3) predictions 100%. In this

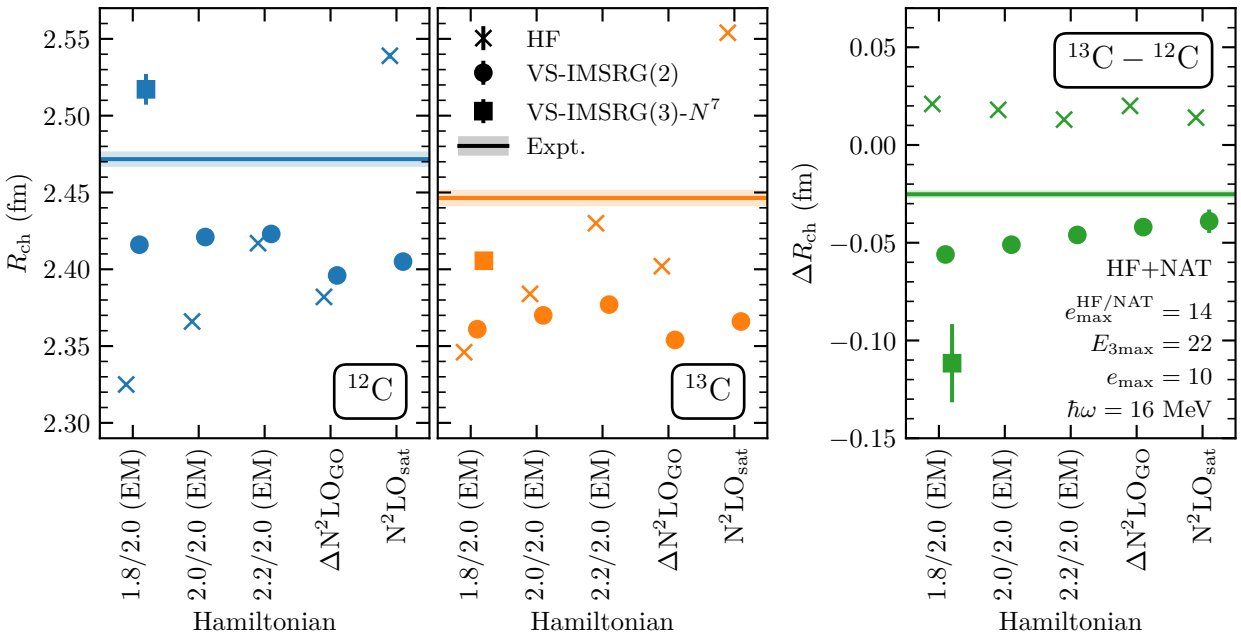

Figure 8.3: Charge radii of ^{12}C and ^{13}C from chiral EFT Hamiltonians. Charge radii R_{ch} of ^{13}C (*center*) and ^{12}C (*left*) along with their difference ΔR_{ch} (*right*) predicted by Hartree-Fock and VS-IMSRG calculations using several Hamiltonians [165, 167, 171]. Our VS-IMSRG calculations use HF+NAT bases computed in an $e_{max}^{HF/NAT} = 14$, $E_{3max} = 22$, $\hbar\omega = 16$ MeV model space before being truncated to $e_{max} = 10$ for the IMSRG calculation. Model-space uncertainties are assessed by variations of $e_{max}^{HF/NAT}$, E_{3max}, and e_{max} for HF and VS-IMSRG(2) calculations and by variations of $e_{max,3b}$ and E_{3max} for VS-IMSRG(3)-N^7 calculations. Experimental values from Ref. [108, 377].

case, given the clearly different structure of ^{12}C and ^{13}C, the predictive power of the IMSRG(3) for the differential charge radius is limited.

8.4 Hamiltonian dependence

A notable trend in Fig. 8.2 is that the charge radius goes from positive at the HF level to negative at the IMSRG(2) level. Standard intuition would expect an increase in the charge radius with increasing mass number as the additional neutron serves to make the proton density more diffuse. Between ^{12}C and ^{13}C and also in many other light systems, this is not the case. An intuitive explanation is that ^{12}C has an anomalously large radius due to its structure as three α particles. This cluster structure is softened out by the addition of a neutron in ^{13}C, ultimately leading to a smaller charge radius. The experimental charge radius difference of $-0.0253\,(14)$ fm [108, 377] is intuitively consistent with this picture, but on its own not necessarily evidence of the relevance of clustering in ^{12}C and ^{13}C.

In Fig. 8.3, we consider IMSRG(2) calculations of charge radii of ^{12}C and ^{13}C along with their difference for several Hamiltonians [165, 167, 171]. We also include the IMSRG(3)-N^7 results for the 1.8/2.0 (EM) Hamiltonian discussed in the previous section. Looking at the absolute charge radii predicted by the different Hamiltonians, we see that at the HF level the predictions are very scattered, but in a correlated way in ^{12}C and ^{13}C. Going to the IMSRG(2), we see that many-body correlations bring the charge radius predictions for the different Hamiltonians into much better agreement [$2.42\,(2)$ fm for ^{12}C and $2.37\,(2)$ fm for ^{13}C]. Both predictions are smaller than the experimental radii, and given the consistency across many

Hamiltonians this suggests that this underprediction is likely not simply a Hamiltonian deficiency but perhaps related to the many-body solution.

This remarkable consistency also extends to the charge radius difference between ^{13}C and ^{12}C, shown in the right panel of Fig. 8.3. All Hamiltonians predict a positive radius difference at the HF level around 0.02 fm, but at the IMSRG(2) level this is brought down consistently to $-0.05\,(1)$ fm. No Hamiltonian gives a prediction that is directly compatible with the experimental value around -0.025 fm, but the many-body uncertainties for this observable are very large, as discussed in the previous section. One clearly sees that Hamiltonian uncertainties are very correlated in ^{12}C and ^{13}C. One also sees that the IMSRG(2) and beyond-mean-field effects more generally are key to producing a decreasing charge radius change from ^{12}C to ^{13}C.

Overview and perspectives

Our work in this chapter explores the VS-IMSRG(3) in converged calculations of carbon isotopes. Despite light systems with cluster structures like ^{12}C and ^{13}C not being ideal applications for the IMSRG, we find that in many cases the IMSRG(3) gives controlled, albeit large corrections to IMSRG(2) predictions. For the charge radius of ^{12}C, we find large corrections with challenging systematics from the IMSRG(2) and IMSRG(3), suggesting that the many-body truncation is insufficient to capture the essential physics relevant for the observable. This also has a pronounced effect on the predicted charge radius difference between ^{13}C and ^{12}C, with the IMSRG(3) giving nearly 100% corrections to this quantity. At the same time, even though this observable is challenging for the IMSRG, it is clear that many-body effects beyond Hartree-Fock are essential to produce a negative charge radius difference between ^{13}C and ^{12}C.

In light systems with pronounced cluster structures, the VS-IMSRG(3)-N^7 should clearly still not be the method of choice. Resolving such cluster structures in the many-body expansion requires either a more complete IMSRG(3) approximation or the inclusion of higher-body operators beyond even the IMSRG(3), making it an inefficient choice to describe systems where exact methods [88, 89], lattice theories that naturally capture clustering [96, 97, 380], and cluster effective theories [54, 381, 382] are available. Employing a more informed reference state in IMSRG calculations, from, for example, a truncated NCSM or Hartree-Fock-Bogoliubov calculation [250, 302], and solving the IMSRG in a multireference formulation may improve this somewhat, but previous studies have found considerable uncertainties for multireference IMSRG and in-medium NCSM calculations in ^{12}C [250]. It is an outstanding task to also include three-body operators in such calculations, which should give more complete insight into the many-body expansion and resulting uncertainties. There are still a few open questions from this study that present interesting avenues for future study: What is the effect of residual three-body operators truncated in the VS-IMSRG(3), and are these able to help with the description of clustering in ^{12}C? What easily accessible operators can be evaluated by many-body methods to quantify clustering, and how significantly do these operators change from the IMSRG(2) to the IMSRG(3) in ^{12}C? We expect to explore the former in the near future, but the latter will be more challenging to explore within the IMSRG, as most approaches to address this use coordinate-space evaluations of the density [380, 383–386].

Chapter 9

IMSRG(3) investigations of calcium isotopes

The calcium isotopic chain is particularly exciting for nuclear structure, both experimentally and theoretically. Experimentally, ^{40}Ca and ^{48}Ca (both $Z = 20$ and $N = 20$ and $N = 28$, respectively) are well established as doubly-magic nuclei, but recent measurements from TITAN at TRIUMF, from ISOLTRAP at ISOLDE, and at the Radioactive Isotope Beam Factory (RIBF) at RIKEN have suggested $N = 32$ in ^{52}Ca and $N = 34$ in ^{54}Ca as new magic numbers [2, 20, 387–389]. On the other hand, measured charge radius differences from COLLAPS at ISOLDE found a puzzlingly large increase in the charge radius of ^{52}Ca relative to ^{48}Ca [307], a trend also observed in potassium, manganese, iron, and nickel isotopes at BECOLA at the National Superconducting Cyclotron Laboratory (NSCL) and at COLLAPS and CRIS at ISOLDE [390–396], calling into question $N = 32$ as a shell closure. Further planned measurements of charge radii of ^{53}Ca and ^{54}Ca at COLLAPS hope to give further insight into these seemingly contradictory trends [397]. Additionally, the neutron drip line in calcium isotopes is not yet determined. ^{60}Ca has been observed at RIBF [398], but with indications that it may not be doubly magic [399, 400], and measurements of the structure of ^{60}Ca and beyond are foreseen at the Facility for Rare Isotope Beams (FRIB) and the Facility for Antiproton and Ion Research (FAIR) [401, 402]. Finally, back in the stable calcium isotopes, high-precision laser spectroscopy measurements are searching for signals of new physics in isotope shifts [403–405], a topic we discuss for stable ytterbium isotopes in Chapter 10.

At the same time, calcium isotopes are a theoretically interesting and accessible region for a variety of reasons. First, calcium nuclei are spherical and relatively light, simplifying the theoretical treatment and reducing the cost of ab initio calculations. Together with the $Z = 20$ shell closure, the (sub)shell closures at $N = 20$, 28, 32, and 34 allowed initial single-reference CC studies with particle-attached extensions to access many isotopes (all doubly-magic nuclei and their neighbors) [37]. Subsequent developments opened the full isotopic chain up to SCGF and multireference IMSRG calculations [38, 302], the valence-space IMSRG [3, 261], and recently Bogoliubov coupled-cluster theory [335]. Ab initio calculations generally see the same signatures suggesting shell closures at $N = 32$ and $N = 34$ as experiment, high 2^+ excitation energies and decreases in two-neutron separation energies beyond the shell closures [3, 37, 39, 44, 302]. At the same time, ab initio calculations currently cannot reproduce the large increase in charge radii from ^{48}Ca to ^{52}Ca [307], with many Hamiltonians and many-body methods giving a similar underprediction. For the neutron dripline in calcium, several ab initio calculations suggest that it lies at ^{60}Ca [335, 406, 407], but the trends of predicted two-neutron separation energies are so close to zero and so flat with increasing N that a dripline between $N = 40$ and 50 or even beyond ^{70}Ca has reasonable probability [44], consistent with the findings from density functional theory [80, 408]. From the IMSRG perspective, the clear challenges

to address in calcium are: the overprediction of the 2^+ energies of ^{48}Ca, ^{52}Ca, and ^{54}Ca relative to experiment [3], a trend also seen in CC calculations at the CCSD level and resolved by the inclusion of three-body operators [39]; and missing trends in charge radii, including the crown between ^{40}Ca and ^{48}Ca and the steep increase from ^{48}Ca to ^{52}Ca [307]. Addressing these challenges requires the IMSRG(3) to quantify the effects of missing three-body operators in the IMSRG(2).

In this chapter, we perform preliminary investigations of the structure of calcium isotopes with the IMSRG(3). We focus our discussion on ^{48}Ca, comparing the IMSRG(3)-N^7 to the VS-IMSRG(3)-N^7 for ground-state properties and considering also spectra in the VS-IMSRG, where the VS-IMSRG(2) overpredicts the first 2^+ excitation energy. We then turn our attention to trends for the IMSRG(3) corrections to charge radii in neutron-rich calcium isotopes, seeking to understand the discrepancies between theory and experiment. We find in all of these cases that we are unable to fully converge the IMSRG(3) contributions with respect to our model-space truncations, so we discuss perspectives for reaching convergence, including more efficient model-space truncations and new computational approaches.

9.1 Improved structure of calcium-48

In this section, we solve for the ground-state properties and low-lying spectrum of ^{48}Ca using the IMSRG and VS-IMSRG. For all calculations, we use the 1.8/2.0 (EM) Hamiltonian [171]. We construct a NAT basis (see Sec. 6.1) using an $e_{\max}^{\mathrm{HF/NAT}} = 16$, $E_{3\max} = 22$ model space with a frequency of $\hbar\omega = 16$ MeV. Following the basis construction, we truncate our model space to $e_{\max} = 12$ for the (VS-)IMSRG solution. At the IMSRG(2) level, we varied this truncation to $e_{\max} = 10$ and found only a 200 keV change in the ground-state energy, suggesting this model space is well converged. For our (VS-)IMSRG(3)-N^7 calculations, we truncate our three-body operators using the model-space parameters $e_{\max,3b}$ and $E_{3\max}$ as described in Sec. 7.5 and investigate convergence with respect to these parameters. All VS-IMSRG calculations decouple a neutron pf-shell valence-space Hamiltonian with the IMSRG++ code [365] for a subsequent diagonalization with KSHELL [370]. Our VS-IMSRG(3)-N^7 calculations use the strategy described in Sec. 7.5, employing a normal-ordered two-body approximation for the initial Hamiltonian and for the final decoupled operators.

9.1.1 Single-reference IMSRG calculations

We begin by performing single-reference IMSRG calculations of the ground state of ^{48}Ca. Accessing excited state properties requires either an equation-of-motion extension on top of the ground-state result [39, 264] or using the valence-space IMSRG, as we consider in the next section.

In Fig. 9.1, we consider the ground-state energy and charge radius of ^{48}Ca in the left and right panels, respectively. We show IMSRG(3)-N^7 results as a function of $e_{\max,3b}$ and $E_{3\max}$ and compare against the experimental value for the ground-state energy and results from coupled-cluster theory employing the same Hamiltonian [40, 371, 409, 410]. Let us first consider the ground-state energy on the left. We see that the IMSRG(2) result lies very close to the experimental value, a feature of the 1.8/2.0 (EM) Hamiltonian and a result of the high precision of the IMSRG(2) for ground-state energies relative to, for example, CCSD. The Λ-CCSD(T) and CCSDT-1 predictions are also very close, overbinding ^{48}Ca by only 3 MeV and 4.5 MeV, respectively.

The IMSRG(3)-N^7 predictions show very systematic convergence behavior with increasing three-body model-space size. We are able to reach the limit $E_{3\max} = 3e_{\max,3b}$ for both $e_{\max,3b} = 4$ and 5 and are nearly able to do so for $e_{\max,3b} = 6$. We find that the IMSRG(3) corrections to the ground-state energy are small and attractive, consistent in sign and magnitude with the difference between the IMSRG(2) and Λ-CCSD(T) predictions. The convergence is, however, notably slower than in ^{16}O in Fig. 7.8. For

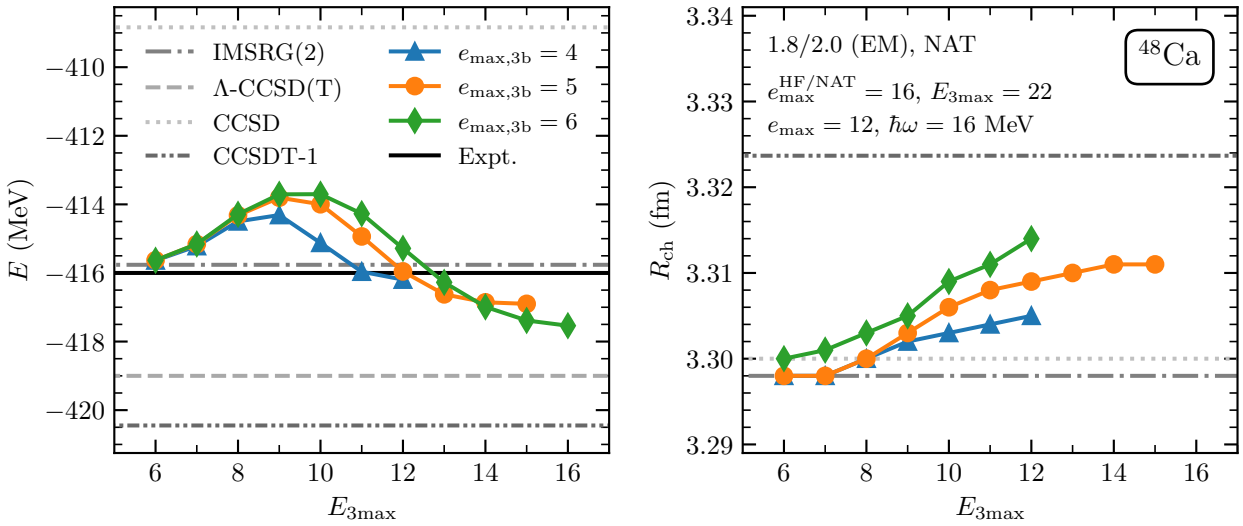

Figure 9.1: Ground-state properties of ^{48}Ca from IMSRG(3) calculations. Ground-state energies E and charge radii R_{ch} from IMSRG(2) and IMSRG(3)-N^7 calculations of ^{48}Ca. We show IMSRG(3)-N^7 predictions as a function of $e_{\mathrm{max,3b}}$ and $E_{3\mathrm{max}}$. All IMSRG calculations use the 1.8/2.0 (EM) Hamiltonian and a NAT basis constructed in an $e_{\mathrm{max}}^{\mathrm{HF/NAT}} = 16$, $E_{3\mathrm{max}} = 22$, $\hbar\omega = 16$ MeV model space before being truncated to $e_{\mathrm{max}} = 12$ for the IMSRG calculation. For comparison, we show the experimental ground-state energy of ^{48}Ca from Ref. [379], the CCSD and CCSDT-1 ground-state energies from F. Bonaiti [409], the Λ-CCSD(T) ground-state energy from Ref. [371], the CCSD charge radius from Ref. [40], and the CCSDT-1 charge radius from Refs. [409, 410].

^{16}O, going from $e_{\mathrm{max,3b}} = 5$ to $e_{\mathrm{max,3b}} = 6$ changed the ground-state energy by about 150 keV, while for ^{48}Ca it changes by 640 keV. This is an unsurprising sign that heavier nuclei require larger three-body model-space truncations to converge the effects of three-body operators. Even at $e_{\mathrm{max,3b}} = 6$, $E_{3\mathrm{max}} = 16$, our model-space uncertainty is still roughly 600 keV, while our IMSRG(3) correction is in total less than 2 MeV. With this in mind, our results are not acceptably converged, but the trend is consistent with coupled-cluster with triples, and the fully converged result will likely lie quite close to the Λ-CCSD(T) value.

We note that Λ-CCSD(T) is a perturbative triples scheme, meaning that the effects of three-body operators are computed once perturbatively rather than solved for fully nonperturbatively in the coupled-cluster equations. The IMSRG(3)-N^7 treats three-body effects nonperturbatively, keeping three-body operators fully in the IMSRG equations, making it a more complete many-body approach than Λ-CCSD(T), more closely related to CCSDT-1. Thus, when fully converged IMSRG(3)-N^7 results are available, we would interpret them as more precise than the Λ-CCSD(T) results and directly comparable to the CCSDT-1 results. All in all, we see nice consistency between the IMSRG(3)-N^7, Λ-CCSD(T), and CCSDT-1 results, suggesting the remaining uncertainty on the ground-state energy is very small, likely around 1 MeV. We also note that the correlation energy for our IMSRG calculations is roughly 110 MeV. Comparing the 2–3 MeV IMSRG(3)-N^7 ground-state energy corrections to the correlation energy, we see that the IMSRG(2) has a many-body uncertainty of around 2% of E_{corr} on ground-state energies.

In the right panel of Fig. 9.1, we consider IMSRG(2) and IMSRG(3)-N^7 predictions for the charge radius. We note that the 1.8/2.0 (EM) Hamiltonian generally gives smaller charge radii than experiment despite predicting binding energies quite well, which can be traced back to a saturation density in nuclear matter that is too high [3, 166, 171]. For this reason, we only compare against results from CCSD and CCSDT-1 from Refs. [40, 409, 410]. The IMSRG(2) and CCSD results are very consistent, agreeing to

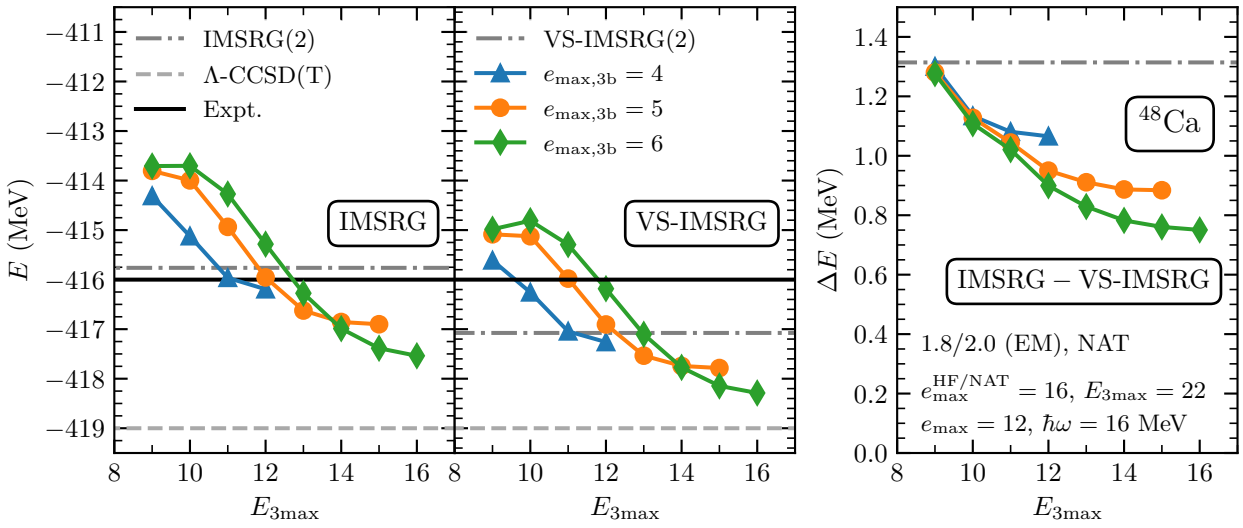

Figure 9.2: Comparison of IMSRG(3) and VS-IMSRG(3) ground-state energies of ^{48}Ca. Ground-state energies E from IMSRG(2) and IMSRG(3)-N^7 calculations of ^{48}Ca (*left*) compared with predictions from VS-IMSRG(2) and VS-IMSRG(3)-N^7 calculations of ^{48}Ca (*center*). On the right we explicitly show the differences of IMSRG and VS-IMSRG ground-state energy predictions ΔE for the same many-body and model-space truncations [for example, the dash-dotted gray line is the difference of the VS-IMSRG(2) value from the IMSRG(2) value]. We show (VS-)IMSRG(3)-N^7 predictions as a function of $e_{\mathrm{max,3b}}$ and $E_{3\mathrm{max}}$. All IMSRG calculations use the 1.8/2.0 (EM) Hamiltonian and a NAT basis constructed in an $e_{\mathrm{max}}^{\mathrm{HF/NAT}} = 16$, $E_{3\mathrm{max}} = 22$, $\hbar\omega = 16$ MeV model space before being truncated to $e_{\mathrm{max}} = 12$ for the IMSRG calculation. For comparison, we show the experimental ground-state energy of ^{48}Ca from Ref. [379] and the Λ-CCSD(T) ground-state energy from Ref. [371].

within 0.002 fm. Comparing this with the NAT reference-state expectation value for the charge radius, 3.277 fm, we find that both IMSRG(2) and CCSD give only small, but very consistent corrections.

Considering the IMSRG(3)-N^7 predictions, we find again that charge radii converge more slowly in our model-space parameters than ground-state energies. Due to computational constraints, we were unable to reach $e_{\mathrm{max,3b}} = 6$, $E_{3\mathrm{max}} = 16$ as for energies, but estimating based on the current convergence pattern, we observe that each step in $e_{\mathrm{max,3b}}$ gives a correction on the order of 0.005 fm. The corrections are towards slightly larger radii, but overall these are relatively small corrections. This tracks well with the intuition that charge radii in most systems are quantitatively captured quite well at the mean-field level and many-body methods only include very small corrections on top of this. Still, the order of magnitude of the full IMSRG(3)-N^7 corrections, which could plausibly be anywhere from 0.02 fm to 0.04 fm, is the same size as the IMSRG(2) corrections to the mean-field prediction. These trends are also consistent with the 1% uncertainty on the charge radius at the CCSD level as assessed by Hagen *et al.* [40] and with the CCSDT-1 results from Ref. [410].

9.1.2 Valence-space IMSRG calculations

We now consider valence-space IMSRG calculations of ^{48}Ca, which are also able to access excited states. We note that (as discussed in Sections 4.3 and 4.4) the decoupling conditions and resulting unitary transformations for the IMSRG and VS-IMSRG are different, but without truncations equivalent. Thus the differences between IMSRG and VS-IMSRG predictions are reflective of the many-body truncation employed. We would expect the IMSRG(3) to reduce differences between single-reference and valence-space results at the IMSRG(2) level due to reduced many-body uncertainties.

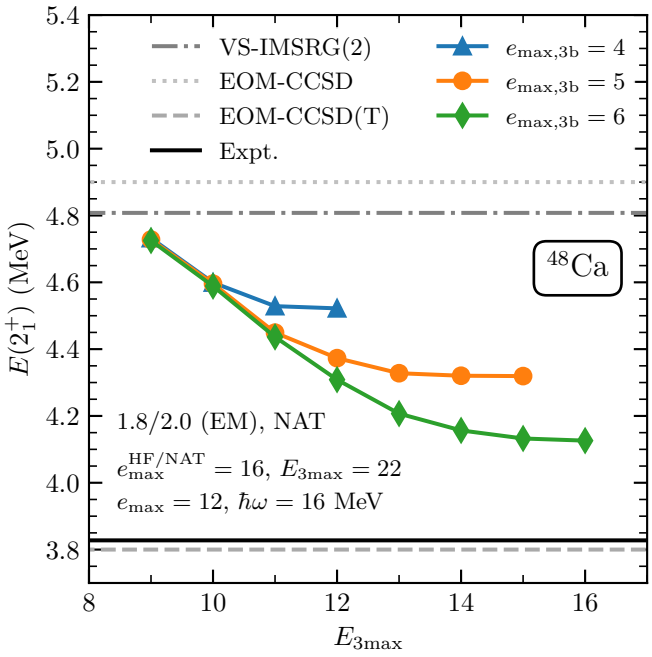

Figure 9.3: Improved 2^+ energy of ^{48}Ca from VS-IMSRG(3) calculations. Excitation energies for the first 2^+ state of ^{48}Ca, $E(2_1^+)$, from VS-IMSRG(2) and VS-IMSRG(3)-N^7 calculations. We show VS-IMSRG(3)-N^7 predictions as a function of $e_{\mathrm{max,3b}}$ and E_{3max}. All IMSRG calculations use the 1.8/2.0 (EM) Hamiltonian and a NAT basis constructed in an $e_{\mathrm{max}}^{\mathrm{HF/NAT}} = 16$, $E_{\mathrm{3max}} = 22$, $\hbar\omega = 16$ MeV model space before being truncated to $e_{\mathrm{max}} = 12$ for the IMSRG calculation. For comparison, we show the experimental value from Ref. [303] and the EOM-CCSD and EOM-CCSD(T) predictions from Ref. [39].

In Fig. 9.2, we compare IMSRG and VS-IMSRG predictions for the ground-state energy of ^{48}Ca employing the same model-space truncations and Hamiltonian. We see that the convergence of the IMSRG(3)-N^7 predictions in the left panel (the same as in Fig. 9.1) and the convergence of the VS-IMSRG(3)-N^7 predictions in the center panel look very similar, simply with an apparent overall offset. This overall offset is the difference between the IMSRG(2) and the VS-IMSRG(2) due to the many-body truncation discussed previously. To gain some insight into this difference and how it changes due to the IMSRG(3)-N^7, we consider the difference explicitly in the panel on the right.

At the IMSRG(2) level, the IMSRG(2) prediction lies 1.3 MeV above the VS-IMSRG(2) prediction. Going to the (VS-)IMSRG(3)-N^7, we see that including three-body operators systematically decreases this difference with increasing three-body model-space truncations. For the largest truncations we consider, with $e_{\mathrm{max,3b}} = 6$, $E_{\mathrm{3max}} = 16$, we find that this difference is decreased to nearly 750 keV. This excellently demonstrates the reduced many-body uncertainty and systematic improvement that the IMSRG(3) offers, in this case improving the consistency between the IMSRG and VS-IMSRG for systems that can be treated in both approaches.

We now turn our attention to the excitation energy of the first 2^+ state of ^{48}Ca. As discussed in Sec. 4.6, this is a case where the VS-IMSRG(2) systematically overpredicts the 2^+ energy, which is an indicator of the doubly-magic nature of ^{48}Ca. This can be seen in Fig. 9.3, comparing the gray dash-dotted line indicating the VS-IMSRG(2) prediction with the solid black line indicating the experimental value. In coupled-cluster theory, predictions using the same 1.8/2.0 (EM) Hamiltonian without triples, the dotted EOM-CCSD line, saw the same overprediction of the 2^+ energy, giving results quite compatible with the VS-IMSRG(2) prediction [39]. Including triples, the dashed EOM-CCSD(T) line, brings the 2^+ energy

down into excellent agreement with experiment, consistent with the excellent agreement for spectra for other calcium isotopes for the 1.8/2.0 (EM) Hamiltonian.

We see that including three-body operators in the IMSRG solution via the VS-IMSRG(3)-N^7 does the same, systematically bringing down the 2^+ energy towards the EOM-CCSD(T) and experimental values. For the largest model-space truncation we consider, $e_{\mathrm{max,3b}} = 6$, $E_{3\mathrm{max}} = 16$, the 2^+ energy is down to 4.15 MeV, a nearly 15% reduction. This establishes excitation energies at shell closures as an observable where the IMSRG(3) is necessary for a quantitative description. This is to be contrasted with ground-state energies and charge radii, where the IMSRG(3) is nice to have for precision and many-body uncertainty quantification but the description at the IMSRG(2) level is already very good.

At the same time, we see that the convergence challenges for ground-state properties are also present for the 2^+ energy. The convergence behavior is systematic, and we are essentially fully converged in $E_{3\mathrm{max}}$ for the truncations shown, but we clearly need to extend our calculations to higher $e_{\mathrm{max,3b}}$ to get a handle on the three-body model-space uncertainty. In the next section, we consider preliminary calculations exploring correlated model-space uncertainties in neighboring calcium isotopes as a way to gain insight into IMSRG(3) corrections without being able to give converged results. Then, in the following section, we discuss perspectives and numerical strategies to surmount the current computational limititations on IMSRG(3) calculations. Nonetheless, the improvements in the description of the structure of ^{48}Ca offered by the VS-IMSRG(3)-N^7 represent a significant step forward for the IMSRG and motivate further developments and applications of the method.

9.2 Trends of IMSRG(3) corrections to charge radii

In this section, motivated by the slow convergence of observables in VS-IMSRG(3)-N^7 calculations with respect to $e_{\mathrm{max,3b}}$ and $E_{3\mathrm{max}}$, we consider correlated model-space uncertainties for VS-IMSRG(3)-N^7 calculations of the charge radii of ^{44}Ca, ^{48}Ca, ^{50}Ca, ^{52}Ca, and ^{54}Ca. We use the 1.8/2.0 (EM) Hamiltonian [171] and construct an HF+NAT basis (see Sec. 6.1.2.2) using an $e_{\mathrm{max}}^{\mathrm{HF/NAT}} = 16$, $E_{3\mathrm{max}} = 24$ model space with a frequency of $\hbar\omega = 16\,\mathrm{MeV}$. Following the basis construction, we truncate our model space to $e_{\mathrm{max}} = 10$ for the VS-IMSRG solution. The $e_{\mathrm{max}} = 10$ truncation gives predictions for charge radii at the VS-IMSRG(2) level that are converged to within 0.003 fm for ^{54}Ca and less for the remaining isotopes.

We are interested in the corrections to the charge radius due to the IMSRG(3),

$$\Delta R_{\mathrm{ch,IMSRG(3)}}(e_{\mathrm{max,3b}}, E_{3\mathrm{max}}) = R_{\mathrm{ch,IMSRG(3)}}(e_{\mathrm{max,3b}}, E_{3\mathrm{max}}) - R_{\mathrm{ch,IMSRG(2)}}\,, \tag{9.1}$$

and show these for different isotope pairs in Fig. 9.4. The different symbol colors indicate different values of $E_{3\mathrm{max}}$, and the different symbols indicate different values of $e_{\mathrm{max,3b}}$. One immediately sees that the IMSRG(3) corrections are highly correlated between different calcium isotopes, even between ^{44}Ca and ^{52}Ca. This is interesting because these systems are already rather far apart, separated by eight neutrons and a shell closure, and quite different in terms of structure. ^{44}Ca is definitely not a doubly-magic nucleus while ^{52}Ca has many features that suggest it is doubly magic.

Such tight correlations as we observe here are very powerful, because they can be determined in small "cheap" model-space sizes and then used to transfer high-fidelity calculations from one isotope into robust predictions for neighboring isotopes based on the correlation. Even without converged calculations for any isotopes, we can use these correlations to give some preliminary insight into what happens to the charge radii of ^{48}Ca and ^{52}Ca due to the IMSRG(3). We note first that all corrections due to the VS-IMSRG(3)-N^7 are towards larger charge radii. Second, we consider how the points lie relative to the black lines, which indicate the case that the IMSRG(3) corrections in both systems are identical. We see that for ^{52}Ca vs. ^{48}Ca,

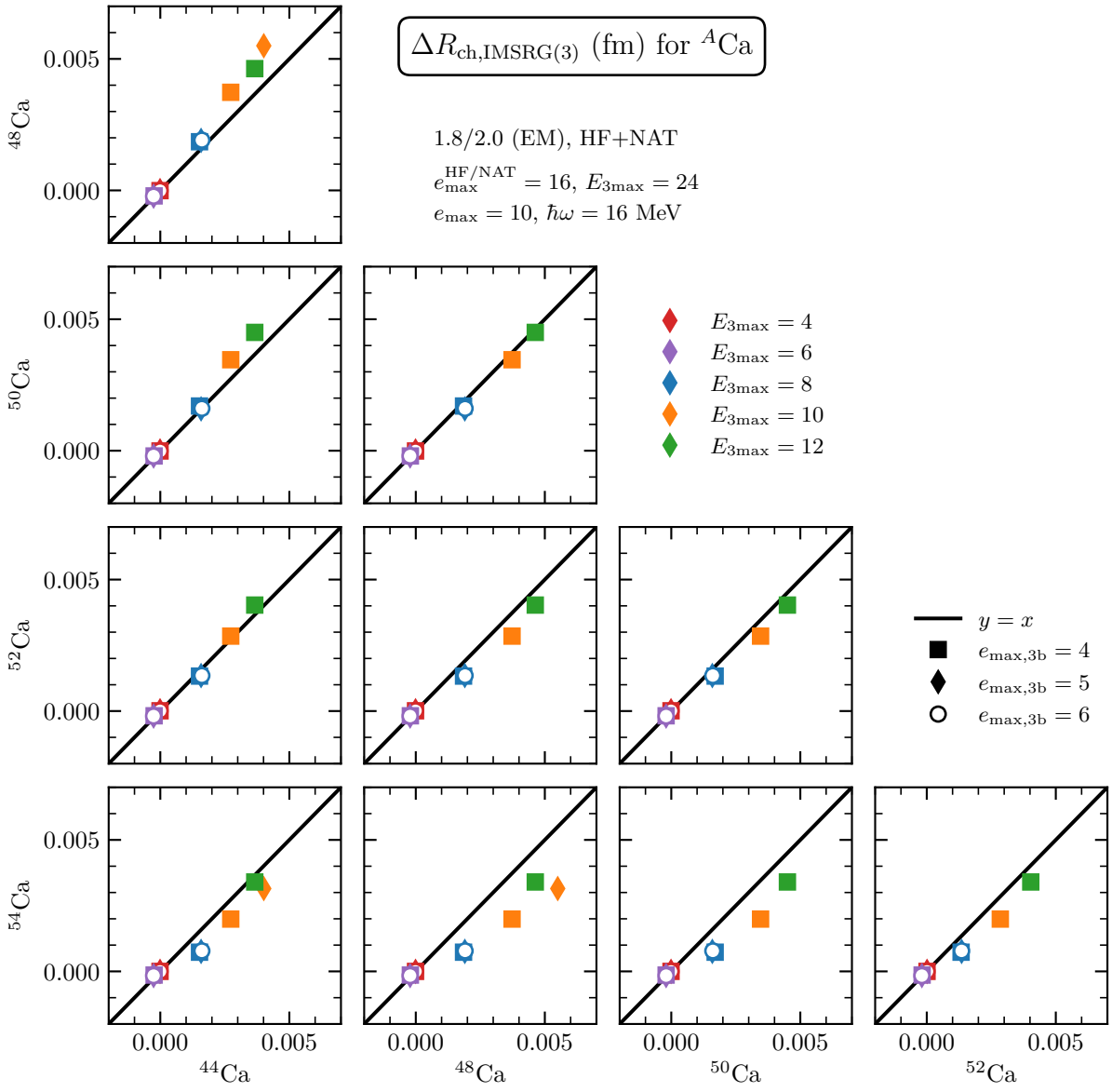

Figure 9.4: VS-IMSRG(3) corrections to calcium charge radii. Correlations of VS-IMSRG(3)-N^7 corrections to charge radii $\Delta R_{\mathrm{ch,IMSRG(3)}}$ of calcium isotopes. We show VS-IMSRG(3)-N^7 predictions as a function of $e_{\mathrm{max,3b}}$ and $E_{3\mathrm{max}}$. We note that not all combinations of $e_{\mathrm{max,3b}}$ and $E_{3\mathrm{max}}$ are shown (for example, $e_{\mathrm{max,3b}} = 6$ is only paired with $E_{3\mathrm{max}} = 4$, 6, and 8) due to available computational time. The black lines show $y = x$, meaning that the IMSRG(3) corrections in both isotopes are identical. All calculations use the 1.8/2.0 (EM) Hamiltonian and an HF+NAT basis constructed in an $e_{\mathrm{max}}^{\mathrm{HF/NAT}} = 16$, $E_{3\mathrm{max}} = 24$, $\hbar\omega = 16\,\mathrm{MeV}$ model space before being truncated to $e_{\mathrm{max}} = 10$ for the IMSRG calculation.

the points all lie below the black line, indicating that the IMSRG(3) corrections are larger for ^{48}Ca than for ^{52}Ca. Looking at ^{48}Ca vs. ^{44}Ca in the top left, we see that the IMSRG(3) corrections for ^{48}Ca are larger than those for ^{44}Ca. Following the correlation to the converged model-space limit, the charge radius corrections for ^{48}Ca will be larger than those for ^{44}Ca or ^{52}Ca. This means that the IMSRG(3) corrections will not produce a crown between ^{40}Ca and ^{48}Ca and will not produce a steeper charge radius increase from ^{48}Ca to ^{52}Ca. We have also observed the same trends in less comprehensive correlation studies using the $\Delta\mathrm{N^2LO_{GO}}$ Hamiltonian.

While the correlations here are very strong, we emphasize that the results are still preliminary, and it is important to establish such correlation behavior with fully converged results before using the correlations to extrapolate. Given the computational limitations of the current approach, this was not possible for this thesis, but will be a priority for upcoming studies where we will have converged results for calcium isotopes. In cases where convergence remains challenging, it would also be nice to have ways to perform controlled model-space extrapolations, either using physically motivated parametrizations as in Refs. [46, 323–325] or using machine learning techniques as in Refs. [411–414].

9.3 Perspectives for converged IMSRG(3) calculations

In the previous sections, we have seen that the three-body model-space truncations we employ, $e_{\mathrm{max,3b}}$ and $E_{3\mathrm{max}}$, are insufficient to converge the effects of three-body operators in IMSRG(3) calculations. In this section, we discuss perspectives for employing more efficient truncations and for new computational strategies, both with the goal of achieving convergence in IMSRG(3) calculations.

While the behavior of the $e_{\mathrm{max,3b}}$ and $E_{3\mathrm{max}}$ truncations is quite systematic, the convergence with respect to these truncations is quite slow when compared to the convergence of triples observed in Ref. [251] using a different, natural-orbitals-based truncation (also discussed in Sec. 6.1.2.3). Using the NAT occupation numbers n_p^{NAT}, the truncated three-hole basis is constructed as

$$\left\{|ijk\rangle\,,\ \bar{n}_i^{\mathrm{NAT}}\bar{n}_j^{\mathrm{NAT}}\bar{n}_k^{\mathrm{NAT}} \geq \varepsilon_{\mathrm{NAT}}\right\}, \tag{9.2}$$

and the three-particle basis is constructed as

$$\left\{\langle abc|\,,\ n_a^{\mathrm{NAT}}n_b^{\mathrm{NAT}}n_c^{\mathrm{NAT}} \geq \varepsilon_{\mathrm{NAT}}\right\}, \tag{9.3}$$

with $\bar{n}_i^{\mathrm{NAT}} = 1 - n_i^{\mathrm{NAT}}$ and a threshold $\varepsilon_{\mathrm{NAT}}$. This truncation emphasizes the inclusion of hole states near the Fermi surface, with n_i^{NAT} considerably less than 1, and particle states near the Fermi surface, with n_a^{NAT} considerably greater than 0, in the three-body basis construction, capturing low-energy correlations around the Fermi surface.

To adapt this strategy to the IMSRG(3), we need to consider a more general basis construction as our three-body operators have more particle-hole blocks than the coupled-cluster triples amplitudes, which only have the ppphhh block. For this purpose, we introduce a general NAT occupation number metric

$$\tilde{n}_p^{\mathrm{NAT}} = \begin{cases} \bar{n}_p^{\mathrm{NAT}} & \text{if } p \text{ is a hole state,} \\ n_p^{\mathrm{NAT}} & \text{if } p \text{ is a particle state.} \end{cases} \tag{9.4}$$

Using this, we can easily construct a truncated three-body basis as

$$\left\{|pqr\rangle\,,\ \tilde{n}_p^{\mathrm{NAT}}\tilde{n}_q^{\mathrm{NAT}}\tilde{n}_r^{\mathrm{NAT}} \geq \varepsilon_{\mathrm{NAT}}\right\} \tag{9.5}$$

without distinguishing between holes and particles. This truncation is exactly identical to Eqs. (9.2) and (9.3) in the hhh and ppp blocks, respectively, but also handles parts of the basis with mixed holes and particles. Equation (9.4) is also easily generalized to a core, valence, and outside partitioning,

$$\tilde{n}_p^{\mathrm{NAT}} = \begin{cases} \bar{n}_p^{\mathrm{NAT}} & \text{if } p \text{ is a core state,} \\ \max(\bar{n}_p^{\mathrm{NAT}}, n_p^{\mathrm{NAT}}) & \text{if } p \text{ is a valence state,} \\ n_p^{\mathrm{NAT}} & \text{if } p \text{ is an outside state.} \end{cases} \tag{9.6}$$

It remains to be seen how this truncation plays out in realistic calculations, but we see a substantial reduction in the number of three-body matrix elements to be stored in our current implementation. As one example, $e_{\mathrm{max,3b}} = 6$, $E_{3\mathrm{max}} = 18$ three-body operators cost 1,422 GB to store in memory.[1] For ^{54}Ca, using an $e_{\mathrm{max}} = 6$ NAT basis and the valence-space NAT truncation metric in Eq. (9.6), choosing a threshold of $\varepsilon_{\mathrm{NAT}} = 10^{-6}$ cuts this down to 233 GB, and choosing a threshold of $\varepsilon_{\mathrm{NAT}} = 10^{-5}$ cuts it down even further to 21 GB. Such values of $\varepsilon_{\mathrm{NAT}}$ with the "average" $\tilde{n}_p^{\mathrm{NAT}}$ in a three-body state around 0.01 are what we anticipate to be necessary to converge our three-body contributions. A key advantage is that this truncation allows us to completely avoid the $e_{\mathrm{max,3b}}$ and $E_{3\mathrm{max}}$ truncations, as it efficiently selects low-lying states in the spectrum, and the same $\varepsilon_{\mathrm{NAT}} = 10^{-6}$ truncation for ^{54}Ca in an $e_{\mathrm{max}} = 12$ basis gives three-body operators that only cost 296 GB to store, down from 6,603,810 GB for untruncated $e_{\mathrm{max}} = 12$ three-body operators.

For future developments of the IMSRG(3), such a truncation will be crucial to make efficient convergence of three-body contributions possible. Adapting our storage of three-body operators to work with this truncation has made it more flexible, and we plan to explore other metrics like the entanglement entropy,

$$s_p = n_p^{\mathrm{NAT}} \log(n_p^{\mathrm{NAT}}) + (1 - n_p^{\mathrm{NAT}}) \log(1 - n_p^{\mathrm{NAT}}) \,, \tag{9.7}$$

to investigate the benefits of intuition from quantum information science in nuclear many-body calculations [355, 357–359].

Another essential development for the IMSRG(3) is the scalable implementation for large-scale supercomputers. The computational needs of the IMSRG(3), simply based on the cost of storing and computing so many three-body matrix elements, are completely different from the IMSRG(2). As a point of reference, the IMSRG(2) can be solved in most cases using less than 192 GB and running for under 24 hours on a single node of a modern supercomputer. The relatively low cost of storing two-body matrix elements, $\mathcal{O}$(1–10 GB), and the ability to efficiently implement most expressions in the IMSRG(2) equations via matrix multiplications make such calculations too costly for a personal computer, but very routine on a supercomputer. Even simply the memory requirements of the IMSRG(3) discussed above require a completely different treatment, as the storage on a single supercomputer node is in general not possible. When one considers the computational cost, in an $e_{\mathrm{max}} = 12$ model space the most expensive term in the IMSRG(2), the $[2,2] \to 2$ commutator, costs about 5 seconds per evaluation. The most expensive term in the IMSRG(3)-N^7, the $[2,2] \to 3$ commutator, costs 1,650 seconds per evaluation in an $e_{\mathrm{max}} = 12$, $e_{\mathrm{max,3b}} = 6$, $E_{3\mathrm{max}} = 16$ model space (evaluated on a single node). This makes it clear that the IMSRG(3) is numerically a problem of completely different scale and requires an appropriately tailored treatment.

The truncations discussed above are one step to making the IMSRG(3) more tractable, but fundamentally any IMSRG(3) implementation will require a distributed numerical solution. Such a distributed solver runs on many supercomputing nodes simultaneously, splitting large memory objects up into small chuncks that

[1] For this discussion, we do not exploit antisymmetry, meaning we store all pqr rather than $p \geq q \geq r$ as is often done to reduce memory costs at the price of increased computational costs.

can be stored and processed on each node independently. In the case of the IMSRG(3), the three-body operators are what must be distributed. The remaining two- and one-body parts may also be distributed or may be stored redundantly on each supercomputer node. The benefit of such an approach is the ability to manage large memory objects via distribution and at the same time apply substantially more computational resources to the problem by using all CPU cores on all nodes rather than being limited only to the cores available on a single node. The challenges lie in identifying an effective distribution scheme and managing communication between nodes for parts of the calculation that need to be synchronized.

We have adopted an approach where we distribute three-body matrix elements across nodes while treating two- and one-body matrix elements redundantly. For the distribution scheme, we follow the general strategy outlined in Ref. [415]. We break our three-body matrix elements O_{pqrstu} into symmetry blocks

$$O^{\xi_{pq},\xi_{st},\xi_3}_{pqr,stu} = O_{pqrstu}\,, \tag{9.8}$$

where ξ_{pq} (ξ_{rs}) is the two-body symmetry block for indices pq (rs) and ξ_3 is the three-body symmetry block.[2] We distribute different ξ_3, ξ_{pq} pairs to different nodes such that if a node has the blocks ξ_3, ξ_{pq} it then has all assoicated ξ_{st} blocks and all matrix elements $O_{pqr,stu}$ belonging to those blocks. This distribution scheme has the advantage that at the IMSRG(3)-N^7 truncation no communication of three-body matrix elements is required. This means each node can solve for its three-body part completely independently, allowing our implementation to scale very efficiently to many nodes.

This implementation is still not complete, but the most expensive terms of the IMSRG(3)-N^7, the $[2,2] \to 3$ and $[2,3] \to 2$ commutators, have been implemented, validated, and optimized in this scheme. The $[2,2] \to 3$ commutator remains by far the most expensive term, but our results look very promising. In a NAT three-body model space with truncations $e_{\max} = 12$ and $\varepsilon_{\text{NAT}} = 10^{-6}$, as discussed above, running on 20 supercomputer nodes allows us to evaluate the $[2,2] \to 3$ commutator in 170 seconds. Typical IMSRG solutions require around 500 commutator evaluations, so this puts the total cost of the $[2,2] \to 3$ commutator at 23.6 hours. Further optimization and scaling out will bring this down even further, so that IMSRG(3)-N^7 calculations can be run routinely with relatively short runtimes.

Overview and perspectives

In the preliminary investigations of calcium isotopes in this chapter, we established the benefits of the IMSRG(3)-N^7 in describing the structure of ^{48}Ca while finding slow convergence in our chosen model-space truncations. The IMSRG(3)-N^7 gives only small corrections to ground-state properties, and we find nice consistency with complementary results from coupled-cluster theory within model-space and many-body uncertainties. For the first 2^+ excitation energy of ^{48}Ca, we find that the IMSRG(3)-N^7 gives the expected improvement, bringing the 2^+ energy down into better agreement with experiment and coupled-cluster calculations including triples. The corrections here are large, over 15% on the total observable, and we establish this as a clear case where the IMSRG(3) offers significant corrections that are important for a quantitative description of the structure of ^{48}Ca. At the same time, we find slow convergence of IMSRG(3) corrections in our model-space parameters. We investigated correlations of IMSRG(3) corrections in charge radius predictions of calcium isotopes and found signs that the charge radius of ^{48}Ca increases more than those of ^{44}Ca and ^{52}Ca.

Still, fully converged IMSRG(3) calculations of calcium isotopes are a high priority to address the various challenges ab initio theory faces. Work on both improved three-body model-space truncations based on

[2] For the purpose of clarity, we discuss this without angular momentum coupling, but in our implementation we do this using angular-momentum-coupled matrix elements.

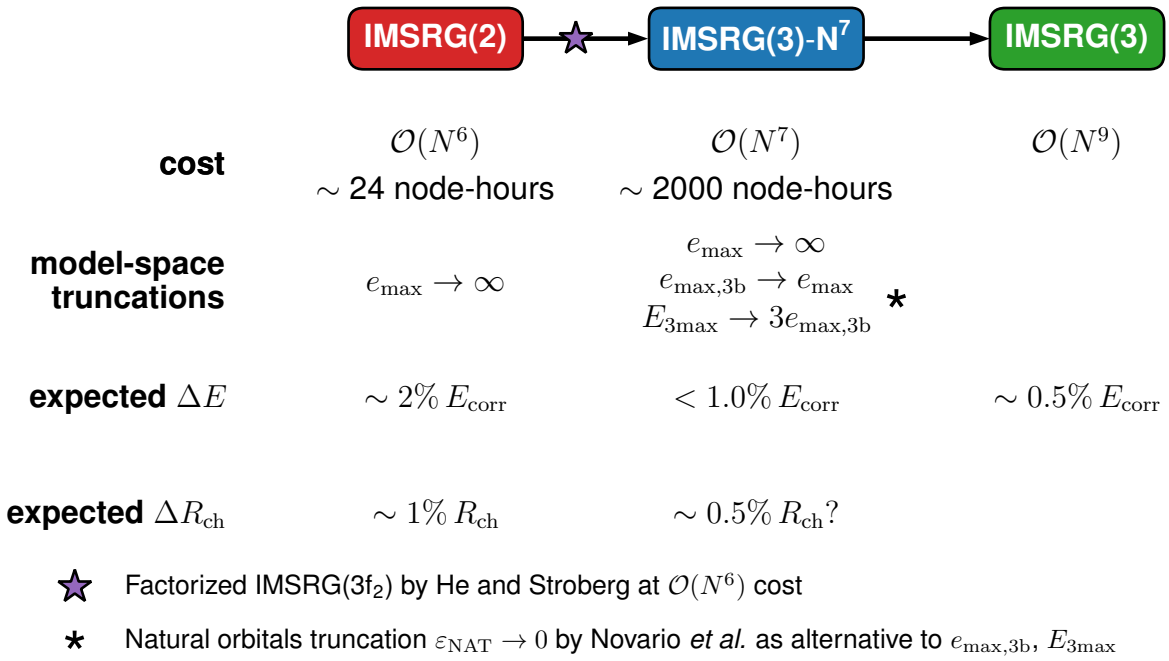

Figure 9.5: Overview of IMSRG(3) methods. A schematic overview of the computational costs, model-space truncations, and expected typical errors for ground-state energies ΔE and charge radii ΔR_{ch} of the IMSRG(2), IMSRG(3)-N^7, and IMSRG(3) approximations. For the IMSRG(3), calculations in realistic model spaces are intractable. ΔE estimates are based on calculations in Chapters 7 and 9, where in many cases exact results are available to benchmark. For ΔR_{ch}, we currently have not performed such benchmarks against exact results, so estimates are based on comparison with CC calculations (including CCSDT-1 results in Ref. [410]) and based on the many-body convergence going from IMSRG(2) to IMSRG(3)-N^7. We highlight promising developments by He and Stroberg [416, 417] to approximate the IMSRG(3)-N^7 at $\mathcal{O}(N^6)$ cost and the outlook to improve our three-body model-space truncations by using the natural orbitals truncation of Ref. [251].

natural orbitals and a scalable numerical implementation designed to meet the computational needs of the IMSRG(3) are important steps in this direction. Once converged IMSRG(3) results are available, systematic studies based on multiple Hamiltonians and the IMSRG(2) and IMSRG(3)-N^7 approximations will give insight into the discrepancies with experiment by allowing us to quantify the many-body uncertainty via the IMSRG(3). Such studies will also benefit from a robust understanding of correlated uncertainties as we explored in Sec. 9.2.

Figure 9.5 shows an overview of IMSRG(3) method developments of this thesis. The IMSRG(3)-N^7 introduced in Chapter 7 is a tractable approximation to the IMSRG(3) that captures many of the improvements in precision that the IMSRG(3) has to offer. Notably, our calculations in Chapter 7 and this chapter establish the remaining IMSRG(3)-N^7 uncertainty on the ground-state energy of spherical medium-mass nuclei at less than 1% of E_{corr}, very comparable to the error of the full IMSRG(3) to exact results observed in Chapter 7. This further establishes the IMSRG(3)-N^7 as a promising way to achieve increased precision in IMSRG calculations, one that is expensive, but still tractable unlike the full IMSRG(3).

The behavior of charge radii in IMSRG(3)-N^7 calculations in this thesis has a less clear interpretation. On one hand, the IMSRG(3)-N^7 corrections seem to be significant when compared to IMSRG(2) corrections to Hartree-Fock charge radius predictions. On the other hand, both the IMSRG(2) and IMSRG(3)-N^7 corrections beyond Hartree-Fock are very small in terms of the total charge radius, at the level of 1% in ^{48}Ca, suggesting they are not terribly important for quantitative predictions for charge radii. For this reason,

the absolute precision of the IMSRG(3)-N^7 for charge radii is not completely clear. As IMSRG(3)-N^7 calculations become more routine, it will be important to establish the precision of IMSRG(3)-N^7, both with thorough comparisons against other high-precision many-body truncations like CCSDT-1 and with benchmarks against exact results in light systems.

A promising alternative to IMSRG(3) with explicit three-body operators has been recently introduced by He and Stroberg [416, 417]. This approach works within the Magnus expansion, where induced three-body operators in the recursive nested commutators evaluated in Eq. (4.44) are treated exactly by considering the explicit evaluation of two nested commutators. In a simple sense, this amounts to evaluating

$$[\Omega, [\Omega, H]] \tag{9.9}$$

with Ω and H both kept at the normal-ordered two-body level but keeping the induced three-body term from $[\Omega, H]$ rather than discarding it as is typically done in the normal-ordered two-body approximation. Doing this naively would be as expensive as the IMSRG(3)-N^7, as one would store the result of $[\Omega, H]^{(3B)}$ in a three-body operator, leading to the same computational limitations as we face in the IMSRG(3)-N^7. However, a key assumption of the approach of Refs. [416, 417] is that the dominant effect of $[\Omega, H]^{(3B)}$ is its contributions in

$$[\Omega, [\Omega, H]^{(3B)}]^{(1B)}, \tag{9.10}$$

$$[\Omega, [\Omega, H]^{(3B)}]^{(2B)}, \tag{9.11}$$

where $[\Omega, H]^{(3B)}$ is only an intermediate and does not need to be stored throughout the IMSRG solution. In this case, Eqs. (9.10) and (9.11) are expanded and evaluated at once. The resulting expressions look closer to those of coupled-cluster theory than the IMSRG, and in fact standard factorization strategies from CC [92, 229, 277] can be used to evaluate these expressions with costs that scale as $\mathcal{O}(N^6)$, exactly the same as the IMSRG(2). How this approach, named the IMSRG($3f_2$), compares to the IMSRG(3)-N^7 in cases where the IMSRG(2) is clearly deficient remains to be understood, but it is a clear innovative improvement over the IMSRG(2) that avoids the leading challenges of any IMSRG(3) approximation with full inclusion of three-body operators.

Chapter 10

New physics searches in ytterbium isotope shifts

Although broadly successful, the standard model (SM) of particle physics has reached its limits and is unable to explain observed phenomena like neutrino masses, matter-antimatter asymmetry, and dark matter. Developing a fundamental understanding of these beyond-standard-model (BSM) phenomena requires us to observe new physics processes. Such studies proceed in two steps: theoretical extensions to the SM, either including explicit new physics or via general EFT parametrizations of BSM physics, are proposed together with potentially observable signals of the BSM theory; and then experimental campaigns are performed to search for these signals using high-energy colliders, astrophysical and cosmological observations, or complementarily high-precision measurements in stable systems (searching for weak signals of rare BSM processes) [34]. Such high-precision tests of the standard model are frequently performed in nuclei, and for these studies an understanding of nuclear structure is essential to isolate the effects of possible new physics.

Recent work [418] has proposed the existence of a new intermediate-mass boson coupling the standard model to an unknown dark sector producing also measureable interactions between electrons and neutrons in atoms. Such interactions would lead to measureable shifts in atomic energy levels in isotopes with increasing neutron number N. These so-called isotope shifts are also sensitive to changes in nuclear structure and are as a result commonly used to extract changes in nuclear charge radii [419] via a linear King-plot analysis (as we discuss later). At sufficiently high experimental precision, nonlinear behavior can also be observed, which may be due to higher-order nuclear structure effects or possibly the proposed new boson.

In this chapter, we discuss a collaborative effort to perform high-precision measurements of atomic and nuclear structure in ytterbium isotopes and explain the observed signals based on atomic and nuclear structure calculations [52]. This work builds on previous studies [420–422] that observed nonlinear behavior in the King-plot analysis in ytterbium isotopes (^{168}Yb, ^{170}Yb, ^{172}Yb, ^{174}Yb, ^{176}Yb), but were limited by experimental precision and uncertainties in the understanding of the nuclear structure of the relevant Yb isotopes. Leveraging the improvements in recent years in the treatment of three-body forces in ab initio nuclear structure calculations [46, 49], the diagonalization of large valence-space Hamiltonians beyond the limits of Lanczos-based approaches [423], and the ability to assess many-body uncertainties via the IMSRG(3) [45], we are able to provide uncertainty-quantified nuclear structure input to interpret the observed signals. Based on this understanding, we are able to adapt the King-plot approach to extract also higher-order nuclear structure information from such high-precision measurements.

The work in this chapter is submitted for review in Ref. [52] in collaboration with the Pentatrap experiment at the Max Planck Institute for Nuclear Physics, the group of Tanja Mehlstäubler at the Physikalisch Technische Bundesanstalt Braunschweig, the group of Elina Fuchs at the Leibniz Universität

Hannover, and Julian C. Berengut at the University of New South Wales. My contributions to Ref. [52] were in the aspects of the study discussed in this chapter. I derived and implemented the $\langle r^4 \rangle$ operator together with Takayuki Miyagi, performing independent derivations and providing independent implementations to validate our results. I performed VS-IMSRG(2) and VS-IMSRG(3)-N^7 calculations of the relevant ytterbium isotopes together with Takayuki Miyagi and Noritaka Shimizu. I assessed the theoretical uncertainties of our results, constructing the correlated statistical model presented in this chapter. Furthermore, I contributed heavily to the King-plot analysis of the data, working closely with Fiona Kirk on both the nonlinearity decomposition and the extraction of $\delta\langle r^4 \rangle$ information from the nonlinearity. My handling of correlated uncertainties in the analysis allowed for robust propagation of data uncertainties to the final results.

10.1 Isotope shifts

In the standard model, for an infinitely heavy point-like nucleus the atomic structure for different isotopes of the same element is identical. This is simply because you always have the same number of electrons in the same external electric field produced by the infinitely heavy nucleus.[1] However, nuclei are both finitely heavy, with masses that are different in different isotopes A and A', and have finite charge distributions that are also different in different isotopes leading to modified potentials within the charge distribution. This leads to small, but measureable shifts in electronic spectrum of the atom, which can be probed via laser spectroscopy performed on a specific atomic transition τ.

Performing such measurements for two isotopes of the same element with masses A and A', one observes an isotope shift of the transition frequency $\nu_\tau^{A,A'} = \nu_\tau^A - \nu_\tau^{A'}$. In a first approximation, the isotope shift can be decomposed as

$$\nu_\tau^{A,A'} \approx \nu_{\tau,\mathrm{MS}}^{A,A'} + \nu_{\tau,\mathrm{FS}}^{A,A'} , \tag{10.1}$$

with a mass shift (MS) due to the changing reduced mass of the electron-nucleus system and a field shift (FS) due to the changing charge radius squared of the nucleus [419, 424]. The mass shift is dominant in light elements, where the nuclear mass changes by significant amounts in neighboring isotopes, while the field shift is dominant in heavy elements, where charge radii are considerably larger and the mass shift is suppressed.

Because the electronic structure of the atom does not affect the nuclear structure, the individual isotope shift contributions factorize into a change in nuclear structure between isotopes and a resulting change in atomic structure for a given transition τ.[2] For Eq. (10.1), this gives

$$\nu_\tau^{A,A'} \approx K_\tau w^{A,A'} + F_\tau \delta\langle r^2 \rangle^{A,A'} . \tag{10.2}$$

The nuclear structure contributions are the difference in inverse nuclear mass ratios $w^{A,A'} = m_{A_\mathrm{ref}}/m_A - m_{A_\mathrm{ref}}/m_{A'}$ with respect to a reference isotope A_ref (in this work we choose the reference isotope ^{172}Yb for the mass ratios) and the difference in the squared charge radius $\delta\langle r^2 \rangle^{A,A'} = \langle r^2 \rangle^A - \langle r^2 \rangle^{A'}$. K_τ and F_τ are the transition-dependent coefficients for the linear response of the electronic structure to the nuclear structure changes, the mass and field shift coefficients, respectively. These atomic coefficients may be computed from electronic structure calculations or fit to data using isotope-shift measurements from multiple transitions in a sufficient number of isotopes.

[1] The first SM correction in this picture comes through the exchange of a Higgs boson, which is extremely suppressed in atomic structure because of the heavy mass of the Higgs boson [418].

[2] Because this change is small and thus perturbative, it can be to a very good approximation linearized [424]. This linear factorization has been demonstrated at the level of 10^{-3} [425], but can be corrected for by explicitly accounting for nonlienar terms [426].

Going beyond our first approximation for the isotope shift in Eq. (10.2), one finds that there are contributions from both higher-order nuclear structure and possibly the interaction of the proposed new boson,

$$\nu_\tau^{A,A'} = K_\tau w^{A,A'} + F_\tau \delta\langle r^2\rangle^{A,A'} + G_\tau^{(2)}(\delta\langle r^2\rangle^2)^{A,A'} + G_\tau^{(4)}\delta\langle r^4\rangle^{A,A'} + \frac{\alpha_{\rm NP}}{\alpha_{\rm EM}} D_\tau h^{A,A'} + \dots . \tag{10.3}$$

The terms given here are:

- the quadratic field shift with coefficient $G_\tau^{(2)}$ and nuclear structure contribution $(\delta\langle r^2\rangle^2)^{A,A'} = (\delta\langle r^2\rangle^{A,A_{\rm ref}})^2 - (\delta\langle r^2\rangle^{A',A_{\rm ref}})^2$ with respect to a reference isotope $A_{\rm ref}$ (in this work we choose the reference isotope ^{176}Yb for the quadratic field shift);
- the quartic shift with coefficient $G_\tau^{(4)}$ and nuclear structure contribution $\delta\langle r^4\rangle^{A,A'} = \langle r^4\rangle^A - \langle r^4\rangle^{A'}$;
- and a shift due to the proposed new boson based on the difference in the number of neutrons in the two isotopes $h^{A,A'} = A - A'$.

The new boson ϕ with mass m_ϕ is postulated to mediate a Yukawa-like interaction between electrons and neutrons with the potential $V_{\rm ne}(r) = \alpha_{\rm NP}\exp(-m_\phi)/r$. The coupling strength $\alpha_{\rm NP} = (-1)^{s+1} y_{\rm n} y_{\rm e}/(4\pi)$ is based on its spin s and its coupling with neutrons ($y_{\rm n}$) and electrons ($y_{\rm e}$) separately. In Eq. (10.3), we normalize this coupling by the fine-structure constant $\alpha_{\rm EM} = e^2/(4\pi)$ with the elementary charge e.

For this work, high-precision mass spectrometry and isotope-shift measurements of five stable, spinless ytterbium isotopes were performed. Both the mass spectrometry and the isotope-shift spectroscopy are up to two orders of magnitude more precise than previous measurements [421, 427, 428]. The isotope mass ratios, which reach a relative precision of a few 10^{-12} corresponding to a relative precision of 10^{-10} for the isotope shifts, were determined by Menno Door and collaborators using highly charged Yb ions in the Penning-trap mass spectrometer PENTATRAP [429] at the Max Planck Institute for Nuclear Physics in Heidelberg [430]. The isotope-shift spectroscopy was performed by Chih-Han Yeh and collaborators at the Physikalisch-Technische Bundesanstalt (PTB) Braunschweig [431] on Yb^+ on the $^2S_{1/2} \to {}^2D_{5/2}$ electric quadrupole transition and the highly forbidden $^2S_{1/2} \to {}^2F_{7/2}$ electric octupole transition with a relative precision as low as 10^{-9}.

Experimentally, the goal of such high-precision measurements is to resolve isotope shifts so precisely that one would be able to detect the effect of the new boson. Theoretically, this requires one to disentangle the standard model effects (including higher-order nuclear structure effects) from a possible new physics contribution. We do this via a King-plot analysis to isolate the signal beyond the leading mass and field shifts, discussed in the next section, and by providing ab initio nuclear structure input to understand this remaining signal, discussed in the following section.

10.2 King-plot analysis

The King plot is a tool to use multiple isotope-shift measurements to reduce Eq. (10.2) to a linear form, allowing one to determine electronic coefficients by fitting to data rather than relying on uncertain electronic structure predictions.

Given isotope shifts for two transitions ν_τ and ν_ρ, one can eliminate one of $\delta\langle r^2\rangle$ and w from Eq. (10.2). Given that nuclear masses can be determined much more precisely than charge radii, one typically eliminates $\delta\langle r^2\rangle$, giving

$$\frac{1}{F_\tau}\nu_\tau{}^{A,A'} - \frac{K_\tau}{F_\tau} w^{A,A'} = \frac{1}{F_\rho}\nu_\rho{}^{A,A'} - \frac{K_\rho}{F_\rho} w^{A,A'} . \tag{10.4}$$

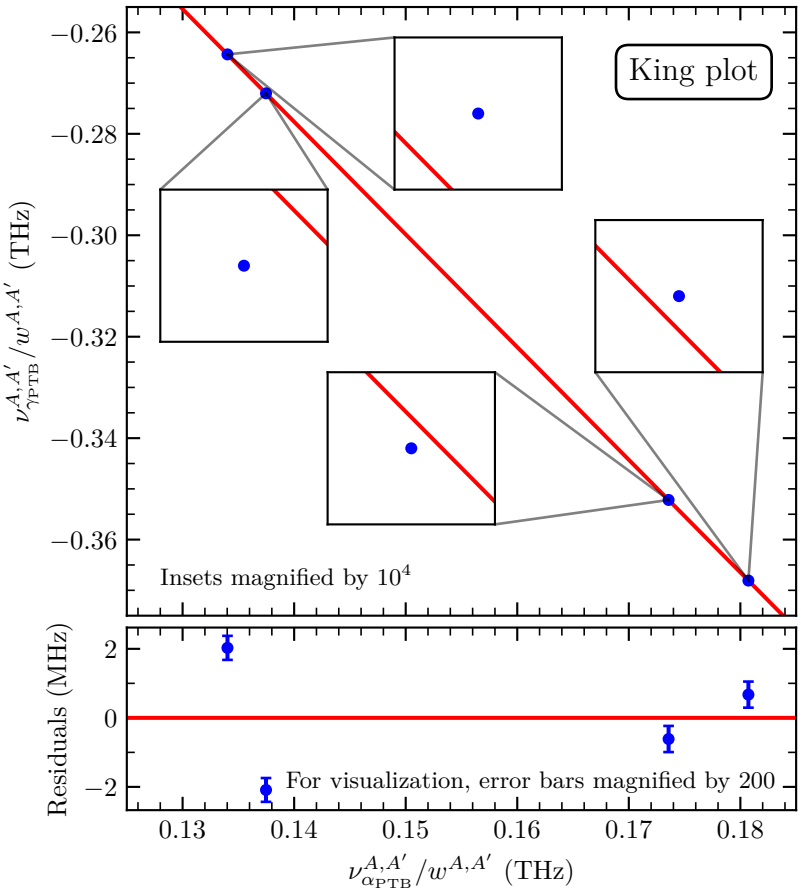

Figure 10.1: Nonlinear King plot of ytterbium isotope shifts. *Top:* King plot of the isotope shifts of the γ_{PTB} transition $\nu^{A,A'}_{\gamma_{\mathrm{PTB}}}$ with respect to the isotope shifts of the α_{PTB} transition $\nu^{A,A'}_{\alpha_{\mathrm{PTB}}}$ normalized with the inverse mass-ratio difference $w^{A,A'}$. The insets are magnified by a factor of 10^4. *Bottom:* Residuals of the linear fit in the King plot. For visibility of the values in the y axis, the uncertainties for both axes are multiplied by a factor of 200. Figure adapted from Ref. [52].

This can be simplified to the linear form

$$\tilde{\nu}^{A,A'}_{\tau} = F_{\tau\rho}\tilde{\nu}^{A,A'}_{\rho} + K_{\tau\rho}\,, \tag{10.5}$$

with the mass-normalized isotope shift $\tilde{\nu}^{A,A'}_{\tau} = \nu^{A,A'}_{\tau}/w^{A,A'}$ and the modified electronic coefficients $F_{\tau\rho} = F_{\tau}/F_{\rho}$ and $K_{\tau\rho} = K_{\tau} - F_{\tau\rho}K_{\rho}$. Measurements of $\nu^{A,A'}$ and $w^{A,A'}$ for two transitions and two isotope pairs (A, A') are sufficient to fit the linear relation, and using more isotope pairs can both reduce fit uncertainties and expose nonlinear behavior.

These so-called "King nonlinearities" are the focus of this work, because all higher-order effects in isotope shifts can be detected as nonlinear behavior deviating from Eq. (10.5).[3] Reexpressing Eq. (10.3) using mass-normalized nuclear structure quantities, one obtains

$$\tilde{\nu}^{A,A'}_{\tau} = F_{\tau\rho}\tilde{\nu}^{A,A'}_{\rho} + K_{\tau\rho} + G^{(2)}_{\tau\rho}(\tilde{\delta}\langle r^2\rangle^2)^{A,A'} + G^{(4)}_{\tau\rho}\tilde{\delta}\langle r^4\rangle^{A,A'} + \frac{\alpha_{\mathrm{NP}}}{\alpha_{\mathrm{EM}}}D_{\tau\rho}\tilde{h}^{A,A'} + \dots\,, \tag{10.6}$$

[3]The exception to this is if higher-order nuclear structure or new physics effects have exactly the same behavior along the isotopic chain as either the mass shift or the field shift.

with

$$(\tilde{\delta}\langle r^2\rangle^2)^{A,A'} = (\delta\langle r^2\rangle^2)^{A,A'}/w^{A,A'}, \tag{10.7}$$
$$\tilde{\delta}\langle r^4\rangle^{A,A'} = \delta\langle r^4\rangle^{A,A'}/w^{A,A'}, \tag{10.8}$$
$$\tilde{h}^{A,A'} = h^{A,A'}/w^{A,A'} \tag{10.9}$$

along with the modified electronic coefficients

$$G^{(2)}_{\tau\rho} = G^{(2)}_{\tau} - F_{\rho\tau}G^{(2)}_{\rho}, \tag{10.10}$$
$$G^{(4)}_{\tau\rho} = G^{(4)}_{\tau} - F_{\rho\tau}G^{(4)}_{\rho}, \tag{10.11}$$
$$D_{\tau\rho} = D_{\tau} - F_{\rho\tau}D_{\rho}\,. \tag{10.12}$$

Observing nonlinear King-plot behavior means that at least one of these additional terms is relevant in the isotope shift, and disentangling which one(s) could potentially point to new physics.

In this work, we focus on the even-mass, stable ytterbium isotopes $^{168\text{–}176}$Yb, using the isotope pairs (A, A') $a = (168, 170)$, $b = (170, 172)$, $c = (172, 174)$, and $d = (174, 176)$. We first consider the King plot of isotope shifts ν for the two transitions measured at the PTB, the $^2S_{1/2} \to {}^2D_{5/2}$ electric quadrupole transition (denoted as α_{PTB}) and the $^2S_{1/2} \to {}^2F_{7/2}$ electric octupole transition (denoted as γ_{PTB}), normalized by the mass ratios w, shown in the top panel of Fig. 10.1. Immediately, one sees that the points for all four isotope pairs clearly lie along a line, reflecting the dominance of the mass and field shifts in the isotope shift. The red line shown is obtained from a weighted linear fit taking into account the relative uncertainties for each isotope pair. Upon closer inspection in the insets in the top panel and in the residuals shown in the bottom panel, one finds that the points for each of the isotope pairs deviate considerably from the linear fit. We note that the precision of the measurements performed in this work is such that both frequency and mass-ratio uncertainties are shown but not visible without considerable magnification. With this, we confirm the King-plot nonlinearity observed in previous work [420–422].

Having confirmed the nonlinearity, the question remains whether this is simply an effect of higher-order nuclear structure or rather the proposed new boson. To understand this, it is convenient to work with four-vectors collecting the measured values or nuclear structure quantities for the four isotope pairs. For example, the isotope shifts and mass ratios considered so far are simply

$$\boldsymbol{\nu}_{\alpha_{\mathrm{PTB}}} = (\nu^a_{\alpha_{\mathrm{PTB}}}, \nu^b_{\alpha_{\mathrm{PTB}}}, \nu^c_{\alpha_{\mathrm{PTB}}}, \nu^d_{\alpha_{\mathrm{PTB}}})\,, \tag{10.13}$$
$$\boldsymbol{\nu}_{\gamma_{\mathrm{PTB}}} = (\nu^a_{\gamma_{\mathrm{PTB}}}, \nu^b_{\gamma_{\mathrm{PTB}}}, \nu^c_{\gamma_{\mathrm{PTB}}}, \nu^d_{\gamma_{\mathrm{PTB}}})\,, \tag{10.14}$$
$$\boldsymbol{w} = (w^a, w^b, w^c, w^d)\,. \tag{10.15}$$

We consider a basis of four vectors for these quantities:

$$\tilde{\boldsymbol{\nu}}_{\delta} = (\nu^a_{\delta}/w^a, \nu^b_{\delta}/w^b, \nu^c_{\delta}/w^c, \nu^d_{\delta}/w^d)\,, \tag{10.16}$$
$$\mathbf{1} = (1, 1, 1, 1)\,, \tag{10.17}$$
$$\boldsymbol{\Lambda}_{+} \propto (\tilde{\nu}^c_{\delta} - \tilde{\nu}^b_{\delta}, \tilde{\nu}^a_{\delta} - \tilde{\nu}^d_{\delta}, \tilde{\nu}^d_{\delta} - \tilde{\nu}^a_{\delta}, \tilde{\nu}^b_{\delta} - \tilde{\nu}^c_{\delta})\,, \tag{10.18}$$
$$\boldsymbol{\Lambda}_{-} \propto (\tilde{\nu}^d_{\delta} - \tilde{\nu}^b_{\delta}, \tilde{\nu}^a_{\delta} - \tilde{\nu}^c_{\delta}, \tilde{\nu}^b_{\delta} - \tilde{\nu}^d_{\delta}, \tilde{\nu}^c_{\delta} - \tilde{\nu}^a_{\delta})\,. \tag{10.19}$$

Here $\boldsymbol{\Lambda}_+$ and $\boldsymbol{\Lambda}_-$ are normalized to 1 Hz (that is, $\sqrt{\boldsymbol{\Lambda}_{+/-} \cdot \boldsymbol{\Lambda}_{+/-}} = 1$ Hz). We use isotope shifts of the $^1S_0 \to {}^3P_0$ transition in Yb [432] (denoted δ) in Eq. (10.16) to set up the full basis with which we analyze all other isotope-shift data. The intuition behind this basis is quite simple: $\mathbf{1}$ and $\tilde{\boldsymbol{\nu}}_{\delta}$ are the basis for the

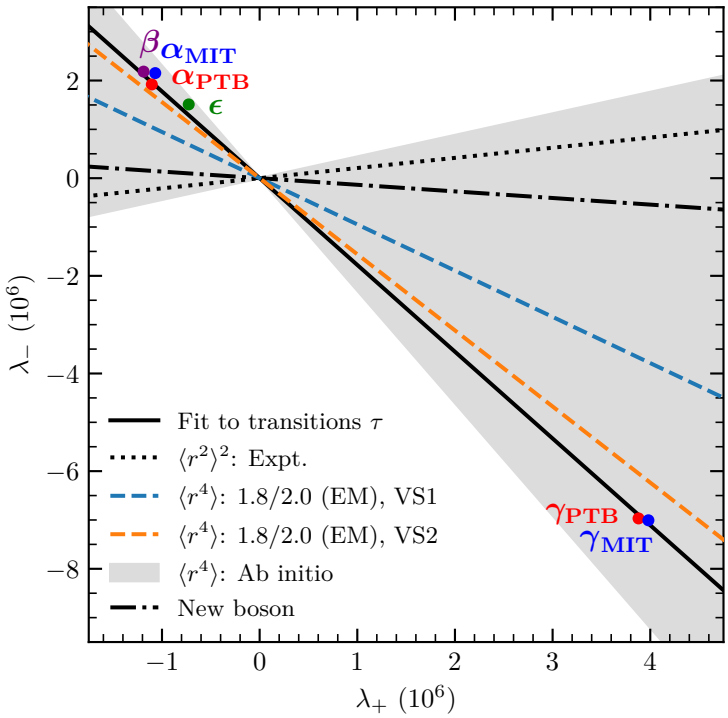

Figure 10.2: Isotope-shift nonlinearity decomposition. Observed and predicted nonlinearities decomposed in the (λ_+, λ_-) plane. The mass-normalized isotope-shift data of the transitions α_{PTB}, β, γ_{PTB}, γ_{MIT}, and ϵ are included in the linear fit through the origin (*solid line*). The slope of this line is compared to the predicted slopes for the $\delta\langle r^2\rangle^2$ (*dotted*), $\delta\langle r^4\rangle$ (*dashed lines and gray band*), and new physics (*dash-dotted*) nonlinearities. Figure adapted from Ref. [52].

linear part of the King plot as in Eq. (10.2);[4] $\mathbf{\Lambda}_+$ and $\mathbf{\Lambda}_-$ (introduced in Ref. [421]) are constructed to be orthogonal to $\mathbf{1}$ and $\tilde{\boldsymbol{\nu}}_\delta$ and thus are the basis for the nonlinear part of the King plot. In summary, any mass-normalized isotope shift can be written as

$$\tilde{\boldsymbol{\nu}}_\tau = F_{\tau\delta}\tilde{\boldsymbol{\nu}}_\delta + K_{\tau\delta}\tilde{\mathbf{1}} + \lambda_+\mathbf{\Lambda}_+ + \lambda_-\mathbf{\Lambda}_- \,, \tag{10.20}$$

where the coefficients λ_+ and λ_- are projections of the mass-normalized isotope shift onto a "King nonlinearity" space.

In Fig. 10.2, we plot the coefficients (λ_+, λ_-) for different mass-normalized isotope shifts measured in ytterbium (α_{MIT}, α_{PTB}, β, γ_{MIT}, γ_{PTB}, ϵ, summarized in Table 10.1), all using the basis defined above in terms of the δ isotope-shift measurements. We find that all points lie essentially on a line passing through the origin (shown by the solid black best fit line), but at different locations for different transitions. The reason for this can be understood quite simply. In general, there are many nonlinearities in isotope shifts due to higher-order nuclear structure, as seen from Eq. (10.3). However, if there is one dominant contribution $x^{A,A'}$ with electronic coefficient X_τ, the mass-normalized isotope shift can be written as

$$\tilde{\boldsymbol{\nu}}_\tau = F_{\tau\delta}\tilde{\boldsymbol{\nu}}_\delta + K_{\tau\delta}\tilde{\mathbf{1}} + X_{\tau\delta}\tilde{\boldsymbol{x}} + \dots \,, \tag{10.21}$$

with $X_{\tau\delta} = X_\tau - F_{\tau\delta}X_\delta$ and $\tilde{x}^{A,A'} = x^{A,A'}/w^{A,A'}$. λ_+ and λ_- are then simply given by the decomposition of $X_{\tau\delta}\tilde{\boldsymbol{x}}$ into $\mathbf{\Lambda}_+$ and $\mathbf{\Lambda}_-$. This is not simply a projection because $\mathbf{\Lambda}_+$ and $\mathbf{\Lambda}_-$ are not orthogonal, but

[4] Note that this is not the same King plot as shown in Fig. 10.1, but the King plot of a given isotope shift with respect to $\nu_\delta^{A,A'}$.

Table 10.1: Summary of ytterbium atomic transitions. Notation and references for the transitions used in the King-plot analysis and the nonlinearity decomposition. Table from Ref. [52].

Notation	Transition	λ (nm)	Refs.
α_{MIT}	$^2S_{1/2} \rightarrow {}^2D_{5/2}$ E2 in Yb^+	411	[420, 421]
α_{PTB}	$^2S_{1/2} \rightarrow {}^2D_{5/2}$ E2 in Yb^+	411	[52]
β	$^2S_{1/2} \rightarrow {}^2D_{3/2}$ E2 in Yb^+	435	[420, 421]
γ_{MIT}	$^2S_{1/2} \rightarrow {}^2F_{7/2}$ E3 in Yb^+	467	[420, 421]
γ_{PTB}	$^2S_{1/2} \rightarrow {}^2F_{7/2}$ E3 in Yb^+	467	[52]
δ	$^1S_0 \rightarrow {}^3P_0$ in Yb	578	[432]
ϵ	$^1S_0 \rightarrow {}^1D_2$ in Yb	361	[422]

it is unique and ultimately λ_+ and λ_- are both proportional to $X_{\tau\delta}$. This has the consequence that in the ratio λ_-/λ_+ the dependence on $X_{\tau\delta}$ (and thus the transition τ) drops out, making the ratio, which is the slope in Fig. 10.2, a transition-independent quantity only sensitive to the nuclear structure part of the isotope-shift nonlinearity $\boldsymbol{x}$, assuming one can neglect all higher-order contributions [426]. This makes the slope of the nonlinearities in different transitions in Fig. 10.2 a very useful tool to identify the nuclear structure contribution to the leading dominant source of nonlinearity in the King plot.

For this, we perform the nonlinearity decomposition into (λ_+, λ_-) for different nuclear structure contributions to isotope shifts in ytterbium. We consider only the slope λ_-/λ_+ and compare a line with the given slope through the origin with the fit to experimental nonlinearities, the solid black line in Fig. 10.2. We start with $\boldsymbol{h}$, the neutron-number change leading to the isotope shift contribution of the postulated new boson. This leads to the dash-dotted black line with a slight negative slope. This slope is completely different from the experimentally observed nonlinearity, meaning that the proposed boson is certainly not the leading source of nonlinearity in ytterbium isotope shifts. So the nonlinearity must be due to some higher-order effects from the nuclear charge distribution. Next, we consider $\boldsymbol{\delta}\langle r^2\rangle^2$, which we compute using experimentally determined squared charge radii from Ref. [360]. The decomposition gives the dotted black line with a slight positive slope, also unable to explain the experimentally observed nonlinearity. We note here that the effect of uncertainties in the $\delta\langle r^2\rangle$ values is smaller than the line in Fig. 10.2.

The final nuclear structure contribution we consider is that of $\boldsymbol{\delta}\langle r^4\rangle$. There is no experimental data for this quantity available, as this would otherwise only be precisely determined in high-precision electron scattering experiments [433]. As a result, we rely on ab initio nuclear theory to predict $\delta\langle r^4\rangle^{A,A'}$ for the relevant isotope pairs, which we discuss in the next section. We provide two representative sets of calculations for $\delta\langle r^4\rangle^{A,A'}$, indicated by the orange and blue dashed lines, and a general uncertainty estimate coming from a correlated statistical error model accounting for EFT and many-body errors in our calculations, indicated by the gray band. The band should be interpreted as an expert assessment of "1σ" uncertainty arising from nuclear theory.

Generally speaking, the uncertainty in our predictions of $\delta\langle r^4\rangle$ leads to a large uncertainty in the predicted slope due to $\delta\langle r^4\rangle$. This is because nuclear theory uncertainties are considerable, but also because the nonlinearity decomposition is quite sensitive to fine changes in trends along the isotopic chain. This means that small independent changes in $\delta\langle r^4\rangle$ for two isotope pairs quickly lead to large shifts in the slope coming from the decomposition. Still, our calculations of $\delta\langle r^4\rangle$ and the assessed uncertainty are better able to explain the observed dominant nonlinearity. This clearly suggests that $\delta\langle r^4\rangle$, which is related to deformation in nuclei, is the dominant source of nonlinearity in ytterbium isotopes, confirming the postulate

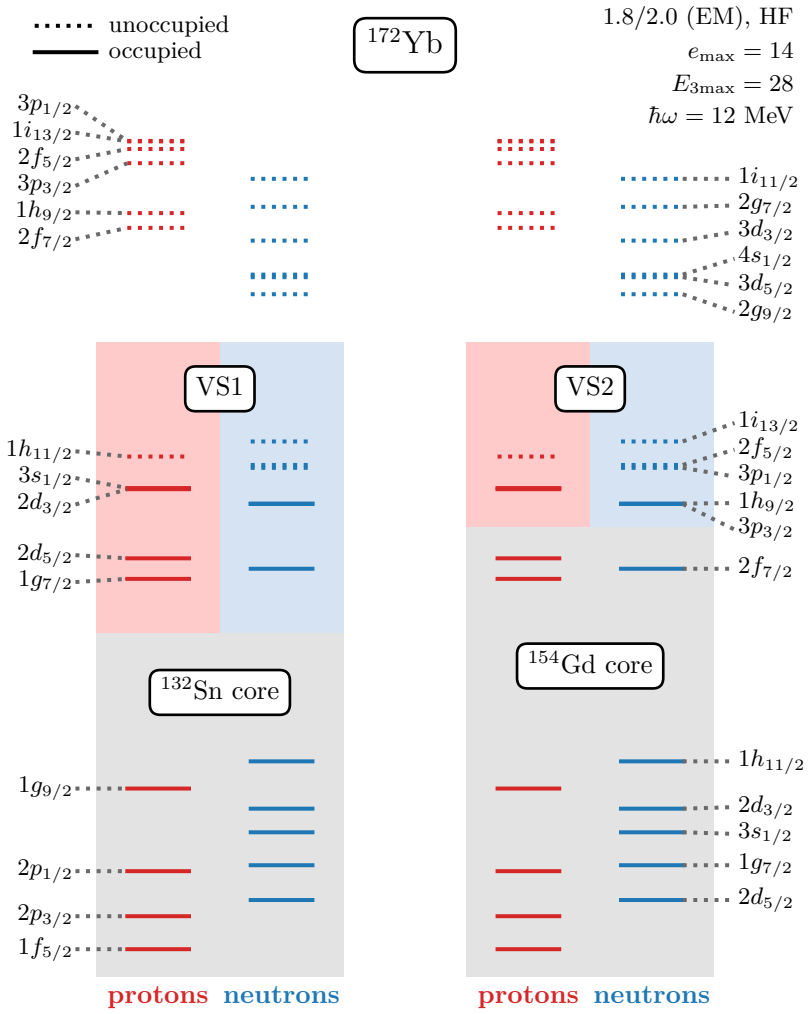

Figure 10.3: Valence spaces for VS-IMSRG calculations. Valence spaces VS1 (*left*) and VS2 (*right*) employed for our VS-IMSRG calculations of ytterbium isotopes. We show the HF single-particle levels for ^{172}Yb computed using the 1.8/2.0 (EM) Hamiltonian in an $e_{\max} = 14$, $E_{3\max} = 28$, $\hbar\omega = 12$ MeV model space. ^{172}Yb has $Z = 70$ protons and $N = 102$ neutrons, leading to the shown occupied (*solid*) and unoccupied (*dotted*) levels. Note that the neutron $1h_{9/2}$ orbital is only partially filled with occupation number $n_p = 8/10 = 0.8$. Both valence spaces share the same upper limits, the proton $1h_{11/2}$ and neutron $1i_{13/2}$ orbitals, but differ in their definition of the decoupled core.

of Ref. [434] and the similar conclusion of Ref. [421] based on density functional theory calculations. In Sec. 10.4, we work under this assumption that the leading nonlinearity is due to $\delta\langle r^4\rangle$ to use the experimental data to extract changes in $\delta\langle r^4\rangle$ across the ytterbium isotopes.

10.3 Ab initio nuclear theory input

The ground-state properties of nuclei, such as $\langle r^2\rangle$ and $\langle r^4\rangle$, can be computed using ab initio nuclear structure theory. Yb isotopes are challenging to describe ab initio due to being heavy and open-shell, and our work leverages recent developments improving the treatment of three-nucleon forces in heavy nuclei [46] and performing large-scale diagonalizations of the many-body Hamiltonian [423]. Our calculations are

performed with the valence-space IMSRG [94, 95, 260], decoupling an effective valence-space Hamiltonian at the IMSRG(2) level that is subsequently diagonalized via large-scale shell-model methods. We solve the IMSRG(2) using the IMSRG++ [365] in an $e_{\max} = 14$ model space based on an underlying harmonic oscillator basis with frequency $\hbar\omega = 12\,\mathrm{MeV}$, including three-nucleon forces with a truncation of $E_{3\max} = 28$ made possible by Refs. [46, 333].

We employ two nuclear Hamiltonians with two- and three-nucleon interactions derived within chiral EFT. The 1.8/2.0 (EM) Hamiltonian [171] is constructed from the N^{3}LO EM 500 NN potential [154], transformed using the similarity renormalization group to a resolution scale of $\lambda = 1.8\,\mathrm{fm}^{-1}$, and N^{2}LO three-nucleon interactions with a regulator cutoff $\Lambda_{3\mathrm{N}} = 2.0\,\mathrm{fm}^{-1}$. It is fit to few-body systems (up to ^{4}He) and predicts ground-state energies, spectra, and differential radius trends well in medium-mass and heavy nuclei [3, 44, 51, 61]. The ΔN^{2}LO$_{\mathrm{GO}}$ Hamiltonian [167] is constructed at N^{2}LO with explicit inclusion of Δ isobars in the EFT and is fit to few-body data and nuclear matter properties and optimized to reproduce bulk properties in medium-mass nuclei. Differences in results obtained by the two Hamiltonians reflect the underlying EFT uncertainty for nuclear forces.

We employ two valence spaces shown in Fig. 10.3: VS1 with a ^{132}Sn core and an active valence space consisting of $1g_{7/2}$, $2d_{5/2}$, $2d_{3/2}$, $3s_{1/2}$, $1h_{11/2}$ proton orbitals and $2f_{7/2}$, $1h_{9/2}$, $1i_{13/2}$, $2f_{5/2}$, $3p_{3/2}$, $3p_{1/2}$ neutron orbitals; and VS2 with a ^{154}Gd core and an active valence space consisting of $2d_{3/2}$, $3s_{1/2}$, $1h_{11/2}$ proton orbitals and $1h_{9/2}$, $1i_{13/2}$, $2f_{5/2}$, $3p_{3/2}$, $3p_{1/2}$ neutron orbitals. Varying the valence space allows us to assess some of the uncertainty due to the employed many-body approximation. Recent developments have made IMSRG calculations at the normal-ordered three-body level available [45]. These calculations can currently not be converged in Yb, but we performed restricted calculations to estimate the order of magnitude of truncated contributions in the IMSRG, another source of many-body uncertainties.

To compute $\langle r^2\rangle$ and $\langle r^4\rangle$, we evaluate the ground-state expectation values of the translationally invariant point-proton radius operators R_{p}^2 and R_{p}^4, with the definitions

$$R_{\mathrm{p}}^2 = \sum_i \Big[(1+\tau_i)\frac{1}{2Z}\Big(1-\frac{2}{A}\Big)+\frac{1}{A^2}\Big]\mathbf{r}_i^2 + \sum_{i<j}\Big[\frac{2}{A^2}-\frac{2}{AZ}\Big(1+\frac{\tau_i+\tau_j}{2}\Big)\Big]\mathbf{r}_i\cdot\mathbf{r}_j\,, \tag{10.22}$$

$$R_{\mathrm{p}}^4 = \sum_i \Big[(1+\tau_i)\frac{1}{2Z}\Big(1-\frac{4}{A}\Big)\Big]\mathbf{r}_i^4 + \sum_{i<j}\frac{-2}{AZ}\big[(1+\tau_i)\mathbf{r}_i^2+(1+\tau_j)\mathbf{r}_j^2\big]\mathbf{r}_i\cdot\mathbf{r}_j + \mathcal{O}(A^{-2})\,. \tag{10.23}$$

We neglect the indicated higher-order contributions in R_{p}^4, which would also include three- and four-body parts but are strongly suppressed. For $\langle r^2\rangle$, we also include the spin-orbit [274] and relativistic Darwin-Foldy [276] corrections and account for the finite size of nucleons.

Our computed values of $\langle r^2\rangle$, $\langle r^4\rangle$, $\delta\langle r^2\rangle$, and $\delta\langle r^4\rangle$ are given in Tables 10.2 and 10.3. We note that we obtained nonphysical results for ^{168}Yb with the ΔN^{2}LO$_{\mathrm{GO}}$ Hamiltonian, with an inversion of proton $2d_{3/2}$ and $1h_{11/2}$ single-particle orbitals at the Hartree-Fock level relative to $^{170\text{–}176}$Yb. For the $\delta\langle r^2\rangle$ and $\delta\langle r^4\rangle$ values in Table 10.3, we obtain extrapolated values for ΔN^{2}LO$_{\mathrm{GO}}$ based on the differences observed for (172, 170) and (170, 168) for the 1.8/2.0 (EM) Hamiltonian in the same valence space. Our results are compared with experimental measurements of $\delta\langle r^2\rangle$ from Ref. [360] and our extraction of $\delta\langle r^4\rangle$ trends (discussed in the next section) in Fig. 10.4 and Fig. 10.5, respectively.

To assess theoretical uncertainties, we employ a correlated statistical uncertainty model. For the propagation of uncertainties in $\delta\langle r^2\rangle$ and $\delta\langle r^4\rangle$ to King-plot analyses, it is essential to account for correlations across isotope pairs. Errors due to truncations in ab initio nuclear theory are very systematic in nature,

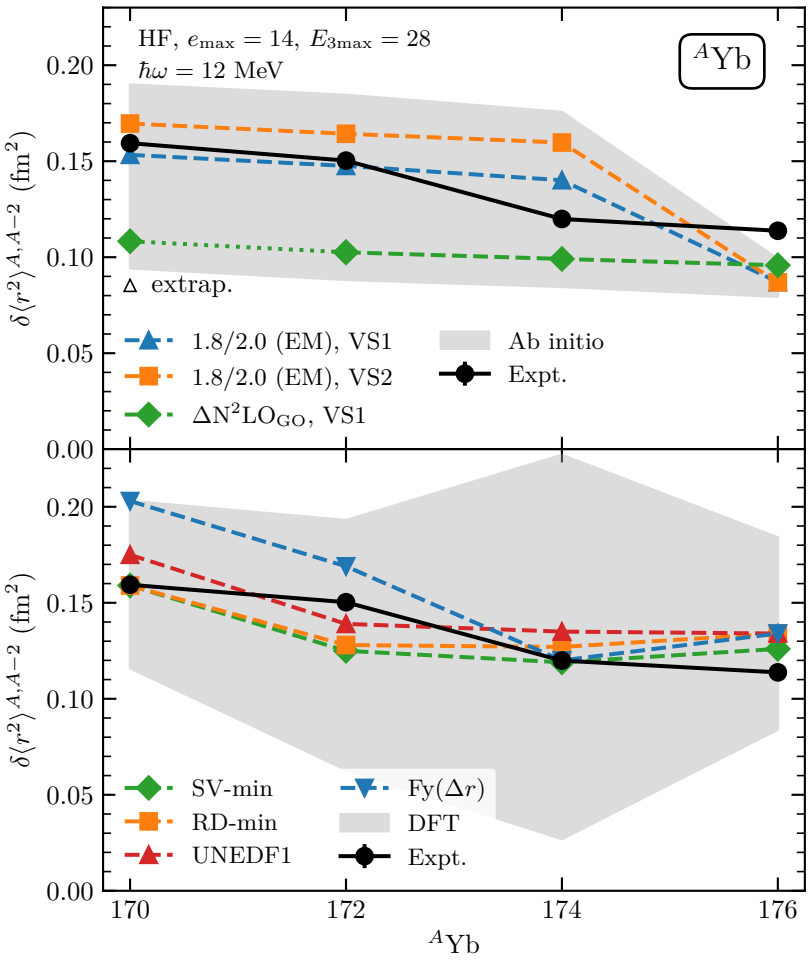

Figure 10.4: Ab initio and DFT $\delta\langle r^2\rangle$ predictions vs. experimental trends. *Top:* $\delta\langle r^2\rangle^{A,A-2}$ values predicted by VS-IMSRG(2) calculations using the 1.8/2.0 (EM) Hamiltonian in valence spaces VS1 and VS2 the ΔN^{2}LO$_{\rm GO}$ Hamiltonian in valence space VS1. All VS-IMSRG(2) calculations employ an HF basis computed in an $e_{\max} = 14$, $E_{3\max} = 28$, $\hbar\omega = 12$ MeV model space. The extrapolated value for $A = 170$ for the ΔN^{2}LO$_{\rm GO}$ Hamiltonian is discussed in the main text. *Bottom:* $\delta\langle r^2\rangle^{A,A-2}$ values predicted by DFT calculations in Ref. [421] using several functionals [SV-min, RD-min, UNEDF1, Fy(Δr)]. We compare nuclear theory predictions with experimental $\delta\langle r^2\rangle^{A,A-2}$ values from Ref. [360]. The gray bands give estimated uncertainties of the theory results. Figure from Ref. [52].

producing similar errors in neighboring isotopes. As a result, strong correlations arise, and we attempt to quantify and account for these in the following.

We assume that a prediction for given observable

$$\mathbf{o} = (o^{(170,168)}, o^{(172,170)}, o^{(174,172)}, o^{(176,174)}) \tag{10.24}$$

(true value unknown) can be understood as

$$\mathbf{o} = \tilde{\mathbf{o}} + \boldsymbol{\varepsilon}_{\rm EFT} + \boldsymbol{\varepsilon}_{\rm VS} + \boldsymbol{\varepsilon}_{\rm MB}\,, \tag{10.25}$$

where $\tilde{\mathbf{o}}$ is the approximate prediction and $\boldsymbol{\varepsilon}_{\rm EFT}$, $\boldsymbol{\varepsilon}_{\rm VS}$, and $\boldsymbol{\varepsilon}_{\rm MB}$ are errors made due the necessary truncations in the EFT for the Hamiltonians, the valence space, and the many-body method, respectively. We choose

$$\tilde{\mathbf{o}} = 0.75\,\mathbf{o}_{\text{1.8/2.0 (EM)},\text{VS1}} + 0.25\,\mathbf{o}_{\Delta\text{N}^2\text{LO}_{\rm GO},\text{VS1}} \tag{10.26}$$

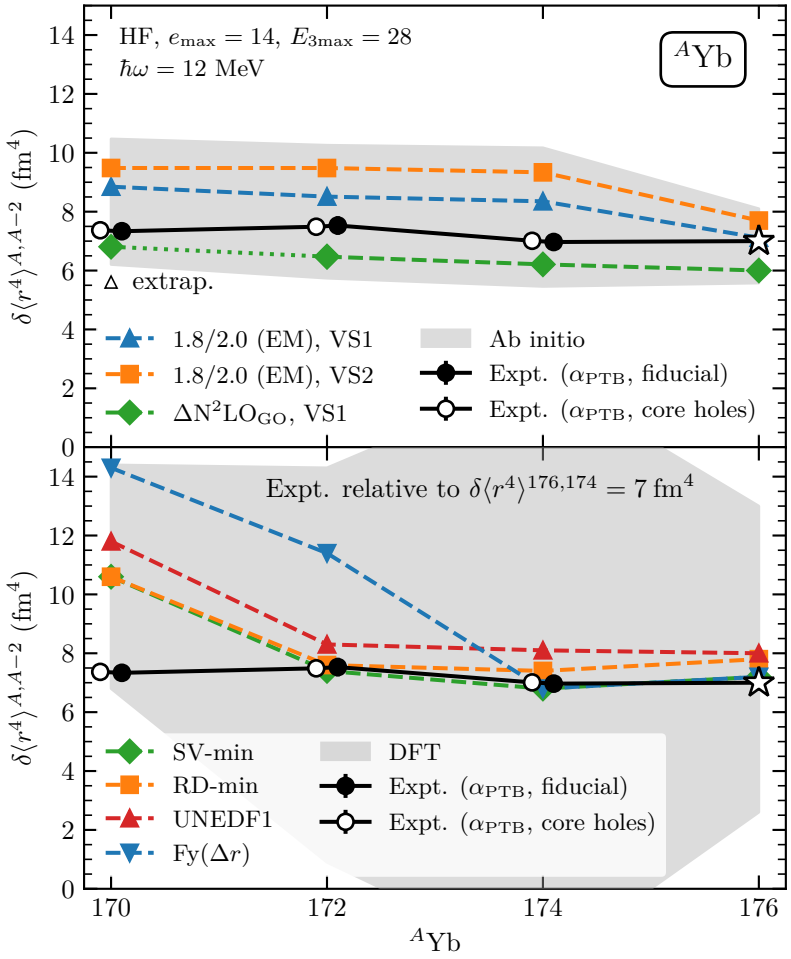

Figure 10.5: Ab initio and DFT $\delta\langle r^4\rangle$ predictions vs. experimental trends. *Top:* $\delta\langle r^4\rangle^{A,A-2}$ values predicted by VS-IMSRG(2) calculations using the 1.8/2.0 (EM) Hamiltonian in valence spaces VS1 and VS2 the ΔN^{2}LO$_{\rm GO}$ Hamiltonian in valence space VS1. All VS-IMSRG(2) calculations employ an HF basis computed in an $e_{\max} = 14$, $E_{3\max} = 28$, $\hbar\omega = 12$ MeV model space. The extrapolated value for $A = 170$ for the ΔN^{2}LO$_{\rm GO}$ Hamiltonian is discussed in the main text. *Bottom:* $\delta\langle r^4\rangle^{A,A-2}$ values predicted by DFT calculations in Ref. [421] using several functionals [SV-min, RD-min, UNEDF1, Fy(Δr)]. We compare nuclear theory predictions with experimental $\delta\langle r^4\rangle^{A,A-2}$ values relative to $\delta\langle r^4\rangle^{176,174} = 7$ fm^4 (*star*) extracted from isotope shifts from the α transitions using atomic theory (*fiducial*, *core holes*). The gray bands give estimated uncertainties of the theory results. Figure from Ref. [52].

based on the reproduction of experimental $\delta\langle r^2\rangle$ values. Additionally, we model the EFT, valence-space, and many-body errors as random variables distributed as multivariate normal distributions,

$$\boldsymbol{\varepsilon}_{\rm EFT} \sim \mathcal{N}(0, \Sigma_{\rm EFT})\,, \tag{10.27}$$
$$\boldsymbol{\varepsilon}_{\rm VS} \sim \mathcal{N}(0, \Sigma_{\rm VS})\,, \tag{10.28}$$
$$\boldsymbol{\varepsilon}_{\rm MB} \sim \mathcal{N}(0, \Sigma_{\rm MB})\,. \tag{10.29}$$

We use full covariance matrices Σ to allow us to consider correlations across isotope pairs in our error model, which we discuss below.

Table 10.2: VS-IMSRG(2) predictions of $\langle r^2 \rangle$ and $\langle r^4 \rangle$. VS-IMSRG(2) predictions of $\langle r^2 \rangle$ and $\langle r^4 \rangle$ for $^{168–176}$Yb using the 1.8/2.0 (EM) Hamiltonian with valence spaces VS1 and VS2 and using the ΔN^{2}LO$_{\text{GO}}$ Hamiltonian with valence space VS1. All VS-IMSRG(2) calculations employ an HF basis computed in an $e_{\max} = 14$, $E_{3\max} = 28$, $\hbar\omega = 12$ MeV model space. Missing results for ^{168}Yb with the ΔN^{2}LO$_{\text{GO}}$ Hamiltonian are discussed in the main text. Table from Ref. [52].

Isotope A	$\langle r^2 \rangle$ (fm^2)			$\langle r^4 \rangle$ (fm^4)		
	1.8/2.0 (EM)		ΔN^{2}LO$_{\text{GO}}$	1.8/2.0 (EM)		ΔN^{2}LO$_{\text{GO}}$
	VS1	VS2	VS1	VS1	VS2	VS1
168	24.233	24.287	(*)	710.4	719.5	(*)
170	24.387	24.457	26.609	719.3	728.9	850.9
172	24.534	24.621	26.711	727.8	738.4	857.4
174	24.674	24.781	26.810	736.2	747.8	863.6
176	24.761	24.868	26.906	743.3	755.5	869.6

Table 10.3: VS-IMSRG(2) predictions of $\delta\langle r^2 \rangle$ and $\delta\langle r^4 \rangle$. VS-IMSRG(2) predictions of $\delta\langle r^2 \rangle$ and $\delta\langle r^4 \rangle$ for neighboring ytterbium isotope pairs in $^{168–176}$Yb using the 1.8/2.0 (EM) Hamiltonian with valence spaces VS1 and VS2 and using the ΔN^{2}LO$_{\text{GO}}$ Hamiltonian with valence space VS1. All VS-IMSRG(2) calculations employ an HF basis computed in an $e_{\max} = 14$, $E_{3\max} = 28$, $\hbar\omega = 12$ MeV model space. Extrapolated results (*) for $(A, A') = (170, 168)$ for the ΔN^{2}LO$_{\text{GO}}$ Hamiltonian are discussed in the main text. Table from Ref. [52].

Isotope pair (A, A')	$\delta\langle r^2 \rangle^{(A,A')}$ (fm^2)			$\delta\langle r^4 \rangle^{(A,A')}$ (fm^4)		
	1.8/2.0 (EM)		ΔN^{2}LO$_{\text{GO}}$	1.8/2.0 (EM)		ΔN^{2}LO$_{\text{GO}}$
	VS1	VS2	VS1	VS1	VS2	VS1
(170,168)	0.153	0.170	0.108(*)	8.85	9.48	6.81(*)
(172,170)	0.148	0.164	0.103	8.51	9.48	6.47
(174,172)	0.140	0.160	0.099	8.35	9.34	6.21
(176,174)	0.087	0.087	0.096	7.11	7.70	6.00

We estimate the variances [i.e., $\boldsymbol{\sigma}_i^2 = \text{diag}(\Sigma_i)$] for our EFT and valence-space errors as

$$\boldsymbol{\sigma}^2_{\text{EFT}} = \left(\mathbf{o}_{1.8/2.0\,(\text{EM}),\text{VS1}} - \mathbf{o}_{\Delta\text{N}^2\text{LO}_{\text{GO}},\text{VS1}}\right)^2 , \tag{10.30}$$

$$\boldsymbol{\sigma}^2_{\text{VS}} = \left(\mathbf{o}_{1.8/2.0\,(\text{EM}),\text{VS1}} - \mathbf{o}_{1.8/2.0\,(\text{EM}),\text{VS2}}\right)^2 . \tag{10.31}$$

To estimate $\boldsymbol{\sigma}^2_{\text{MB}}$, we performed VS-IMSRG(3)-N^7 calculations for ^{172}Yb [45]. VS-IMSRG(3) calculations cannot currently be converged in Yb, but by including restricted three-body operators in the calculations, we gain insight into the magnitude of the VS-IMSRG(3) corrections. Moreover, calculations in calcium have shown that the three-body corrections are strongly correlated across systems (with a correlation coefficient $r \geq 0.99$, see Fig. 9.4). We find the VS-IMSRG(3) corrections for $\langle r^2 \rangle$ and $\langle r^4 \rangle$ in ^{172}Yb to be on the order of 0.06 fm^2 and 2 fm^4, respectively. Assuming a size extensive scaling of radius corrections and exploiting the strong correlation between neighboring isotopes, we find small many-body uncertainties $\boldsymbol{\sigma}^2_{\text{MB}}$ for the differential quantities $\delta\langle r^2 \rangle$ and $\delta\langle r^4 \rangle$. All employed standard deviations are given in Table 10.4.

Finally, the covariance between $\varepsilon_i^{(A,A-2)}$ and $\varepsilon_i^{(B,B-2)}$ ($i \in \{\text{EFT}, \text{VS}\}$) is estimated as

$$\text{cov}(\varepsilon_i^{(A,A-2)}, \varepsilon_i^{(B,B-2)}) = r_i^{(A-B)/2} \sigma_i^{(A,A-2)} \sigma_i^{(B,B-2)} , \tag{10.32}$$

Table 10.4: Uncertainty estimates for VS-IMSRG(2) predictions. Assessed standard deviations σ for $\delta\langle r^2\rangle$ and $\delta\langle r^4\rangle$ EFT, valence-space, and many-body errors. Table from Ref. [52].

Isotope pair (A, A')	$\delta\langle r^2\rangle^{(A,A')}$ (fm^2)			$\delta\langle r^4\rangle^{(A,A')}$ (fm^4)		
	$\sigma_{\mathrm{EFT}}^{(A,A')}$	$\sigma_{\mathrm{VS}}^{(A,A')}$	$\sigma_{\mathrm{MB}}^{(A,A')}$	$\sigma_{\mathrm{EFT}}^{(A,A')}$	$\sigma_{\mathrm{VS}}^{(A,A')}$	$\sigma_{\mathrm{MB}}^{(A,A')}$
(170,168)	0.045	0.016	0.005	2.04	0.63	0.15
(172,170)	0.045	0.017	0.005	2.04	0.97	0.16
(174,172)	0.041	0.020	0.005	2.14	0.98	0.16
(176,174)	0.009	0.001	0.005	1.11	0.58	0.16

assuming an exponentially decaying correlation with a correlation r_i. Based on tests of different correlation values against our computed values, we found $r_{\mathrm{EFT}} = 0.99$ and $r_{\mathrm{VS}} = 0.97$. For the many-body uncertainties, we conservatively assumed no correlations.

We emphasize that these uncertainties and the underlying variances are not meant to be interpreted statistically but rather as an expert assessment of underlying parameters in our model to estimate correlated uncertainties and propagate those to King-plot nonlinearity analyses. We find this model to work well for $\delta\langle r^2\rangle$ when compared to experimental values and expect it to work similarly well for $\delta\langle r^4\rangle$.

10.4 Extraction of higher-order nuclear structure information

Assuming that the leading source of nonlinearity in the King plot is $\delta\langle r^4\rangle$, we can use isotope-shift measurements to extract information on this quantity. We proceed in two steps: Using the precise nuclear mass and frequency measurements presented in this work, we construct the quantities

$$\hat{\nu}_\tau^{a,r} = \nu_\tau^a - \frac{w^a}{w^r}\nu_\tau^r \,, \tag{10.33}$$

where τ is the transition index, $r = (174, 176)$ denotes the reference isotope pair, and $a \in \{(168, 170), (170, 172), (172, 174)\}$ is an isotope pair index. Approximating Eq. (10.3) by

$$\nu_\tau^a \approx F_\tau \delta\langle r^2\rangle^a + K_\tau w^a + G_\tau^{(4)} \delta\langle r^4\rangle^a \,, \tag{10.34}$$

we obtain

$$\hat{\nu}_\tau^{a,r} \approx F_\tau D^{a,r} + G_\tau^{(4)} Q^{a,r} \,, \tag{10.35}$$

where the isotope-pair-dependent quantity

$$D^{a,r} = \delta\langle r^2\rangle^a - \frac{w^a}{w^r}\delta\langle r^2\rangle^r \,, \tag{10.36}$$

can be constructed from the charge radius measurements tabulated in Ref. [360], and

$$Q^{a,r} = \delta\langle r^4\rangle^a - \frac{w^a}{w^r}\delta\langle r^4\rangle^r \tag{10.37}$$

describes the evolution of $\delta\langle r^4\rangle$ along the isotope chain. Following the King-plot approach, we perform a linear fit in isotope-pair space, fitting F_τ to

$$\hat{\boldsymbol{\nu}}_\tau^r \approx F_\tau \mathbf{D}^r \,, \tag{10.38}$$

Table 10.5: Quartic shift coefficients. Electronic $G_\tau^{(4)}$ coefficients of the transitions τ defined in Table 10.1. Two approaches outlined in Ref. [52], "fiducial" and "core holes," are used, which represents one form of uncertainty assessment. Table adapted from Ref. [52].

Transition	$G_\tau^{(4)}$ (MHz/fm^4)	
τ	Fiducial	Core holes
α	8.76	10.80
β	8.75	11.00
γ	−19.47	−30.38
δ	7.12	7.57
ϵ	9.91	10.41

Table 10.6: Experimental trends for $\delta\langle r^4\rangle$. Experimental $\delta\langle r^4\rangle^{A,A-2}$ values relative to $\delta\langle r^4\rangle^{176,174} = 7\,\text{fm}^4$ extracted from isotope shifts from the α_{PTB} transitions using atomic theory. Uncertainties and covariances are propagated from input uncertainties. Table from Ref. [52].

Isotope pair $a = (A, A')$	$\delta\langle r^4\rangle^a$ (fm^4)	cov($\delta\langle r^4\rangle^a$, $\delta\langle r^4\rangle^b$) (fm^8) Isotope pair $b = (A, A')$		
		(170,168)	(172,170)	(174,172)
(170,168)	7.33 (27)	0.076	−0.088	−0.010
(172,170)	7.53 (32)	−0.088	0.104	0.006
(174,172)	6.97 (28)	−0.010	0.006	0.079
(176,174)	7 (reference)			

where $\mathbf{x}^r = (x^{a,r}, x^{b,r}, x^{c,r}, x^{d,r})$, $x \in \{\hat{\nu}_\tau, D\}$. In this way, the precision of the isotope-shift measurements and nuclear mass measurements is exploited and field shift coefficients F_τ can be obtained with relative uncertainties at the level of $\approx 0.3\,\%$.

Next, we subtract the fit results from $\hat{\nu}^{a,r}$ and obtain the residuals

$$\hat{\nu}_\tau^{a,r} - F_\tau D^{a,r} = G_\tau^{(4)} Q^{a,r}\,. \tag{10.39}$$

Making use of the calculated electronic coefficients $G_\tau^{(4)}$, which are listed in Table 10.5 we deduce three independent objects $Q^{a,r}$ per isotope shift transition τ. Fixing $r = (174, 176)$ and $\tau = \alpha_{\text{PTB}}$ and choosing a value $\delta\langle r^4\rangle^r = -7\,\text{fm}^4$, we are able to extract $\delta\langle r^4\rangle$ values for the remaining isotope pairs, given in Table 10.6. We choose the reference value $\delta\langle r^4\rangle^r = -7\,\text{fm}^4$ informed by predictions from ab initio nuclear structure theory and density functional theory shown in Fig. 10.5, which all predict this value to lie between 6–8 fm^4. Beyond this chosen reference value, uncertainties and covariances are obtained by propagating uncertainties from experimental input (ν_τ^a, w^a, and $\delta\langle r^2\rangle^a$) and atomic theory ($G_\tau^{(4)}$) assuming independent normal distributions. The dominant source of uncertainty is $\delta\langle r^2\rangle^{(170,168)}$, and we also understand this uncertainty to lead to correlations in the fit in Eq. (10.38), leading to the considerable anti-correlation between $\delta\langle r^4\rangle^{(170,168)}$ and $\delta\langle r^4\rangle^{(172,170)}$.

We note that the approach outlined here to extract information on $\delta\langle r^4\rangle$ from a King-plot nonlinearity is unable to give information on the absolute scale of $\delta\langle r^4\rangle$. This is simply because we are considering only the nonlinearity, but $\delta\langle r^4\rangle$ also produces an isotope-shift contribution parallel to the linear field shift. We

are unable to disentangle this contribution from the dominant field shift, so our approach is only able to make statements about how $\delta\langle r^4\rangle$ changes across the isotopic chain.

These values are compared with predictions for ab initio nuclear structure theory and density functional theory in Fig. 10.5. Our extracted $\delta\langle r^4\rangle$ values show a weak decrease between $\delta\langle r^4\rangle^{(172,170)}$ and $\delta\langle r^4\rangle^{(174,172)}$ and otherwise flat trend in $\delta\langle r^4\rangle$ across the ytterbium isotopes studied here. Comparing this to the discussed nuclear structure calculations, we find that the flatter $\delta\langle r^4\rangle$ trends of ab initio calculations more closely reproduce the extracted trends. However, within the large theoretical uncertainties our results are compatible with both ab initio nuclear structure theory and density functional theory predictions.

Overview and perspectives

This work, particularly on the state-of-the-art VS-IMSRG calculations of ytterbium isotopes, establishes $\delta\langle r^4\rangle$ as the source of the leading nonlinearity in ytterbium isotope shifts. Based on this information, we use the King-plot analysis to turn the high-precision measurement of nonlinear isotope shifts into an experimental determination of changes in $\delta\langle r^4\rangle$ along the isotopic chain. This novel observable serves as a useful test for nuclear structure theory where high-precision isotope-shift measurements are possible. In particular, $\delta\langle r^4\rangle$ is related to deformation, and access to this observable can provide complementary insight for comparison with different ab initio nuclear theory approaches to capturing deformation in many-body calculations. The main conclusions of this work are: $\delta\langle r^4\rangle$ is the leading source of nonlinearity in ytterbium isotope shifts, not the proposed new boson; this makes it possible to extract changes in $\delta\langle r^4\rangle$ from precise measurements, unlocking a new nuclear structure observable; and the remaining nonlinearity signal can be used to set bounds on the coupling of the proposed new boson.

For future nonlinear isotope-shift studies, ytterbium seems less attractive due to its complicated nuclear structure, which will make disentangling nuclear structure effects from new physics challenging. Interesting alternatives are calcium, tin, and xenon isotopes, with relatively simple nuclear structure in calcium and tin and also many stable isotopes. Studying more isotope pairs in such systems provides the King-plot analysis with more data that can be used to control for uncertain higher-order nuclear structure effects and increase sensitivity to BSM physics. At the same time, such measurements can also give more insight into the nuclear structure of the isotopes through $\delta\langle r^4\rangle$. In all of these efforts, there is a key role to be played by ab initio nuclear structure theory, providing uncertainty-quantified predictions to explain observed signals and enhance our understanding of physics within and beyond the standard model.

Chapter 11

Conclusion

This thesis makes significant strides towards a more complete description of nuclear structure using ab initio methods. In particular, we have established developments allowing more efficient and higher-precision calculations in the IMSRG. We explored applications in light, medium-mass, and heavy nuclei made possible by the developments in this thesis, improving our ab initio understanding of the structure of these systems.

The key method developments were on the improved inclusion of three-nucleon forces in many-body calculations, on informed truncations for many-body calculations, and on extensions of the IMSRG to the next order of the method, including also normal-ordered three-body operators. The inclusion of 3N forces in many-body calculations has been a long-standing challenge for nuclear structure theory, requiring substantial truncations $E_{3\mathrm{max}}$ that limited the application to heavy systems. Critically, 3N forces are typically included in many-body calculations at the normal-ordered two-body level as effective two-body interactions, and we introduce a way to compute these effective two-body interactions via normal ordering in a Jacobi basis, avoiding the $E_{3\mathrm{max}}$ truncation altogether [49]. We benchmarked this approach against traditional normal ordering approaches in light and medium-mass systems, finding excellent agreement and systematic behavior of our truncations in angular momentum quantum numbers. We used this new Jacobi normal ordering approach to obtain converged ground-state predictions for ^{132}Sn and ^{208}Pb, two systems that were far out of reach just five years ago. This opens up the new frontier of nuclei with mass numbers $A \gtrsim 100$ to ab initio calculations.

While many-body expansion methods like the IMSRG are scalable to heavy systems, they are still computationally challenging especially when using high-precision approximations like the IMSRG(3). We explored two ways to make informed truncations for many-body calculations. In the first approach [106], we optimized the computational basis for our many-body calculations by constructing the perturbatively improved NAT basis. In this basis, we were able to show substantially reduced dependence on our underlying basis parameters, notably the harmonic oscillator frequency $\hbar\omega$, and much faster convergence in our basis size. This serves to accelerate many-body calculations substantially, especially in medium-mass nuclei, where the smaller basis sizes lead to an order-of-magnitude reduction in the cost of IMSRG calculations. In the second approach [107], we investigated a more fine-tuned importance truncation approach to IMSRG calculations. We presented a variety of ways to assess the importance of two-body matrix elements in the IMSRG(2), allowing us to make informed truncations and compress the IMSRG(2) calculations by as much as 99%. The benefits of this IT-IMSRG(2) were most pronounced for soft Hamiltonians in large model spaces, but we found that this approach could also be robustly applied to harder Hamiltonians for selected importance measures. We have not yet succeeded in actually exploiting this compression computationally, but this work, along with the successes of factorizations of nuclear forces and few- and many-body methods [331, 435–438], demonstrates that nuclear many-body calculations are generally highly

redundant. Developing compressed operator bases is a promising way to make calculations much cheaper, which would unlock higher-order many-body methods like the IMSRG(3) at reasonable computational cost.

A key challenge for the IMSRG in nuclear structure has been the restriction to the IMSRG(2) approximation. While generally very successful, we understand that this approximation has its limits. The extension of the IMSRG to the normal-ordered three-body level, the IMSRG(3), allows for both higher-precision many-body calculations where the IMSRG(2) is insufficient and for quantification of many-body truncation uncertainties in IMSRG calculations. We developed the IMSRG(3) in this thesis [45], establishing the systematic behavior of the method by comparing IMSRG(2) and IMSRG(3) calculations with results from exact diagonalizations. We found systematic improvement through the IMSRG(3), and this improvement was also found in lower-cost approximations of the IMSRG(3). These lower-cost approximations are scalable to larger model spaces and heavier nuclei, paving the path to realistic "IMSRG(3)" calculations for nuclear structure. The IMSRG(3) is a milestone for nuclear structure theory, and in the coming years many high-precision, fully uncertainty-quantified ab initio studies will be possible based on the developments of this thesis.

The applications considered in this thesis are centered around the IMSRG(3), where we are able to understand many-body uncertainties using the IMSRG(2) and IMSRG(3) together. In collaboration with the all-optical charge radius measurement at COALA, we studied the IMSRG(2) and IMSRG(3) in ^{12}C and ^{13}C [108]. In most cases, we found that the behavior of our calculations was systematic, with the IMSRG(3) giving significant, but controlled corrections to energies and charge radii. A notable exception is the charge radius of ^{12}C, where IMSRG(3) corrections are very large and show challenging model-space convergence patterns. This behavior seems to be related to the cluster structure of ^{12}C, which is generally challenging for many-body expansion methods. Nevertheless, we establish many-body correlations beyond Hartree-Fock as essential to producing a decreasing charge radius from ^{12}C to ^{13}C.

In calcium isotopes, we performed preliminary investigations of the structure of ^{48}Ca and neighboring systems with the IMSRG(3). In these systems, we are unfortunately unable to fully converge our IMSRG(3) calculations in our three-body model-space truncations. Still, we very clearly see the benefits of the IMSRG(3) over the IMSRG(2) in the description of the structure of these isotopes. We see that IMSRG(3) corrections to ground-state energies and charge radii are small and under control, consistent with other many-body methods. The IMSRG(3) brings the single-reference and valence-space description of ^{48}Ca into systematically better agreement, reflecting the reduced many-body uncertainties. The IMSRG(3) also gives significant corrections to the first 2^+ energy of ^{48}Ca, resolving a long-standing challenge of the IMSRG(2), which systematically overpredicts this quantity. Furthermore, we found that correlated IMSRG(3) corrections to charge radii suggest that the long-standing puzzle of the large charge radius of ^{52}Ca relative to ^{48}Ca will not be resolved by the IMSRG(3), but is likely due to uncertainties in nuclear forces. Still, we expect in the near future to be able to provide fully converged IMSRG(3) predictions for calcium isotopes, making more robust statements on many-body uncertainties for calcium charge radii possible.

In stable ytterbium isotopes, we provided ab initio predictions for the charge radius observables $\langle r^2 \rangle$ and $\langle r^4 \rangle$ using the VS-IMSRG as part of a collaborative search for new physics in isotope-shift measurements in ytterbium [52] (in collaboration with high-precision mass spectrometry performed at the Max Planck Institute for Nuclear Physics and high-precision laser spectroscopy performed at the PTB Braunschweig along with atomic and particle theorists). These high-precision measurements found a nonlinear King plot for the isotope shifts, which could potentially be attributed to new physics beyond the standard model but must be disentangled from higher-order nuclear structure effects. Our VS-IMSRG(2) predictions, coupled with a correlated uncertainty assessment of Hamiltonian and many-body uncertainties using also the IMSRG(3), allowed us to interpret the nonlinear King plot as being primarily due to nuclear structure,

specifically due to $\delta\langle r^4\rangle$, which is related to the deformation of the ytterbium isotopes. This allowed us to extract information about $\delta\langle r^4\rangle$ from the measured data, giving access to a new observable to test nuclear structure theory. This study highlights the growing importance of ab initio nuclear structure predictions in searches for new physics in nuclei and atoms. In such searches, nuclear structure effects need to be clearly identified and disentangled to isolate any signal of BSM physics, and ab initio calculations provide a way to do that with both predictive power and fully quantified uncertainties.

The developments of this thesis touch many aspects of ab initio nuclear structure, providing both method developments and applications to improve our understanding of the structure of nuclei. We are growing closer to a comprehensive ab initio description of the entire nuclear chart with fully quantified uncertainties, and the development of the IMSRG(3) in this thesis is a key step in that direction. Specifically, the IMSRG(3) will provide both higher precision and an understanding of many-body uncertainties in nuclear structure calculations in the future. These aspects will be key to provide controlled ab initio predictions for new measurements in exotic nuclei, for the structure of atomic nuclei in astrophysical environments relevant for the rapid neutron-capture process, and for nuclear structure effects in new physics searches.

Acknowledgments

I am immensely privileged to have many positive influences in my life, and their support has been instrumental in all the steps that have led to this thesis.

The foundation of all that I've done and all that I've become is my family. My parents, Christiane Heinz-Neidhart and Ulrich Heinz, have allowed me to become who I am, supporting my health, my education, and my personal development through the many stages of my life so far. They are wise, open-minded, and unwavering, and I am incredibly proud to be their son. My younger brother, Michael Heinz, is my closest friend, and there is nobody I trust more. Michael is an irreplacable partner for conversations, games, travel, food, and all of the fun and difficult things in between. I am incredibly proud to be his brother.

Equally irreplacable in this work is my thesis advisor, Achim Schwenk. Achim is a phenomenal teacher and collaborator, and I have learned (and will continue to learn) so much from him about diverse topics, from physics and science to career and life planning. He has encouraged and supported my research, my career, and me as a person in many ways, including summer schools, workshop and conference participations, seminar travel, and many fascinating, challenging research projects. At the same time, Achim's friendly, candid nature has fostered an open, inclusive environment in his group, which I cherish. In addition to his deep physics knowledge and keen intuition, I greatly respect Achim's empathy, charisma, advocacy, and general sense for good living and hope to emulate these qualities.

I have been privileged to be mentored and supervised by other great scientists too. During my time in Darmstadt, Alex Tichai and Kai Hebeler have been important pillars of support and provided plenty of creative ideas and feedback for my research. I value their broad knowledge of nuclear physics and their consistent availability for questions and discussions very highly. For all technical things related to the IMSRG and many discussions beyond, Ragnar Stroberg has been an excellent mentor and collaborator. Many of the developments in this thesis are based on improvements of the IMSRG(3) developed during an extended research visit with Ragnar at Argonne National Laboratory, and I thank Ragnar and the Argonne National Laboratory Nuclear Theory Group for their hospitality. Moreover, I am grateful to Ragnar for publishing and sharing his IMSRG++ code [365], which has served as an excellent base for many developments on the IMSRG in this thesis. Thomas Papenbrock supported this thesis from the start as an external mentor in my Ph.D. committee meetings alongside Alex and Achim. Thomas's insights and recommendations shaped the research directions we pursued, and his advice on matters ranging from career to job applications to intuition for nuclei and many-body theory has been a key force shaping my further scientific career.

I am also grateful to my former research supervisors during my undergraduate studies. Dick Furnstahl patiently supervised my Bachelor's research and thesis at the Ohio State University, allowing me to work my way into research and computational physics starting in my first year of college. I am grateful for Dick's generous supervision, for how he brings his vast knowledge to a clear point in his teaching, and for how he makes research so accessible to early undergraduate students through casual group meetings, collaborative debugging, research scholarships, and support for conference participations. Dick continues to be a mentor

and a colleague I greatly respect, and I enjoy getting to discuss new developments with him whenever I come back to visit. Ron Soltz supervised my summer research internship at Lawrence Livermore National Laboratory, an experience that introduced me to the vibrant national lab research environment and further solidified my resolve to pursue graduate studies.

In addition to Achim, Kai, and Alex, I have had the privilege to work with Pierre Arthuis, Jan Hoppe, Takayuki Miyagi, Tom Plies, and Lars Zurek on a variety of developments on the IMSRG and on decompositions for nuclear forces. I thank them for discussions, cross-checking, brainstorming, and debugging. In particular, I am grateful to Jan, Alex, and Takayuki for interesting collaborations on IMSRG developments, and I thank Tom for excellent work exploring decompositions for uncertainty quantification for low-resolution nuclear forces. Additionally, I thank Takayuki for sharing his NuHamil code [333], which has been exceptionally useful for many applications in this thesis.

The atmosphere of the Institute for Nuclear Physics Theory Center at the TU Darmstadt has provided an excellent setting for performing this research. I thank the secretaries, Genette Kluckner, Stephanie Müller, and Konstanze Schmechel, for managing administrative and bureaucratic tasks, and I especially thank Stephanie for all the work she put in to support my arrival in Darmstadt, for processing all of my travel requests and reimbursements, and for handling it all with such ease. The STRONGINT group is unique in its excellence, its diversity, and its friendliness, and I have enjoyed sharing offices, group meetings, lunches, and much more with Phillip Klos, Victoria Durant, Marc Schönborn, Toño Coello Pérez, Joel Lynn, Sebastian König, Timon Seibel, Mirko Plößer, Svenja Greif, Yeunhwan Lim, Corbinian Wellenhofer, Zoe Heck, Jan Hoppe, Rodric Seutin, Tyler Gorda, Sabrina Huth, Florian Walkenhorst, Jonas Keller, Lars Zurek, Takayuki Miyagi, Kai Hebeler, Catharina Brase, Alex Tichai, Faruk Alp, Hannah Göttling, Margarida Companys, Pierre Arthuis, Yannick Dietz, Anna Hensel, Tom Plies, Samet Dokur, Luis Hoff, Max Cincar, Isak Svensson, Melissa Mendez, and Andrea Porro. I want to especially thank Sabrina for all her help when I arrived in Darmstadt initially, also helping me to feel comfortable in the group with coffee breaks and office discussions, and for organizing Schoppestunde ("happy hour") and Christmas market visits, which helped me get to know many people better early on. I have also benefited from discussions with others in the theory center, notably Robert Roth, Marco Knöll, Hans-Werner Hammer, Fabian Brauneis, and Almudena Arcones.

My research has received valuable input and feedback from the scientific community at large, leading to many ongoing projects and collaborations. I thank Antoine Belley, Scott Bogner, Francesca Bonaiti, Gaute Hagen, Heiko Hergert, Martin Hoferichter, Jason Holt, Gustav Jansen, Sebastian König, Dean Lee, Justin Lietz, Frederic Noël, Brendan Reed, and Ingo Tews for discussions and collaborations on different aspects of many-body theory, and I thank Julian Berengut, Klaus Blaum, Menno Door, Elina Fuchs, Fiona Kirk, Tanja Mehlstäubler, Tim Lellinger, Patrick Müller, Laura Renth, Wilfried Nörtershäuser, Alexandre Obertelli, and Indy Yeh for discussions and collaborations related to experimental measurements in atoms and nuclei.

I thank my examiners, Achim Schwenk, Thomas Papenbrock, Alexandre Obertelli, and Enno Giese, for participating in my defense and giving valuable feedback on my dissertation. I thank Pierre Arthuis, Hannah Göttling, Kai Hebeler, Achim Schwenk, Isak Svensson, Alex Tichai, and Lars Zurek for proof-reading this thesis. I am particularly grateful to Hannah and Isak for reading early versions of the thesis. I also thank Francesca Bonaiti for quickly providing coupled-cluster results for comparison in ^{48}Ca.

Having family in Germany made arriving and settling in much easier and living here more familiar. I am grateful to Jutta and Martin Schröter, Richard Heinz, Lea and Jürgen Dambeck, Karl-Joachim Neidhart, and Ulrike Kutsch for wonderful times vacationing, hiking, grilling, and celebrating together in addition to their advice regarding life in Germany.

My friends in Darmstadt have made the time here lively and fun, for which I am very grateful. I thank Alex, Andrea, Antoine, Catharina, Faruk, Francesca, Hannah, Ingo, Isak, Lars, Lukas, Marco, Margarida, Pierre, Sabrina, Takayuki, and Toño for sharing good conversations, good travels, good food, good drinks, good movies, good sports, good games, and many wonderful hours far too late into the night over the past six years.

Last, but not least, my friends from "back home" have been a sturdy backbone I've always been able to rely on. I thank Nick, Michael, Mubasil, Carson, Dennis, Andy, Ian, and Henry for being themselves and for understanding me so well, allowing us to have uninhibited fun together whereever we are, in Germany, Luxembourg, South Korea, Vietnam, Singapore, Slovenia, Los Angeles, Palo Alto, Seattle, Chicago, plain old Hilliard, or simply online.

This work was supported in part by the European Research Council (ERC) under the European Union's Horizon 2020 research and innovation programme (Grant Agreement No. 101020842), by the Deutsche Forschungsgemeinschaft (DFG, German Research Foundation) – Projektnummer 279384907 – SFB 1245, and by the Studienstiftung des deutschen Volkes (German Academic Scholarship Foundation) through a Ph.D. scholarship.

I gratefully acknowledge the Gauss Centre for Supercomputing e.V. (www.gauss-centre.eu) for funding these projects by providing computing time through the John von Neumann Institute for Computing (NIC) on the GCS Supercomputer JUWELS at Jülich Supercomputing Centre (JSC) and the computing time provided on the high-performance computer Lichtenberg at the NHR Centers NHR4CES at TU Darmstadt. I also thank Kai Hebeler for managing the local STRONGINT supercomputing cluster, which has been invaluable for development, debugging, and heavy production runs.

Appendix

Appendix A

Abbreviations

Fundamental physics and nuclear forces:

SM	standard model
BSM	beyond standard model
QCD	quantum chromodynamics
EFT	effective field theory
LEC	low-energy constant
NN	nucleon-nucleon
3N	three-nucleon
4N	four-nucleon
LO	leading order
NLO	next-to-leading order
N^2LO	next-to-next-to-leading order
N^3LO	next-to-next-to-next-to-leading order
N^4LO	next-to-next-to-next-to-next-to-leading order
RG	renormalization group
SRG	similarity renormalization group

Many-body methods:

QMC	quantum Monte Carlo
FCI	full configuration interaction
NCSM	no-core shell model
DFT	density functional theory
HO	harmonic oscillator
HF	Hartree-Fock
NAT	natural orbitals

MBPT	many-body perturbation theory
CC	coupled cluster
CCSD	coupled cluster with singles and doubles
CCSDT	coupled cluster with singles, doubles, and triples
SCGF	self-consistent Green's function
ADC	algebraic diagrammatic construction
IMSRG	in-medium similarity renormalization group
VS-IMSRG	valence-space in-medium similarity renormalization group
NO2B	normal-ordered two-body
IT	importance truncation / importance-truncated
IT-NCSM	importance-truncated no-core shell model
IT-IMSRG	importance-truncated in-medium similarity renormalization group

Institutions, facilities, and experiments:

TU Darmstadt	Technische Universität Darmstadt
COALA	Collinear Apparatus for Laser Spectroscopy and Applied Science
RIBF	Radioactive Isotope Beam Factory
FRIB	Facility for Rare Isotope Beams
FAIR	Facility for Antiproton and Ion Research
NSCL	National Superconducting Cyclotron Laboratory
PTB	Physikalisch Technische Bundesanstalt
ERC	European Research Council
DFG	Deutsche Forschungsgemeinschaft
NIC	John von Neumann Institute for Computing
JSC	Jülich Supercomputing Centre

Miscellaneous:

BCH	Baker-Campbell-Hausdorff
CSC	compressed sparse column
DOK	dictionary of keys
MS	mass shift
FS	field shift
EM	Entem, Machleidt
EKM	Epelbaum, Krebs, Meißner

Appendix B

IMSRG fundamental commutators

For the commutator of a normal-ordered K-body operator $A^{(\mathrm{KB})}$ and a normal-ordered L-body operator $B^{(\mathrm{LB})}$, the resulting operator has different normal-ordered M-body parts $C^{(\mathrm{MB})}$:

$$[A^{(\mathrm{KB})}, B^{(\mathrm{LB})}] = \sum_{M=|K-L|}^{K+L-1} C^{(\mathrm{MB})}. \tag{B.1}$$

We isolate the different M-body parts that arise from the commutator of a K-body operator and an L-body operator, using the following schematic notation in terms of their many-body ranks:

$$[K, L] \to M\,. \tag{B.2}$$

These are the fundamental commutators of the IMSRG, the basic computational unit that must be implemented.

In the following, we provide the nonantisymmetrized expressions for the matrix elements of the fundamental commutators required by the IMSRG(3). For the two- and three-body parts, the matrix elements must be antisymmetrized by applying the appropriate two- and three-body antisymmetrizer. The expressions were derived using the automated normal-ordering tool DRUDGE [233], and, in cases where our expressions did not match those provided in Ref. [94], the results were verified by hand. The section headings employ the schematic notation introduced above, where $[K, L] \to \circ$ is short for

$$[A^{(\mathrm{KB})}, B^{(\mathrm{LB})}] \to C\,. \tag{B.3}$$

To avoid notational clutter, we only denote the many-body rank for the zero-body part, $C^{(0\mathrm{B})}$, and use the convention

$$C_{12} = C_{12}^{(1\mathrm{B})}\,, \tag{B.4}$$

$$C_{1234} = C_{1234}^{(2\mathrm{B})}\,, \tag{B.5}$$

$$C_{123456} = C_{123456}^{(3\mathrm{B})}\,, \tag{B.6}$$

where the many-body rank is obvious from the number of indices. Moreover, use the convention that the indices 1, 2, 3, ... are used for external indices on the resulting matrix elements of C and the indices p, q, r, ... are used for internal indices appearing only on matrix elements of A and B, which are summed over in the fundamental commutator.

B.1 $[1,1] \to \circ$

$$C_{12} = \sum_p \left(A_{1p} B_{p2} - B_{1p} A_{p2} \right), \tag{B.7}$$

$$C^{(0\mathrm{B})} = \sum_{pq} (n_p \bar{n}_q - \bar{n}_p n_q) A_{pq} B_{qp}\,, \tag{B.8}$$

with $\bar{n}_p \equiv 1 - n_p$ and the one-body matrix elements of the result C_{12}.

B.2 $[1,2] \to \circ$

$$C_{1234} = 2 \sum_p \left(A_{1p} B_{p234} - A_{p3} B_{12p4} \right), \tag{B.9}$$

$$C_{12} = \sum_{pq} (n_p \bar{n}_q - \bar{n}_p n_q) A_{pq} B_{1q2p}\,. \tag{B.10}$$

B.3 $[2,2] \to \circ$

$$C_{123456} = 9 \sum_p \left(A_{3p45} B_{126p} - B_{3p45} A_{126p} \right), \tag{B.11}$$

$$\begin{aligned} C_{1234} = {} & \frac{1}{2} \sum_{pq} (\bar{n}_p \bar{n}_q - n_p n_q) \left(A_{12pq} B_{pq34} - B_{12pq} A_{pq34} \right) \\ & - 4 \sum_{pq} (n_p \bar{n}_q - \bar{n}_p n_q) A_{p23q} B_{1qp4}\,, \end{aligned} \tag{B.12}$$

$$C_{12} = \frac{1}{2} \sum_{pqr} (\bar{n}_p \bar{n}_q n_r + n_p n_q \bar{n}_r) \left(A_{1rpq} B_{pq2r} - B_{1rpq} A_{pq2r} \right), \tag{B.13}$$

$$C^{(0\mathrm{B})} = \frac{1}{4} \sum_{pqrs} (n_p n_q \bar{n}_r \bar{n}_s - \bar{n}_p \bar{n}_q n_r n_s) A_{pqrs} B_{rspq}\,. \tag{B.14}$$

B.4 $[1,3] \to \circ$

$$C_{123456} = 3 \sum_p \left(A_{3p} B_{12p456} - A_{p6} B_{12345p} \right), \tag{B.15}$$

$$C_{1234} = \sum_{pq} (n_p \bar{n}_q - \bar{n}_p n_q) A_{pq} B_{12q34p}\,. \tag{B.16}$$

B.5 $[2,3] \to \circ$

$$C_{123456} = \frac{3}{2}\sum_{pq}(\bar{n}_p\bar{n}_q - n_p n_q)\left(A_{12pq}B_{pq3456} - A_{pq45}B_{123pq6}\right) + 9\sum_{pq}(\bar{n}_p n_q - n_p\bar{n}_q)A_{3pq6}B_{12q45p}\,, \tag{B.17}$$

$$C_{1234} = \sum_{pqr}(\bar{n}_p\bar{n}_q n_r + n_p n_q\bar{n}_r)\left(A_{r1pq}B_{pq234r} - A_{pqr3}B_{12rpq4}\right), \tag{B.18}$$

$$C_{12} = \frac{1}{4}\sum_{pqrs}(n_p n_q\bar{n}_r\bar{n}_s - \bar{n}_p\bar{n}_q n_r n_s)A_{pqrs}B_{rs1pq2}\,. \tag{B.19}$$

B.6 $[3,3] \to \circ$

$$C_{123456} = \frac{1}{6}\sum_{pqr}(n_p n_q n_r + \bar{n}_p\bar{n}_q\bar{n}_r)\left(A_{123pqr}B_{pqr456} - B_{123pqr}A_{pqr456}\right) + \frac{9}{2}\sum_{pqr}(\bar{n}_p\bar{n}_q n_r + n_p n_q\bar{n}_r)\left(A_{pq345r}B_{12rpq6} - B_{pq345r}A_{12rpq6}\right), \tag{B.20}$$

$$C_{1234} = \frac{1}{6}\sum_{pqrs}(\bar{n}_p\bar{n}_q\bar{n}_r n_s - n_p n_q n_r\bar{n}_s)\left(A_{12spqr}B_{pqr34s} - B_{12spqr}A_{pqr34s}\right) + \sum_{pqrs}(n_p n_q\bar{n}_r\bar{n}_s - \bar{n}_p\bar{n}_q n_r n_s)A_{pq1rs3}B_{rs2pq4}\,, \tag{B.21}$$

$$C_{12} = \frac{1}{12}\sum_{pqrst}(n_p n_q n_r\bar{n}_s\bar{n}_t + \bar{n}_p\bar{n}_q\bar{n}_r n_s n_t)\left(A_{st1pqr}B_{pqrst2} - B_{st1pqr}A_{pqrst2}\right), \tag{B.22}$$

$$C^{(0B)} = \frac{1}{36}\sum_{pqrstu}(n_p n_q n_r\bar{n}_s\bar{n}_t\bar{n}_u - \bar{n}_p\bar{n}_q\bar{n}_r n_s n_t n_u)A_{pqrstu}B_{stupqr}\,. \tag{B.23}$$

B.7 Corrections to Hergert *et al.*, Phys. Rep. 621, 165 (2016)

Our expressions above correct a few errors in the published expressions of Ref. [94]. The differences are:

1. Our expression for the $[1,3] \to 2$ commutator has an overall factor of $1/4$ relative to that of Ref. [94].
2. We include an additional term in the $[2,3] \to 3$ commutator that is missing in Ref. [94].
3. We provide an expression for the $[2,3] \to 2$ commutator that is generally valid. The expression given in Ref. [94] is valid only when one of A and B is Hermitian and the other is anti-Hermitian.

B.8 Practical considerations

The commutators given above are completely general, applicable to any many-body problem with indistinguishable fermions with interactions resolved in some single-particle basis. For nuclear physics, it is generally relevant to work in an angular-momentum-reduced formalism, which exploits the rotational invariance of nuclei and nuclear Hamiltonians to substantially reduce the computational cost of calculations. This can be done automatically based on the expressions above using the AMC code [439], and we provide complete angular momentum coupled expressions for the fundamental commutators given above in Ref. [45].

Bibliography

[1] National Research Council, *Nuclear Physics: Exploring the Heart of Matter* (The National Academies Press, Washington, D.C., 2013).

[2] F. Wienholtz, D. Beck, K. Blaum, Ch. Borgmann, M. Breitenfeldt, *et al.*, "Masses of exotic calcium isotopes pin down nuclear forces," Nature **498**, 346 (2013).

[3] J. Simonis, S. R. Stroberg, K. Hebeler, J. D. Holt, and A. Schwenk, "Saturation with chiral interactions and consequences for finite nuclei," Phys. Rev. C **96**, 014303 (2017), arXiv:1704.02915.

[4] Z. H. Sun, A. Ekström, C. Forssén, G. Hagen, G. R. Jansen, and T. Papenbrock, "Multiscale physics of atomic nuclei from first principles," arXiv:2404.00058.

[5] K. Hebeler, J. M. Lattimer, C. J. Pethick, and A. Schwenk, "Equation of state and neutron star properties constrained by nuclear physics and observation," Astrophys. J. **773**, 11 (2013), arXiv:1303.4662.

[6] S. K. Greif, K. Hebeler, J. M. Lattimer, C. J. Pethick, and A. Schwenk, "Equation of state constraints from nuclear physics, neutron star masses, and future moment of inertia measurements," Astrophys. J. **901**, 155 (2020), arXiv:2005.14164.

[7] I. Tews, "Quantum Monte Carlo methods for astrophysical applications," Front. Phys. **8**, 153 (2020).

[8] C. Drischler, J. W. Holt, and C. Wellenhofer, "Chiral effective field theory and the high-density nuclear equation of state," Annu. Rev. Nucl. Part. Sci. **71**, 403 (2021), arXiv:2101.01709.

[9] S. Huth, P. T. H. Pang, I. Tews, T. Dietrich, A. Le Fèvre, A. Schwenk, W. Trautmann, K. Agarwal, M. Bulla, M. W. Coughlin, and C. Van Den Broeck, "Constraining neutron-star matter with microscopic and macroscopic collisions," Nature **606**, 276 (2022), arXiv:2107.06229.

[10] C. J. Pethick and D. G. Ravenhall, "Matter at large neutron excess and the physics of neutron-star crusts," Annu. Rev. Nucl. Part. Sci. **45**, 429 (1995).

[11] J. M. Lattimer, "The nuclear equation of state and neutron star masses," Annu. Rev. Nucl. Part. Sci. **62**, 485 (2012), arXiv:1305.3510.

[12] J. M. Lattimer and M. Prakash, "The equation of state of hot, dense matter and neutron stars," Phys. Rep. **621**, 127 (2016), arXiv:1512.07820.

[13] M. V. Zhukov, B. V. Danilin, D. V. Fedorov, J. M. Bang, I. J. Thompson, and J. S. Vaagen, "Bound state properties of Borromean halo nuclei: ^{6}He and ^{11}Li," Phys. Rep. **231**, 151 (1993).

[14] P. G. Hansen, A. S. Jensen, and B. Jonson, "Nuclear halos," Annu. Rev. Nucl. Part. Sci. **45**, 591 (1995).

[15] S. Frauendorf, "Spontaneous symmetry breaking in rotating nuclei," Rev. Mod. Phys. **73**, 463 (2001).

[16] B. Jonson, "Light dripline nuclei," Phys. Rep. **389**, 1 (2004).

[17] O. Sorlin and M.-G. Porquet, "Nuclear magic numbers: New features far from stability," Prog. Part. Nucl. Phys. **61**, 602 (2008), arXiv:0805.2561.

[18] K. Heyde and J. L. Wood, "Shape coexistence in atomic nuclei," Rev. Mod. Phys. **83**, 1467 (2011).

[19] T. Baumann, A. Spyrou, and M. Thoennessen, "Nuclear structure experiments along the neutron drip line," Rep. Prog. Phys. **75**, 036301 (2012).

[20] D. Steppenbeck, S. Takeuchi, N. Aoi, P. Doornenbal, M. Matsushita, *et al.*, "Evidence for a new nuclear 'magic number' from the level structure of ^{54}Ca," Nature **502**, 207 (2013).

[21] S. Frauendorf and A. Macchiavelli, "Overview of neutron-proton pairing," Prog. Part. Nucl. Phys. **78**, 24 (2014), arXiv:1405.1652.

[22] M. Freer, H. Horiuchi, Y. Kanada-En'yo, D. Lee, and U.-G. Meißner, "Microscopic clustering in light nuclei," Rev. Mod. Phys. **90**, 035004 (2018), arXiv:1705.06192.

[23] A. D. Ayangeakaa, R. V. F. Janssens, S. Zhu, D. Little, J. Henderson, *et al.*, "Evidence for rigid triaxial deformation in ^{76}Ge from a model-independent analysis," Phys. Rev. Lett. **123**, 102501 (2019), arXiv:1909.03270.

[24] T. Otsuka, A. Gade, O. Sorlin, T. Suzuki, and Y. Utsuno, "Evolution of shell structure in exotic nuclei," Rev. Mod. Phys. **92**, 015002 (2020), arXiv:1805.06501.

[25] A. Hamaker, E. Leistenschneider, R. Jain, G. Bollen, S. A. Giuliani, K. Lund, W. Nazarewicz, L. Neufcourt, C. R. Nicoloff, D. Puentes, R. Ringle, C. S. Sumithrarachchi, and I. T. Yandow, "Precision mass measurement of lightweight self-conjugate nucleus ^{80}Zr," Nat. Phys. **17**, 1408 (2021), arXiv:2108.13419.

[26] M. R. Mumpower, R. Surman, G. C. McLaughlin, and A. Aprahamian, "The impact of individual nuclear properties on r-process nucleosynthesis," Prog. Part. Nucl. Phys. **86**, 86 (2016), arXiv:1508.07352.

[27] D. Martin, A. Arcones, W. Nazarewicz, and E. Olsen, "Impact of nuclear mass uncertainties on the r process," Phys. Rev. Lett. **116**, 121101 (2016), arXiv:1512.03158.

[28] C. J. Horowitz, A. Arcones, B. Côté, I. Dillmann, W. Nazarewicz, *et al.*, "r-process nucleosynthesis: Connecting rare-isotope beam facilities with the cosmos," J. Phys. G: Nucl. Part. Phys. **46**, 083001 (2019), arXiv:1805.04637.

[29] J. Barnes, Y. L. Zhu, K. A. Lund, T. M. Sprouse, N. Vassh, G. C. McLaughlin, M. R. Mumpower, and R. Surman, "Kilonovae across the nuclear physics landscape: The impact of nuclear physics uncertainties on r-process-powered emission," Astrophys. J. **918**, 44 (2021), arXiv:2010.11182.

[30] Y.-Z. Qian and G. J. Wasserburg, "Where, oh where has the r-process gone?" Phys. Rep. **442**, 237 (2007), arXiv:0708.1767.

[31] B. P. Abbott, R. Abbott, T. D. Abbott, F. Acernese, K. Ackley, *et al.*, "Multi-messenger observations of a binary neutron star merger," Astrophys. J. Lett. **848**, L12 (2017), arXiv:1710.05833.

[32] J. J. Cowan, C. Sneden, J. E. Lawler, A. Aprahamian, M. Wiescher, K. Langanke, G. Martínez-Pinedo, and F.-K. Thielemann, "Origin of the heaviest elements: The rapid neutron-capture process," Rev. Mod. Phys. **93**, 015002 (2021), arXiv:1901.01410.

[33] J. Engel and J. Menéndez, "Status and future of nuclear matrix elements for neutrinoless double-beta decay: A review," Rep. Prog. Phys. **80**, 046301 (2017), arXiv:1610.06548.

[34] M. S. Safronova, D. Budker, D. DeMille, D. F. J. Kimball, A. Derevianko, and C. W. Clark, "Search for new physics with atoms and molecules," Rev. Mod. Phys. **90**, 025008 (2018), arXiv:1710.01833.

[35] P. Gysbers, G. Hagen, J. D. Holt, G. R. Jansen, T. D. Morris, P. Navrátil, T. Papenbrock, S. Quaglioni, A. Schwenk, S. R. Stroberg, and K. A. Wendt, "Discrepancy between experimental and theoretical β-decay rates resolved from first principles," Nat. Phys. **15**, 428 (2019), arXiv:1903.00047.

[36] A. Belley, C. G. Payne, S. R. Stroberg, T. Miyagi, and J. D. Holt, "*Ab initio* neutrinoless double-beta decay matrix elements for ^{48}Ca, ^{76}Ge, and ^{82}Se," Phys. Rev. Lett. **126**, 042502 (2021), arXiv:2008.06588.

[37] G. Hagen, M. Hjorth-Jensen, G. R. Jansen, R. Machleidt, and T. Papenbrock, "Evolution of shell structure in neutron-rich calcium isotopes," Phys. Rev. Lett. **109**, 032502 (2012), arXiv:1204.3612.

[38] V. Somà, A. Cipollone, C. Barbieri, P. Navrátil, and T. Duguet, "Chiral two- and three-nucleon forces along medium-mass isotope chains," Phys. Rev. C **89**, 061301 (2014), arXiv:1312.2068.

[39] G. Hagen, G. R. Jansen, and T. Papenbrock, "Structure of ^{78}Ni from first-principles computations," Phys. Rev. Lett. **117**, 172501 (2016), arXiv:1605.01477.

[40] G. Hagen, A. Ekström, C. Forssén, G. R. Jansen, W. Nazarewicz, T. Papenbrock, K. A. Wendt, S. Bacca, N. Barnea, B. Carlsson, C. Drischler, K. Hebeler, M. Hjorth-Jensen, M. Miorelli, G. Orlandini, A. Schwenk, and J. Simonis, "Neutron and weak-charge distributions of the ^{48}Ca nucleus," Nat. Phys. **12**, 186 (2016), arXiv:1509.07169.

[41] T. D. Morris, J. Simonis, S. R. Stroberg, C. Stumpf, G. Hagen, J. D. Holt, G. R. Jansen, T. Papenbrock, R. Roth, and A. Schwenk, "Structure of the lightest tin isotopes," Phys. Rev. Lett. **120**, 152503 (2018), arXiv:1709.02786.

[42] R. Taniuchi, C. Santamaria, P. Doornenbal, A. Obertelli, K. Yoneda, *et al.*, "^{78}Ni revealed as a doubly magic stronghold against nuclear deformation," Nature **569**, 53 (2019), arXiv:1912.05978.

[43] P. Arthuis, C. Barbieri, M. Vorabbi, and P. Finelli, "*Ab initio* computation of charge densities for Sn and Xe isotopes," Phys. Rev. Lett. **125**, 182501 (2020), arXiv:2002.02214.

[44] S. R. Stroberg, J. D. Holt, A. Schwenk, and J. Simonis, "*Ab initio* limits of atomic nuclei," Phys. Rev. Lett. **126**, 022501 (2021), arXiv:1905.10475.

[45] M. Heinz, A. Tichai, J. Hoppe, K. Hebeler, and A. Schwenk, "In-medium similarity renormalization group with three-body operators," Phys. Rev. C **103**, 044318 (2021), arXiv:2102.11172.

[46] T. Miyagi, S. R. Stroberg, P. Navrátil, K. Hebeler, and J. D. Holt, "Converged *ab initio* calculations of heavy nuclei," Phys. Rev. C **105**, 014302 (2022), arXiv:2104.04688.

[47] B. S. Hu, W. G. Jiang, T. Miyagi, Z. H. Sun, A. Ekström, C. Forssén, G. Hagen, J. D. Holt, T. Papenbrock, S. R. Stroberg, and I. Vernon, "Ab initio predictions link the neutron skin of ^{208}Pb to nuclear forces," Nat. Phys. **18**, 1196 (2022), arXiv:2112.01125.

[48] F. Bonaiti, S. Bacca, and G. Hagen, "*Ab initio* coupled-cluster calculations of ground and dipole excited states in ^{8}He," Phys. Rev. C **105**, 034313 (2022), arXiv:2112.08210.

[49] K. Hebeler, V. Durant, J. Hoppe, M. Heinz, A. Schwenk, J. Simonis, and A. Tichai, "Normal ordering of three-nucleon interactions for *ab initio* calculations of heavy nuclei," Phys. Rev. C **107**, 024310 (2023), arXiv:2211.16262.

[50] Y. Kondo, N. L. Achouri, H. Al Falou, L. Atar, T. Aumann, *et al.*, "First observation of ^{28}O," Nature **620**, 965 (2023).

[51] P. Arthuis, K. Hebeler, and A. Schwenk, "Neutron-rich nuclei and neutron skins from chiral low-resolution interactions," arXiv:2401.06675.

[52] M. Door, C.-H. Yeh, M. Heinz, F. Kirk, C. Lyu, *et al.*, "Search for new bosons with ytterbium isotope shifts," arXiv:2403.07792.

[53] S. Weinberg, "Phenomenological Lagrangians," Phys. A: Stat. Mech. Appl. **96**, 327 (1979).

[54] H.-W. Hammer, S. König, and U. van Kolck, "Nuclear effective field theory: Status and perspectives," Rev. Mod. Phys. **92**, 025004 (2020), arXiv:1906.12122.

[55] S. Weinberg, "Nuclear forces from chiral lagrangians," Phys. Lett. B **251**, 288 (1990).

[56] E. Epelbaum, H.-W. Hammer, and U.-G. Meißner, "Modern theory of nuclear forces," Rev. Mod. Phys. **81**, 1773 (2009), arXiv:0811.1338.

[57] R. Machleidt and D. R. Entem, "Chiral effective field theory and nuclear forces," Phys. Rep. **503**, 1 (2011), arXiv:1105.2919.

[58] M. Piarulli and I. Tews, "Local nucleon-nucleon and three-nucleon interactions within chiral effective field theory," Front. Phys. **7**, 245 (2020), arXiv:2002.00032.

[59] H.-W. Hammer, A. Nogga, and A. Schwenk, "*Colloquium*: Three-body forces: From cold atoms to nuclei," Rev. Mod. Phys. **85**, 197 (2013), arXiv:1210.4273.

[60] K. Hebeler, J. D. Holt, J. Menéndez, and A. Schwenk, "Nuclear forces and their impact on neutron-rich nuclei and neutron-rich matter," Annu. Rev. Nucl. Part. Sci. **65**, 457 (2015), arXiv:1508.06893.

[61] K. Hebeler, "Three-nucleon forces: Implementation and applications to atomic nuclei and dense matter," Phys. Rep. **890**, 1 (2021), arXiv:2002.09548.

[62] K. G. Wilson and J. Kogut, "The renormalization group and the ϵ expansion," Phys. Rep. **12**, 75 (1974).

[63] S. D. Głazek and K. G. Wilson, "Perturbative renormalization group for Hamiltonians," Phys. Rev. D **49**, 4214 (1994).

[64] F. Wegner, "Flow-equations for Hamiltonians," Ann. Phys. **506**, 77 (1994).

[65] S. K. Bogner, T. T. S. Kuo, A. Schwenk, D. R. Entem, and R. Machleidt, "Towards a model-independent low momentum nucleon-nucleon interaction," Phys. Lett. B **576**, 265 (2003), arXiv:nucl-th/0108041.

[66] S. K. Bogner, T. T. S. Kuo, and A. Schwenk, "Model-independent low momentum nucleon interaction from phase shift equivalence," Phys. Rep. **386**, 1 (2003), arXiv:nucl-th/0305035.

[67] S. K. Bogner, R. J. Furnstahl, and R. J. Perry, "Similarity renormalization group for nucleon-nucleon interactions," Phys. Rev. C **75**, 061001(R) (2007), arXiv:nucl-th/0611045.

[68] S. K. Bogner, R. J. Furnstahl, and A. Schwenk, "From low-momentum interactions to nuclear structure," Prog. Part. Nucl. Phys. **65**, 94 (2010), arXiv:0912.3688.

[69] R. J. Furnstahl and K. Hebeler, "New applications of renormalization group methods in nuclear physics," Rep. Prog. Phys. **76**, 126301 (2013), arXiv:1305.3800.

[70] I. Tews, Z. Davoudi, A. Ekström, J. D. Holt, K. Becker, *et al.*, "Nuclear forces for precision nuclear physics: A collection of perspectives," Few-Body Sys. **63**, 67 (2022), arXiv:2202.01105.

[71] M. Goeppert Mayer, "On closed shells in nuclei," Phys. Rev. **74**, 235 (1948).

[72] O. Haxel, J. H. D. Jensen, and H. E. Suess, "On the "magic numbers" in nuclear structure," Phys. Rev. **75**, 1766 (1949).

[73] M. Hjorth-Jensen, T. T. S. Kuo, and E. Osnes, "Realistic effective interactions for nuclear systems," Phys. Rep. **261**, 125 (1995).

[74] B. A. Brown, "The nuclear shell model towards the drip lines," Prog. Part. Nucl. Phys. **47**, 517 (2001).

[75] J. Dobaczewski, W. Nazarewicz, and M. V. Stoitsov, "Nuclear ground-state properties from mean-field calculations," Eur. Phys. J. A **15**, 21 (2002), arXiv:nucl-th/0203060.

[76] M. Bender, P.-H. Heenen, and P.-G. Reinhard, "Self-consistent mean-field models for nuclear structure," Rev. Mod. Phys. **75**, 121 (2003).

[77] E. Caurier, G. Martínez-Pinedo, F. Nowacki, A. Poves, and A. P. Zuker, "The shell model as a unified view of nuclear structure," Rev. Mod. Phys. **77**, 427 (2005), arXiv:nucl-th/0402046.

[78] T. Otsuka and D. Abe, "Mean field properties of exotic nuclei and the tensor force," Prog. Part. Nucl. Phys. **59**, 425 (2007).

[79] J. E. Drut, R. J. Furnstahl, and L. Platter, "Toward *ab initio* density functional theory for nuclei," Prog. Part. Nucl. Phys. **64**, 120 (2010), arXiv:0906.1463.

[80] J. Erler, N. Birge, M. Kortelainen, W. Nazarewicz, E. Olsen, A. M. Perhac, and M. Stoitsov, "The limits of the nuclear landscape," Nature **486**, 509 (2012).

[81] M. Kortelainen, J. McDonnell, W. Nazarewicz, E. Olsen, P.-G. Reinhard, J. Sarich, N. Schunck, S. M. Wild, D. Davesne, J. Erler, and A. Pastore, "Nuclear energy density optimization: Shell structure," Phys. Rev. C **89**, 054314 (2014), arXiv:1312.1746.

[82] P.-G. Reinhard and W. Nazarewicz, "Toward a global description of nuclear charge radii: Exploring the Fayans energy density functional," Phys. Rev. C **95**, 064328 (2017), arXiv:1704.07430.

[83] A. Bulgac, M. M. Forbes, S. Jin, R. Navarro Pérez, and N. Schunck, "Minimal nuclear energy density functional," Phys. Rev. C **97**, 044313 (2018), arXiv:1708.08771.

[84] L. Batail, D. Davesne, S. Péru, P. Becker, A. Pastore, and J. Navarro, "A three-ranged Gogny interaction in touch with pion exchange: Promising results to improve infinite matter properties," Eur. Phys. J. A **59**, 173 (2023), arXiv:2212.00400.

[85] L. Zurek, S. K. Bogner, R. J. Furnstahl, R. Navarro Pérez, N. Schunck, and A. Schwenk, "Optimized nuclear energy density functionals including long-range pion contributions," Phys. Rev. C **109**, 014319 (2024), arXiv:2307.13568.

[86] H. Hergert, "A guided tour of *ab initio* nuclear many-body theory," Front. Phys. **8**, 379 (2020), arXiv:2008.05061.

[87] S. C. Pieper and R. B. Wiringa, "Quantum Monte Carlo calculations of light nuclei," Annu. Rev. Nucl. Part. Sci. **51**, 53 (2001), arXiv:nucl-th/0103005.

[88] J. Carlson, S. Gandolfi, F. Pederiva, S. C. Pieper, R. Schiavilla, K. E. Schmidt, and R. B. Wiringa, "Quantum Monte Carlo methods for nuclear physics," Rev. Mod. Phys. **87**, 1067 (2015), arXiv:1412.3081.

[89] B. R. Barrett, P. Navrátil, and J. P. Vary, "*Ab initio* no core shell model," Prog. Part. Nucl. Phys. **69**, 131 (2013).

[90] J. E. Lynn, I. Tews, S. Gandolfi, and A. Lovato, "Quantum Monte Carlo methods in nuclear physics: Recent advances," Annu. Rev. Nucl. Part. Sci. **69**, 279 (2019), arXiv:1901.04868.

[91] A. Tichai, R. Roth, and T. Duguet, "Many-body perturbation theories for finite nuclei," Front. Phys. **8**, 164 (2020), arXiv:2001.10433.

[92] G. Hagen, T. Papenbrock, M. Hjorth-Jensen, and D. J. Dean, "Coupled-cluster computations of atomic nuclei," Rep. Prog. Phys. **77**, 096302 (2014), arXiv:1312.7872.

[93] W. H. Dickhoff and C. Barbieri, "Self-consistent Green's function method for nuclei and nuclear matter," Prog. Part. Nucl. Phys. **52**, 377 (2004), arXiv:nucl-th/0402034.

[94] H. Hergert, S. K. Bogner, T. D. Morris, A. Schwenk, and K. Tsukiyama, "The in-medium similarity renormalization group: A novel *ab initio* method for nuclei," Phys. Rep. **621**, 165 (2016), arXiv:1512.06956.

[95] S. R. Stroberg, H. Hergert, S. K. Bogner, and J. D. Holt, "Nonempirical interactions for the nuclear shell model: An update," Annu. Rev. Nucl. Part. Sci. **69**, 307 (2019), arXiv:1902.06154.

[96] D. Lee, "Lattice simulations for few- and many-body systems," Prog. Part. Nucl. Phys. **63**, 117 (2009), arXiv:0804.3501.

[97] T. A. Lähde, E. Epelbaum, H. Krebs, D. Lee, U.-G. Meißner, and G. Rupak, "Lattice effective field theory for medium-mass nuclei," Phys. Lett. B **732**, 110 (2014), arXiv:1311.0477.

[98] T. A. Lähde and U.-G. Meißner, *Nuclear Lattice Effective Field Theory: An Introduction*, Lecture Notes in Physics, Vol. 957 (Springer International Publishing, Cham, 2019).

[99] R. Trotta, "Bayes in the sky: Bayesian inference and model selection in cosmology," Contemp. Phys. **49**, 71 (2008), arXiv:0803.4089.

[100] R. J. Furnstahl, N. Klco, D. R. Phillips, and S. Wesolowski, "Quantifying truncation errors in effective field theory," Phys. Rev. C **92**, 024005 (2015), arXiv:1506.01343.

[101] W. G. Jiang and C. Forssén, "Bayesian probability updates using sampling/importance resampling: Applications in nuclear theory," Front. Phys. **10**, 1058809 (2022), arXiv:2210.02507.

[102] D. Frame, R. He, I. Ipsen, D. Lee, D. Lee, and E. Rrapaj, "Eigenvector continuation with subspace learning," Phys. Rev. Lett. **121**, 032501 (2018), arXiv:1711.07090.

[103] J. A. Melendez, C. Drischler, R. J. Furnstahl, A. J. Garcia, and X. Zhang, "Model reduction methods for nuclear emulators," J. Phys. G: Nucl. Part. Phys. **49**, 102001 (2022), arXiv:2203.05528.

[104] C. Drischler, J. A. Melendez, R. J. Furnstahl, A. J. Garcia, and X. Zhang, "BUQEYE guide to projection-based emulators in nuclear physics," Front. Phys. **10**, 1092931 (2023), arXiv:2212.04912.

[105] T. Duguet, A. Ekström, R. J. Furnstahl, S. König, and D. Lee, "Eigenvector continuation and projection-based emulators," arXiv:2310.19419.

[106] J. Hoppe, A. Tichai, M. Heinz, K. Hebeler, and A. Schwenk, "Natural orbitals for many-body expansion methods," Phys. Rev. C **103**, 014321 (2021), arXiv:2009.04701.

[107] J. Hoppe, A. Tichai, M. Heinz, K. Hebeler, and A. Schwenk, "Importance truncation for the in-medium similarity renormalization group," Phys. Rev. C **105**, 034324 (2022), arXiv:2110.09390.

[108] P. Müller, M. Heinz, P. Imgram, K. König, B. Maaß, T. Miyagi, W. Nörtershäuser, A. Schwenk, *et al.*, in preparation.

[109] H. Yukawa, "On the interaction of elementary particles. I," Proc. Phys. Math. Soc. Japan **17**, 48 (1935).

[110] T. Hamada and I. D. Johnston, "A potential model representation of two-nucleon data below 315 MeV," Nucl. Phys. **34**, 382 (1962).

[111] R. B. Wiringa, V. G. J. Stoks, and R. Schiavilla, "Accurate nucleon-nucleon potential with charge-independence breaking," Phys. Rev. C **51**, 38 (1995), arXiv:nucl-th/9408016.

[112] R. V. Reid, "Local phenomenological nucleon-nucleon potentials," Ann. Phys. **50**, 411 (1968).

[113] M. Lacombe, B. Loiseau, J. M. Richard, R. Vinh Mau, J. Côté, P. Pirès, and R. de Tourreil, "Parametrization of the Paris N-N potential," Phys. Rev. C **21**, 861 (1980).

[114] V. G. J. Stoks, R. A. M. Klomp, C. P. F. Terheggen, and J. J. de Swart, "Construction of high-quality NN potential models," Phys. Rev. C **49**, 2950 (1994), arXiv:nucl-th/9406039.

[115] R. Machleidt, K. Holinde, and Ch. Elster, "The Bonn meson-exchange model for the nucleon-nucleon interaction," Phys. Rep. **149**, 1 (1987).

[116] R. Machleidt, "High-precision, charge-dependent Bonn nucleon-nucleon potential," Phys. Rev. C **63**, 024001 (2001), arXiv:nucl-th/0006014.

[117] J. Fujita and H. Miyazawa, "Pion theory of three-body forces," Prog. Theor. Phys. **17**, 360 (1957).

[118] A. C. Phillips, "Consistency of the low-energy three-nucleon observables and the separable interaction model," Nucl. Phys. A **107**, 209 (1968).

[119] J. A. Tjon, "Bound states of ^{4}He with local interactions," Phys. Lett. B **56**, 217 (1975).

[120] J. Carlson, V. R. Pandharipande, and R. B. Wiringa, "Three-nucleon interaction in 3-, 4- and ∞-body systems," Nucl. Phys. A **401**, 59 (1983).

[121] R. B. Wiringa, V. Fiks, and A. Fabrocini, "Equation of state for dense nucleon matter," Phys. Rev. C **38**, 1010 (1988).

[122] B. S. Pudliner, V. R. Pandharipande, J. Carlson, and R. B. Wiringa, "Quantum Monte Carlo calculations of $A \leq 6$ nuclei," Phys. Rev. Lett. **74**, 4396 (1995), arXiv:nucl-th/9502031.

[123] S. C. Pieper, V. R. Pandharipande, R. B. Wiringa, and J. Carlson, "Realistic models of pion-exchange three-nucleon interactions," Phys. Rev. C **64**, 014001 (2001), arXiv:nucl-th/0102004.

[124] S. C. Pieper, K. Varga, and R. B. Wiringa, "Quantum Monte Carlo calculations of $A = 9$, 10 nuclei," Phys. Rev. C **66**, 044310 (2002), arXiv:nucl-th/0206061.

[125] E. Epelbaum, A. Nogga, W. Glöckle, H. Kamada, U.-G. Meißner, and H. Witała, "Three-nucleon forces from chiral effective field theory," Phys. Rev. C **66**, 064001 (2002), arXiv:nucl-th/0208023.

[126] T. Otsuka, T. Suzuki, J. D. Holt, A. Schwenk, and Y. Akaishi, "Three-body forces and the limit of oxygen isotopes," Phys. Rev. Lett. **105**, 032501 (2010).

[127] A. Lovato, O. Benhar, S. Fantoni, and K. E. Schmidt, "Comparative study of three-nucleon potentials in nuclear matter," Phys. Rev. C **85**, 024003 (2012), arXiv:1109.5489.

[128] S. Weinberg, "Effective chiral lagrangians for nucleon-pion interactions and nuclear forces," Nucl. Phys. B **363**, 3 (1991).

[129] C. Ordóñez, L. Ray, and U. van Kolck, "Nucleon-nucleon potential from an effective chiral Lagrangian," Phys. Rev. Lett. **72**, 1982 (1994).

[130] C. Ordóñez, L. Ray, and U. van Kolck, "Two-nucleon potential from chiral Lagrangians," Phys. Rev. C **53**, 2086 (1996), arXiv:hep-ph/9511380.

[131] T.-S. Park, K. Kubodera, D.-P. Min, and M. Rho, "Effective field theory for low-energy two-nucleon systems," Phys. Rev. C **58**, R637(R) (1998), arXiv:hep-ph/9711463.

[132] E. Epelbaum, W. Glöckle, and U.-G. Meißner, "Nuclear forces from chiral Lagrangians using the method of unitary transformation (I): Formalism," Nucl. Phys. A **637**, 107 (1998), arXiv:nucl-th/9801064.

[133] D. B. Kaplan, M. J. Savage, and M. B. Wise, "Two-nucleon systems from effective field theory," Nucl. Phys. B **534**, 329 (1998), arXiv:nucl-th/9802075.

[134] D. R. Entem and R. Machleidt, "Accurate nucleon-nucleon potential based upon chiral perturbation theory," Phys. Lett. B **524**, 93 (2002), arXiv:nucl-th/0108057.

[135] R. J. Furnstahl, D. R. Phillips, and S. Wesolowski, "A recipe for EFT uncertainty quantification in nuclear physics," J. Phys. G: Nucl. Part. Phys. **42**, 034028 (2015), arXiv:1407.0657.

[136] N. Ishii, S. Aoki, and T. Hatsuda, "Nuclear force from lattice QCD," Phys. Rev. Lett. **99**, 022001 (2007), arXiv:nucl-th/0611096.

[137] T. Hatsuda, S. Aoki, N. Ishii, and H. Nemura, "From lattice QCD to nuclear force," Mod. Phys. Lett. A **23**, 2265 (2008).

[138] S. Aoki, T. Hatsuda, and N. Ishii, "Theoretical foundation of the nuclear force in QCD and its applications to central and tensor forces in quenched lattice QCD simulations," Prog. Theor. Phys. **123**, 89 (2010), arXiv:0909.5585.

[139] S. R. Beane, W. Detmold, K. Orginos, and M. J. Savage, "Nuclear physics from lattice QCD," Prog. Part. Nucl. Phys. **66**, 1 (2011), arXiv:1004.2935.

[140] E. Chang, Z. Davoudi, W. Detmold, A. S. Gambhir, K. Orginos, M. J. Savage, P. E. Shanahan, M. L. Wagman, and F. Winter (NPLQCD Collaboration), "Scalar, axial, and tensor interactions of light nuclei from lattice QCD," Phys. Rev. Lett. **120**, 152002 (2018), arXiv:1712.03221.

[141] R. A. Briceño, J. J. Dudek, and R. D. Young, "Scattering processes and resonances from lattice QCD," Rev. Mod. Phys. **90**, 025001 (2018), arXiv:1706.06223.

[142] C. Drischler, W. Haxton, K. McElvain, E. Mereghetti, A. Nicholson, P. Vranas, and A. Walker-Loud, "Towards grounding nuclear physics in QCD," Prog. Part. Nucl. Phys. **121**, 103888 (2021), arXiv:1910.07961.

[143] J. Gasser and H. Leutwyler, "On the low energy structure of QCD," Phys. Lett. B **125**, 321 (1983).

[144] J. Gasser and H. Leutwyler, "Chiral perturbation theory to one loop," Ann. Phys. **158**, 142 (1984).

[145] J. Gasser and H. Leutwyler, "Chiral perturbation theory: Expansions in the mass of the strange quark," Nucl. Phys. B **250**, 465 (1985).

[146] N. Fettes, U.-G. Meißner, M. Mojžiš, and S. Steininger, "The chiral effective pion-nucleon Lagrangian of order p^4," Ann. Phys. **283**, 273 (2000), arXiv:hep-ph/0001308.

[147] S. Scherer and M. R. Schindler, *A Primer for Chiral Perturbation Theory*, Lecture Notes in Physics, Vol. 830 (Springer, Berlin, 2012).

[148] H. Pagels, "Departures from chiral symmetry," Phys. Rep. **16**, 219 (1975).

[149] G. A. Miller, B. M. K. Nefkens, and I. Šlaus, "Charge symmetry, quarks and mesons," Phys. Rep. **194**, 1 (1990).

[150] V. Bernard, N. Kaiser, and U.-G. Meißner, "Chiral dynamics in nucleons and nuclei," Int. J. Mod. Phys. E **04**, 193 (1995), arXiv:hep-ph/9501384.

[151] E. Tiesinga, P. J. Mohr, D. B. Newell, and B. N. Taylor, "CODATA recommended values of the fundamental physical constants: 2018," Rev. Mod. Phys. **93**, 025010 (2021).
[152] M. Hoferichter, J. Ruiz De Elvira, B. Kubis, and U.-G. Meißner, "Matching pion-nucleon Roy-Steiner equations to chiral perturbation theory," Phys. Rev. Lett. **115**, 192301 (2015), arXiv:1507.07552.
[153] P. Reinert, H. Krebs, and E. Epelbaum, "Precision determination of pion-nucleon coupling constants using effective field theory," Phys. Rev. Lett. **126**, 092501 (2021), arXiv:2006.15360.
[154] D. R. Entem and R. Machleidt, "Accurate charge-dependent nucleon-nucleon potential at fourth order of chiral perturbation theory," Phys. Rev. C **68**, 041001(R) (2003), arXiv:nucl-th/0304018.
[155] E. Epelbaum, H. Krebs, and U.-G. Meißner, "Precision nucleon-nucleon potential at fifth order in the chiral expansion," Phys. Rev. Lett. **115**, 122301 (2015), arXiv:1412.4623.
[156] S. Binder, A. Calci, E. Epelbaum, R. J. Furnstahl, J. Golak, *et al.* (LENPIC Collaboration), "Few-nucleon systems with state-of-the-art chiral nucleon-nucleon forces," Phys. Rev. C **93**, 044002 (2016), arXiv:1505.07218.
[157] D. R. Entem, R. Machleidt, and Y. Nosyk, "High-quality two-nucleon potentials up to fifth order of the chiral expansion," Phys. Rev. C **96**, 024004 (2017), arXiv:1703.05454.
[158] S. Binder, A. Calci, E. Epelbaum, R. J. Furnstahl, J. Golak, *et al.* (LENPIC Collaboration), "Few-nucleon and many-nucleon systems with semilocal coordinate-space regularized chiral nucleon-nucleon forces," Phys. Rev. C **98**, 014002 (2018), arXiv:1802.08584.
[159] P. Reinert, H. Krebs, and E. Epelbaum, "Semilocal momentum-space regularized chiral two-nucleon potentials up to fifth order," Eur. Phys. J. A **54**, 86 (2018), arXiv:1711.08821.
[160] R. Somasundaram, J. E. Lynn, L. Huth, A. Schwenk, and I. Tews, "Maximally local two-nucleon interactions at N^3LO in Δ-less chiral effective field theory," Phys. Rev. C **109**, 034005 (2024), arXiv:2306.13579.
[161] E. Epelbaum, "Four-nucleon force in chiral effective field theory," Phys. Lett. B **639**, 456 (2006), arXiv:nucl-th/0511025.
[162] E. Epelbaum, "Four-nucleon force using the method of unitary transformation," Eur. Phys. J. A **34**, 197 (2007), arXiv:0710.4250.
[163] I. Tews, T. Krüger, K. Hebeler, and A. Schwenk, "Neutron matter at next-to-next-to-next-to-leading order in chiral effective field theory," Phys. Rev. Lett. **110**, 032504 (2013), arXiv:1206.0025.
[164] S. Schulz, *Four-nucleon forces in ab initio nuclear structure*, Ph.D. thesis, Technische Universität Darmstadt (2018).
[165] A. Ekström, G. R. Jansen, K. A. Wendt, G. Hagen, T. Papenbrock, B. D. Carlsson, C. Forssén, M. Hjorth-Jensen, P. Navrátil, and W. Nazarewicz, "Accurate nuclear radii and binding energies from a chiral interaction," Phys. Rev. C **91**, 051301(R) (2015), arXiv:1502.04682.
[166] C. Drischler, K. Hebeler, and A. Schwenk, "Chiral interactions up to next-to-next-to-next-to-leading order and nuclear saturation," Phys. Rev. Lett. **122**, 042501 (2019), arXiv:1710.08220.
[167] W. G. Jiang, A. Ekström, C. Forssén, G. Hagen, G. R. Jansen, and T. Papenbrock, "Accurate bulk properties of nuclei from $A = 2$ to ∞ from potentials with Δ isobars," Phys. Rev. C **102**, 054301 (2020), arXiv:2006.16774.
[168] H. Krebs, E. Epelbaum, and U.-G. Meißner, "Nuclear forces with Δ excitations up to next-to-next-to-leading order, part I: Peripheral nucleon-nucleon waves," Eur. Phys. J. A **32**, 127 (2007), arXiv:nucl-th/0703087.
[169] E. Epelbaum, H. Krebs, and U.-G. Meißner, "Δ-excitations and the three-nucleon force," Nucl. Phys. A **806**, 65 (2008), arXiv:0712.1969.
[170] A. Ekström, G. Hagen, T. D. Morris, T. Papenbrock, and P. D. Schwartz, "Δ isobars and nuclear saturation," Phys. Rev. C **97**, 024332 (2018), arXiv:1707.09028.
[171] K. Hebeler, S. K. Bogner, R. J. Furnstahl, A. Nogga, and A. Schwenk, "Improved nuclear matter calculations from chiral low-momentum interactions," Phys. Rev. C **83**, 031301(R) (2011), arXiv:1012.3381.
[172] E. Epelbaum, W. Glöckle, and U.-G. Meißner, "Nuclear forces from chiral Lagrangians using the method of unitary transformation II: The two-nucleon system," Nucl. Phys. A **671**, 295 (2000), arXiv:nucl-th/9910064.
[173] A. Ekström, G. Baardsen, C. Forssén, G. Hagen, M. Hjorth-Jensen, G. R. Jansen, R. Machleidt, W. Nazarewicz, T. Papenbrock, J. Sarich, and S. M. Wild, "Optimized chiral nucleon-nucleon interaction at next-to-next-to-leading order," Phys. Rev. Lett. **110**, 192502 (2013), arXiv:1303.4674.
[174] A. Gezerlis, I. Tews, E. Epelbaum, S. Gandolfi, K. Hebeler, A. Nogga, and A. Schwenk, "Quantum Monte Carlo calculations with chiral effective field theory interactions," Phys. Rev. Lett. **111**, 032501 (2013), arXiv:1303.6243.
[175] A. Gezerlis, I. Tews, E. Epelbaum, M. Freunek, S. Gandolfi, K. Hebeler, A. Nogga, and A. Schwenk, "Local chiral effective field theory interactions and quantum Monte Carlo applications," Phys. Rev. C **90**, 054323 (2014), arXiv:1406.0454.
[176] E. Epelbaum, H. Krebs, and U.-G. Meißner, "Improved chiral nucleon-nucleon potential up to next-to-next-to-next-to-leading order," Eur. Phys. J. A **51**, 53 (2015), arXiv:1412.0142.
[177] M. Piarulli, L. Girlanda, R. Schiavilla, R. Navarro Pérez, J. E. Amaro, and E. Ruiz Arriola, "Minimally nonlocal nucleon-nucleon potentials with chiral two-pion exchange including Δ resonances," Phys. Rev. C **91**, 024003 (2015), arXiv:1412.6446.
[178] M. Piarulli, L. Girlanda, R. Schiavilla, A. Kievsky, A. Lovato, L. E. Marcucci, S. C. Pieper, M. Viviani, and R. B. Wiringa, "Local chiral potentials with Δ-intermediate states and the structure of light nuclei," Phys. Rev. C **94**, 054007 (2016), arXiv:1606.06335.

[179] B. D. Carlsson, A. Ekström, C. Forssén, D. F. Strömberg, G. R. Jansen, O. Lilja, M. Lindby, B. A. Mattsson, and K. A. Wendt, "Uncertainty analysis and order-by-order optimization of chiral nuclear interactions," Phys. Rev. X **6**, 011019 (2016), arXiv:1506.02466.

[180] E. Epelbaum, J. Golak, K. Hebeler, T. Hüther, H. Kamada, H. Krebs, P. Maris, U.-G. Meißner, A. Nogga, R. Roth, R. Skibiński, K. Topolnicki, J. P. Vary, K. Vobig, and H. Witała (LENPIC Collaboration), "Few- and many-nucleon systems with semilocal coordinate-space regularized chiral two- and three-body forces," Phys. Rev. C **99**, 024313 (2019), arXiv:1807.02848.

[181] P. Maris, R. Roth, E. Epelbaum, R. J. Furnstahl, J. Golak, *et al.* (LENPIC Collaboration), "Nuclear properties with semilocal momentum-space regularized chiral interactions beyond N^2LO," Phys. Rev. C **106**, 064002 (2022), arXiv:2206.13303.

[182] S. R. Beane, P. F. Bedaque, M. J. Savage, and U. van Kolck, "Towards a perturbative theory of nuclear forces," Nucl. Phys. A **700**, 377 (2002), arXiv:nucl-th/0104030.

[183] A. Nogga, R. G. E. Timmermans, and U. van Kolck, "Renormalization of one-pion exchange and power counting," Phys. Rev. C **72**, 054006 (2005), arXiv:nucl-th/0506005.

[184] E. Epelbaum, A. M. Gasparyan, J. Gegelia, and U.-G. Meißner, "How (not) to renormalize integral equations with singular potentials in effective field theory," Eur. Phys. J. A **54**, 186 (2018), arXiv:1810.02646.

[185] J. Hoppe, C. Drischler, K. Hebeler, A. Schwenk, and J. Simonis, "Probing chiral interactions up to next-to-next-to-next-to-leading order in medium-mass nuclei," Phys. Rev. C **100**, 024318 (2019), arXiv:1904.12611.

[186] V. Somà, P. Navrátil, F. Raimondi, C. Barbieri, and T. Duguet, "Novel chiral Hamiltonian and observables in light and medium-mass nuclei," Phys. Rev. C **101**, 014318 (2020), arXiv:1907.09790.

[187] S. Elhatisari, L. Bovermann, Y.-Z. Ma, E. Epelbaum, D. Frame, *et al.*, "Wavefunction matching for solving quantum many-body problems," Nature (2024), 10.1038/s41586-024-07422-z, arXiv:2210.17488.

[188] R. Machleidt, "What is *ab initio*?" Few-Body Syst. **64**, 77 (2023), arXiv:2307.06416.

[189] S. D. Głazek and K. G. Wilson, "Renormalization of Hamiltonians," Phys. Rev. D **48**, 5863 (1993).

[190] E. D. Jurgenson, P. Navrátil, and R. J. Furnstahl, "Evolution of nuclear many-body forces with the similarity renormalization group," Phys. Rev. Lett. **103**, 082501 (2009), arXiv:0905.1873.

[191] E. D. Jurgenson, P. Navrátil, and R. J. Furnstahl, "Evolving nuclear many-body forces with the similarity renormalization group," Phys. Rev. C **83**, 034301 (2011), arXiv:1011.4085.

[192] K. Hebeler, "Momentum-space evolution of chiral three-nucleon forces," Phys. Rev. C **85**, 021002(R) (2012), arXiv:1201.0169.

[193] S. K. Bogner, R. J. Furnstahl, P. Maris, R. J. Perry, A. Schwenk, and J. P. Vary, "Convergence in the no-core shell model with low-momentum two-nucleon interactions," Nucl. Phys. A **801**, 21 (2008), arXiv:0708.3754.

[194] E. D. Jurgenson, S. K. Bogner, R. J. Furnstahl, and R. J. Perry, "Decoupling in the similarity renormalization group for nucleon-nucleon forces," Phys. Rev. C **78**, 014003 (2008), arXiv:0711.4252.

[195] R. Roth, J. Langhammer, A. Calci, S. Binder, and P. Navrátil, "Similarity-transformed chiral NN+3N interactions for the *ab initio* description of ^{12}C and ^{16}O," Phys. Rev. Lett. **107**, 072501 (2011), arXiv:1105.3173.

[196] R. Roth, A. Calci, J. Langhammer, and S. Binder, "Evolved chiral NN+3N Hamiltonians for *ab initio* nuclear structure calculations," Phys. Rev. C **90**, 024325 (2014), arXiv:1311.3563.

[197] J. A. Melendez, R. J. Furnstahl, D. R. Phillips, M. T. Pratola, and S. Wesolowski, "Quantifying correlated truncation errors in effective field theory," Phys. Rev. C **100**, 044001 (2019), arXiv:1904.10581.

[198] C. Drischler, R. J. Furnstahl, J. A. Melendez, and D. R. Phillips, "How well do we know the neutron-matter equation of state at the densities inside neutron stars? A Bayesian approach with correlated uncertainties," Phys. Rev. Lett. **125**, 202702 (2020), arXiv:2004.07232.

[199] C. Drischler, J. A. Melendez, R. J. Furnstahl, and D. R. Phillips, "Quantifying uncertainties and correlations in the nuclear-matter equation of state," Phys. Rev. C **102**, 054315 (2020), arXiv:2004.07805.

[200] S. Wesolowski, N. Klco, R. J. Furnstahl, D. R. Phillips, and A. Thapaliya, "Bayesian parameter estimation for effective field theories," J. Phys. G: Nucl. Part. Phys. **43**, 074001 (2016), arXiv:1511.03618.

[201] S. Wesolowski, R. J. Furnstahl, J. A. Melendez, and D. R. Phillips, "Exploring Bayesian parameter estimation for chiral effective field theory using nucleon-nucleon phase shifts," J. Phys. G: Nucl. Part. Phys. **46**, 045102 (2019), arXiv:1808.08211.

[202] S. Wesolowski, I. Svensson, A. Ekström, C. Forssén, R. J. Furnstahl, J. A. Melendez, and D. R. Phillips, "Rigorous constraints on three-nucleon forces in chiral effective field theory from fast and accurate calculations of few-body observables," Phys. Rev. C **104**, 064001 (2021), arXiv:2104.04441.

[203] I. Svensson, A. Ekström, and C. Forssén, "Bayesian parameter estimation in chiral effective field theory using the Hamiltonian Monte Carlo method," Phys. Rev. C **105**, 014004 (2022), arXiv:2110.04011.

[204] I. Svensson, A. Ekström, and C. Forssén, "Bayesian estimation of the low-energy constants up to fourth order in the nucleon-nucleon sector of chiral effective field theory," Phys. Rev. C **107**, 014001 (2023), arXiv:2206.08250.

[205] J. A. Melendez, R. J. Furnstahl, H. W. Grießhammer, J. A. McGovern, D. R. Phillips, and M. T. Pratola, "Designing optimal experiments: An application to proton Compton scattering," Eur. Phys. J. A **57**, 81 (2021), arXiv:2004.11307.

[206] A. F. M. Smith and A. E. Gelfand, "Bayesian statistics without tears: A sampling-resampling perspective," Am. Stat. **46**, 84 (1992).

[207] I. Vernon, M. Goldstein, and R. G. Bower, "Galaxy formation: A Bayesian uncertainty analysis," Bayesian Anal. **5**, 619 (2010).

[208] I. Vernon, M. Goldstein, and R. G. Bower, "Galaxy formation: Bayesian history matching for the observable universe," Statist. Sci. **29**, 81 (2014).

[209] A. Ekström and G. Hagen, "Global sensitivity analysis of bulk properties of an atomic nucleus," Phys. Rev. Lett. **123**, 252501 (2019), arXiv:1910.02922.

[210] S. König, A. Ekström, K. Hebeler, D. Lee, and A. Schwenk, "Eigenvector continuation as an efficient and accurate emulator for uncertainty quantification," Phys. Lett. B **810**, 135814 (2020), arXiv:1909.08446.

[211] P. Demol, T. Duguet, A. Ekström, M. Frosini, K. Hebeler, S. König, D. Lee, A. Schwenk, V. Somà, and A. Tichai, "Improved many-body expansions from eigenvector continuation," Phys. Rev. C **101**, 041302(R) (2020), arXiv:1911.12578.

[212] R. J. Furnstahl, A. J. Garcia, P. J. Millican, and X. Zhang, "Efficient emulators for scattering using eigenvector continuation," Phys. Lett. B **809**, 135719 (2020), arXiv:2007.03635.

[213] A. Sarkar and D. Lee, "Convergence of eigenvector continuation," Phys. Rev. Lett. **126**, 032501 (2021), arXiv:2004.07651.

[214] C. Drischler, M. Quinonez, P. G. Giuliani, A. E. Lovell, and F. M. Nunes, "Toward emulating nuclear reactions using eigenvector continuation," Phys. Lett. B **823**, 136777 (2021), arXiv:2108.08269.

[215] J. A. Melendez, C. Drischler, A. J. Garcia, R. J. Furnstahl, and X. Zhang, "Fast & accurate emulation of two-body scattering observables without wave functions," Phys. Lett. B **821**, 136608 (2021), arXiv:2106.15608.

[216] A. Sarkar and D. Lee, "Self-learning emulators and eigenvector continuation," Phys. Rev. Research **4**, 023214 (2022), arXiv:2107.13449.

[217] S. Yoshida and N. Shimizu, "Constructing approximate shell-model wavefunctions by eigenvector continuation," Prog. Theor. Exp. Phys. **2022**, 053D02 (2022), arXiv:2105.08256.

[218] N. Yapa and S. König, "Volume extrapolation via eigenvector continuation," Phys. Rev. C **106**, 014309 (2022), arXiv:2201.08313.

[219] X. Zhang and R. J. Furnstahl, "Fast emulation of quantum three-body scattering," Phys. Rev. C **105**, 064004 (2022), arXiv:2110.04269.

[220] A. L. Anderson, G. L. O'Donnell, and J. Piekarewicz, "Applications of reduced-basis methods to the nuclear single-particle spectrum," Phys. Rev. C **106**, L031302 (2022), arXiv:2206.14889.

[221] M. Companys Franzke, A. Tichai, K. Hebeler, and A. Schwenk, "Excited states from eigenvector continuation: The anharmonic oscillator," Phys. Lett. B **830**, 137101 (2022), arXiv:2108.02824.

[222] N. Yapa, K. Fossez, and S. König, "Eigenvector continuation for emulating and extrapolating two-body resonances," Phys. Rev. C **107**, 064316 (2023), arXiv:2303.06139.

[223] P. G. Giuliani, K. Godbey, E. Bonilla, F. Viens, and J. Piekarewicz, "Bayes goes fast: Uncertainty quantification for a covariant energy density functional emulated by the reduced basis method," Front. Phys. **10**, 1054524 (2023), arXiv:2209.13039.

[224] A. J. Garcia, C. Drischler, R. J. Furnstahl, J. A. Melendez, and X. Zhang, "Wave-function-based emulation for nucleon-nucleon scattering in momentum space," Phys. Rev. C **107**, 054001 (2023), arXiv:2301.05093.

[225] M. Companys Franzke, A. Tichai, K. Hebeler, and A. Schwenk, "Eigenvector continuation for the pairing Hamiltonian," Phys. Rev. C **109**, 024311 (2024), arXiv:2302.08373.

[226] A. L. Fetter and J. D. Walecka, *Quantum Theory of Many-Particle Systems* (McGraw-Hill, San Francisco, 1971).

[227] P. Ring and P. Schuck, *The Nuclear Many-Body Problem*, 1st ed., Theoretical and Mathematical Physics (Springer, New York, 1980).

[228] A. Szabo and N. S. Ostlund, *Modern Quantum Chemistry: Introduction to Advanced Electronic Structure Theory* (McGraw-Hill, New York, 1989).

[229] I. Shavitt and R. J. Bartlett, *Many-Body Methods in Chemistry and Physics: MBPT and Coupled-Cluster Theory*, Cambridge Molecular Science (Cambridge University Press, Cambridge, 2009).

[230] A. Altland and B. D. Simons, *Condensed Matter Field Theory*, 2nd ed. (Cambridge University Press, Cambridge, 2010).

[231] W. Kutzelnigg and D. Mukherjee, "Normal order and extended Wick theorem for a multiconfiguration reference wave function," J. Chem. Phys. **107**, 432 (1997).

[232] G. C. Wick, "The evaluation of the collision matrix," Phys. Rev. **80**, 268 (1950).

[233] J. Zhao and G. E. Scuseria, `https://github.com/tschijnmo/drudge` (2017).

[234] J. C. Slater, "The self consistent field and the structure of atoms," Phys. Rev. **32**, 339 (1928).

[235] D. R. Hartree, "The wave mechanics of an atom with a non-Coulomb central field. Part II. Some results and discussion," Math. Proc. Camb. Phil. Soc. **24**, 111 (1928).

[236] V. Fock, "Näherungsmethode zur Lösung des quantenmechanischen Mehrkörperproblems," Z. Physik **61**, 126 (1930).

[237] B. Friman, K. Hebeler, A. Schwenk, and L. Tolós, "Neutron matter from low-momentum interactions," Prog. Theor. Phys. Suppl. **168**, 639 (2007), arXiv:0704.1404.

[238] K. Hebeler and A. Schwenk, "Chiral three-nucleon forces and neutron matter," Phys. Rev. C **82**, 014314 (2010), arXiv:0911.0483.

[239] C. Drischler, K. Hebeler, and A. Schwenk, "Asymmetric nuclear matter based on chiral two- and three-nucleon interactions," Phys. Rev. C **93**, 054314 (2016), arXiv:1510.06728.

[240] C. Drischler, A. Carbone, K. Hebeler, and A. Schwenk, "Neutron matter from chiral two- and three-nucleon calculations up to N^3LO," Phys. Rev. C **94**, 054307 (2016), arXiv:1608.05615.

[241] J. Keller, C. Wellenhofer, K. Hebeler, and A. Schwenk, "Neutron matter at finite temperature based on chiral effective field theory interactions," Phys. Rev. C **103**, 055806 (2021), arXiv:2011.05855.

[242] J. Keller, K. Hebeler, and A. Schwenk, "Nuclear equation of state for arbitrary proton fraction and temperature based on chiral effective field theory and a Gaussian process emulator," Phys. Rev. Lett. **130**, 072701 (2023), arXiv:2204.14016.

[243] A. Tichai, J. Langhammer, S. Binder, and R. Roth, "Hartree-Fock many-body perturbation theory for nuclear ground-states," Phys. Lett. B **756**, 283 (2016), arXiv:1601.03703.

[244] A. Tichai, P. Arthuis, T. Duguet, H. Hergert, V. Somà, and R. Roth, "Bogoliubov many-body perturbation theory for open-shell nuclei," Phys. Lett. B **786**, 195 (2018), arXiv:1806.10931.

[245] B. S. Hu, T. Li, and F. R. Xu, "Ab initio Rayleigh-Schrödinger perturbation calculation including three-body force," arXiv:1810.08804.

[246] S. Drożdż, S. Nishizaki, J. Speth, and J. Wambach, "The nuclear response within extended RPA theories," Phys. Rep. **197**, 1 (1990).

[247] P. Papakonstantinou and R. Roth, "Second random phase approximation and renormalized realistic interactions," Phys. Lett. B **671**, 356 (2009).

[248] P. Papakonstantinou and R. Roth, "Large-scale second random-phase approximation calculations with finite-range interactions," Phys. Rev. C **81**, 024317 (2010), arXiv:0910.1674.

[249] J. M. Yao, J. Engel, L. J. Wang, C. F. Jiao, and H. Hergert, "Generator-coordinate reference states for spectra and $0\nu\beta\beta$ decay in the in-medium similarity renormalization group," Phys. Rev. C **98**, 054311 (2018), arXiv:1807.11053.

[250] E. Gebrerufael, K. Vobig, H. Hergert, and R. Roth, "*Ab initio* description of open-shell nuclei: Merging no-core shell model and in-medium similarity renormalization group," Phys. Rev. Lett. **118**, 152503 (2017), arXiv:1610.05254.

[251] S. J. Novario, G. Hagen, G. R. Jansen, and T. Papenbrock, "Charge radii of exotic neon and magnesium isotopes," Phys. Rev. C **102**, 051303(R) (2020), arXiv:2007.06684.

[252] G. Hagen, S. J. Novario, Z. H. Sun, T. Papenbrock, G. R. Jansen, J. G. Lietz, T. Duguet, and A. Tichai, "Angular-momentum projection in coupled-cluster theory: Structure of ^{34}Mg," Phys. Rev. C **105**, 064311 (2022), arXiv:2201.07298.

[253] V. Somà, C. Barbieri, and T. Duguet, "*Ab initio* Gorkov-Green's function calculations of open-shell nuclei," Phys. Rev. C **87**, 011303(R) (2013), arXiv:1208.2472.

[254] M. Frosini, T. Duguet, J.-P. Ebran, and V. Somà, "Multi-reference many-body perturbation theory for nuclei: I. Novel PGCM-PT formalism," Eur. Phys. J. A **58**, 62 (2022), arXiv:2110.15737.

[255] M. Frosini, T. Duguet, J.-P. Ebran, B. Bally, T. Mongelli, T. R. Rodríguez, R. Roth, and V. Somà, "Multi-reference many-body perturbation theory for nuclei: II. Ab initio study of neon isotopes via PGCM and IM-NCSM calculations," Eur. Phys. J. A **58**, 63 (2022), arXiv:2111.00797.

[256] M. Frosini, T. Duguet, J.-P. Ebran, B. Bally, H. Hergert, T. R. Rodríguez, R. Roth, J. M. Yao, and V. Somà, "Multi-reference many-body perturbation theory for nuclei: III. Ab initio calculations at second order in PGCM-PT," Eur. Phys. J. A **58**, 64 (2022), arXiv:2111.01461.

[257] P. Arthuis, T. Duguet, A. Tichai, R.-D. Lasseri, and J.-P. Ebran, "ADG: Automated generation and evaluation of many-body diagrams I. Bogoliubov many-body perturbation theory," Comput. Phys. Commun. **240**, 202 (2019), arXiv:1809.01187.

[258] P. Arthuis, A. Tichai, J. Ripoche, and T. Duguet, "ADG: Automated generation and evaluation of many-body diagrams II. Particle-number projected Bogoliubov many-body perturbation theory," Comput. Phys. Commun. **261**, 107677 (2021), arXiv:2007.01661.

[259] A. Tichai, J. Müller, K. Vobig, and R. Roth, "Natural orbitals for *ab initio* no-core shell model calculations," Phys. Rev. C **99**, 034321 (2019), arXiv:1809.07571.

[260] K. Tsukiyama, S. K. Bogner, and A. Schwenk, "In-medium similarity renormalization group for nuclei," Phys. Rev. Lett. **106**, 222502 (2011), arXiv:1006.3639.

[261] S. R. Stroberg, A. Calci, H. Hergert, J. D. Holt, S. K. Bogner, R. Roth, and A. Schwenk, "Nucleus-dependent valence-space approach to nuclear structure," Phys. Rev. Lett. **118**, 032502 (2017), arXiv:1607.03229.

[262] S. K. Bogner, H. Hergert, J. D. Holt, A. Schwenk, S. Binder, A. Calci, J. Langhammer, and R. Roth, "Nonperturbative shell-model interactions from the in-medium similarity renormalization group," Phys. Rev. Lett. **113**, 142501 (2014), arXiv:1402.1407.

[263] S. R. Stroberg, H. Hergert, J. D. Holt, S. K. Bogner, and A. Schwenk, "Ground and excited states of doubly open-shell nuclei from *ab initio* valence-space Hamiltonians," Phys. Rev. C **93**, 051301(R) (2016), arXiv:1511.02802.

[264] N. M. Parzuchowski, T. D. Morris, and S. K. Bogner, "*Ab initio* excited states from the in-medium similarity renormalization group," Phys. Rev. C **95**, 044304 (2017), arXiv:1611.00661.

[265] N. M. Parzuchowski, *Nuclear spectroscopy with the in-medium similarity renormalization group*, Ph.D. thesis, Michigan State University (2017).

[266] N. M. Parzuchowski, S. R. Stroberg, P. Navrátil, H. Hergert, and S. K. Bogner, "*Ab initio* electromagnetic observables with the in-medium similarity renormalization group," Phys. Rev. C **96**, 034324 (2017), arXiv:1705.05511.

[267] J. Henderson, G. Hackman, P. Ruotsalainen, S. R. Stroberg, K. D. Launey, *et al.*, "Testing microscopically derived descriptions of nuclear collectivity: Coulomb excitation of ^{22}Mg," Phys. Lett. B **782**, 468 (2018), arXiv:1709.03948.

[268] B. S. Hu, J. Padua-Argüelles, S. Leutheusser, T. Miyagi, S. R. Stroberg, and J. D. Holt, "*Ab initio* structure factors for spin-dependent dark matter direct detection," Phys. Rev. Lett. **128**, 072502 (2022), arXiv:2109.00193.

[269] S. R. Stroberg, "Beta decay in medium-mass nuclei with the in-medium similarity renormalization group," Particles **4**, 521 (2021), arXiv:2109.13462.

[270] J. M. Yao, I. Ginnett, A. Belley, T. Miyagi, R. Wirth, S. Bogner, J. Engel, H. Hergert, J. D. Holt, and S. R. Stroberg, "*Ab initio* studies of the double–Gamow-Teller transition and its correlation with neutrinoless double-β decay," Phys. Rev. C **106**, 014315 (2022), arXiv:2204.12971.

[271] B. S. Hu, Q. Wu, Z. H. Sun, and F. R. Xu, "*Ab initio* Gamow in-medium similarity renormalization group with resonance and continuum," Phys. Rev. C **99**, 061302 (2019), arXiv:1906.10539.

[272] J. M. Yao, B. Bally, J. Engel, R. Wirth, T. R. Rodríguez, and H. Hergert, "*Ab initio* treatment of collective correlations and the neutrinoless double beta decay of ^{48}Ca," Phys. Rev. Lett. **124**, 232501 (2020), arXiv:1908.05424.

[273] J. M. Yao, A. Belley, R. Wirth, T. Miyagi, C. G. Payne, S. R. Stroberg, H. Hergert, and J. D. Holt, "*Ab initio* benchmarks of neutrinoless double-β decay in light nuclei with a chiral Hamiltonian," Phys. Rev. C **103**, 014315 (2021), arXiv:2010.08609.

[274] A. Ong, J. C. Berengut, and V. V. Flambaum, "Effect of spin-orbit nuclear charge density corrections due to the anomalous magnetic moment on halonuclei," Phys. Rev. C **82**, 014320 (2010), arXiv:1006.5508.

[275] M. Hoferichter, J. Menéndez, and A. Schwenk, "Coherent elastic neutrino-nucleus scattering: EFT analysis and nuclear responses," Phys. Rev. D **102**, 074018 (2020), arXiv:2007.08529.

[276] J. L. Friar, J. Martorell, and D. W. L. Sprung, "Nuclear sizes and the isotope shift," Phys. Rev. A **56**, 4579 (1997), arXiv:nucl-th/9707016.

[277] G. Hagen, T. Papenbrock, D. J. Dean, A. Schwenk, A. Nogga, M. Włoch, and P. Piecuch, "Coupled-cluster theory for three-body Hamiltonians," Phys. Rev. C **76**, 034302 (2007), arXiv:0704.2854.

[278] S. Binder, J. Langhammer, A. Calci, and R. Roth, "*Ab initio* path to heavy nuclei," Phys. Lett. B **736**, 119 (2014), arXiv:1312.5685.

[279] R. Roth, S. Binder, K. Vobig, A. Calci, J. Langhammer, and P. Navrátil, "Medium-mass nuclei with normal-ordered chiral NN+3N interactions," Phys. Rev. Lett. **109**, 052501 (2012), arXiv:1112.0287.

[280] T. D. Morris, *Systematic improvements of ab-initio in-medium similarity renormalization group calculations*, Ph.D. thesis, Michigan State University (2016).

[281] J. F. Dawson, I. Talmi, and J. D. Walecka, "A calculation of the level spectrum of ^{18}O from the free two-nucleon potential," Ann. Phys. **18**, 339 (1962).

[282] T. T. S. Kuo and G. E. Brown, "Structure of finite nuclei and the free nucleon-nucleon interaction: An application to ^{18}O and ^{18}F," Nucl. Phys. **85**, 40 (1966).

[283] T. T. S. Kuo, "State dependence of shell-model reaction matrix elements," Nucl. Phys. A **103**, 71 (1967).

[284] T. T. S. Kuo and G. E. Brown, "Reaction matrix elements for the 0f-1p shell nuclei," Nucl. Phys. A **114**, 241 (1968).

[285] T. T. S. Kuo and E. Osnes, *Folded-Diagram Theory of the Effective Interaction in Nuclei, Atoms and Molecules*, Lecture Notes in Physics, Vol. 364 (Springer, Berlin, 1990).

[286] S. Cohen and D. Kurath, "Effective interactions for the 1p shell," Nucl. Phys. **73**, 1 (1965).

[287] A. Poves and A. P. Zuker, "Theoretical spectroscopy and the fp shell," Phys. Rep. **70**, 235 (1981).

[288] B. H. Wildenthal, "Empirical strengths of spin operators in nuclei," Prog. Part. Nucl. Phys. **11**, 5 (1984).

[289] B. A. Brown and B. H. Wildenthal, "Status of the nuclear shell model," Annu. Rev. Nucl. Part. Sci. **38**, 29 (1988).

[290] E. Caurier, G. Martínez-Pinedo, F. Nowacki, A. Poves, J. Retamosa, and A. P. Zuker, "Full 0$\hbar\omega$ shell model calculation of the binding energies of the 1$f_{7/2}$ nuclei," Phys. Rev. C **59**, 2033 (1999), arXiv:nucl-th/9809068.

[291] A. Poves, J. Sánchez-Solano, E. Caurier, and F. Nowacki, "Shell model study of the isobaric chains $A = 50$, $A = 51$ and $A = 52$," Nucl. Phys. A **694**, 157 (2001), arXiv:nucl-th/0012077.

[292] B. A. Brown and W. A. Richter, "New "USD" Hamiltonians for the *sd* shell," Phys. Rev. C **74**, 034315 (2006).

[293] E. D. Jurgenson and R. J. Furnstahl, "Similarity renormalization group evolution of many-body forces in a one-dimensional model," Nucl. Phys. A **818**, 152 (2009), arXiv:0809.4199.

[294] E. D. Jurgenson, P. Maris, R. J. Furnstahl, P. Navrátil, W. E. Ormand, and J. P. Vary, "Structure of p-shell nuclei using three-nucleon interactions evolved with the similarity renormalization group," Phys. Rev. C **87**, 054312 (2013), arXiv:1302.5473.

[295] W. Magnus, "On the exponential solution of differential equations for a linear operator," Comm. Pure Appl. Math. **7**, 649 (1954).

[296] S. Blanes, F. Casas, J. A. Oteo, and J. Ros, "The Magnus expansion and some of its applications," Phys. Rep. **470**, 151 (2009), arXiv:0810.5488.

[297] T. D. Morris, N. M. Parzuchowski, and S. K. Bogner, "Magnus expansion and in-medium similarity renormalization group," Phys. Rev. C **92**, 034331 (2015), arXiv:1507.06725.

[298] G. R. Jansen, M. D. Schuster, A. Signoracci, G. Hagen, and P. Navrátil, "Open *sd*-shell nuclei from first principles," Phys. Rev. C **94**, 011301(R) (2016), arXiv:1511.00757.

[299] Z. H. Sun, T. D. Morris, G. Hagen, G. R. Jansen, and T. Papenbrock, "Shell-model coupled-cluster method for open-shell nuclei," Phys. Rev. C **98**, 054320 (2018), arXiv:1806.07405.

[300] Z. H. Sun, G. Hagen, G. R. Jansen, and T. Papenbrock, "Effective shell-model interaction for nuclei "southeast" of ^{100}Sn," Phys. Rev. C **104**, 064310 (2021), arXiv:2107.14314.

[301] H. Hergert, S. Binder, A. Calci, J. Langhammer, and R. Roth, "*Ab initio* calculations of even oxygen isotopes with chiral two-plus-three-nucleon interactions," Phys. Rev. Lett. **110**, 242501 (2013), arXiv:1302.7294.

[302] H. Hergert, S. K. Bogner, T. D. Morris, S. Binder, A. Calci, J. Langhammer, and R. Roth, "*Ab initio* multireference in-medium similarity renormalization group calculations of even calcium and nickel isotopes," Phys. Rev. C **90**, 041302(R) (2014), arXiv:1408.6555.

[303] "Evaluated Nuclear Structure Data File (ENSDF)," `https://www.nndc.bnl.gov/ensdf/` (2024).

[304] M. Miorelli, S. Bacca, G. Hagen, and T. Papenbrock, "Computing the dipole polarizability of ^{48}Ca with increased precision," Phys. Rev. C **98**, 014324 (2018), arXiv:1804.01718.

[305] S. Kaufmann, J. Simonis, S. Bacca, J. Billowes, M. L. Bissell, *et al.*, "Charge radius of the short-lived ^{68}Ni and correlation with the dipole polarizability," Phys. Rev. Lett. **124**, 132502 (2020), arXiv:2003.06353.

[306] S. R. Stroberg, J. Henderson, G. Hackman, P. Ruotsalainen, G. Hagen, and J. D. Holt, "Systematics of $E2$ strength in the *sd* shell with the valence-space in-medium similarity renormalization group," Phys. Rev. C **105**, 034333 (2022), arXiv:2203.15342.

[307] R. F. Garcia Ruiz, M. L. Bissell, K. Blaum, A. Ekström, N. Frömmgen, *et al.*, "Unexpectedly large charge radii of neutron-rich calcium isotopes," Nat. Phys. **12**, 594 (2016), arXiv:1602.07906.

[308] T. Miyagi, S. R. Stroberg, J. D. Holt, and N. Shimizu, "*Ab initio* multishell valence-space Hamiltonians and the island of inversion," Phys. Rev. C **102**, 034320 (2020), arXiv:2004.12969.

[309] M. Kortelainen, Z. H. Sun, G. Hagen, W. Nazarewicz, T. Papenbrock, and P.-G. Reinhard, "Universal trend of charge radii of even-even Ca-Zn nuclei," Phys. Rev. C **105**, L021303 (2022), arXiv:2111.12464.

[310] E. Caurier, K. Langanke, G. Martínez-Pinedo, F. Nowacki, and P. Vogel, "Shell model description of isotope shifts in calcium," Phys. Lett. B **522**, 240 (2001), arXiv:nucl-th/0102047.

[311] A. J. Miller, K. Minamisono, A. Klose, D. Garand, C. Kujawa, *et al.*, "Proton superfluidity and charge radii in proton-rich calcium isotopes," Nat. Phys. **15**, 432 (2019).

[312] P.-G. Reinhard, J. O'Neal, S. M. Wild, and W. Nazarewicz, "Extended Fayans energy density functional: Optimization and analysis," arXiv:2402.15380.

[313] Y. S. Lee, S. A. Kucharski, and R. J. Bartlett, "A coupled cluster approach with triple excitations," J. Chem. Phys. **81**, 5906 (1984).

[314] J. Noga and R. J. Bartlett, "The full CCSDT model for molecular electronic structure," J. Chem. Phys. **86**, 7041 (1987).

[315] G. E. Scuseria and H. F. Schaefer, "A new implementation of the full CCSDT model for molecular electronic structure," Chem. Phys. Lett. **152**, 382 (1988).

[316] P. Piecuch and M. Włoch, "Renormalized coupled-cluster methods exploiting left eigenstates of the similarity-transformed Hamiltonian," J. Chem. Phys. **123**, 224105 (2005).

[317] A. G. Taube and R. J. Bartlett, "Improving upon CCSD(T): ΛCCSD(T). I. Potential energy surfaces," J. Chem. Phys. **128**, 044110 (2008).

[318] A. G. Taube and R. J. Bartlett, "Improving upon CCSD(T): ΛCCSD(T). II. Stationary formulation and derivatives," J. Chem. Phys. **128**, 044111 (2008).

[319] S. Binder, P. Piecuch, A. Calci, J. Langhammer, P. Navrátil, and R. Roth, "Extension of coupled-cluster theory with a noniterative treatment of connected triply excited clusters to three-body Hamiltonians," Phys. Rev. C **88**, 054319 (2013), arXiv:1309.1123.

[320] D. A. Varshalovich, A. N. Moskalev, and V. K. Khersonskii, *Quantum Theory of Angular Momentum* (World Scientific, Singapore, 1988).

[321] R. J. Furnstahl, G. Hagen, and T. Papenbrock, "Corrections to nuclear energies and radii in finite oscillator spaces," Phys. Rev. C **86**, 031301(R) (2012), arXiv:1207.6100.

[322] S. N. More, A. Ekström, R. J. Furnstahl, G. Hagen, and T. Papenbrock, "Universal properties of infrared oscillator basis extrapolations," Phys. Rev. C **87**, 044326 (2013), arXiv:1302.3815.

[323] R. J. Furnstahl, S. N. More, and T. Papenbrock, "Systematic expansion for infrared oscillator basis extrapolations," Phys. Rev. C **89**, 044301 (2014), arXiv:1312.6876.

[324] S. König, S. K. Bogner, R. J. Furnstahl, S. N. More, and T. Papenbrock, "Ultraviolet extrapolations in finite oscillator bases," Phys. Rev. C **90**, 064007 (2014), arXiv:1409.5997.

[325] R. J. Furnstahl, G. Hagen, T. Papenbrock, and K. A. Wendt, "Infrared extrapolations for atomic nuclei," J. Phys. G: Nucl. Part. Phys. **42**, 034032 (2015), arXiv:1408.0252.

[326] M. Moshinsky, "Transformation brackets for harmonic oscillator functions," Nucl. Phys. **13**, 104 (1959).

[327] B. Buck and A. C. Merchant, "A simple expression for the general oscillator bracket," Nucl. Phys. A **600**, 387 (1996).

[328] G. P. Kamuntavičius, R. K. Kalinauskas, B. R. Barrett, S. Mickevičius, and D. Germanas, "The general harmonic-oscillator brackets: Compact expression, symmetries, sums and Fortran code," Nucl. Phys. A **695**, 191 (2001), arXiv:nucl-th/0105009.

[329] D. Ursescu, M. Tomaselli, T. Kuehl, and S. Fritzsche, "Symbolic algorithms for the computation of Moshinsky brackets and nuclear matrix elements," Comput. Phys. Commun. **173**, 140 (2005).

[330] R. Roth, "Importance truncation for large-scale configuration interaction approaches," Phys. Rev. C **79**, 064324 (2009), arXiv:0903.4605.

[331] A. Tichai, J. Ripoche, and T. Duguet, "Pre-processing the nuclear many-body problem: Importance truncation versus tensor factorization techniques," Eur. Phys. J. A **55**, 90 (2019), arXiv:1902.09043.

[332] A. Porro, V. Somà, A. Tichai, and T. Duguet, "Importance truncation in non-perturbative many-body techniques: Gorkov self-consistent Green's function calculations," Eur. Phys. J. A **57**, 297 (2021), arXiv:2103.14544.

[333] T. Miyagi, "NuHamil: A numerical code to generate nuclear two- and three-body matrix elements from chiral effective field theory," Eur. Phys. J. A **59**, 150 (2023), arXiv:2302.07962.

[334] P. Demol, M. Frosini, A. Tichai, V. Somà, and T. Duguet, "Bogoliubov many-body perturbation theory under constraint," Ann. Phys. **424**, 168358 (2021), arXiv:2002.02724.

[335] A. Tichai, P. Demol, and T. Duguet, "Towards heavy-mass *ab initio* nuclear structure: Open-shell Ca, Ni and Sn isotopes from Bogoliubov coupled-cluster theory," Phys. Lett. B **851**, 138571 (2024), arXiv:2307.15619.

[336] Q. Yuan, S. Q. Fan, B. S. Hu, J. G. Li, S. Zhang, S. M. Wang, Z. H. Sun, Y. Z. Ma, and F. R. Xu, "Deformed in-medium similarity renormalization group," Phys. Rev. C **105**, L061303 (2022), arXiv:2204.07301.

[337] A. L. Fitzpatrick, W. Haxton, E. Katz, N. Lubbers, and Y. Xu, "The effective field theory of dark matter direct detection," J. Cosmol. Astropart. Phys. **2013**, 004 (2013), arXiv:1203.3542.

[338] D. Gazda, R. Catena, and C. Forssén, "*Ab initio* nuclear response functions for dark matter searches," Phys. Rev. D **95**, 103011 (2017), arXiv:1612.09165.

[339] P.-O. Löwdin, "Quantum theory of many-particle systems. I. Physical interpretations by means of density matrices, natural spin-orbitals, and convergence problems in the method of configurational interaction," Phys. Rev. **97**, 1474 (1955).

[340] C. F. Bender and E. R. Davidson, "A natural orbital based energy calculation for helium hydride and lithium hydride," J. Phys. Chem. **70**, 2675 (1966).

[341] E. R. Davidson, "Properties and uses of natural orbitals," Rev. Mod. Phys. **44**, 451 (1972).

[342] P. J. Hay, "On the calculation of natural orbitals by perturbation theory," J. Chem. Phys. **59**, 2468 (1973).

[343] A. K. Q. Siu and E. F. Hayes, "Configuration interaction procedure based on the calculation of perturbation theory natural orbitals: Applications to H_2 and LiH," J. Chem. Phys. **61**, 37 (1974).

[344] K. H. Thunemann, J. Römelt, S. D. Peyerimhoff, and R. J. Buenker, "A study of the convergence in iterative natural orbital procedures," Int. J. Quantum Chem. **11**, 743 (1977).

[345] H. Jørgen, Aa. Jensen, P. Jørgensen, H. Ågren, and J. Olsen, "Second-order Møller-Plesset perturbation theory as a configuration and orbital generator in multiconfiguration self-consistent field calculations," J. Chem. Phys. **88**, 3834 (1988).

[346] W. Klopper, J. Noga, H. Koch, and T. Helgaker, "Multiple basis sets in calculations of triples corrections in coupled-cluster theory," Theor. Chem. Acc. **97**, 164 (1997).

[347] M. S. Gordon, M. W. Schmidt, G. M. Chaban, K. R. Glaesemann, W. J. Stevens, and C. Gonzalez, "A natural orbital diagnostic for multiconfigurational character in correlated wave functions," J. Chem. Phys. **110**, 4199 (1999).

[348] F. Neese, A. Hansen, and D. G. Liakos, "Efficient and accurate approximations to the local coupled cluster singles doubles method using a truncated pair natural orbital basis," J. Chem. Phys. **131**, 064103 (2009).

[349] F. Neese, F. Wennmohs, and A. Hansen, "Efficient and accurate local approximations to coupled-electron pair approaches: An attempt to revive the pair natural orbital method," J. Chem. Phys. **130**, 114108 (2009).

[350] D. G. Liakos and F. Neese, "Improved correlation energy extrapolation schemes based on local pair natural orbital methods," J. Phys. Chem. A **116**, 4801 (2012).

[351] C. Riplinger and F. Neese, "An efficient and near linear scaling pair natural orbital based local coupled cluster method," J. Chem. Phys. **138**, 034106 (2013).

[352] D. G. Liakos and F. Neese, "Is it possible to obtain coupled cluster quality energies at near density functional theory cost? Domain-based local pair natural orbital coupled cluster vs modern density functional theory," J. Chem. Theory Comput. **11**, 4054 (2015).

[353] D. G. Liakos, M. Sparta, M. K. Kesharwani, J. M. L. Martin, and F. Neese, "Exploring the accuracy limits of local pair natural orbital coupled-cluster theory," J. Chem. Theory Comput. **11**, 1525 (2015).

[354] Ch. Constantinou, M. A. Caprio, J. P. Vary, and P. Maris, "Natural orbital description of the halo nucleus ^{6}He," Nucl. Sci. Tech. **28**, 179 (2017), arXiv:1605.04976.

[355] C. E. P. Robin, M. J. Savage, and N. Pillet, "Entanglement rearrangement in self-consistent nuclear structure calculations," Phys. Rev. C **103**, 034325 (2021), arXiv:2007.09157.

[356] P. J. Fasano, Ch. Constantinou, M. A. Caprio, P. Maris, and J. P. Vary, "Natural orbitals for the *ab initio* no-core configuration interaction approach," Phys. Rev. C **105**, 054301 (2022), arXiv:2112.04027.

[357] Z. H. Sun, G. Hagen, and T. Papenbrock, "Coupled-cluster theory for strong entanglement in nuclei," Phys. Rev. C **108**, 014307 (2023), arXiv:2305.07577.

[358] S. M. Hengstenberg, C. E. P. Robin, and M. J. Savage, "Multi-body entanglement and information rearrangement in nuclear many-body systems: A study of the Lipkin-Meshkov-Glick model," Eur. Phys. J. A **59**, 231 (2023), arXiv:2306.16535.

[359] A. Tichai, S. Knecht, A. Kruppa, Ö. Legeza, C. P. Moca, A. Schwenk, M. A. Werner, and G. Zarand, "Combining the in-medium similarity renormalization group with the density matrix renormalization group: Shell structure and information entropy," Phys. Lett. B **845**, 138139 (2023), arXiv:2207.01438.

[360] I. Angeli and K. P. Marinova, "Table of experimental nuclear ground state charge radii: An update," At. Data Nucl. Data Tables **99**, 69 (2013).

[361] M. Wang, G. Audi, F. G. Kondev, W. Huang, S. Naimi, and X. Xu, "The AME2016 atomic mass evaluation (II). Tables, graphs and references," Chinese Phys. C **41**, 030003 (2017).

[362] J. D. Watts and R. J. Bartlett, "Economical triple excitation equation-of-motion coupled-cluster methods for excitation energies," Chem. Phys. Lett. **233**, 81 (1995).

[363] M. K. G. Kruse, E. D. Jurgenson, P. Navrátil, B. R. Barrett, and W. E. Ormand, "Extrapolation uncertainties in the importance-truncated no-core shell model," Phys. Rev. C **87**, 044301 (2013), arXiv:1302.1226.

[364] J. Hoppe, *The in-medium similarity renormalization group for ab initio nuclear structure: Method advances and new applications*, Ph.D. thesis, Technische Universität Darmstadt (2022).

[365] S. R. Stroberg *et al.*, `https://github.com/ragnarstroberg/imsrg` (2024).

[366] C. Sanderson and R. Curtin, "Armadillo: A template-based C++ library for linear algebra," J. Open Source Softw. **1**, 26 (2016).

[367] C. Sanderson and R. Curtin, "A user-friendly hybrid sparse matrix class in C++," in *Mathematical Software – ICMS 2018: 6th International Conference, South Bend, IN, USA, July 24-27, 2018, Proceedings*, Lecture Notes in Computer Science, Vol. 10931 (Springer International Publishing, Cham, 2018) arXiv:1805.03380.

[368] M. Heinz, *Analysis of three-body effects in the in-medium similarity renormalization group*, Master's thesis, Technische Universität Darmstadt (2020).

[369] C. W. Johnson, W. E. Ormand, K. S. McElvain, and H. Shan, "BIGSTICK: A flexible configuration-interaction shell-model code," arXiv:1801.08432.

[370] N. Shimizu, T. Mizusaki, Y. Utsuno, and Y. Tsunoda, "Thick-restart block Lanczos method for large-scale shell-model calculations," Comput. Phys. Commun. **244**, 372 (2019), arXiv:1902.02064.

[371] Z. H. Sun, C. A. Bell, G. Hagen, and T. Papenbrock, "How to renormalize coupled cluster theory," Phys. Rev. C **106**, L061302 (2022), arXiv:2205.12990.

[372] P. Imgram, K. König, J. Krämer, T. Ratajczyk, B. Maaß, P. Müller, F. Sommer, and W. Nörtershäuser, "High-precision collinear laser spectroscopy at the Collinear Apparatus for Laser Spectroscopy and Applied Physics (COALA)," Hyperfine Interact. **241**, 48 (2020).

[373] K. König, J. Krämer, C. Geppert, P. Imgram, B. Maaß, T. Ratajczyk, and W. Nörtershäuser, "A new Collinear Apparatus for Laser Spectroscopy and Applied Science (COALA)," Rev. Sci. Instrum. **91**, 081301 (2020).

[374] P. Imgram, *High-precision laser spectroscopy of helium-like carbon* $^{12}C^{4+}$, Ph.D. thesis, Technische Universität Darmstadt (2022).

[375] P. Imgram, K. König, B. Maaß, P. Müller, and W. Nörtershäuser, "Collinear laser spectroscopy of $2\ ^3S_1 \rightarrow 2\ ^3P_J$ transitions in helium-like $^{12}C^{4+}$," Phys. Rev. Lett. **131**, 243001 (2023), arXiv:2311.15863.

[376] P. Imgram, K. König, B. Maaß, P. Müller, and W. Nörtershäuser, "Collinear laser spectroscopy of highly charged ions produced with an electron-beam ion source," Phys. Rev. A **108**, 062809 (2023), arXiv:2311.15943.

[377] P. Müller, *Laserspectroscopic determination of the nuclear charge radius of* ^{13}C, Ph.D. thesis, Technische Universität Darmstadt (2024).

[378] R. L. Workman *et al.* (Particle Data Group), "Review of particle physics," Prog. Theor. Exp. Phys. **2022**, 083C01 (2022).

[379] M. Wang, W. Huang, F. Kondev, G. Audi, and S. Naimi, "The AME 2020 atomic mass evaluation (II). Tables, graphs and references," Chinese Phys. C **45**, 030003 (2021).

[380] E. Epelbaum, H. Krebs, D. Lee, and U.-G. Meißner, "*Ab initio* calculation of the Hoyle state," Phys. Rev. Lett. **106**, 192501 (2011), arXiv:1101.2547.

[381] C. A. Bertulani, H.-W. Hammer, and U. van Kolck, "Effective field theory for halo nuclei: Shallow p-wave states," Nucl. Phys. A **712**, 37 (2002), arXiv:nucl-th/0205063.

[382] H.-W. Hammer, C. Ji, and D. R. Phillips, "Effective field theory description of halo nuclei," J. Phys. G: Nucl. Part. Phys. **44**, 103002 (2017), arXiv:1702.08605.

[383] T. Neff and H. Feldmeier, "Cluster structures within fermionic molecular dynamics," Nucl. Phys. A **738**, 357 (2004), arXiv:nucl-th/0312130.

[384] M. Chernykh, H. Feldmeier, T. Neff, P. Von Neumann-Cosel, and A. Richter, "Structure of the Hoyle state in ^{12}C," Phys. Rev. Lett. **98**, 032501 (2007).

[385] E. Epelbaum, H. Krebs, T. A. Lähde, D. Lee, and U.-G. Meißner, "Structure and rotations of the Hoyle state," Phys. Rev. Lett. **109**, 252501 (2012), arXiv:1101.2547.

[386] T. Otsuka, T. Abe, T. Yoshida, Y. Tsunoda, N. Shimizu, N. Itagaki, Y. Utsuno, J. Vary, P. Maris, and H. Ueno, "α-clustering in atomic nuclei from first principles with statistical learning and the Hoyle state character," Nat. Commun. **13**, 2234 (2022).

[387] A. T. Gallant, J. C. Bale, T. Brunner, U. Chowdhury, S. Ettenauer, *et al.*, "New precision mass measurements of neutron-rich calcium and potassium isotopes and three-nucleon forces," Phys. Rev. Lett. **109**, 032506 (2012).

[388] M. Enciu, H. N. Liu, A. Obertelli, P. Doornenbal, F. Nowacki, *et al.*, "Extended $p_{3/2}$ neutron orbital and the $N = 32$ shell closure in ^{52}Ca," Phys. Rev. Lett. **129**, 262501 (2022).

[389] M. Enciu, *Extended $p_{3/2}$ neutron orbital and the $N = 32$ shell closure in* ^{52}Ca, Ph.D. thesis, Technische Universität Darmstadt (2023).

[390] K. Kreim, M. L. Bissell, J. Papuga, K. Blaum, M. De Rydt, *et al.*, "Nuclear charge radii of potassium isotopes beyond $N = 28$," Phys. Lett. B **731**, 97 (2014), arXiv:1310.5171.

[391] H. Heylen, C. Babcock, R. Beerwerth, J. Billowes, M. L. Bissell, *et al.*, "Changes in nuclear structure along the Mn isotopic chain studied via charge radii," Phys. Rev. C **94**, 054321 (2016), arXiv:1609.05021.

[392] K. Minamisono, D. M. Rossi, R. Beerwerth, S. Fritzsche, D. Garand, *et al.*, "Charge radii of neutron deficient ^{52,53}Fe produced by projectile fragmentation," Phys. Rev. Lett. **117**, 252501 (2016).

[393] Á. Koszorús, X. F. Yang, W. G. Jiang, S. J. Novario, S. W. Bai, *et al.*, "Charge radii of exotic potassium isotopes challenge nuclear theory and the magic character of $N = 32$," Nat. Phys. **17**, 439 (2021), arXiv:2012.01864.

[394] F. Sommer, *Nuclear charge radii across the $N = Z = 28$ shell closure in nickel isotopes*, Ph.D. thesis, Technische Universität Darmstadt (2021).

[395] F. Sommer, K. König, D. M. Rossi, N. Everett, D. Garand, *et al.*, "Charge radii of ^{55,56}Ni reveal a surprisingly similar behavior at $N = 28$ in Ca and Ni isotopes," Phys. Rev. Lett. **129**, 132501 (2022), arXiv:2210.01924.

[396] S. Malbrunot-Ettenauer, S. Kaufmann, S. Bacca, C. Barbieri, J. Billowes, *et al.*, "Nuclear charge radii of the nickel isotopes $^{58-68,70}$Ni," Phys. Rev. Lett. **128**, 022502 (2022), arXiv:2112.03382.

[397] T. Lellinger, Ph.D. thesis to be submitted to the Technische Universität Darmstadt.

[398] O. B. Tarasov, D. S. Ahn, D. Bazin, N. Fukuda, A. Gade, *et al.*, "Discovery of ^{60}Ca and implications for the stability of ^{70}Ca," Phys. Rev. Lett. **121**, 022501 (2018).

[399] M. L. Cortés, W. Rodriguez, P. Doornenbal, A. Obertelli, J. D. Holt, *et al.*, "Shell evolution of $N = 40$ isotones towards ^{60}Ca: First spectroscopy of ^{62}Ti," Phys. Lett. B **800**, 135071 (2020), arXiv:1912.07887.

[400] S. Chen, F. Browne, P. Doornenbal, J. Lee, A. Obertelli, *et al.*, "Level structures of ^{56,58}Ca cast doubt on a doubly magic ^{60}Ca," Phys. Lett. B **843**, 138025 (2023), arXiv:2307.07077.

[401] A. Gade and B. M. Sherrill, "NSCL and FRIB at Michigan State University: Nuclear science at the limits of stability," Phys. Scr. **91**, 053003 (2016).

[402] M. Durante, P. Indelicato, B. Jonson, V. Koch, K. Langanke, U.-G. Meißner, E. Nappi, T. Nilsson, Th. Stöhlker, E. Widmann, and M. Wiescher, "All the fun of the FAIR: Fundamental physics at the facility for antiproton and ion research," Phys. Scr. **94**, 033001 (2019), arXiv:1903.05693.

[403] J. C. Berengut, D. Budker, C. Delaunay, V. V. Flambaum, C. Frugiuele, E. Fuchs, C. Grojean, R. Harnik, R. Ozeri, G. Perez, and Y. Soreq, "Probing new long-range interactions by isotope shift spectroscopy," Phys. Rev. Lett. **120**, 091801 (2018), arXiv:1704.05068.

[404] C. Solaro, S. Meyer, K. Fisher, J. C. Berengut, E. Fuchs, and M. Drewsen, "Improved isotope-shift-based bounds on bosons beyond the standard model through measurements of the ^{2}D$_{3/2}$ $-^2$ D$_{5/2}$ interval in Ca$^+$," Phys. Rev. Lett. **125**, 123003 (2020), arXiv:2005.00529.

[405] T. T. Chang, B. B. Awazi, J. C. Berengut, E. Fuchs, and S. C. Doret, "Systematic-free limit on new light scalar bosons via isotope shift spectroscopy in Ca$^+$," arXiv:2311.17337.

[406] G. Hagen, P. Hagen, H.-W. Hammer, and L. Platter, "Efimov physics around the neutron-rich ^{60}Ca isotope," Phys. Rev. Lett. **111**, 132501 (2013), arXiv:1306.3661.

[407] J. D. Holt, J. Menéndez, J. Simonis, and A. Schwenk, "Three-nucleon forces and spectroscopy of neutron-rich calcium isotopes," Phys. Rev. C **90**, 024312 (2014), arXiv:1405.7602.

[408] L. Neufcourt, Y. Cao, W. Nazarewicz, E. Olsen, and F. Viens, "Neutron drip line in the Ca region from Bayesian model averaging," Phys. Rev. Lett. **122**, 062502 (2019), arXiv:1901.07632.

[409] F. Bonaiti, private communication.

[410] J. Simonis, S. Bacca, and G. Hagen, "First principles electromagnetic responses in medium-mass nuclei: Recent progress from coupled-cluster theory," Eur. Phys. J. A **55**, 241 (2019), arXiv:1905.02055.

[411] G. A. Negoita, J. P. Vary, G. R. Luecke, P. Maris, A. M. Shirokov, I. J. Shin, Y. Kim, E. G. Ng, C. Yang, M. Lockner, and G. M. Prabhu, "Deep learning: Extrapolation tool for *ab initio* nuclear theory," Phys. Rev. C **99**, 054308 (2019), arXiv:1810.04009.

[412] W. G. Jiang, G. Hagen, and T. Papenbrock, "Extrapolation of nuclear structure observables with artificial neural networks," Phys. Rev. C **100**, 054326 (2019), arXiv:1905.06317.

[413] M. Knöll, T. Wolfgruber, M. L. Agel, C. Wenz, and R. Roth, "Machine learning for the prediction of converged energies from ab initio nuclear structure calculations," Phys. Lett. B **839**, 137781 (2023), arXiv:2207.03828.

[414] T. Wolfgruber, M. Knöll, and R. Roth, "Precise neural network predictions of energies and radii from the no-core shell model," arXiv:2310.05256.

[415] G. Hagen and H. A. Nam, "Computational aspects of nuclear coupled-cluster theory," Prog. Theor. Phys. Suppl. **196**, 102 (2012), arXiv:1203.3765.

[416] S. R. Stroberg, "Factorized approximations of IMSRG(3)," talk given at TRIUMF workshop on Progress in Ab Initio Nuclear Theory (2024).

[417] B. C. He and S. R. Stroberg, "Factorized approximation to the IMSRG(3)," arXiv:2405.19594.

[418] C. Delaunay, R. Ozeri, G. Perez, and Y. Soreq, "Probing atomic Higgs-like forces at the precision frontier," Phys. Rev. D **96**, 093001 (2017), arXiv:1601.05087.

[419] K. Blaum, J. Dilling, and W. Nörtershäuser, "Precision atomic physics techniques for nuclear physics with radioactive beams," Phys. Scr. **2013**, 014017 (2013), arXiv:1210.4045.

[420] I. Counts, J. Hur, D. P. L. Aude Craik, H. Jeon, C. Leung, J. C. Berengut, A. Geddes, A. Kawasaki, W. Jhe, and V. Vuletić, "Evidence for nonlinear isotope shift in Yb^+ search for new boson," Phys. Rev. Lett. **125**, 123002 (2020), arXiv:2004.11383.

[421] J. Hur, D. P. L. Aude Craik, I. Counts, E. Knyazev, L. Caldwell, C. Leung, S. Pandey, J. C. Berengut, A. Geddes, W. Nazarewicz, P.-G. Reinhard, A. Kawasaki, H. Jeon, W. Jhe, and V. Vuletić, "Evidence of two-source King plot nonlinearity in spectroscopic search for new boson," Phys. Rev. Lett. **128**, 163201 (2022), arXiv:2201.03578.

[422] N. L. Figueroa, J. C. Berengut, V. A. Dzuba, V. V. Flambaum, D. Budker, and D. Antypas, "Precision determination of isotope shifts in ytterbium and implications for new physics," Phys. Rev. Lett. **128**, 073001 (2022), arXiv:2111.01429.

[423] N. Shimizu, Y. Tsunoda, Y. Utsuno, and T. Otsuka, "Variational approach with the superposition of the symmetry-restored quasiparticle vacua for nuclear shell-model calculations," Phys. Rev. C **103**, 014312 (2021), arXiv:2011.03157.

[424] W. H. King, *Isotope Shifts in Atomic Spectra* (Plenum Press, New York, 1984).

[425] E. C. Seltzer, "K x-ray isotope shifts," Phys. Rev. **188**, 1916 (1969).

[426] V. V. Flambaum, A. J. Geddes, and A. V. Viatkina, "Isotope shift, nonlinearity of King plots, and the search for new particles," Phys. Rev. A **97**, 032510 (2018), arXiv:1709.00600.

[427] R. Rana, M. Höcker, and E. G. Myers, "Atomic masses of strontium and ytterbium," Phys. Rev. A **86**, 050502(R) (2012).

[428] D. A. Nesterenko, R. P. de Groote, T. Eronen, Z. Ge, M. Hukkanen, A. Jokinen, and A. Kankainen, "High-precision mass measurement of ^{168}Yb for verification of nonlinear isotope shift," Int. J. Mass Spectrom. **458**, 116435 (2020), arXiv:2007.13375.

[429] J. Repp, C. Böhm, J. R. Crespo López-Urrutia, A. Dörr, S. Eliseev, S. George, M. Goncharov, Y. N. Novikov, C. Roux, S. Sturm, S. Ulmer, and K. Blaum, "PENTATRAP: A novel cryogenic multi-Penning-trap experiment for high-precision mass measurements on highly charged ions," Appl. Phys. B **107**, 983 (2012), arXiv:1110.2919.

[430] M. Door, Ph.D. thesis to be submitted to the Ruprecht-Karls-Universität Heidelberg.

[431] C.-H. Yeh, Ph.D. thesis to be submitted to the Leibniz Universität Hannover.

[432] K. Ono, Y. Saito, T. Ishiyama, T. Higomoto, T. Takano, Y. Takasu, Y. Yamamoto, M. Tanaka, and Y. Takahashi, "Observation of nonlinearity of generalized King plot in the search for new boson," Phys. Rev. X **12**, 021033 (2022), arXiv:2110.13544.

[433] H. Kurasawa, T. Suda, and T. Suzuki, "The mean square radius of the neutron distribution and the skin thickness derived from electron scattering," Prog. Theor. Exp. Phys. **2021**, 013D02 (2021), arXiv:2009.00759.

[434] S. O. Allehabi, V. A. Dzuba, V. V. Flambaum, and A. V. Afanasjev, "Nuclear deformation as a source of the nonlinearity of the King plot in the Yb^+ ion," Phys. Rev. A **103**, L030801 (2021), arXiv:2012.04043.

[435] A. Tichai, P. Arthuis, K. Hebeler, M. Heinz, J. Hoppe, and A. Schwenk, "Low-rank matrix decompositions for *ab initio* nuclear structure," Phys. Lett. B **821**, 136623 (2021), arXiv:2105.03935.

[436] B. Zhu, R. Wirth, and H. Hergert, "Singular value decomposition and similarity renormalization group evolution of nuclear interactions," Phys. Rev. C **104**, 044002 (2021), arXiv:2106.01302.

[437] A. Tichai, P. Arthuis, K. Hebeler, M. Heinz, J. Hoppe, A. Schwenk, and L. Zurek, "Least-square approach for singular value decompositions of scattering problems," Phys. Rev. C **106**, 024320 (2022), arXiv:2205.10087.

[438] A. Tichai, P. Arthuis, K. Hebeler, M. Heinz, J. Hoppe, T. Miyagi, A. Schwenk, and L. Zurek, "Low-rank decompositions of three-nucleon forces via randomized projections," arXiv:2307.15572.

[439] A. Tichai, R. Wirth, J. Ripoche, and T. Duguet, "Symmetry reduction of tensor networks in many-body theory: I. Automated symbolic evaluation of $SU(2)$ algebra," Eur. Phys. J. A **56**, 272 (2020), arXiv:2002.05011.

Erklärung zur Dissertation

Gemäß §9 Abs. 1 Promotionsordnung

Die Dissertation ist von mir mit einem Verzeichnis aller benutzten Quellen versehen. Ich erkläre, dass ich die Arbeit – abgesehen von den in ihr ausdrücklich genannten Hilfen – selbstständig verfasst habe. Ich erkläre, dass die elektronische Version mit der schriftlichen Version übereinstimmt.

Darmstadt, den 4. Juni 2024

Matthias Heinz